Final Report

Active Control Methods for Multi-Dimensional Vibration of Thin-Walled Rotor Structures

Matthew O. T. Cole
Department of Mechanical Engineering
Chiang Mai University

15th June 2019

Grant Contract No. BRG5980013

Final Report

Active Control Methods for Multi-Dimensional Vibration of Thin-Walled Rotor Structures

Matthew O. T. Cole
Department of Mechanical Engineering
Chiang Mai University

Wichaphon Fakkaew
School of Engineering
University of Phayao

Project funded by the Thailand Research Fund and Chiang Mai University

Confidentiality and copyright

ABSTRACT

Project code:	BRG5980013
Project title:	Active control methods for multi-dimensional vibration of thin-walled rotor structures
Investigator:	Matthew O. T. Cole
Co-investigator:	Wichaphon Fakkaew
Email address:	motcole@dome.eng.cmu.ac.th, wichaphon.fa@up.ac.th
Project period:	15^{th} June 2016 - 14^{th} June 2019

To extend envelops of operation and performance, rotating machines are evolving away from solid-shaft design topologies towards more complex thin-walled rotor structures. Modern dynamic analysis methods can deal with rotating structures having complex three-dimensional geometric forms. However, there has been little published research on how realistic whole-rotor dynamic models can be exploited in the design of active vibration control systems. This project will address this deficiency by conducting basic research on the application of advanced active bearing technology with thin-walled rotor structures. The main focus of the work was vibration behavior and control methodologies. The main research outcomes were

1. New theoretical models of dynamic behavior of thin-walled rotors based on shell theory, with experimental validations.

2. New models of vibration excitation in thin-walled rotor structures due to asymmetry, including non-circularity effects, with experimental validations.

3. Development of a novel distributed actuation active magnetic bearings and associated sensing and control approaches for thin-walled rotors.

4. Development of active control approaches for whole rotor vibration subject to shaft bending and shell distortion.

The research findings are relevant to the design and operation of various machine types, particularly turbomachinery. They may also be used for new applications in the alternative energy field, such as wind and tidal power, where novel lightweight rotor/turbine structures may be realized using the active bearing technology developed through this project.

Keywords: structural vibration, rotating machines, rotordynamics, magnetic bearings, vibration control

Acknowledgments

I am very grateful for the financial support from the Thailand Research Fund and Chiang Mai University that made possible the work described in this report. This funding has been very important in enabling me to continue working in Thailand as a lecturer and also pursue my research interests in rotordynamics and control. The work for this project was completed in collaboration with the co-investigator Dr Wichaphon Fakkaew (University of Phayao), and with vital contributions from research associates Dr Chakkapong Chamroon (University of Phayao) and Mr Ziv Brand (Chiang Mai University and Nevdev Nuclear Research Centre, Israel). I am also grateful to the staff and student members of the Motion and Control Laboratory, Department of Mechanical Engineering, CMU, for their fruitful discussions and assistance, especially Dr Theeraphong Wongratanphisan, Dr Radom Pongvutitham and Dr Pinyo Puangmali.

Executive summary

In rotating machine design, achieving high stiffness-to-mass ratio for rotating parts is often a key requirement for extending envelops of operation and performance. This has led to the introduction of hollow shaft rotor designs for several machine types, including turbomachines. In addition to specialized applications, thin-walled rotor topologies can play a significant role in future lightweight turbo-machine design. Research is needed to improve our understanding of the dynamic behavior of thin-walled rotor structures and the complex three-dimensional vibration to which they are susceptible. New approaches for active rotor vibration control and active bearing technology are also required. The aim of this project was to address this need by conducting basic research on the dynamic behaviour of thin-walled rotor structures and developing new methods for active control of rotordynamic stability and structural vibration.

The research findings from this project are relevant to the design and operation of complex rotor structures in various machine types including turbomachinery and fans. The findings may also be used for new applications in the alternative energy field, such as wind and tidal power, where novel lightweight rotor/turbine structures may be designed and operated using the results from this research.

The research outcomes from the work may summarised based on five key publications from the project:

1. "An active magnetic bearing for thin-walled rotors: Vibrational dynamics and stabilizing control", (*IEEE/ASME Transactions on Mechatronics*)

A new active magnetic bearing design and control approach for supporting thin-walled rotor structures was developed and tested. The design embodies a distributed actuation scheme, synthesized from a theoretical description of rotor vibration with the aim of decoupling the levitation control system dynamics from the flexural dynamics of the rotor wall. The approach was validated by both analytical and experimental studies focusing on stability and vibration behavior for a short-length rotor-bearing system. The results will motivate further application of the distributed actuation approach for more complex thin-walled rotor systems, including those with multiple bearing units or multi-directional actuator distributions. This will facilitate new approaches to rotor-bearing system design and active vibration control for various machine types.

2. "Vibration due to non-circularity of a rotating ring having discrete radial supports - with application to thin-walled rotor/magnetic bearing systems", (*Journal of Sound and Vibration*)

A new mathematical model for the vibration of a thin-walled cylindrical rotor subject to small non-circularity and coupled to space-fixed bearing supports was developed. Rotor non-circularity was shown to give rise to multi-harmonic excitation of the rotor-bearing structure. Whether a resonance occurs at a predicted critical speed depends on the multi-

plicity and symmetry of the bearing supports. Generally, a large number of evenly spaced identical supports will eliminate the possibility of low order resonance conditions. The modelling approach was also applied to a thin-walled rotor-AMB system by accounting for feedback controlled electromagnetic actuators within the formulation.

3. "Model and control system development for a distributed actuation magnetic bearing and thin-walled rotor subject to noncircularity" (*ASME Journal of Vibration and Acoustics*)

A control approach was developed for reducing the vibration of a flexible thin-walled rotor supported by a distributed actuation magnetic bearing. Although direct measurements of rotor noncircularity may be used to compensate its effect on position signals used for feedback control, multi-harmonic vibration may still arise due to measurement error and other excitation mechanisms. An approach for harmonic vibration control has therefore been introduced that achieves effective vibration suppression without requiring information on the rotor shape. Experiments were conducted on a short thin-walled rotor with single DAMB to confirm the efficacy of the proposed methods in preventing resonance during operation. In future work, extending the approach for application with longer thin-walled rotors having DAMB support in multiple planes will be considered.

4. "On the vibrational dynamics of thin-walled rotating cylinders: A theoretical and experimental study utilizing active magnetic bearings", (*International Journal of Mechanical Sciences* - under revision)

This work defined and experimentally verified a 3-dimensional multi-mode model for the vibration behaviour of a thin-walled cylindrical rotor based on shell theory. The described model can provide a complete and accurate description of the vibrational dynamics of a thin-walled cylindrical rotor for a practical range of excitation types and rotational speeds. The described theoretical model may be used to construct benchmark cases for validation of finite element codes for rotating shell structures. It also has good suitability for use in the design of active vibration control strategies. This will be considered in future work.

5. "Controllability and actuator placement optimization for active damping of a thin rotating ring with piezo patch transducers", (*Journal of Sound and Vibration* - under review)

In this work, the optimal placement of piezoelectric actuators for suppressing elastic vibration of a thin rotating ring was investigated. A theoretical model for flexural dynamics involving bending and extension in the plane of a rotation was adopted and a time-weighted controllability metric used to calculate the optimal locations of actuators for a given set of targeted modes and range of rotational speeds. Experimental results confirmed the suitability of the theoretical models and quantitative analysis of speed-dependent control influence for the actuator/sensor placement problem. The results have important implications and may be extended for cases with more complex thin-walled rotating structures, where the impact of rotation effects on controllability should be accounted for in the design of active vibration control strategies.

The publication outputs from the project inlcuded one conference paper and six journal papers derived from the work (four published and two currently under review/revision).

The main aspect of the project where the original objectives were not fully met was in extending the work to more complex systems involving bladed rotor structures. As there

were considerable challenges in the modelling and dynamic analysis of simple cylindrical thin-walled structures, the project work focused on these cases only. However, the results are promising and the extension to bladed rotors appears to be feasible for the active bearing technology and active control techniques developed in the present work.

In terms of collaborations and other related outcomes, the project activities have contributed to the career development of young academics at the University of Phayao. Dr Whichaphon Fakkaew, the co-investigator for the project has been able to advance to Assistant Professor status. Also, Dr Chakkapong Chamroon has now applied for Assistant Professor status. This has been possible due to their collaboration and co-authoring of papers for this project.

The project has involved international collaboration with a visiting researcher from Nevdev Nuclear Research Centre, Israel (Mr Ziv Brand). This collaboration has focused on the application of piezoelectric actuation and sensing for active vibration control of thin-walled rotor structures. Joint publications have included a conference paper, to be presented at the 3rd International Conference on Control Technology and Applications (Hong Kong in August 2019). A draft manuscript for a journal paper has also been completed and is now under review for the Journal of Sound and Vibration.

Short term impact from the project has included the application and award of a follow-on research grant from the TRF on Compact Affordable Kinetic Energy Storage (CAKES 1 Project RGU6280014). This work will apply the research findings from the present project in the creation of a prototype for a compact lightweight flywheel energy storage system. The anticipation is that successful demonstration of the concept may lead to the commercial production of a small flywheel energy storage system for use as an Uninterruptible Power Supply (UPS) device.

Chapter 1

Introduction

1.1 Problem statement

In rotating machine design, achieving high stiffness-to-mass ratio for rotating parts is often a key requirement for extending envelops of operation and performance. This has led to the introduction of hollow shaft rotor designs for several machine types, including turbo-machines [58, 9, 29]. Modern additive manufacturing methods such as metal deposition and optimized composite shell fabrication will further support the creation of more complex thin-walled rotor structures [40]. In addition to specialized applications, thin-walled rotor topologies can play a significant role in future lightweight turbo-machine design [61]. Research is needed to improve our understanding of the dynamic behavior of thin-walled rotor structures and the complex three-dimensional vibration to which they are susceptible. New approaches for active rotor vibration control and active bearing technology are also required. The aim of this project was to address this need by conducting basic research on the dynamic behaviour of thin-walled rotor structures and developing new methods for active control of rotordynamic stability and structural vibration.

The research findings from this project are relevant to the design and operation of complex rotor structures in various machine types including turbomachinery and fans. The findings may also be used for new applications in the alternative energy field, such as wind and tidal power, where novel lightweight rotor/turbine structures may be designed and operated using the results from this research.

1.2 Outline of report

The work undertaken focuses on three main aspects which are: rotordynamic modelling; bearing/actuator design and operation; and control system design and implementation. The first two chapters describe the development of theoretical models for vibration behaviour of a thin-walled ring (2D) and long cylinder (3D) rotor. Chapter 2 describes a general analytical model for the vibration behaviour of a rotating thin-walled cylinder based on Love's shell theory. Numerical methods are explained and results for natural frequency and mode-shape characteristics presented. Chapter 3 focuses on the simplification of the general 3D model for the case of a short-length cylinder/ring with radial bearing supports. Numerical predictions of vibration excitation due to the combined effects of rotation and noncircularity are also presented. Chapter 4 describes the development of a novel type of active magneic bearing for supporting thin-walled rotors. Basic design equations and stability analysis are provided based on the 2D rotating ring model. Experimental validations confirm the effectiveness of the DAMB design and accuracy of the

theoretical rotordynamic models based on shell theory. Chapter 5 presents an advanced control system design that is appled with the DAMB to suppress vibration caused by rotor unbalance and non-circularity. Chapter 6 described a novel experimenal thin-walled rotor system with two radial DAMBs and presents results on dynamic behaviour and validation of the theoretical 3D model based on shell theory.

In summary, the structure for the remainder of the report is as follows:

Chapter 2 Theoretical model for 3D vibration of a a thin-walled rotor

Chapter 3 Thin rotating ring model and vibration arising due to noncircularity

Chapter 4 A distributed actuation magnetic bearing (DAMB) for thin-walled rotors: design, modelling and test results

Chapter 5 Advanced controller design for a DAMB-rotor system

Chapter 6 Experimental thin-walled rotor/DAMB system: vibration behviour and 3D model verification

Chapter 7 Conclusions and summary of project outputs

1.3 Research objectives

The objectives have, in essence, remained unchanged from those in the project proposal. These objectives were to

1. Formulate a general modelling approach for whole-rotor dynamics that will accurately predict coupled vibration of substructures and is well-suited, in both form and complexity, to modern dynamic analysis and active controller design procedures.

2. Develop, implement and evaluate novel AMB-based distributed actuation and sensing schemes suitable for large diameter and thin-walled rotor structures.

3. Determine methodologies for optimal and robust controller design that can effectively suppress coupled substructure vibration based on whole-rotor models.

4. Conduct lab-based testing on experimental systems in order to validate the modelling approaches and control methodologies arising from objectives 1 - 3.

Chapter 2

Theoretical model for 3D vibration of a thin-walled rotor

2.1 Introduction

Rotating cylindrical shell structures are essential components in various mechanical systems and processes. Gear and shaft transmissions, wheel, roller and tire assemblies, thin-walled tubes under machining, and turbo-machine rotors, are common examples. Vibration characteristics of rotating cylindrical shells differ from those of stationary shells due to the effects of centrifugal and Coriolis forces as well as initial hoop tension. The presence of Coriolis forces leads to traveling-wave phenomenon for free vibration, as first reported in 1890 by Bryan [4]. Distinct natural wave speeds arise for forward and backward-traveling waves, and these can vary significantly with rotational speed [21, 70]. Various thin-shell theories (characterized by differing sets of strain-displacement relations) may be used to derive the equations of motion [56, 47, 38, 1]. In terms of simplicity and accuracy, the theory of Love is often considered appropriate [42, 32], although a drawback of the theory is that certain rigid-body motions will not be correctly described [64].

For free vibration of cylindrical shells, analytical solutions for the displacement field can be expressed as two multiplicative components: the angular mode-shape function that describes the circumferential traveling waves and the axial mode-shape function that describes longitudinal deformation and which depends on the boundary conditions. For simply supported boundary conditions, the axial functions will involve known sine and cosine functions [38, 69, 63, 71]. To deal with other types of boundary conditions, some authors have used characteristic mode shapes for beam bending as approximate axial modal functions [32, 43, 49]. Unfortunately, the frequency characteristics obtained in this way are of limited accuracy as the governing equations cannot be exactly satisfied. More accurate results can be obtained with series functions such as differential quadrature functions [31], Fourier series [73] or orthogonal polynomials [72]. However, such solutions can require many terms to obtain accurate results for general sets of boundary conditions.

Exact axial mode shapes for arbitrary homogeneous boundary conditions can be expressed as a finite sum of weighted exponential functions [25]. As the exact solutions satisfy both the equations of motion and boundary conditions, they involve orthogonal functions. This property is important for decoupling the modal response equations in the case of forced vibration. Alujevic et al. [1] employed this approach to find exact solutions for free vibration of a free-free rotating cylinder. As the method is semi-analytical, care must be taken to formulate the solution in a way that avoids numerical conditioning problems. Natural frequency values were compared with published experimental data [75, 68]

and good agreement was shown, but only for non-rotating cases. Also, non-zero natural frequencies were obtained for rigid-body tilting modes, even without rotation, due to the aforementioned limitation of Love's theory. Experimental studies on the vibration of short rotating cylindrical shells have been undertaken previously, and the applicability of simplified 2D shell/ring models shown [22]. The case of rotating cylindrical shells of short axial length subject to harmonic excitation has also been investigated in the context of rolling tire vibration and noise [38, 49, 33].

This chapter described the creation of a analytical model for the vibration behaviour of a rotating thin-walled cylinder based on Love's shell theory. The model is descritized in modal form with speed-dependent coefficients. This simple parametric form is well-suited for rotodynamic analysis and the prediction of forced vibration response. The application and experimental verification of this model on a rotor-AMB system is described later in chapter 4.

2.2 Rotating cylindrical shell model

2.2.1 Governing equations

A uniform cylindrical shell, rotating at constant angular speed Ω about its axis, may be considered as shown in Fig. 2.1a. The radius, axial length and thickness are denoted by R, L and d, respectively. Let $x_0y_0z_0$ and xyz be local Cartesian coordinate systems fixed at the undeformed and deformed middle surface within the cylinder wall. The components of displacement along the undeformed axes are denoted by $u_r(\theta,\, z,\, t)$, $v_r(\theta,\, z,\, t)$ and $w_r(\theta,\, z,\, t)$. The cylinder is homogeneous, isotropic and linearly elastic with Young's modulus E, Poisson ratio ν and density ρ. It is assumed that the axis of rotation aligns with z_0. Figure 2.1b shows the internal forces and couples acting on a shell element, which are aligned with deformed coordinate axes. Here, $Q_0 = \rho d R^2\Omega^2$ is the mean circumferential stress due to centrifugal loading. The components of the external force per unit area are denoted by f_x, f_y, and f_z. The equations of motion with respect to the undeformed rotating coordinate system may be derived as

$$\frac{1}{R}\frac{\partial Q_{yx}}{\partial\theta} + \frac{\partial Q_{zx}}{\partial z} + \frac{Q_{yy}}{R} + \frac{Q_0}{R}\left(1 + \frac{\partial\beta_z}{\partial\theta}\right) + f_x = \rho d\left(\ddot{u}_r + 2\Omega\dot{v}_r + \Omega^2(R - u_r)\right) \quad (2.1)$$

$$\frac{1}{R}\frac{\partial Q_{yy}}{\partial\theta} + \frac{\partial Q_{zy}}{\partial z} - \frac{Q_{yx}}{R} + \frac{Q_0}{R}\left(\frac{\partial\epsilon_z}{\partial\theta} - \beta_z\right) + f_y = \rho d\left(\ddot{v}_r - 2\Omega\dot{u}_r - \Omega^2 v_r\right) \quad (2.2)$$

$$\frac{1}{R}\frac{\partial Q_{yz}}{\partial\theta} + \frac{\partial Q_{zz}}{\partial z} - \frac{Q_0}{R}\frac{\partial\beta_x}{\partial\theta} + f_z = \rho d\ddot{w}_r \quad (2.3)$$

$$Q_{yx} = \frac{1}{R}\frac{\partial M_{yy}}{\partial\theta} + \frac{\partial M_{zy}}{\partial z}, \quad Q_{zx} = -\frac{1}{R}\frac{\partial M_{yz}}{\partial z} - \frac{\partial M_{zz}}{\partial z} \quad (2.4)$$

Also, $Q_{yz} = Q_{zy}$ and $M_{yz} = -M_{zy}$.

The derivation of these equations can be found in other sources, although some differences are seen for the terms in Ω^2 and Q_0, depending on whether the equations of motion are formulated and linearized using the deformed or undeformed coordinate system [32]. In our derivation, the acceleration and force components were related by applying Newton-Euler's equations in the undeformed axis system, with the assumption that rotation occurs about the undisplaced cylinder axis (aligned with the z_0 axis).

The internal forces/moments are described by the constitutive equations from Kirchhoff-Love theory [45]:

$$[Q_{yy},\, Q_{zz},\, Q_{zy}] = C\left[\epsilon_y + \nu\epsilon_z,\ \epsilon_z + \nu\epsilon_y,\ \tfrac{1-\nu}{2}\gamma_{yz}\right] \quad (2.5)$$

$$[M_{yy},\, M_{zz},\, M_{yz}] = D\left[-\frac{1}{R}\frac{\partial\beta_z}{\partial\theta} - \nu\frac{\partial\beta_y}{\partial z},\ \frac{\partial\beta_y}{\partial z} + \frac{\nu}{R}\frac{\partial\beta_z}{\partial\theta},\ \frac{1-\nu}{2R}\left(\frac{\partial\beta_y}{\partial\theta} + \frac{\partial\beta_z}{\partial z}\right)\right] \quad (2.6)$$

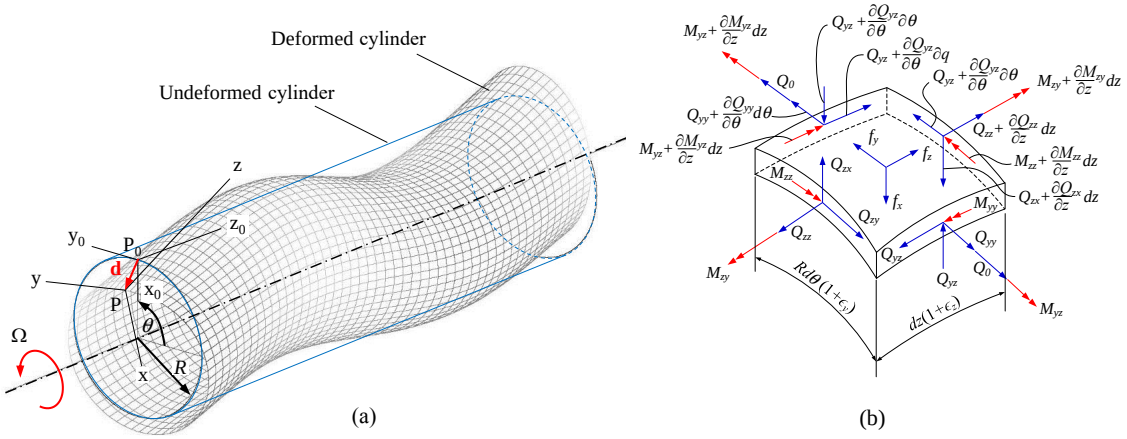

Figure 2.1: Thin-walled cylindrical rotor model: (a) coordinate systems (b) internal forces/moments acting on shell element

with $C = \frac{Ed}{1-\nu^2}$ and $D = \frac{Ed}{12(1-\nu^2)}$ and

$$\epsilon_y = \frac{1}{R}\frac{\partial v_r}{\partial \theta} - \frac{u_r}{R}, \quad \epsilon_z = \frac{\partial w_r}{\partial z}, \quad \gamma_{yz} = \frac{\partial v_r}{\partial z} + \frac{1}{R}\frac{\partial w_r}{\partial \theta}, \tag{2.7}$$

$$\beta_x = -\frac{1}{R}\frac{\partial w_r}{\partial \theta}, \quad \beta_y = \frac{\partial u_r}{\partial z}, \quad \beta_z = \frac{1}{R}\frac{\partial u_r}{\partial \theta} + \frac{v_r}{R}. \tag{2.8}$$

To describe the interaction with space-fixed elements (which for a rotor system may include bearing supports and other stator-mounted parts), a transformation to stationary-frame coordinates is required. Stationary-frame displacements are defined by $u(\phi,\, z,\, t) = u_r(\theta,\, z,\, t)$, $v(\phi,\, z,\, t) = v_r(\theta,\, z,\, t)$ and $w(\phi,\, z,\, t) = w_r(\theta,\, z,\, t)$, where $\phi = \theta + \Omega t$. The following relations hold for each pair of variables:

$$\frac{\partial u_r}{\partial \theta} = \frac{\partial u}{\partial \phi}, \quad \dot{u}_r = \dot{u} + \Omega\frac{\partial u}{\partial \phi}, \quad \ddot{u}_r = \ddot{u} + 2\Omega\frac{\partial \dot{u}}{\partial \phi} + \Omega^2\frac{\partial^2 u}{\partial \phi^2} \tag{2.9}$$

Using Eqs (2.4)-(2.6) in Eqs (2.1)-(2.3) and applying Eq. (2.9) gives

$$\begin{aligned}
L_x(u,\, v,\, w) + f_x &= \rho d\left[\ddot{u} + 2\Omega\left(\frac{\partial \dot{u}}{\partial \phi} + \dot{v}\right) + \Omega^2\left(\frac{\partial v}{\partial \phi} - u\right)\right] \\
L_y(u,\, v,\, w) + f_y &= \rho d\left[\ddot{v} + 2\Omega\left(\frac{\partial \dot{v}}{\partial \phi} - \dot{u}\right) + \Omega^2\frac{\partial}{\partial \phi}\left(\frac{\partial v}{\partial \phi} - u - R\frac{\partial w}{\partial z}\right)\right] \\
L_z(u,\, v,\, w) + f_z &= \rho d\left[\ddot{w} + 2\Omega\frac{\partial \dot{w}}{\partial \phi}\right]
\end{aligned} \tag{2.10}$$

where

$$\begin{aligned}
L_x(u,\, v,\, w) &= C\left[\frac{1}{R^2}\left(\frac{\partial v}{\partial \phi} - u\right) + \frac{\nu}{R}\frac{\partial w}{\partial z}\right] - D\left[\frac{\partial^4 u}{\partial z^4} + \frac{1}{R^2}\frac{\partial^3 v}{\partial \phi \partial z^2} + \frac{2}{R^2}\frac{\partial^4 u}{\partial \phi^2 \partial z^2} + \frac{1}{R^4}\frac{\partial^4 u}{\partial \phi^4} + \frac{1}{R^4}\frac{\partial^3 v}{\partial \phi^3}\right] \\
L_y(u,\, v,\, w) &= C\left[\frac{1-\nu}{2}\frac{\partial^2 v}{\partial z^2} + \frac{1+\nu}{2R}\frac{\partial^2 w}{\partial \phi \partial z} + \frac{1}{R^2}\left(\frac{\partial^2 v}{\partial \phi^2} - \frac{\partial u}{\partial \phi}\right)\right] + D\left[\frac{1-\nu}{2R^2}\frac{\partial^2 v}{\partial z^2} + \frac{1}{R^4}\frac{\partial^2 v}{\partial \phi^2} + \frac{1}{R^4}\frac{\partial^3 u}{\partial \phi^3} + \frac{1}{R^2}\frac{\partial^3 u}{\partial \phi \partial z^2}\right] \\
L_z(u,\, v,\, w) &= C\left[\frac{\partial^2 w}{\partial z^2} + \frac{1+\nu}{2R}\frac{\partial^2 v}{\partial \phi \partial z} - \frac{\nu}{R}\frac{\partial u}{\partial z} + \frac{1-\nu}{2R^2}\frac{\partial^2 w}{\partial \phi^2}\right]
\end{aligned}$$

For rotordynamic analysis, it is appropriate to consider free boundaries at both ends of the cylinder. According to Fig. 2.1b, there are five resultant forces at the end surfaces. As the order of the equations of motion is four, only four boundary constraints are needed. Kirchhoff effective shear stress resultants [32, 69] are used to combine shear force and moment values as $V_{zx} = Q_{zx} + \frac{1}{R}\frac{\partial M_{zy}}{\partial \theta}$ and $V_{zy} = Q_{zy} - \frac{1}{R}M_{zy}$. Setting $Q_{zz} = M_{zz} =$

$V_{zx} = V_{zy} = 0$ at the boundaries then yields

$$\begin{aligned}
\left[\frac{\partial w}{\partial z} + \frac{\nu}{R}\left(\frac{\partial v}{\partial \phi} - u\right)\right]_{z=\pm L/2} &= 0 \\
\left[\frac{\partial^2 u}{\partial z^2} + \frac{\nu}{R^2}\left(\frac{\partial^2 u}{\partial \phi^2} + \frac{\partial v}{\partial \phi}\right)\right]_{z=\pm L/2} &= 0 \\
\left[\frac{1}{R^2}\frac{\partial^2 v}{\partial \phi \partial z} + \frac{2-\nu}{R^2}\frac{\partial^3 u}{\partial \phi^2 \partial z} + \frac{\partial^3 u}{\partial z^3}\right]_{z=\pm L/2} &= 0 \\
\left[\frac{\partial v}{\partial z} + \frac{1}{R}\frac{\partial w}{\partial \phi} + \frac{h^2}{12R^2}\left(\frac{\partial v}{\partial z} + 2\frac{\partial^2 u}{\partial \phi \partial z}\right)\right]_{z=\pm L/2} &= 0
\end{aligned} \tag{2.11}$$

2.2.2 Exact solutions for free vibration

To obtain solutions for free vibration, the external forces are set to zero and the following forms assumed:

$$u = \alpha e^{\lambda z}\cos(m\phi \pm \omega_m t), \quad v = -\beta e^{\lambda z}\sin(m\phi \pm \omega_m t), \quad w = \gamma e^{\lambda z}\cos(m\phi \pm \omega_m t) \tag{2.12}$$

where m is the integer-valued circumferential wavenumber, ω_m is the natural frequency and λ, α, β and γ are arbitrary constants. Note that the '+' and '−' correspond to the backward and forward traveling wave solutions, respectively. Substituting Eq. (2.12) into Eq. (2.10), yields

$$\begin{bmatrix} a_4\lambda^4 + a_2\lambda^2 + a_0 + a_\omega, & d_2\lambda^2 + d_0 + d_\omega, & e_1\lambda \\ d_2\lambda^2 + d_0 + d_\omega, & b_2\lambda^2 + b_0 + b_\omega, & (f_1 + f_2)\lambda \\ -e_1\lambda, & -f_1\lambda, & c_2\lambda^2 + c_0 + c_\omega \end{bmatrix} \begin{bmatrix} \alpha \\ \beta \\ \gamma \end{bmatrix} = 0 \tag{2.13}$$

where, with $\delta = d^2/12R^2$, the coefficients are given by

$$\begin{aligned}
&a_4 = -\delta R^4, \quad a_2 = 2\delta m^2 R^2, \quad a_0 = -\delta m^4 - 1, \quad a_\omega = \tfrac{\rho h R^2}{C}(\omega_m^2 + \Omega^2 \pm 2\Omega\omega_m m), \\
&b_2 = \tfrac{1-\nu}{2}(1+\delta)R^2, \quad b_0 = -(1+\delta)m^2, \quad b_\omega = \tfrac{\rho h R^2}{C}(\omega_m^2 + \Omega^2 m^2 \pm 2\Omega\omega_m m), \\
&c_2 = R^2, \quad c_0 = -\tfrac{1-\nu}{2}m^2, \quad c_\omega = \tfrac{\rho h R^2}{C}(\omega_m^2 \pm 2\Omega\omega_m m) \\
&d_2 = \delta m R^2 \quad d_0 = -\delta m^3 - m, \quad d_\omega = \tfrac{\rho h R^2}{C}(\Omega^2 m \pm 2\Omega\omega_m), \\
&e_1 = \nu R, \quad f_1 = \tfrac{1+\nu}{2}mR, \quad f_2 = \tfrac{\rho h R^3}{C}\Omega^2 m
\end{aligned}$$

The equations of motion can be satisfied only if the determinant of the matrix in Eq. (2.13) is zero. This yields a biquartic polynomial in λ:

$$A_8\lambda^8 + A_6\lambda^6 + A_4\lambda^4 + A_2\lambda^2 + A_0 = 0 \tag{2.14}$$

where the coefficients are defined in appendix A. The displacements can therefore be expressed

$$u = U(z)\cos(m\phi \pm \omega_m t), \quad v = -V(z)\sin(m\phi \pm \omega_m t), \quad w = W(z)\cos(m\phi \pm \omega_m t) \tag{2.15}$$

where the z-dependent factors are a linear combination of the eight eigensolutions:

$$U(z) = \sum_{k=1}^{8} C_k\alpha_k \exp(\lambda_k z), \; V(z) = \sum_{k=1}^{8} C_k\beta_k \exp(\lambda_k z), \; W(z) = \sum_{k=1}^{8} C_k\gamma_k \exp(\lambda_k z). \tag{2.16}$$

Here, C_k are complex constants, to be determined. At this stage, the roots λ_k must be calculated by assuming a value for the frequency ω_m and then solving Eq. (2.14). The corresponding eigenvectors $\Psi_k = [\alpha_k, \beta_k, \gamma_k]^T$ can then be constructed from the null space of the matrix in Eq. (2.13). The axial mode shape function $G(z) = [U(z), V(z), W(z)]^T$ can be changed from complex to real-valued representation according to

$$G(z) = \sum_{k=1}^{8} C_k \Psi_k \exp(\lambda_k z) = \sum_{k=1}^{8} \kappa_k \Gamma_k(z) \tag{2.17}$$

where $\Gamma_k(z) : \mathbb{R} \to \mathbb{R}^3$ are given in appendix B for each possible type of root for Eq. (2.14). The real coefficients κ_k must be determined such that $G(z)$ satisfies the boundary conditions. This will only be possible if a correct natural frequency value has been assumed for ω_m. Although the transformation to real functions and coefficients in Eq. (2.17) complicates the formulation, it simplifies the solution procedure and helps in avoiding numerical conditioning problems. Equation (2.17) may be expressed in the matrix form:

$$G(z) = \mathbf{\Gamma}(z) K \tag{2.18}$$

where $K = \left[\begin{array}{cccc} \kappa_1 & \kappa_2 & \ldots & \kappa_8 \end{array} \right]^T$ and $\mathbf{\Gamma}(z) = \left[\begin{array}{cccc} \Gamma_1(z) & \Gamma_2(z) & \ldots & \Gamma_8(z) \end{array} \right]$ is a 3×8 matrix. By substituting Eq. (2.15) into Eq. (2.11), the boundary constraints may be expressed

$$\mathbf{B} K = 0, \tag{2.19}$$

where

$$\mathbf{B} = \left[\begin{array}{c} [\mathbf{B}_0 \mathbf{\Gamma}(z) + \mathbf{B}_1 \mathbf{\Gamma}'(z) + \mathbf{B}_2 \mathbf{\Gamma}''(z) + \mathbf{B}_3 \mathbf{\Gamma}'''(z)]_{z=-L/2} \\ [\mathbf{B}_0 \mathbf{\Gamma}(z) + \mathbf{B}_1 \mathbf{\Gamma}'(z) + \mathbf{B}_2 \mathbf{\Gamma}''(z) + \mathbf{B}_3 \mathbf{\Gamma}'''(z)]_{z=L/2} \end{array} \right]$$

with

$$\mathbf{B}_0 = \left[\begin{array}{ccc} -\nu & -\nu m & 0 \\ -\nu m^2 & -\nu m & 0 \\ 0 & 0 & m/R \\ 0 & 0 & 0 \end{array} \right], \quad \mathbf{B}_1 = \left[\begin{array}{ccc} 0 & 0 & R \\ 0 & 0 & 0 \\ 2\delta m & 1+\delta & 0 \\ -(2-\nu)m^2 & -m & 0 \end{array} \right],$$

$$\mathbf{B}_2 = \left[\begin{array}{ccc} 0 & 0 & 0 \\ R^2 & 0 & 0 \\ 0 & 0 & 0 \\ 0 & 0 & 0 \end{array} \right], \quad \mathbf{B}_3 = \left[\begin{array}{ccc} 0 & 0 & 0 \\ 0 & 0 & 0 \\ 0 & 0 & 0 \\ R^2 & 0 & 0 \end{array} \right].$$

The determinant of $\mathbf{B}$ must be zero in order to obtain a non-trivial solution for K.

To determine the natural frequencies, the frequency range of interest is first discretized. Each frequency value is then substituted into Eq. (2.14), with m set to a fixed integer, in order to solve for λ_k and corresponding Ψ_k. It is then possible to construct $\mathbf{B}$ and calculate its determinant. Existence of a solution is indicated by a change in the sign of the determinant for two adjacent frequencies. A secant method can then be used to refine the solution to the required accuracy. The coefficient vector K can then be calculated by construction from the null space of $\mathbf{B}$ e.g. using a singular value decomposition algorithm. If $G(z)$ is represented using complex coefficients and functions, then the determinant of $\mathbf{B}$ can take complex values. In this case, the zero-crossing method cannot be used and finding the natural frequencies becomes more difficult.

Equation (2.16) is valid only if the roots λ_k are non-zero. For $m = 1$ and $\omega_m = 0$, the coefficient A_0 vanishes and so there are two zero-valued roots. In addition, for $m = 0$ and

Table 2.1: Physical properties of cylinder for case study

Parameter	Symbol	Value	Units
Length	L	0.8	m
Radius	R	0.0815	m
Wall thickness	d	0.00306	m
Young's modulus	E	2.08×10^{11}	$\mathrm{N/m}^2$
Density	ρ	7850	$\mathrm{kg/m}^3$
Poisson's ratio	ν	0.3	

$\omega_m = 0$, both A_0 and A_2 vanish and this give four zero-valued roots. These solutions, which correspond to the rigid-body modes, are not correctly represented by Eq. (2.16). However, a simpler form for $G(z)$ may be assumed and substituted into Eq. (2.10) to obtain the corresponding natural frequencies. This approach is described in detail in section 2.2.3.

2.2.3 Numerical solutions and preliminary analysis

Numerical results were obtained using physical properties listed in Table 2.1. These match the experimental system described later in chapter 6. For the experimental system, the recorded data relates to bending mode vibration within a frequency range of 0-2000 Hz. For construction of a theoretical model, a broader range of natural frequencies and mode types was first considered. Figure 2.2 shows the natural frequencies for the non-rotating cylinder, obtained by the solution method in section 2.2.2 (with $\Omega = 0$). Selected mode shapes are shown in Figs 2.3 and 2.4. The mode shapes may be classified as out-of-surface bending or in-surface shear and extensional, depending on the dominant displacement directions. For the z-dependent mode shape function, the notation $G_{mn}(z)$ is adopted where the index m is the circumferential wavenumber, as previously defined. For the bending modes, the index n is equal to the number of nodes (zero-crossings) of $U(z)$.

Natural frequencies for bending modes are shown in Fig. 2.2a. The modes with $m = 1$ include the rigid-body translation and tilting modes (with $n = 0, 1$, respectively), as well as the beam bending modes ($n > 1$), as shown in Fig. 2.3. Note that, for a given value of n, the trend of changing natural frequency with increasing circumferential wavenumber m depends on the length-to-radius ratio of the cylinder.

Modes with $m = 0$ include those for which either axial extension or bending are dominant, as shown in Fig. 2.4. For modes where the axial extension is dominant, then n^* denotes the number of nodes of $W(z)$. The natural frequencies shown in Fig. 2.2b also include torsional shear modes, as indicated by $\square$ symbols. Modes with $n^* = 0$ are axial shear modes, while other modes for which $m \neq 0$ and $n^* \neq 0$ involve more complex in-surface shear and extension, some examples of which are also shown in Fig. 2.4. For the experimental tests, the excitation of these modes is negligible.

To obain the physically correct results for the rigid-body modes, solutions were constructed using the assumed modes method. For cases with $m = 0$, setting $G(z) = [\alpha,\, \beta,\, \gamma]^T$ in Eq. (2.15) and substituting into Eq. (2.10) yields $\omega_{0,0} = \omega_{0,0^*} = 0$, and $G_{0,0}(z) = [0,\, 0,\, 1]^T$, $G_{0,0^*}(z) = [0,\, 1,\, 0]^T$, which correspond to translation along the z-axis and rotation about the z-axis, respectively. For $m = 1$, setting $G(z) = [\alpha,\, \beta,\, \gamma]^T$ and $G(z) = [\alpha z,\, \beta z,\, R]^T$, yields $\omega_{1,0} = \omega_{1,1} = 0$ and $G_{1,0}(z) = [1,\, -1,\, 0]^T$, $G_{1,1}(z) = [z,\, -z,\, R]^T$, which describe lateral translation and tilting motions. For the flexible modes, the exact solution method was used to find the natural frequencies and mode shapes in all cases.

To obtain exact solutions for the rotating cylinder, the same solution method may be

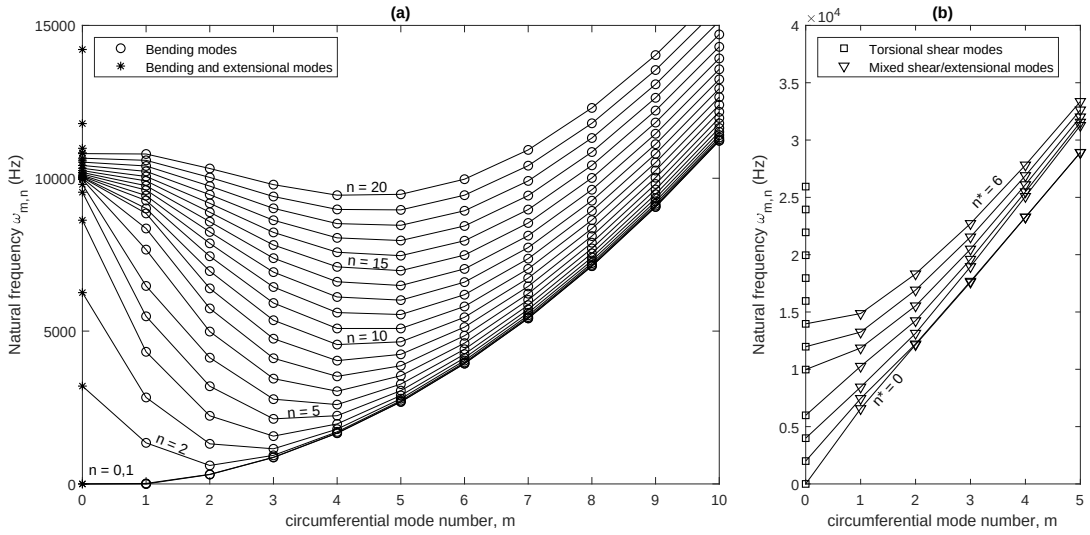

Figure 2.2: The natural frequencies of a non-rotating cylindrical shell with properties in Table 2.1: a) bending and extensional modes, b) torsional and mixed shear/extensional modes

applied but with Ω set to non-zero value in Eq. (2.13).

2.3 Speed-dependent rotordynamic model

2.3.1 Mode-shape invariance and modal decoupling

To construct a speed-dependent parametric model, the issues of orthogonality and invariance of the mode shape functions is first considered. Substituting the zero-speed eigensolutions in Eq. (2.10) yields

$$\mathcal{K}_{mn} = -\omega_{mn}^2 G_{mn}, \quad \Omega = 0 \tag{2.20}$$

where

$$\mathcal{K}_{mn} = \frac{C}{\rho d R^2} \begin{bmatrix} a_4 U_{mn}'''' + a_2 U_{mn}'' + a_0 U_{mn} + d_2 V_{mn}'' + d_0 V_{mn} + e_1 W_{mn}' \\ d_2 U_{mn}'' + d_0 U_{mn} + b_2 V_{mn}'' + b_0 V_{mn} + f_1 W_{mn}' \\ -e_1 U_{mn}' - f_1 V_{mn}' + c_2 W_{mn}'' + c_0 W_{mn} \end{bmatrix} \tag{2.21}$$

For the case with rotation,

$$\left.\begin{aligned} \mathcal{K}_{mn} &= -(\omega_{mn}^b)^2 G_{mn} - 2\Omega\omega_{mn}^b \mathbf{\Lambda}_m G_{mn} - \Omega^2 \mathbf{\Pi}_m G_{mn} \\ \mathcal{K}_{mn} &= -(\omega_{mn}^f)^2 G_{mn} + 2\Omega\omega_{mn}^f \mathbf{\Lambda}_m G_{mn} - \Omega^2 \mathbf{\Pi}_m G_{mn} \end{aligned}\right\} \quad \Omega \neq 0 \tag{2.22}$$

where the backward and forward mode frequencies are denoted ω_{mn}^b and ω_{mn}^f, respectively. If the centrifugal stress term in Eq. (2.2) associated with the axial strain gradient $\left(\frac{Q_0}{R}\frac{\partial \epsilon_z}{\partial \theta}\right)$ is neglected (so that $f_2 = 0$ in Eq. (2.13)) then both $\mathbf{\Lambda}_m$ and $\mathbf{\Pi}_m$ have symmetric forms:

$$\mathbf{\Lambda}_m = \begin{bmatrix} m & 1 & 0 \\ 1 & m & 0 \\ 0 & 0 & m \end{bmatrix}, \quad \mathbf{\Pi}_m = \begin{bmatrix} 1 & m & 0 \\ m & m^2 & 0 \\ 0 & 0 & 0 \end{bmatrix} \tag{2.23}$$

The boundary constraints from Eq. (2.11), are

$$\begin{aligned}\left[W'_{mn} - \tfrac{\nu}{R}\left(U_{mn} + mV_{mn}\right)\right]_{z=\pm L/2} &= 0\\ \left[U''_{mn} - \tfrac{\nu}{R^2}\left(m^2 U_{mn} + mV_{mn}\right)\right]_{z=\pm L/2} &= 0\\ \left[U'''_{mn} - (2-\nu)\tfrac{m^2}{R^2}U'_{mn} - \tfrac{m}{R^2}V'_{mn}\right]_{z=\pm L/2} &= 0\\ \left[2\delta m U'_{mn} + (1+\delta)\,V'_{mn} + \tfrac{m}{R}W_{mn}\right]_{z=\pm L/2} &= 0\end{aligned} \tag{2.24}$$

By applying Eq. (2.24), it can be shown that

$$\int_{-L/2}^{L/2} G_{mq}^T \mathcal{K}_{mn} - G_{mn}^T \mathcal{K}_{mq} dz = 0. \tag{2.25}$$

Therefore, from Eq. (2.20), $(\omega_{mn}^2 - \omega_{mq}^2)\int_{-L/2}^{L/2} G_{mq}^T G_{mn} dz = 0$. Since $\omega_{mn} \neq \omega_{mq}$, it can be concluded that

$$\int_{-L/2}^{L/2} G_{mq}^T G_{mn} dz = \begin{cases} a_{mn}, & q = n \\ 0, & q \neq n \end{cases} \tag{2.26}$$

where $a_{mn} = \int_{-L/2}^{L/2} G_{mn}^T G_{mn} dz$. This implies orthogonality of the stationary mode shapes.

Using Eq. (2.20) to substitute for $\mathcal{K}_{mn}$ in Eq. (2.22) and applying Eq. (2.26), it may be shown that, if $\mathbf{\Lambda}_m = \mathbf{\Lambda}_m^T$ and $\mathbf{\Pi}_m = \mathbf{\Pi}_m^T$, then $(\omega_{mn}^b - \omega_{mq}^b)\int_{-L/2}^{L/2} G_{mq}^T \mathbf{\Lambda}_m G_{mn} dz = 0$. Since $\omega_{mn}^b \neq \omega_{mq}^b$, it can be concluded

$$\int_{-L/2}^{L/2} G_{mq}^T \mathbf{\Lambda}_m G_{mn} dz = \begin{cases} m a_{mn} + b_{mn}, & q = n \\ 0, & q \neq n \end{cases} \tag{2.27}$$

where $b_{mn} = 2\int_{-L/2}^{L/2} U_{mn} V_{mn} dz$. It then also follows from Eq. (2.22), that

$$\int_{-L/2}^{L/2} G_{mq}^T \mathbf{\Pi}_m G_{mn} dz = \begin{cases} c_{mn}, & q = n \\ 0, & q \neq n \end{cases} \tag{2.28}$$

where $c_{mn} = \int_{-L/2}^{L/2} (U_{mn} + mV_{mn})^2 dz$. Note that the coefficient c_{mn} is a measure of the circumferential extension. With no extension, $u = \partial v/\partial\theta$ and so $U_{mn} + mV_{mn} = 0$.

The implication of equations (2.27) and (2.28) is that, with symmetric matrices $\mathbf{\Lambda}_m$ and $\mathbf{\Pi}_m$ (as in Eq. (2.23)), the zero-speed mode shapes G_{mn} are also eigensolutions of Eq. (2.22), i.e. the mode shapes are unaffected by rotation. Now, substituting Eq. (2.20) into Eq. (2.22), then premultiplying by G_{mn}^T and integrating over $z \in [-L/2, L/2]$ yields a set of quadratic equations for the natural frequencies, the solutions for which are

$$\omega_{mn}^{b,f} = \sqrt{\omega_{mn}^2 + \Omega^2\left[\left(m + \tfrac{b_{mn}}{a_{mn}}\right)^2 - \tfrac{c_{mn}}{a_{mn}}\right]} \mp \Omega\left(m + \tfrac{b_{mn}}{a_{mn}}\right) \tag{2.29}$$

Here, the lower value corresponds to the backwards wave solution. Table 2.2 shows natural frequency values for the cylindrical rotor (Table 2.1) for two cases: 1) based on exact solution with inclusion of the $\partial\epsilon_z/\partial\phi$ term in Eq. (2.2); and 2) using the formula from Eq. (2.29), which neglects the $\partial\epsilon_z/\partial\theta$ term. For the first ten bending modes, there is agreement within four significant figures when $\Omega/2\pi$=30 Hz. For higher rotational speeds, the difference becomes more apparent for higher order modes, although agreement within

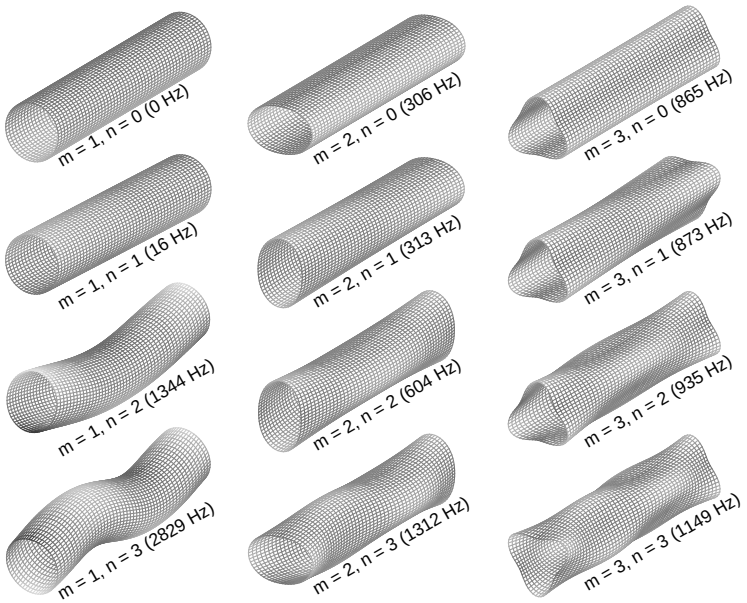

Figure 2.3: Example mode shapes for free vibration of cylindrical shell in low natural frequency range

three significant figures is still obtained for the cases shown with $\Omega/2\pi$=300 Hz. The formula Eq. (2.29) can be used directly to construct a Campbell diagram for the free rotating cylinder, as shown in Fig. 2.5. The decoupling equations (2.27) and (2.28) also facilitate the construction of a parametric speed-dependent model for forced vibration, as described in section 2.3.2.

2.3.2 Parametric model for forced vibration

For the prediction of forced vibration involving rigid-body and bending mode excitation ($m \geq 1$), a truncated modal expansion is adopted where $p_{mn}(t)$ and $q_{mn}(t)$ are modal response variables:

$$\begin{aligned} u(\phi, z, t) &= \sum_{m=1}^{M} \sum_{n=0}^{N} U_{mn}(z) \left[p_{mn}(t) \sin m\phi + q_{mn}(t) \cos m\phi \right] \\ v(\phi, z, t) &= \sum_{m=1}^{M} \sum_{n=0}^{N} V_{mn}(z) \left[p_{mn}(t) \cos m\phi - q_{mn}(t) \sin m\phi \right] \\ w(\phi, z, t) &= \sum_{m=1}^{M} \sum_{n=0}^{N} W_{mn}(z) \left[p_{mn}(t) \sin m\phi + q_{mn}(t) \cos m\phi \right] \end{aligned} \tag{2.30}$$

Suppose an external point load $P(t) = [P_x(t),\, P_y(t),\, P_z(t)]^T$ is applied at $(\phi, z) = (\phi_P, z_P)$, then

$$[f_x,\, f_y,\, f_z]^T = \tfrac{1}{R} P(t) \delta(\phi - \phi_P) \delta(z - z_P) \tag{2.31}$$

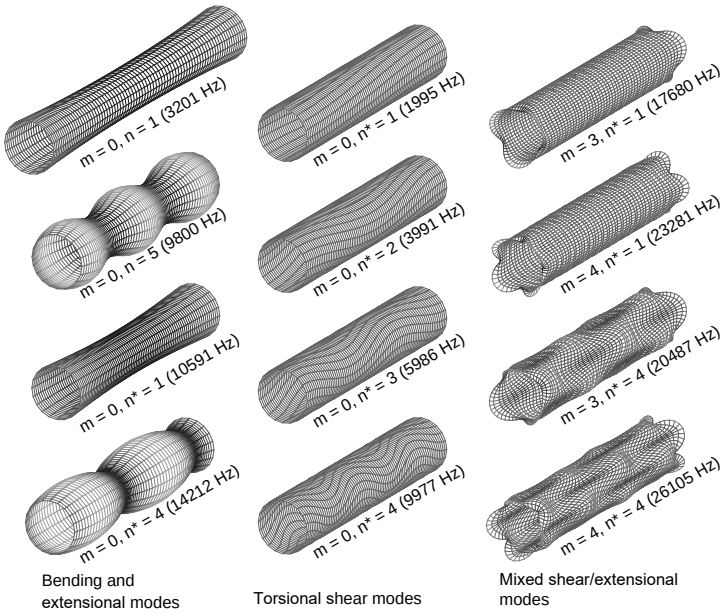

Figure 2.4: Example mode shapes for free vibration of cylindrical shell in high natural frequency range

Table 2.2: Numerical results for bending mode dynamics of free cylinder. Natural frequency values are shown from exact solution and from using parametric formula Eq. (2.29)

	$\Omega/2\pi = 0$ Hz			$\Omega/2\pi = 30$ Hz				$\Omega/2\pi = 300$ Hz			
mode shape indices		coefficients		formula		exact		formula		exact	
	ω_{mn}	$\frac{b_{mn}}{a_{mn}}$	$\frac{c_{mn}}{a_{mn}}$	ω^f_{mn}	ω^b_{mn}	ω^f_{mn}	ω^b_{mn}	ω^f_{mn}	ω^b_{mn}	ω^f_{mn}	ω^b_{mn}
	(Hz)			(Hz)		(Hz)		(Hz)		(Hz)	
$m = 2$, $n = 0$	305.99	-0.80022	7.5358e-7	344.09	272.10	344.09	272.10	832.35	112.49	832.16	112.51
$m = 2$, $n = 1$	313.40	-0.79535	1.4149e-6	351.61	279.33	351.61	279.33	839.75	116.96	839.49	116.95
$m = 2$, $n = 2$	603.90	-0.78598	1.8652e-4	641.41	568.57	641.40	568.55	1069.4	341.00	1067.7	339.47
$m = 3$, $n = 0$	865.19	-0.60054	5.3070e-6	940.16	796.19	940.16	796.19	1845.3	405.65	1845.3	405.70
$m = 3$, $n = 1$	872.60	-0.59996	9.7775e-6	947.57	803.56	947.56	803.56	1851.3	411.29	1850.9	411.28
$m = 3$, $n = 2$	934.81	-0.59975	6.8217e-5	1009.6	865.57	1009.6	865.56	1900.1	459.91	1899.2	459.35
$m = 3$, $n = 3$	1149.1	-0.59998	2.8198e-4	1223.4	1079.4	1223.4	1079.4	2076.1	636.05	2074.3	634.59
$m = 2$, $n = 3$	1311.9	-0.77816	6.4058e-4	1349.1	1275.7	1349.0	1275.7	1728.7	995.57	1726.0	993.10
$m = 1$, $n = 2$	1344.1	-0.86113	1.0239e-3	1348.3	1339.9	1348.3	1339.9	1386.4	1303.1	1384.2	1300.9
$m = 4$, $n = 2$	1703.6	-0.4725	5.9478e-5	1812.7	1601.0	1812.7	1601.0	3063.8	947.26	3063.1	947.00

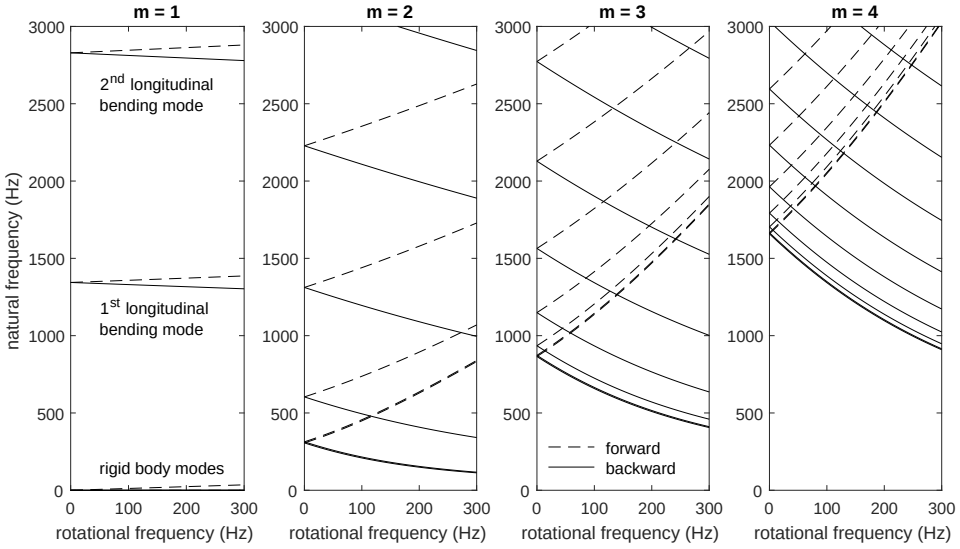

Figure 2.5: Campbell diagram for free rotating cylinder with properties in Table 2.1.

Substituting Eqs (2.30) and (2.31) into Eq. (2.10) and exploiting the orthogonality properties of $\sin m\theta$ and $\cos m\theta$ yields a set of $2M$ equations:

$$\begin{aligned}\sum_{n=0}^{\infty}\mathcal{K}_{mn}p_{mn}+\mathcal{F}_m^p&=\sum_{n=0}^{\infty}\left[G_{mn}\ddot{p}_{mn}-2\Omega\mathbf{\Lambda}_m G_{mn}\dot{q}_{mn}-\Omega^2\mathbf{\Pi}_m G_{mn}p_{mn}\right]\\ \sum_{n=0}^{\infty}\mathcal{K}_{mn}q_{mn}+\mathcal{F}_m^q&=\sum_{n=0}^{\infty}\left[G_{mn}\ddot{q}_{mn}+2\Omega\mathbf{\Lambda}_m G_{mn}\dot{p}_{mn}-\Omega^2\mathbf{\Pi}_m G_{mn}q_{mn}\right]\end{aligned} \tag{2.32}$$

where $\mathcal{F}_m^{p,q}=(\rho\pi Rd)^{-1}\mathbf{H}_m^{p,q}(\phi_P)P(t)\delta(z-z_P)$ with $\mathbf{H}_m^p(\phi)=\mathrm{diag}\left([\sin m\theta\phi,\,\cos m\phi,\,\sin m\phi]\right)$ and $\mathbf{H}_m^q(\phi)=\mathrm{diag}\left([\cos m\phi,\,-\sin m\phi,\,\cos m\phi]\right)$. Substituting $\mathcal{K}_{mn}=-\omega_{mn}^2G_{mn}$, and pre-multiplying by G_{mq}^T, then integrating over $z\in[-L/2,L/2]$ and applying orthogonality properties from Eqs. (2.26)-(2.28), yields

$$\begin{aligned}\ddot{p}_{mn}-2\Omega\left(m+\tfrac{b_{mn}}{a_{mn}}\right)\dot{q}_{mn}+\left(\omega_{mn}^2-\Omega^2\tfrac{c_{mn}}{a_{mn}}\right)p_{mn}&=\tfrac{1}{\mu_{mn}}G_{mn}^T(z_P)\mathbf{H}_m^p(\phi_P)P(t)\\ \ddot{q}_{mn}+2\Omega\left(m+\tfrac{b_{mn}}{a_{mn}}\right)\dot{p}_{mn}+\left(\omega_{mn}^2-\Omega^2\tfrac{c_{mn}}{a_{mn}}\right)q_{mn}&=\tfrac{1}{\mu_{mn}}G_{mn}^T(z_P)\mathbf{H}_m^q(\phi_P)P(t)\end{aligned} \tag{2.33}$$

where $\mu_{mn}=\rho\pi Rda_{mn}$.

It can be easily verified that the rigid-body dynamics are correctly represented by Eq. (2.33) when the assumed mode shapes given in section 2.2.3 are adopted. Of special importance for rotordynamic analysis are the tilting modes with $G_{1,1}(z)=[z,\,-z,\,R]^T$, as these are subject to gyroscopic effects when the cylinder is rotating. For this case, $a_{11}=\frac{1}{6}L^3+R^2L$, $b_{11}=-\frac{1}{6}L^3$, $c_{11}=0$ and so Eq. (2.33) becomes

$$\begin{aligned}(\tfrac{1}{12}m_0L^2+\tfrac{1}{2}m_0R^2)\ddot{p}_{11}-\Omega m_0R^2\dot{q}_{11}&=z_P\sin(\phi_P)P_x(t)-z_P\cos(\phi_P)P_y(t)+R\sin(\phi_p)P_z(t)\\ (\tfrac{1}{12}m_0L^2+\tfrac{1}{2}m_0R^2)\ddot{q}_{11}+\Omega m_0R^2\dot{p}_{11}&=z_P\cos(\theta\phi_P)P_x(t)+z_P\sin(\phi_P)P_y(t)+R\cos(\phi_P)P_z(t)\end{aligned} \tag{2.34}$$

where $m_0=2\rho\pi RhL$ is the total mass of the cylinder. Here, the gyroscopic cross-coupling terms, which involve the axial moment of inertia $I_{zz}=m_0R^2$, result in non-zero natural frequencies for conical precession.

Equation (2.33) can be written in matrix form for multiple point loads P_j, and with the inclusion of damping, as

$$\mathbf{M}_{mn}\ddot{\xi}_{mn} + (\mathbf{C}_{mn} + 2\Omega\mathbf{J}_{mn})\,\dot{\xi}_{mn} + \left(\mathbf{K}_{mn} - \Omega^2\mathbf{K}^{\Omega}_{mn}\right)\xi_{mn} = \sum_j \mathbf{E}_{mn}(\phi_j, z_j)P_j(t) \quad (2.35)$$

where $\xi^T_{mn} = [p_{mn},\, q_{mn}]$ and

$$\mathbf{M}_{mn} = \mu_{mn}\begin{bmatrix} 1 & 0 \\ 0 & 1 \end{bmatrix},\ \mathbf{J}_{mn} = \mu_{mn}\left(m + \frac{b_{mn}}{a_{mn}}\right)\begin{bmatrix} 0 & -1 \\ 1 & 0 \end{bmatrix},$$

$$\mathbf{E}_{mn}(\theta, z) = \begin{bmatrix} U_{mn}(z)\sin m\phi & V_{mn}(z)\cos m\phi & W_{mn}(z)\sin m\phi \\ U_{mn}(z)\cos m\phi & V_{mn}(z)\sin m\phi & W_{mn}(z)\cos m\phi \end{bmatrix},$$

$$\mathbf{K}_{mn} = \omega^2_{mn}\mathbf{M}_{mn},\ \mathbf{K}^{\Omega}_{mn} = \frac{c_{mn}}{a_{mn}}\mathbf{M}_{mn},\ \mathbf{C}_{mn} = 2\zeta_{mn}\mathbf{K}_{mn}.$$

Combining the uncoupled equations (2.35) for all $2M(N+1)$ modes gives

$$\mathbf{M}\ddot{\boldsymbol{\xi}} + (\mathbf{C} + 2\Omega\mathbf{J})\,\dot{\boldsymbol{\xi}} + \left(\mathbf{K} - \Omega^2\mathbf{K}_{\boldsymbol{\Omega}}\right)\boldsymbol{\xi} = \sum_j \mathbf{E}(\phi_j, z_j)P_j(t) \quad (2.36)$$

where $\boldsymbol{\xi}^T = (\xi^T_1,\, \xi^T_2,\, ...,\xi^T_M) \in \mathbb{R}^{2M(N+1)}$, with $\xi^T_m = \left[\xi^T_{m0},\, \xi^T_{m1},\, ...,\xi^T_{mN}\right]$. Consequently, $\mathbf{M}$, $\mathbf{C}$, $\mathbf{J}$, $\mathbf{K}$, $\mathbf{K}_{\boldsymbol{\Omega}} \in \mathbb{R}^{2M(N+1)\times 2M(N+1)}$ are block diagonal matrices in correspondence with Eq. (2.35). Also, $\mathbf{E} \in \mathbb{R}^{2M(N+1)\times 3}$ and the displacements at an arbitrary space-fixed location can be expressed

$$[u(\phi, z, t), v(\phi, z, t), w(\phi, z, t)]^T = \mathbf{E}^T(\phi, z)\boldsymbol{\xi}(t) \quad (2.37)$$

2.4 Chapter summary

This chapter has defined a 3-dimensional multi-mode model for the vibration behaviour of a thin-walled cylindrical rotor based on shell theory. The shown invariance properties of the mode-shapes allows the construction of a discrete model having a simple parametric dependency on rotational speed, with negligible impact on accuracy. Results from the parametric model for speed-dependent natural frequencies (Eq. (2.29)) indicate that, for the low order bending modes, the effect from circumferential extension is very small. An implication of this point is that, even for experiments with higher rotational speeds, the correctness of the centripetal (Ω^2) terms in the equations of motion may not be exposed unless modes with significant in-surface extension are excited and identified. The described theoretical model may be used to construct benchmark cases for validation of finite element codes for rotating shell structures. Further work to experimentally verify the described shell theory model for a test case rotor system is presented in chapter 6.

Chapter 3

Vibration of a thin rotating ring subject to noncircularity

3.1 Introduction

The vibration within the walls of a simple thin-walled rotor shares similarities with the in-plane vibrations of rings, for which Coriolis and centripetal accelerations give rise to rotational-speed-dependent splitting of natural frequencies for foward and backward circumferential waves [27, 22]. The motivation for the present study was to better understand the underlying mechanism for vibrational excitation of a thin-walled rotor supported by active magnetic bearings. Vibration is seen to arise due to imperfect symmetry of the rotor cross-section and its accurate prediction may play an important role in machine design, manufacture and operation. A suitable dynamic model must incorporate mathemetical descriptions of rotor non-circularity and space-fixed bearing elements in order to establish the forced vibration behaviour under rotation.

Limitations in manufacturing processes will cause profile variations in hollow cylindrical structures of nominally annular cross-section. Although a number of studies on the free vibration of imperfect rings can be found in the literature, these deal almost exclusively with non-rotating rings. Imperfections may be introduced as small initial displacements [2], or variation of the ring cross section [34, 26], or perturbations of the uniform mass density and bending stiffness [3]. An elliptical ring has also been considered as a special case of an imperfect circular ring [35]. In most of these studies, the Rayleigh-Ritz approach has been used to determine the perturbations in natural frequencies and mode shapes for free vibration. The effect of uneven mass distribution for a spinning resonator ring in a MEMs device was studied in Ref. [37].

Machine rotor/shaft structures are usually supported by space-fixed bearing components with certain stiffness and damping characteristics. For a thin-walled rotor, bearing interactions occuring at discrete angular positions may result in significant changes in modal properties for wall vibration. The related problem of free vibration of a non-rotating thin ring on a general elastic foundations was solved in Ref. [77] via both perturbation and Galerkin methods. Similar behaviour is seen in models of vibration in meshing compliant gears which couple through space-fixed discrete stiffnesses [18, 5].

The vibration of a rotating ring under forced conditions, both with and without constraints, was studied by Carrier [6] for a few special cases. Closed form solutions to the harmonic and periodic forced vibration of rotating rings have been reported by Huang and Soedel [33]. Response solutions for rotating tires based on rings with elastic foundations under various loading situations have also been published [76, 38], while an experimental

study on tire vibration can be found in Ref. [39].

Previous studies on forced vibration have been limited to the case of perfect rings subject to exogenous forcing. To the authors' knowledge, the mechanism for self-excitation due to imperfect geometry of a hollow cylindrical rotor with discrete supports has not previously been dealt with. In this chapter, a model is developed for vibration of a short thin-walled rotor where non-circularity is represented by an initial deflection of the rotor wall. Using a Fourier series description of non-circularity, a general model for the interaction of the rotor with space-fixed discrete spring-damper supports is derived. A numerical study is then undertaken to investigate the influence of multiplicity and symmetry of discrete spring-damper supports on the resonance behaviour of the rotor.

3.2 2D rotor model based on thin inextensible rotating ring

The governing equations for a rotating cylindrical shell may be simplified for the case of a short length thin ring. In this case, the axial variation (z-dependency) of all variables is neglected and deformation is assumed to occur in the form of bending in the plane of rotation only, i.e. without twisting of the shell. With the incorporation of small noncircularity, the geometry may be considered as shown in Fig. 3.1. The rotor has circumference length L_c and rectangular cross-section of depth d and length l. Uniform density ρ and modulus of elasticity E are assumed. The rotor is supported by space-fixed discrete bearing elements, shown here as radial spring-damper units. The XY axes are a fixed reference frame, while the reference frame X′Y′ rotates with the rotor at constant angular speed Ω about the fixed axis through O.

To derive the equations of motion we consider that non-circularity is introduced as an initial plastic deformation of a perfect circular ring so that its neutral plane is perturbed from a reference circle centred on the coordinate axes, as shown in Fig. 3.1a. Then, additional displacements arise under motion due to elastic deformation. The local reference frame for the displacement at a given point P is shown by axes x_0y_0 and the deformation frame is denoted by axes xy. The displacements of the cylinder wall in radial (x_0) direction and tangential (y_0) direction with respect to the reference circle are defined as

$$U(\theta,t) = u_{r0}(\theta) + u_r(\theta,t), \quad V(\theta,t) = v_{r0}(\theta) + v_r(\theta,t)$$

where $u_{r0}(\theta)$ and $v_{r0}(\theta)$ are the initial equilibrium displacements due to non-circularity and $u_r(\theta,t)$ and $v_r(\theta,t)$ are the displacements due to vibration. Under these assumptions we may apply an inextensibility condition to both the plastic and elastic components of the deformation:

$$u_r = v_r', \quad u_{r0} = v_{r0}' \tag{3.1}$$

The equations of motion for a differential element may be obtained from (2.1)-(2.8) under assumption that all variables are independent of z, giving the simplified set of equations

$$\frac{1}{R}\frac{\partial Q_{yx}}{\partial\theta} + \frac{Q_{yy}}{R} + \frac{Q_0}{R}\left(1 + \frac{\partial\beta_z}{\partial\theta}\right) + f_x = \rho h\left(\ddot{U} + 2\Omega\dot{V} + \Omega^2(R-U)\right) \tag{3.2}$$

$$\frac{1}{R}\frac{\partial Q_{yy}}{\partial\theta} - \frac{Q_{yx}}{R} - \frac{Q_0}{R}\beta_z + f_y = \rho h\left(\ddot{V} - 2\Omega\dot{U} - \Omega^2 V\right) \tag{3.3}$$

$$Q_{yx} = \frac{1}{R}\frac{\partial M_{yy}}{\partial\theta} \tag{3.4}$$

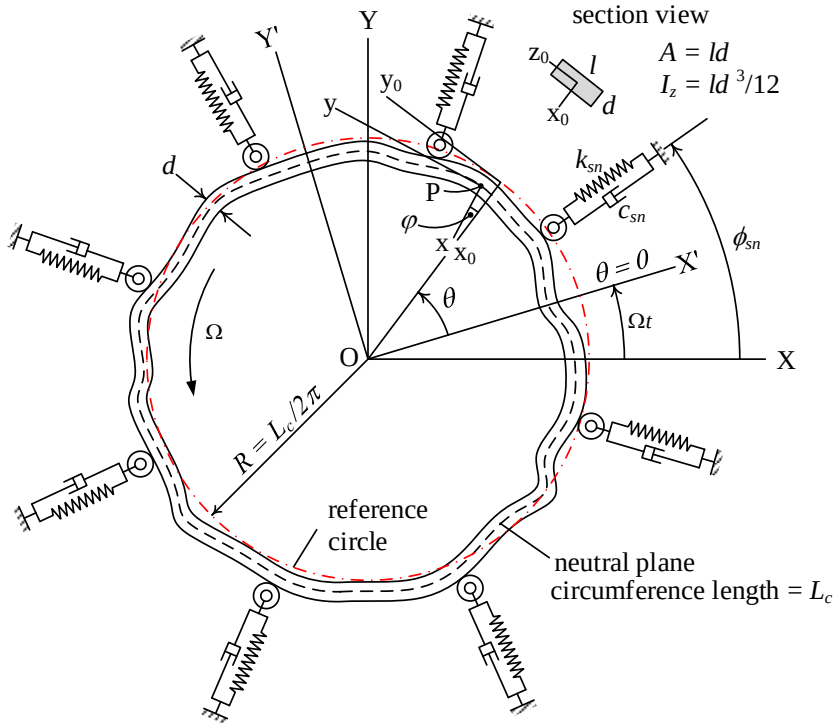

Figure 3.1: (a) Schematic of a non-circular thin-walled cylindrical rotor with space-fixed discrete spring-damper modules (b) Rotor segment Free-Body-Diagram

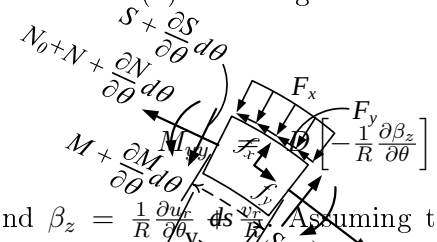

(a)

(b)

with $D = \frac{Ed^3}{12(1-\nu^2)}$ and $\beta_z = \frac{1}{R}\frac{\partial u_r}{\partial \theta}$. Assuming the mean hoop stress is given by $Q_0 = \rho R\Omega^2$, then Equations (3.2) - (3.5) may be combined to eliminate the normal sress Q_{yy} and radial shear stress Q_{yx}. Then, applying the inextensibility conditions Eq. (3.1) and neglecting nonlinear terms yields

$$\left(\frac{\partial^2 \ddot{v}_r}{\partial\theta^2} - \ddot{v}_r\right) + 4\Omega\frac{\partial \dot{v}_r}{\partial\theta} - \Omega^2\left(\frac{\partial^4 v_r}{\partial\theta^4} + 3\frac{\partial^2 v_r}{\partial\theta^2}\right) + \omega_0^2\left(1 + \tau\frac{d}{dt}\right)\left(\frac{\partial^6 v_r}{\partial\theta^6} + 2\frac{\partial^4 v_r}{\partial\theta^4} + \frac{\partial^2 v_r}{\partial\theta^2}\right) = \frac{1}{\rho d l}\frac{\partial f_r}{\partial\theta} = \Omega^2\left(\frac{\partial^3 u_{r0}}{\partial\theta^4} + 3\frac{\partial u_{r0}}{\partial\theta}\right) \tag{3.6}$$

where $\omega_0^2 = \frac{Ed^2}{12\rho R^4}$.

This reduced (1–D) governing equation (Eq. (3.6)) is consistent with some previous studies [22, 28]. However, the effect of additional damping and non-circularity terms in combination with space-fixed bearing supports, which are critical aspects for rotordynamic prediction, have not previously been considered. Endo et al. [22] showed experimentally that the (low order) natural frequencies for free vibration of a thin rotating ring corresponded well with the unforced version of this equation even though the inextensibility assumption is applied. For further comparison, two alternative but more complex models are given in the appendix that take account of circumferential extension and give further

insight on the validity of Eq. (3.6). Note that the non-circularity terms on the right side are constant (time-independent) forcing terms that, for the free rotor, produce a deformation that tends to cancel the initial non-circularity as the rotational speed increases, i.e. an initially non-circular rotor becomes circular as the rotational speed tends to infinity. This behaviour, which is intuitively reasonable, is seen only when inextensibility is assumed for both the elastic and initial plastic deformation, as in Eq. (3.1). With the addition of discrete bearing supports, the impact of non-circularity on vibration is more complex.

3.2.1 2–D model without inextensibility assumption

A two-dimensional model for vibration of a thin rotating ring may be obtained from Eqs (23.2)-(3.5) without the inextensibility assumption by applying $Q_{yy} = \frac{E}{R}(v_r' - u_r)$, yielding rotating frame equations of motion as

$$\frac{E}{\rho R^2}(v_r' - u_r) - \frac{Ed^2}{12\rho R^4}(u_r'''' + v_r''') + \Omega^2(u_r'' + v_r' + u_r) = \ddot{u}_r + 2\Omega\dot{v}_r \tag{3.7}$$

$$\frac{E}{\rho R^2}(v_r'' - u_r') + \frac{Ed^2}{12\rho R^4}(u_r''' + v_r'') + \Omega^2 u_r' = \ddot{v}_r - 2\Omega\dot{u}_r \tag{3.8}$$

These equations are still consistent with Love's approximation theory for thin shells [46]. Substituting the free vibration solution in the form

$$\begin{bmatrix} u_r \\ v_r \end{bmatrix} = \begin{bmatrix} Ae^{j(m\theta+\omega t)} \\ jBe^{j(m\theta+\omega t)} \end{bmatrix} \tag{3.9}$$

leads to the following eigenvalue problem for natural frequencies ω:

$$\begin{bmatrix} -1-\delta m^4-(m^2-1)\overline{\Omega}^2+\overline{\omega}^2 & -m-\delta m^3-m\overline{\Omega}^2+2\overline{\Omega}\overline{\omega} \\ -m-\delta m^3-m\overline{\Omega}^2+2\overline{\Omega}\overline{\omega} & -(1+\delta)m^2+\overline{\omega}^2 \end{bmatrix} \begin{bmatrix} A \\ B \end{bmatrix} = 0 \tag{3.10}$$

where $\overline{\Omega} = \Omega R\sqrt{\rho/E}, \overline{\omega} = \omega R\sqrt{\rho/E}$ and $\delta = d^2/12R^2$. The characteristic equation is thus quartic in $\overline{\omega}$ and (for each value of m) yields four natural frequencies. The two lower frequencies relate to predominantly flexural modes (for which $u_r \approx v_r'$) while the two higher frequencies are extensional modes. Under the assumption $\delta m^2 \ll 1$, the natural frequencies (for $\Omega = 0$) follow as

$$\omega_f = \pm\omega_0 \frac{m(m^2-1)}{\sqrt{m^2+1}}, \quad \omega_e = \pm\omega_0 \frac{2R}{d}\sqrt{3(m^2+1)} \tag{3.11}$$

The first frequency matches that for the inextensible ring model Eq. (3.6), thereby confirming its validity for cases where $dm \ll 2\sqrt{3}\,R$. The exact value from (3.10) will be somewhat lower, however.

3.2.2 2–D shell model with DMV approximations

A possible simplification for thin-shell cylinders is to neglect the radial shear stress term in the tangential acceleration Eq. (3.8). A further approximation made in Donnellâ-Mushtariâ-Vlasov (DMV) theory, is that the contribution of the tangential displacement to the bending strain is negligible [78]. Under these assumptions, Eq. (3.10) simplifies to

$$\begin{bmatrix} -1-\delta m^4-(m^2-1)\overline{\Omega}^2+\overline{\omega}^2 & -m-m\overline{\Omega}^2+2\overline{\Omega}\overline{\omega} \\ -m-m\overline{\Omega}^2+2\overline{\Omega}\overline{\omega} & -m^2+\overline{\omega}^2 \end{bmatrix} \begin{bmatrix} A \\ B \end{bmatrix} = 0 \tag{3.12}$$

Although commonly applied, the validity of this model for a thin-walled rotor-bearing system should be verified by comparison with the results from Eq. (3.10).

3.3 Rotor-bearing system model

To describe the rotor interaction with space-fixed bearing supports, it is convenient to express motion in terms of fixed-frame coordinates. For a given point on the rotor, the fixed-frame angular position is $\phi = \theta + \Omega t$. We define $u(\phi,t)$, $v(\phi,t)$, $u_0(\phi,t)$ and $F_x^*(\phi,t)$ as the radial and tangential displacement, non-circularity and distributed radial force as functions of ϕ, respectively. For each of these parameters, $y_r(\theta,t) = y(\phi(\theta,t),t)$ and so the following relations hold

$$\frac{\partial y_r}{\partial \theta} = \frac{\partial y}{\partial \phi}, \quad \dot{y}_r = \dot{y} + \Omega \frac{\partial y}{\partial \phi} \tag{3.13}$$

Using these transformations in Eq. (3.6) gives the equation of motion in stationary frame coordinates as

$$\begin{aligned} &\left(\frac{\partial^2 \ddot{v}}{\partial \phi^2} - \ddot{v}\right) + 2\Omega\left(\frac{\partial^3 \dot{v}}{\partial \phi^3} + \frac{\partial \dot{v}}{\partial \phi}\right) \\ &\quad + \omega_0^2\left(1 + \tau\Omega\frac{\partial}{\partial \phi} + \tau\frac{d}{dt}\right)\left(\frac{\partial^6 v}{\partial \phi^6} + 2\frac{\partial^4 v}{\partial \phi^4} + \frac{\partial^2 v}{\partial^2 \phi}\right) \\ &\quad - \frac{1}{\rho d l}\frac{\partial F_x^*}{\partial \phi} = \Omega^2\left(\frac{\partial^3 u_0}{\partial \phi^3} + 3\frac{\partial u_0}{\partial \phi}\right) \end{aligned} \tag{3.14}$$

3.3.1 Discrete model

The non-circularity can be approximated by a truncated Fourier series in the form

$$u_{r0}(\theta) = \sum_{j=1}^{M} [a_j \cos j\theta + b_j \sin j\theta] \tag{3.15}$$

where $a_j = \frac{1}{\pi}\int_0^{2\pi} u_{r0} \cos j\theta \, d\theta$ and $b_j = \frac{1}{\pi}\int_0^{2\pi} u_{r0} \sin j\theta \, d\theta$. The displacement component due to non-circularity $u_0(\phi,t) = u_{r0}(\phi - \Omega t)$ is then given by

$$\begin{aligned} u_0(\phi,t) &= \sum_{j=1}^{M} (a_j \cos j\Omega t - b_j \sin j\Omega t)\cos j\phi \\ &\quad + \sum_{j=1}^{M} (a_j \sin j\Omega t + b_j \cos j\Omega t)\sin j\phi \end{aligned} \tag{3.16}$$

Since the $j = 1$ coefficients relate to the ring offset, the reference circle centre may be chosen such that a_1 and b_1 are zero, i.e. collocated with the mass-centre of the cylinder.

Discrete radial bearing forces $F_{sn}(t)$, applied at angular positions ϕ_{sn} and indexed by n, may be modelled by

$$F_x^*(\phi,t) = \frac{1}{R}\sum_{n=1}^{N_s} F_{sn}(t)\delta(\phi - \phi_{sn}) \tag{3.17}$$

where $\delta(.)$ denotes the Dirac delta function.

Suppose a solution to Eq. (3.14) can be approximated by

$$u(\phi,t) = \frac{\partial v(\phi,t)}{\partial \phi} \approx \sum_{m=1}^{M} [p_m(t)\sin m\phi + q_m(t)\cos m\phi] \tag{3.18}$$

where $\sin m\phi$ and $\cos m\phi$ are the mode shapes for undamped free vibration and $p_m(t)$ and $q_m(t)$ are the m^{th} modal radial displacements, with m being the nodal index. Substituting Eqs (3.16), (3.17) and (3.18) into Eq. (3.14) and exploiting the orthogonality properties of $\cos m\phi$ and $\sin m\phi$ yields a set of $2M$ equations:

$$\begin{aligned}
&\ddot{p}_m - \Omega g_m \dot{q}_m + \tau k_m \dot{p}_m + k_m p_m - \Omega\tau m k_m q_m \\
&\qquad -l_m \sum_{n=1}^{N_z} F_{sn} \sin m\phi_{sn} = -\Omega^2 h_m \left[a_m \sin m\Omega t + b_m \cos m\Omega t\right] \qquad (3.19)\\
&\ddot{q}_m + \Omega g_m \dot{p}_m + \tau k_m \dot{q}_m + k_m q_m + \Omega\tau m k_m p_m \\
&\qquad -l_m \sum_{n=1}^{N_z} F_{sn} \cos m\phi_{sn} = -\Omega^2 h_m \left[-b_m \sin m\Omega t + a_m \cos m\Omega t\right] \qquad (3.20)
\end{aligned}$$

where $k_m = \omega_0^2 \frac{m^2(m^2-1)^2}{m^2+1}$, $h_m = \frac{m^2(m^2-3)}{m^2+1}$, $g_m = \frac{2m(m^2-1)}{m^2+1}$, $l_m = \frac{m^2}{\rho\pi AR(m^2+1)}$.

By defining vectors $\mathbf{x} = [p_1\ q_1\ p_2\ q_2 \ldots p_M\ q_M]^{\mathrm{T}}$ and $\mathbf{F}_s = [F_{s1}\ F_{s2}\ \ldots\ F_{sN_s}]^{\mathrm{T}}$, equations (3.19) and (3.20) can be rewritten in matrix form as

$$\begin{aligned}
&\ddot{\mathbf{x}} + (\tau\mathbf{C}_0 - \Omega\mathbf{C}_1)\dot{\mathbf{x}} + (\mathbf{K}_0 - \tau\Omega\mathbf{K}_1)\mathbf{x} - \mathbf{L}\mathbf{E}_s^T\mathbf{F}_s \\
&\qquad = -\Omega^2\mathbf{H}_0 \sum_{m=1}^{M} \left[\mathbf{W}_{2m-1} \sin m\Omega t + \mathbf{W}_{2m} \cos m\Omega t\right] \qquad (3.21)
\end{aligned}$$

where the block-diagonal matrices involve submatrices

$$\mathbf{I}_2 = \begin{bmatrix} 1 & 0 \\ 0 & 1 \end{bmatrix}, \quad \mathbf{J}_2 = \begin{bmatrix} 0 & 1 \\ -1 & 0 \end{bmatrix}$$

and are given by

$$\begin{aligned}
\mathbf{C}_0 &= \mathrm{diag}\left(\ k_1\mathbf{I}_2,\ \ k_2\mathbf{I}_2,\ \ \ldots\ \ k_M\mathbf{I}_2\ \right),\\
\mathbf{C}_1 &= \mathrm{diag}\left(\ g_1\mathbf{J}_2,\ \ g_2\mathbf{J}_2,\ \ \ldots\ \ g_M\mathbf{J}_2\ \right),\\
\mathbf{K}_0 &= \mathrm{diag}\left(\ k_1\mathbf{I}_2,\ \ k_2\mathbf{I}_2,\ \ \ldots\ \ k_M\mathbf{I}_2\ \right),\\
\mathbf{K}_1 &= \mathrm{diag}\left(\ k_1\mathbf{J}_2,\ \ 2k_2\mathbf{J}_2,\ \ \ldots\ \ Mk_M\mathbf{J}_2\ \right),\\
\mathbf{H}_0 &= \mathrm{diag}\left(\ h_1\mathbf{I}_2,\ \ h_2\mathbf{I}_2,\ \ \ldots\ \ h_M\mathbf{I}_2\ \right),\\
\mathbf{L} &= \mathrm{diag}\left(\ l_1\mathbf{I}_2,\ \ l_2\mathbf{I}_2,\ \ \ldots\ \ l_M\mathbf{I}_2\ \right),\\
\mathbf{W} &= \mathrm{diag}\left(\ (a_1\mathbf{I}_2 + b_1\mathbf{J}_2),\ \ (a_2\mathbf{I}_2 + b_2\mathbf{J}_2),\ \ \ldots\ \ (a_M\mathbf{I}_2 + b_M\mathbf{J}_2)\ \right)
\end{aligned}$$

Also, $\mathbf{W}_j$ denotes the j^{th} column of $\mathbf{W}$. The matrix $\mathbf{E}_s$ is a force distibution matrix that introduces a modal coupling according to the support positions:

$$\mathbf{E}_s = \begin{bmatrix}
\sin\phi_{s1} & \cos\phi_{s1} & \sin 2\phi_{s1} & \cos 2\phi_{s1} & \cdots & \sin M\phi_{s1} & \cos M\phi_{s1} \\
\sin\phi_{s2} & \cos\phi_{s2} & \sin 2\phi_{s2} & \cos 2\phi_{s2} & \cdots & \sin M\phi_{s2} & \cos M\phi_{s2} \\
\vdots & \vdots & \vdots & \vdots & & \vdots & \vdots \\
\sin\phi_{sN_s} & \cos\phi_{sN_s} & \sin 2\phi_{sN_s} & \cos 2\phi_{sN_s} & \cdots & \sin M\phi_{sN_s} & \cos M\phi_{sN_s}
\end{bmatrix}$$

A set of radial displacements $\mathbf{y} = [y(\phi_1, t)\ y(\phi_2, t) \ldots y(\phi_K, t)]^{\mathrm{T}}$ may be defined for a general set of fixed angular positions $\phi_1, ..., \phi_K$. These will equal the summation of the displacements due to elastic deflection and the initial non-circularity, as given respectively by Eqs (3.16) and (3.18):

$$\mathbf{y} = \mathbf{u} + \mathbf{u}_0 = \mathbf{E}\left(\mathbf{x} + \sum_{m=1}^{M} \left(\mathbf{W}_{2m-1} \sin m\Omega t + \mathbf{W}_{2m} \cos m\Omega t\right)\right) \qquad (3.22)$$

where

$$\mathbf{E} = \begin{bmatrix} \sin\phi_1 & \cos\phi_1 & \sin 2\phi_1 & \cos 2\phi_1 & \cdots & \sin M\phi_1 & \cos M\phi_1 \\ \sin\phi_2 & \cos\phi_2 & \sin 2\phi_2 & \cos 2\phi_2 & \cdots & \sin M\phi_2 & \cos M\phi_2 \\ \vdots & \vdots & \vdots & \vdots & & \vdots & \vdots \\ \sin\phi_K & \cos\phi_K & \sin 2\phi_K & \cos 2\phi_K & \cdots & \sin M\phi_K & \cos M\phi_K \end{bmatrix}.$$

In practice, the vibration of the rotor wall may be observed by measuring the rotor surface position using non-contact sensors such as proximity probes or laser vibrometers.

3.3.2 Discrete space-fixed spring-damper supports

For a discrete radial bearing unit with linear stiffness and damping properties (with coefficients k_{sn} and c_{sn}, respectively), the applied force is given by

$$F_{sn}(t) = F_{0n} + c_{sn}\dot{y}(\phi_{sn}, t) + k_{sn}y(\phi_{sn}, t) \tag{3.23}$$

where F_{0n} is a preload. From Eq. (3.22), the bearing forces may be expressed in matrix form as

$$\begin{aligned} \mathbf{F}_s &= \mathbf{F}_0 + \mathbf{C}_s\mathbf{E}_s\dot{\mathbf{x}} + \mathbf{K}_s\mathbf{E}_s\mathbf{x} \\ &+ (\Omega\mathbf{C}_s\mathbf{E}_s\mathbf{S} + \mathbf{K}_s\mathbf{E}_s)\sum_{m=1}^{M}(\mathbf{W}_{2m-1}\cos m\Omega t + \mathbf{W}_{2m}\sin m\Omega t) \end{aligned} \tag{3.24}$$

where

$$\begin{aligned} \mathbf{C}_s &= \mathrm{diag}\left(\ c_{s1},\ \ c_{s2},\ \ \ldots\ \ c_{sN_s}\ \right), \\ \mathbf{K}_s &= \mathrm{diag}\left(\ k_{s1},\ \ k_{s2},\ \ \ldots\ \ k_{sN_s}\ \right), \\ \mathbf{S} &= \mathrm{diag}\left(\ \mathbf{J}_2,\ \ 2\mathbf{J}_2,\ \ \ldots\ \ M\mathbf{J}_2\ \right) \end{aligned}$$

Substituting Eq. (3.24) in Eq. (3.21) and rearranging yields

$$\ddot{\mathbf{x}} + \mathbf{C}_\Omega\dot{\mathbf{x}} + \mathbf{K}_\Omega x = \mathbf{f}_0 + \mathbf{H}_\Omega\sum_{m=1}^{M}(\mathbf{W}_{2m-1}\sin m\Omega t + \mathbf{W}_{2m}\cos m\Omega t) \tag{3.25}$$

where

$$\begin{aligned} \mathbf{C}_\Omega &= \tau\mathbf{C}_0 + \mathbf{L}\mathbf{E}_s^{\mathrm{T}}\mathbf{C}_s\mathbf{E}_s - \Omega\mathbf{C}_1 \\ \mathbf{K}_\Omega &= \mathbf{K}_0 + \mathbf{L}\mathbf{E}_s^{\mathrm{T}}\mathbf{K}_s\mathbf{E}_s - \tau\Omega\mathbf{K}_1 \\ \mathbf{H}_\Omega &= -\Omega^2\mathbf{H} - \Omega\mathbf{L}\mathbf{E}_s^{\mathrm{T}}\mathbf{C}_s\mathbf{E}_s\mathbf{S} - \mathbf{L}\mathbf{E}_s^{\mathrm{T}}\mathbf{K}_s\mathbf{E}_s \\ \mathbf{f}_0 &= -\mathbf{L}\mathbf{E}_s^{\mathrm{T}}\mathbf{F}_0 \end{aligned}$$

Equation (3.25) describes the forced response behaviour due to non-circularity, where the mechanism for excitation is embodied via the time-dependent terms on the right side of the equation. The excitation behaviour depends critically on the matrices $\mathbf{E}_s^{\mathrm{T}}\mathbf{K}_s\mathbf{E}_s$ and $\mathbf{E}_s^{\mathrm{T}}\mathbf{C}_s\mathbf{E}_s$, which depend on the bearing unit characteristics and locations. To reveal the nature of this influence, numerical results are presented in Section 3.

3.3.3 Steady-state solution

It may be assumed, based on linearity, that the solution for steady-state vibration takes the form

$$\mathbf{x}(t) = \mathbf{A}_0 + \sum_{m=1}^{M} \left(\mathbf{A}_m(\Omega) \sin m\Omega t + \mathbf{B}_m(\Omega) \cos m\Omega t\right) \tag{3.26}$$

where $\mathbf{A}_m, \mathbf{B}_m \in \mathcal{R}^{2M\times 1}$. After substituting Eq. (3.26) in Eq. (3.25) and using the method of undetermined coefficients, we obtain

$$\mathbf{A}_0 = \mathbf{K}_{\Omega=0}\mathbf{f}_0 \tag{3.27}$$

$$\begin{bmatrix} \mathbf{A}_m \\ \mathbf{B}_m \end{bmatrix} = \begin{bmatrix} \mathbf{K}_\Omega - (m\Omega)^2\mathbf{I} & -m\Omega\mathbf{C}_\Omega \\ m\Omega\mathbf{C}_\Omega & \mathbf{K}_\Omega - (m\Omega)^2\mathbf{I} \end{bmatrix}^{-1} \begin{bmatrix} \mathbf{H}_\Omega\mathbf{W}_{2m-1} \\ \mathbf{H}_\Omega\mathbf{W}_{2m} \end{bmatrix} \tag{3.28}$$

where $\mathbf{I} \in \mathcal{R}^{2M\times 2M}$ is the identity matrix.

From a practical point of view, it is useful to be able to predict the vibration of the rotor wall that would be observed at a fixed point in the stationary frame. This is important when the rotor has finite clearances with surrounding components that are fixed in space. It will also correspond to the vibration that would be measured by surface proximity sensors. The solution can be obtained by substituting Eq. (3.26) into Eq. (3.22):

$$\mathbf{y} = -\mathbf{E}\mathbf{A}_0 - \mathbf{E}\sum_{m=1}^{M} \left[(\mathbf{A}_m + \mathbf{W}_{2m-1}) \sin m\Omega t + (\mathbf{B}_m + \mathbf{W}_{2m}) \cos m\Omega t\right] \tag{3.29}$$

3.4 Numerical study

To investigate the vibration behaviour of a thin-walled rotor for cases with spring-damper supports, a numerical study has been undertaken. The considered properties correspond to an experimental rotor with length 51 mm, radius 111 mm and wall thickness to radius ratio $d/R = 5/179$. The rotor was manufactured by electric discharge machining from martensitic stainless steel (grade 420 J). Further properties are given in Table 3.1. Table 3.2 shows the natural frequencies for free vibration of the rotor obtained from the inextensible ring model Eq. (3.6) and from 2–D thin-shell models, as detailed in the appendix. The difference between the inextensible case and full 2–D model is very small, as expected for the given d/R value. With the classical DMV assumptions for thin shells there are significant differences. Importantly, the neglected terms result in an erroneous imbalance of internal forces and so the natural frequency for the rigid body modes ($m = 1$) is non-zero. Such errors are unacceptable for combined rotor-bearing system modelling where the modified dynamics, including rigid body modes, must be captured accurately.

Firstly, the case of unsymmetrical two-spring supports will be presented to show the basic behaviour predicted by the proposed model (Eq. (3.25)). Cases with symmetrical and unsymmetrical bearing supports will then be compared to examine the effects from symmetry and multiplicity.

3.4.1 Unsymmetrical two-spring supports

Two orthogonal supports are considered with the following properties

$$\phi_{s1} = 0 \text{ rad}, k_{s1} = 90 \text{ kN m}^{-1}, c_{s1} = 9 \text{ N s m}^{-1}$$

$$\phi_{s2} = \pi/2 \text{ rad}, k_{s2} = 22.5 \text{ kN m}^{-1}, c_{s2} = 2.25 \text{ N s m}^{-1}$$

Table 3.1: Rotor properties

Parameter	Symbol	Value	Units
Rotor radius	R	111.0	mm
Wall thickness	d	3.1	mm
Material density	ρ	7740	$\mathrm{kg\,m^{-3}}$
Young's modulus	E	2×10^{11}	$\mathrm{N\,m^{-2}}$
Axial length	l	51	mm

Table 3.2: Theoretical natural frequencies (in Hz) for flexural vibration of free non-rotating rotor

	m				
Model	1	2	3	4	5
Inextensible ring model (Eq. (3.6))	0	157.673	445.965	855.099	1382.88
2–D thin-shell model (Eq. (3.10))	0	157.659	445.918	855.001	1382.71
2–D model with DMV assumptions (Eq. (3.12))	41.550	210.226	501.698	912.080	1440.46

Zero preload is assumed ($\mathbf{f}_0 = 0$). The material relaxation time is 0.1 μs. All calculations are based on a 24^{th} order model ($M = 24$) for the rotor in Table 3.1.

For presentation of the results, the non-circularity is considered with coefficients $a_m = 0$ μm and $b_m = 1$ μm, $m = 1, 2, ..., 24$. For observation at a single location, and in accordance with Eq. (3.29), the vibration response may be defined in terms of the following amplitude/phase parameters:

$$\left.\begin{array}{l} \alpha_m(\Omega) = -\mathbf{E}(\mathbf{A}_m + \mathbf{W}_{2m-1}), \quad \beta_m(\Omega) = -\mathbf{E}(\mathbf{B}_m + \mathbf{W}_{2m}), \\ Y_m(\Omega) = \sqrt{\alpha_m^2 + \beta_m^2}, \quad \psi_m(\Omega) = \tan^{-1}(\beta_m/\alpha_m) \end{array}\right\} \tag{3.30}$$

The observed vibration can then be expressed

$$y_1(t) = \sum_{m=1}^{M} Y_m(\Omega) \sin(m\Omega t + \psi_m(\Omega)) \tag{3.31}$$

Equation (3.25) shows that, for a given speed Ω, the forcing frequencies are $\omega = \Omega, 2\Omega, 3\Omega$, ..., 24Ω. The response amplitudes $Y_m(\Omega)$ may be evaluated for each harmonic frequency $m\Omega$ based on Eqs (3.28) and (3.30).

Suppose that the observation of vibration is made at angular position $\phi_1 = \pi/24$ rad. A plot of the amplitude of each harmonic component of the vibration over the $(\Omega, m\Omega)$ plane is shown in Fig. 3.2. For illustration, harmonic amplitudes for a rotational frequency of 60 Hz are highlighted as vertical lines at points (60, $60m$) Hz having height Y_m. For varying rotational speed, the frequency response due to the m^{th} non-circularity component is defined in the domain $\omega = m\Omega$.

The Campbell diagram shown in Fig. 3.3a was constructed from the numerical eigensolutions for Eq. (3.25) for a set of discrete Ω values. The resonant peaks in Fig. 3.2 align with the natural frequencies shown in the Campbell diagram. Note that some splitting of the natural frequencies occurs at zero speed due to the asymmetry of the discrete supports. The 'front' view of Y_4 as a function of Ω is shown in Fig. 3.3b. Resonance conditions are observed for Y_4 at the intersections of the line $\omega = 4\Omega$ and the natural frequency lines

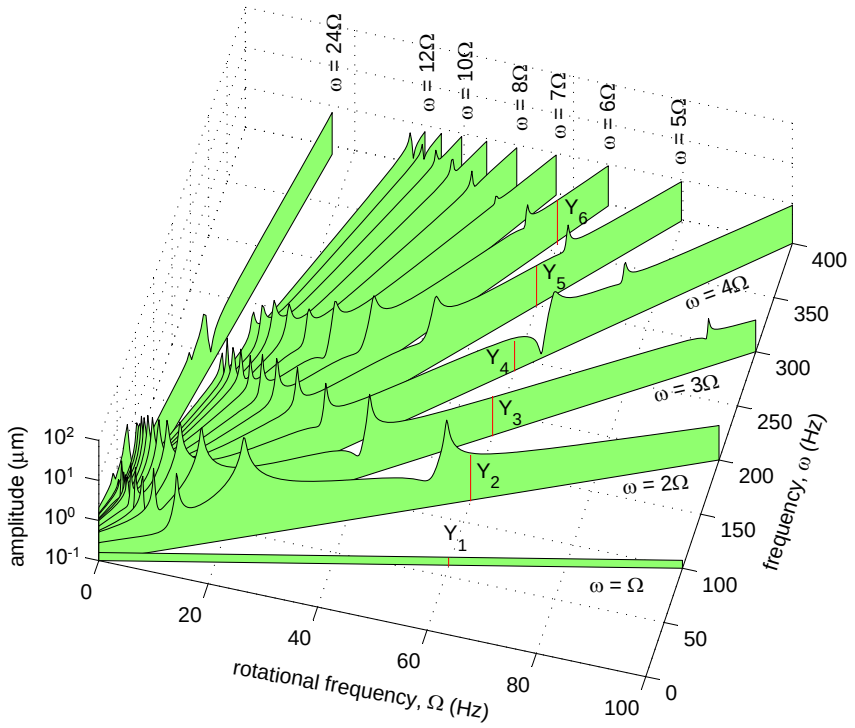

Figure 3.2: Response amplitudes due to non-circularity excitation

in the Campbell diagram. Clearly, if the rotor has high order non-circularity then many resonance conditions can arise during spin-up or spin-down.

3.4.2 Effect of symmetry and number of supports

To show the effects from symmetry and multiplicity of supports, four different cases are considered, as detailed in Table 3.3. Equal support stiffness and damping $k_s = 17\,450\ \mathrm{N\,m^{-1}}$, $c_s = 1.7450\ \mathrm{N\,s\,m^{-1}}$ are assigned for the 3-support cases and $k_s = 4131\ \mathrm{N\,m^{-1}}$, $c_s = 0.413\ \mathrm{N\,s\,m^{-1}}$ for the 12-support cases.

The Campbell diagrams for the cases with non-symmetrical supports are shown in Fig. 3.4a, and the harmonic response amplitudes $Y_{2,\ldots,5}$ shown in Fig. 3.4b and c. The natural frequencies of the two rigid body modes are split for these cases. The flexible mode natural frequencies depend on the stiffness of the supports but are not affected significantly by the symmetry or number of supports, as the support stiffness is relatively low. Resonant peaks are seen at all crossing points of the lines $\omega = m\Omega$ and the natural frequency lines in the Campbell diagram.

For the symmetrical cases with equally spaced supports, the Campbell diagrams are shown in Fig. 3.5a, and the response amplitude $Y_{2,\ldots,5}$ for each case shown in Fig. 3.5b and c. For these cases, a resonance occurs at only some crossing points. Also resonance is not seen at all if there is a sufficient number of supports (see Fig. 3.5c).

These phenomena can be related to the structure of the matrix $\mathbf{H}_\Omega$ in Eq. (3.25), as this matrix determines the coupling of each excitation harmonic with each mode. The dominant term in $\mathbf{H}_\Omega$ is $\mathbf{L}\mathbf{E}_s^{\mathrm{T}}\mathbf{K}_s\mathbf{E}_s$. The 2×2 submatrices that make up $\mathbf{E}_s^{\mathrm{T}}\mathbf{K}_s\mathbf{E}_s$ are

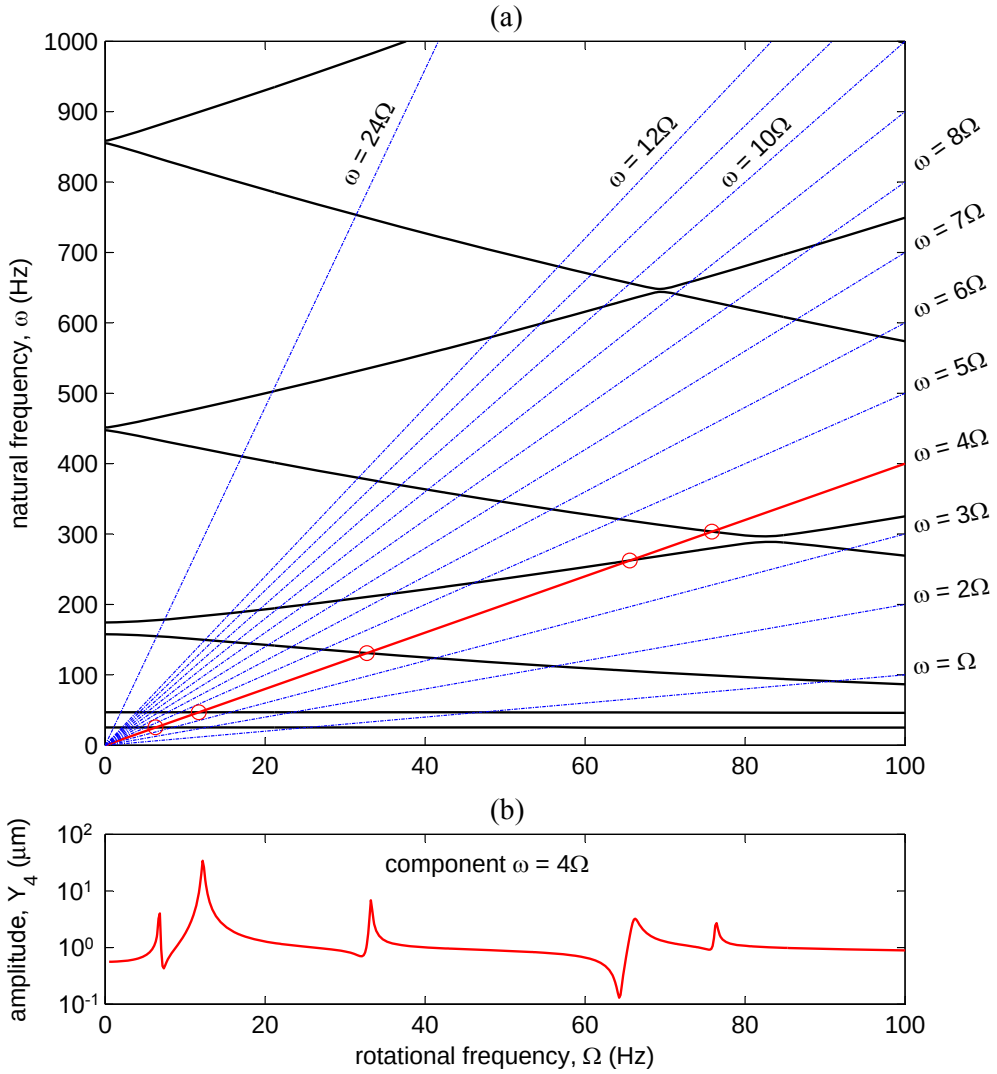

Figure 3.3: (a) Campbell diagram (b) Response amplitude in domain $\omega = 4\Omega$

Table 3.3: Cases with different numbers and positions of supports

Supports	Support positions
3 symmetrical	$0, \frac{2\pi}{3}, \frac{4\pi}{3}$
3 non-symmetrical	$0, \frac{8\pi}{9}, \frac{23\pi}{18}$
12 symmetrical	$0, \frac{\pi}{6}, \frac{2\pi}{6}, \frac{3\pi}{6}, ..., \frac{11\pi}{6}$
12 non-symmetrical	$0, \frac{\pi}{21}, \frac{2\pi}{21}, \frac{4\pi}{21}, \frac{6\pi}{21}, \frac{9\pi}{21}, \frac{12\pi}{21}, \frac{16\pi}{21}, \frac{20\pi}{21}, \frac{25\pi}{21}, \frac{30\pi}{21}, \frac{36\pi}{21}$

given by

$$K_{ij} = k_s \sum_{n=1}^{N_s} \begin{bmatrix} \sin i\phi_{sn} \sin j\phi_{sn} & \sin i\phi_{sn} \cos j\phi_{sn} \\ \cos i\phi_{sn} \sin j\phi_{sn} & \cos i\phi_{sn} \cos j\phi_{sn} \end{bmatrix}. \tag{3.32}$$

This matrix determines the excitation of the mode with nodal index i by the j^{th} non-circularity harmonic. From the numerical study, it is found that if the off-diagonal submatrices ($i \neq j$) are non-zero then one or more resonances are observed. For non-symmetrical supports, $K_{ij} \neq 0$ for $i \neq j$, and this leads to a coupling of every non-circularity excitation harmonic with every rotor mode. In the case of symmetrical supports, $K_{ij} = 0$ for all $i \neq j$ and $i + j < N_s$ and so resonance is only oberved for some crossings involving sufficiently high nodal index and non-circularity harmonic. In addition, if the number of supports N_s is larger than the model order then $\mathbf{E}_s^{\mathrm{T}} \mathbf{K}_s \mathbf{E}_s$ becomes a diagonal matrix and no resonance is observed. Physically, with many identical supports, a given location fixed on the rotor does not experience any variation in loading from the supports and, therefore, there is no excitation from non-circularity.

Clearly, the resonance of a rotating non-circular ring interacting with space-fixed support can be avoided by having a sufficient number of identical evenly spaced supports. An alternative approach to avoid resonance with active magnetic bearing supports is to generate a distribution of actuation forces that couples only with the rigid body modes (by satisfying an orthogonality condition with respect to the flexural mode shapes). A system design based on this scheme has been tested, and results are described in the following section.

3.5 Chapter summary

This chapter has introduced a mathematical model for the vibration of a thin-walled cylindrical rotor subject to small non-circularity and coupled to space-fixed bearing supports. Rotor non-circularity has been shown to give rise to multi-harmonic excitation of the rotor-bearing structure. Whether a resonance occurs at a predicted critical speed depends on the multiplicity and symmetry of the bearing supports. Generally, a large number of evenly spaced identical supports will eliminate the possibility of low order resonance conditions. The modelling approach can also be applied to thin-walled rotor-AMB systems by accounting for feedback controlled electromagnetic actuators within the formulation. This is considered in detail in chapter 5. A limitation of the simplified 2D model is that axial variation in wall deflection was not addressed by the modelling.

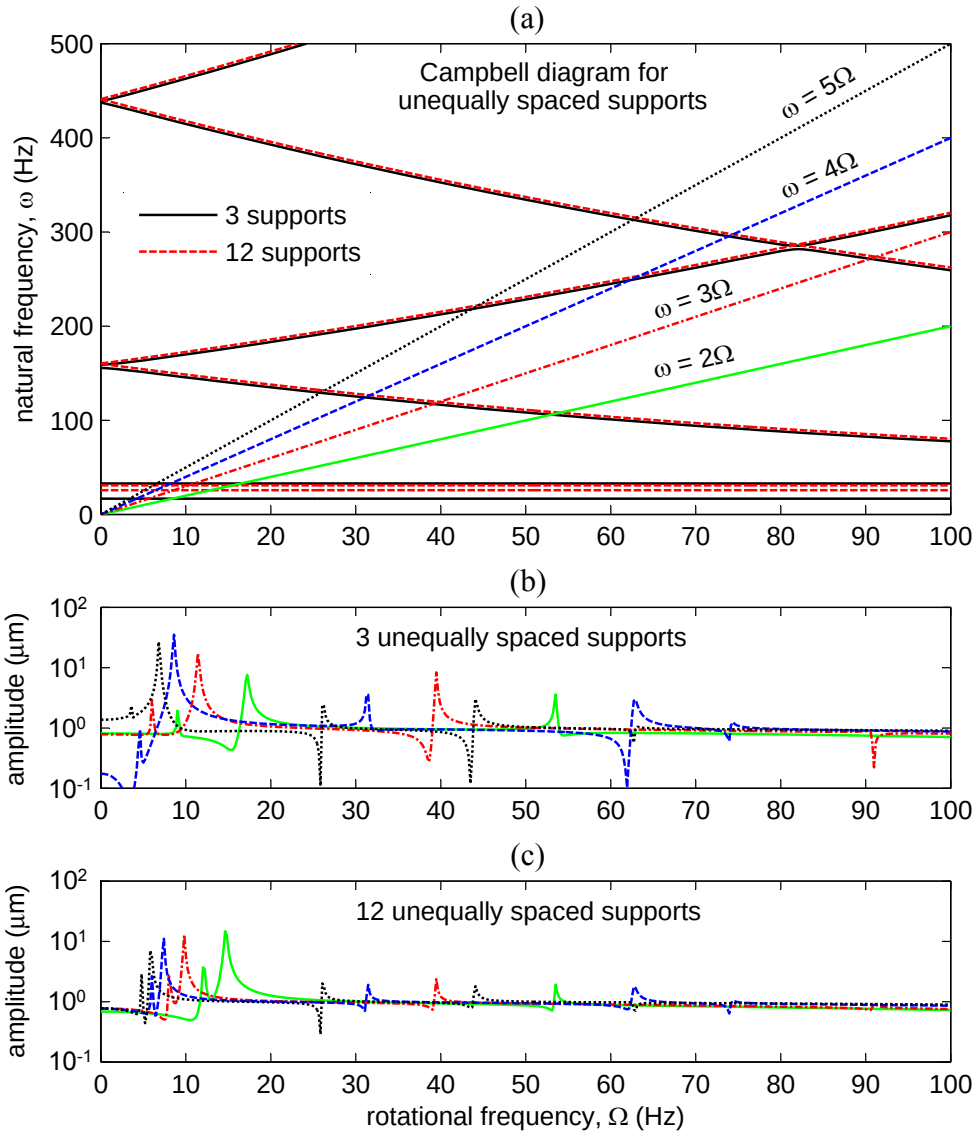

Figure 3.4: (a) Campbell diagram for unequally spaced supports (b) Response harmonic amplitudes $Y_{2,\ldots,5}$ for 3 supports (c) Response harmonic amplitudes $Y_{2,\ldots,5}$ for 12 supports

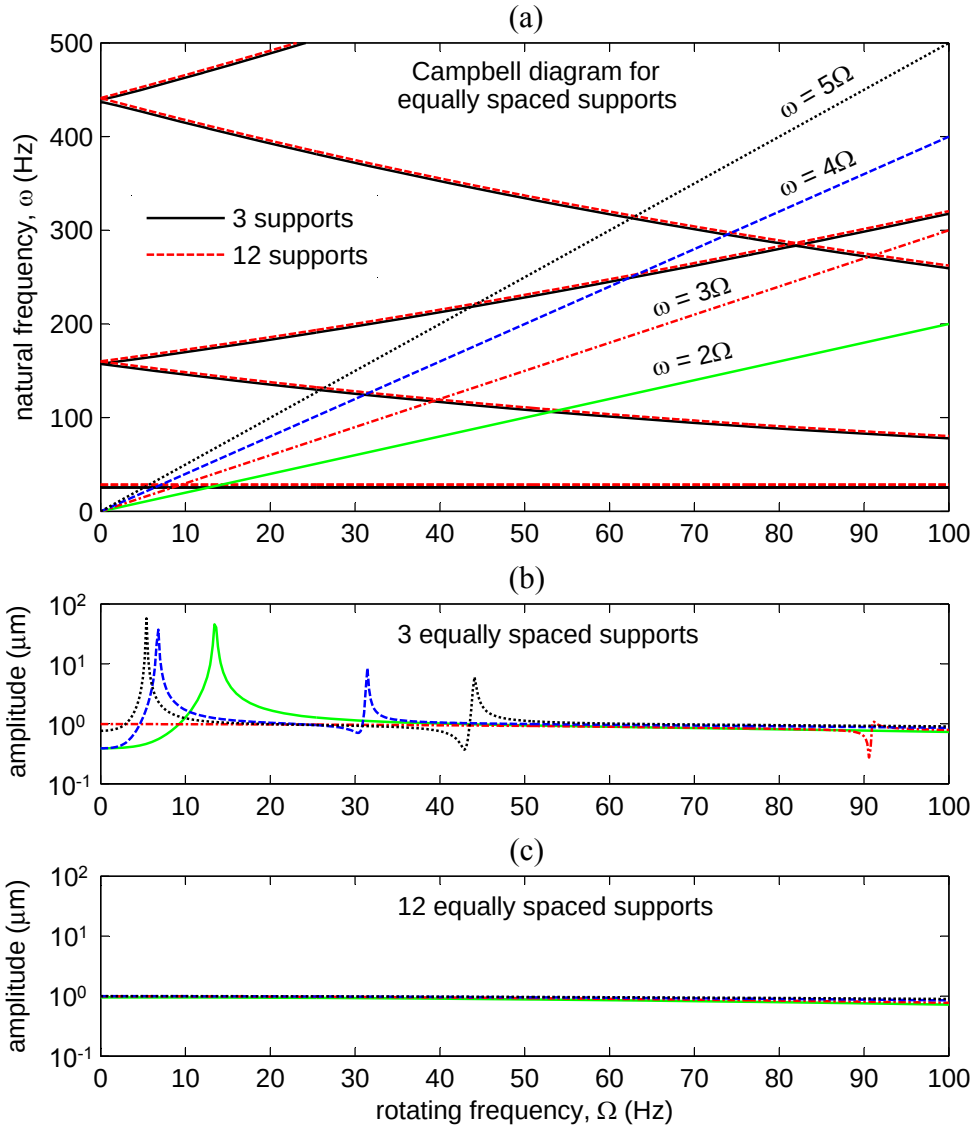

Figure 3.5: (a) Campbell diagram for equally spaced supports (b) Response harmonic amplitudes $Y_{2,\ldots,5}$ for 3 supports (c) Response harmonic amplitudes $Y_{2,\ldots,5}$ for 12 supports

Chapter 4

A distributed actuation magnetic bearing for thin-walled rotors

4.1 Introduction

For all rotating machinery, vibration phenomena arise from the interaction of rotating parts with fixed bearing components. Classical rotordynamic considerations deal primarily with lateral vibration of rotors due to asymmetries arising in manufacture and installation, such as rotor unbalance or component misalignments [27, 66]. A key issue is that the natural modes of vibration for the rotor-bearing structure give rise to critical speeds at which resonance occurs during operation. Damping of rotor flexible modes to allow supercritical operation can be achieved with passive components, such as magnetic or squeeze-film dampers [44, 80], or by active techniques e.g. with actuated bearings [57, 59]. For systems with active magnetic bearings (AMBs), optimized feedback controller designs can be usefully applied [15, 55, 53, 81]. Active control methods that involve direct vibration cancellation are also possible, e.g. based on adaptive cancellation [54, 16, 24], notch-filtering of feedback signals [30] or repetitive control methods [19].

For hollow rotors, the natural frequencies for vibration due to lateral bending will become much higher than the rotational frequency range if the ratio of wall-thickness to radius is sufficiently small. However, excitation of vibration within the wall of the rotor then becomes a new concern. Further issues may relate to stress-concentration that occurs where the rotor wall connects with supporting bearing components. One possible approach to overcome these issues is through the use of distributed AMB elements that can support a rotating component by applying forces over a larger surface area than is possible with mechanical bearings. The potential to apply control forces to actively suppress vibration within the wall structure of the rotor is also significant.

This paper introduces a new design topology and control approach for the integration of a distributed AMB with a thin-walled rotor. Although AMB designs for hollow cylinder and ring-like rotors have been previously reported, the rotor walls were sufficiently thick that their distortion could be neglected, and so control considerations focused on rigid body dynamics [65] or vibration due to lateral bending [50]. In this paper, a hollow rotor is considered for which the walls are so thin that their flexibility cannot be neglected in the actuation and control strategy. Although the results here involve analysis and experimentation on a short cylindrical rotor, an applicability to more complex rotor structures is foreseen and may be evaluated fully in subsequent work.

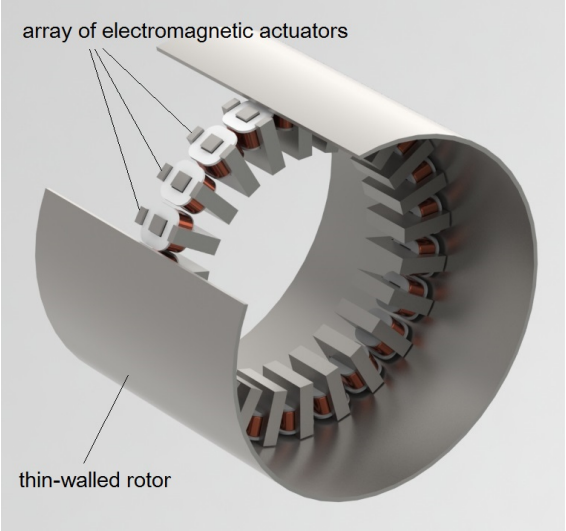

Figure 4.1: Multi-actuator radial AMB concept for interfacing with a thin-walled cylindrical rotor (cutaway).

4.2 Conceptual approach

A concept for active bearing interfacing with a thin-walled rotor structure is exemplified by the circular array of electromagnetic actuators shown in Fig. 4.1. This topology would be appropriate for an internal radial bearing applied to a hollow rotor/shaft system. Similar concepts for internal/external radial, thrust and combination bearings can also be envisaged. For reasons that will become clear, the j^{th} actuator has a number of independently powered coils (indexed by k) with number of turns N_{kj} and regulated current $i_{kj}(t)$. Neglecting eddy current and saturation effects, the magnetic field strength B_j within the actuator core is given by (see [82])

$$B_j = \frac{\mu_0}{l_{iron}/\mu_r + 2s_j} \sum_k N_{kj} i_{kj} \tag{4.1}$$

where l_{iron} is the mean flux path length through the actuator core and rotor wall, s_j is the size of the air gap between the rotor and actuator, μ_0 is the permeability of free space and μ_r is the relative permeability of the core material. The geometry of an archetypal E-shaped actuator is shown in Fig. 4.2. With a further assumption of uniform magnetic field, the attractive force between the actuator and rotor is

$$F_j = \frac{A_p}{\mu_0} B_j^2 \tag{4.2}$$

where A_p is the pole-face area.

A main difference between the proposed topology and that of a standard AMB is the number and size of the electromagnets. The potential utility of any AMB is dependent on the load capacity for a given axial length of bearing. The specific load capacity (force per unit area) is fundamentally limited only by magnetic flux saturation, which is material-dependent. Therefore, downsizing of the actuator to match the wall thickness should have little effect on the overall capacity if the total pole face area is preserved. Rather, the main issue that arises is that the same current-turns must be realized with a smaller coil volume, and this introduces more localized heat generation and stringent cooling requirements. For

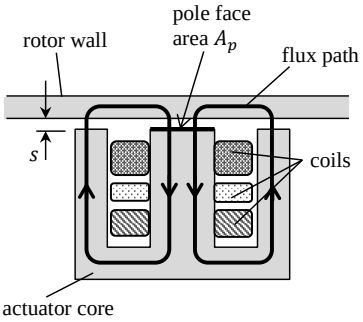

Figure 4.2: Compact E-core actuator geometry.

the tested realization of the concept introduced in this paper, the actuators were operated sufficiently below maximum capacity that heat generation could be managed by passive cooling.

The state of the art for AMB control is to use d.c. servo amplifiers to achieve a controlled variation of the coil currents around a mean 'bias' value [**?**]. Although this causes the uncontrolled bearing to have unstable negative stiffness properties, it allows the design of feedback control algorithms based on linearized models. To make effective use of a large array of actuators, the current in every coil should be varied according to real-time measurements of rotor motion. It is beneficial, for reasons of cost, reliability, weight and size, if this can be achieved with the minimum possible number of drives and sensors.

For industrial applications, it is also desirable that feedback control strategies can be designed using simple models or test procedures, at least to achieve initial levitation and stable operation of a rotor. It is with this motivation that an actuation strategy is proposed (in Section IV) for flexural mode decoupling such that the consideration of rigid body dynamics and PD gain tuning is sufficient to achieve stable operation with acceptable vibration behavior during rotation. The expectation is that more sophisticated model-based feedback control or vibration suppression algorithms may then be designed and implemented as add-on controllers to improve overall performance with regard to flexible mode damping and vibration suppression. However, such extensions are outside the scope of the current paper.

4.3 Dynamic behavior of a thin-walled rotor

4.3.1 Wall vibration

To understand the interaction of rotor wall vibration with AMB operation, a mathematical model is first developed based on the established shell-theory for vibration of thin-walled cylinders [46], but with modifications that take account of rotational effects [27, 22]. According to Fig. 4.3, a reference frame (X', Y', Z) rotates with the rotor at constant angular speed Ω about the fixed axis OZ which is the axis of symmetry for the undeformed rotor. Deformation of the cylinder walls in the radial x-direction is given by $u_r(t, \theta)$ and deformation in the tangential y-direction is given by $v_r(t, \theta)$ where θ is the angular position defined relative to the reference line OX', fixed in the rotating frame. The governing equations may be derived as shown in Chapter 3, leading to

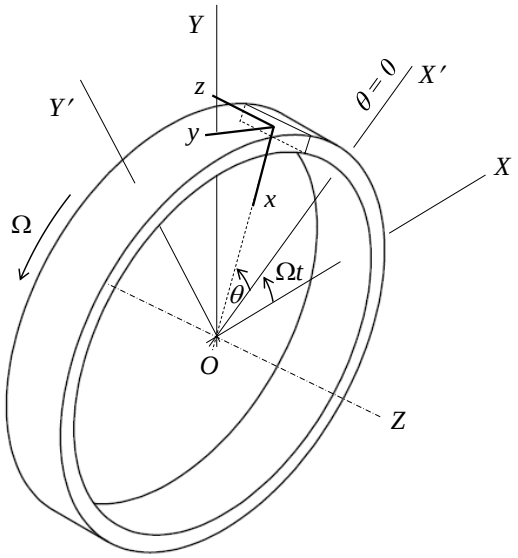

Figure 4.3: Local (x, y, z) and fixed global (X, Y, Z) coordinate systems for describing vibration of a hollow cylindrical rotor.

$$\left(\frac{\partial^2 \ddot{v}_r}{\partial\theta^2} - \ddot{v}_r\right) + 4\Omega\frac{\partial \dot{v}_r}{\partial\theta} - \Omega^2\left(\frac{\partial^4 v_r}{\partial\theta^4} + 3\frac{\partial^2 v_r}{\partial\theta^2}\right) + \omega_0^2\left(1 + \tau\frac{d}{dt}\right)\left(\frac{\partial^6 v_r}{\partial\theta^6} + 2\frac{\partial^4 v_r}{\partial\theta^4} + \frac{\partial^2 v_r}{\partial\theta^2}\right) = \frac{1}{\rho dl}\frac{\partial f_x}{\partial\theta} \quad (4.3)$$

where $\omega_0 = \sqrt{EI_z/\rho r^4 A}$ and the assumption of circumferential inextensibility $u_r = \partial v_r/\partial\theta$ has been applied [?].

Solutions to (4.3) can be obtained in the form $u_m(t,\theta) = P_m(t)\sin m\theta + Q_m(t)\cos m\theta$ where m is the nodal index and corresponds to the (integer) number of wavelengths that fit within the rotor circumference. The corresponding mode shapes for the first four modes are shown in Fig. 4.4. Writing Eq. (4.3) in terms of $u_r = \partial v_r/\partial\theta$ and then substituting $u_r = P_m(t)\sin m\theta + Q_m(t)\cos m\theta$ and exploiting the orthogonality properties of $\cos m\theta$ and $\sin m\theta$ leads to

$$(m^2+1)\ddot{P}_m + 4\Omega m\dot{Q}_m + \tau\omega_0^2 m^2(m^2-1)^2\dot{P}_m + [\Omega^2 m^2(m^2-3) + \omega_0^2 m^2(m^2-1)^2]P_m = \frac{m^2\sin m\theta_F}{\pi\rho r A}F \quad (4.4)$$

$$(m^2+1)\ddot{Q}_m - 4\Omega m\dot{P}_m + \tau\omega_0^2 m^2(m^2-1)^2\dot{Q}_m + [\Omega^2 m^2(m^2-3) + \omega_0^2 m^2(m^2-1)^2]Q_m = \frac{m^2\cos m\theta_F}{\pi\rho r A}F. \quad (4.5)$$

Here, a force F from a single bearing actuator has been accounted for by assuming the force is applied in the radial x-direction at position $\theta = \theta_F$ so that $f_x = \delta(\theta - \theta_F)F/r$. Equations (4.4) and (4.5) can be expressed in first-order matrix form

$$\dot{X}_m = A_m^R X_m + B_m(\theta_F)F, \quad m = 1, ..., \infty \quad (4.6)$$

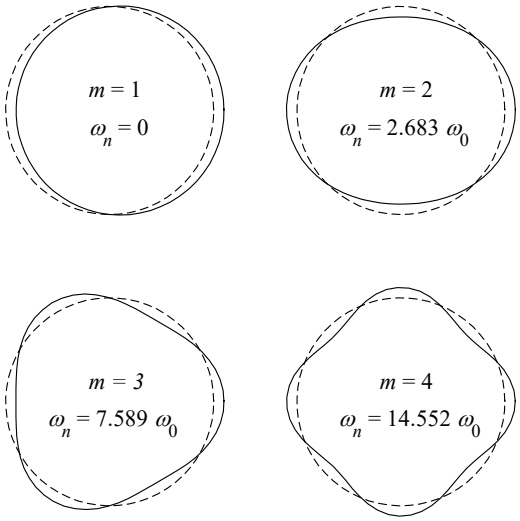

Figure 4.4: Mode shapes for vibration of the walls of a hollow rotor. Natural frequencies are shown for non-rotating case.

where $X_m = [P_m \; Q_m \; \dot{P}_m \; \dot{Q}_m]^T$ and

$$A_m^R = \begin{bmatrix} 0 & 0 & 1 & 0 \\ 0 & 0 & 0 & 1 \\ -k_m - \Omega^2 d_m & 0 & -\tau k_m & -\Omega g_m \\ 0 & -k_m - \Omega^2 d_m & \Omega g_m & -\tau k_m \end{bmatrix}$$

$$B_m(\theta) = b_m \begin{bmatrix} 0 & 0 & \sin m\theta & \cos m\theta \end{bmatrix}^T$$

with

$$d_m = \frac{m^2(m^2-3)}{m^2+1}, \quad k_m = \omega_0^2 \frac{m^2(m^2-1)^2}{m^2+1}$$

$$g_m = \frac{4m}{m^2+1}, \quad b_m = \frac{m^2}{\pi \rho r A (m^2+1)}.$$

The solution for wall vibration is given by

$$u(t,\theta) = \sum_{m=1}^{\infty} u_m(t,\theta) = \sum_{m=1}^{\infty} P_m(t) \sin m\theta + Q_m(t) \cos m\theta \tag{4.7}$$

where $P_m(t)$ and $Q_m(t)$ satisfy (4.6).

4.3.2 Fixed-frame dynamics

A transformation to stationary frame coordinates may be undertaken by defining the fixed frame angular position as $\phi = \theta + \Omega t$. Then, the radial displacement is $u_m(t,\phi) = P_m(t) \sin m(\phi - \Omega t) + Q_m(t) \cos m(\phi - \Omega t) = p_m(t) \sin m\Omega t + q_m(t) \cos m\Omega t$ where p_m and q_m are fixed-frame modal displacement variables. This transformation involves a rotation matrix:

$$\begin{bmatrix} P_m \\ Q_m \end{bmatrix} = \begin{bmatrix} \cos m\Omega t & -\sin m\Omega t \\ \sin m\Omega t & \cos m\Omega t \end{bmatrix} \begin{bmatrix} p_m \\ q_m \end{bmatrix}.$$

By substituting this expression in (4.6) and assuming the force F is applied at a fixed angular position ϕ_F in the stationary frame, so that $\theta_F = \phi_F - \Omega t$, we can finally derive the fixed-frame state space equations describing the vibratory dynamics of the free rotor:

$$\begin{bmatrix} \dot{x}_m \\ \ddot{x}_m \end{bmatrix} = \begin{bmatrix} 0_{2\times2} & I_{2\times2} \\ \Delta_m(\Omega) & \Sigma_m(\Omega) \end{bmatrix} \begin{bmatrix} x_m \\ \dot{x}_m \end{bmatrix} + B_m(\phi_F)F, \quad m = 1, ..., \infty \tag{4.8}$$

where $x_m = [p_m \; q_m]^T$ and

$$\Delta_m(\Omega) = \begin{bmatrix} -k_m & m\Omega\tau k_m \\ -m\Omega\tau k_m & -k_m \end{bmatrix}, \; \Sigma_m(\Omega) = \begin{bmatrix} -\tau k_m & -\Omega g_m + 2m\Omega \\ \Omega g_m - 2m\Omega & -\tau k_m \end{bmatrix}.$$

The deflection of the rotor wall at angular position ϕ is

$$u(t, \phi) = \sum_{m=1}^{\infty} p_m(t) \sin m\phi + q_m(t) \cos m\phi. \tag{4.9}$$

The natural frequencies for free vibration, and the variation in their values with rotational speed, are important for rotordynamic behavior. These may be determined from the eigenmodes of equation (4.6) and (4.8) for observation in the rotating frame and fixed frame respectively. For each integer value of the nodal index m there are two natural modes. For non-zero rotational speed, their natural frequencies are distinct due to the Coriolis terms $\pm\Omega g_m$ in (4.6). For flexural vibration ($m > 1$) the lower frequency mode corresponds to a forward traveling wave while the higher frequency mode is a backward traveling wave. The $m = 1$ mode involves rigid body translation and both natural frequencies are equal to the rotational frequency (for rotating frame observation). Campbell diagrams for the free rotor are shown in Fig. 4.5.

To assess the potential for excitation of these modes, the natural frequencies should also be evaluated in the fixed frame (Fig. 4.5b). It may be observed from the eigenvectors of A_m^F that, for each value of the nodal index $m > 1$, the natural frequency for the forward traveling wave (which is now the higher value) increases monotonically with increasing rotational speed. For the backward traveling waves, the observed frequency decreases with increasing speed, converging toward zero. The potential for resonance may be anticipated due to excitation sources having frequencies that are harmonics of the rotational frequency, as also shown in Fig. 4.5b. The presence of higher harmonics could lead to many resonance conditions during spin-up/spin-down as indicated by the crossing points in Fig. 4.5b. These would arise due to unwanted asymmetries associated with the rotor geometry (non-circularity) or material properties. These characteristics are examined more closely for the experimental rotor-bearing system under closed loop control in Section (4.5).

4.4 System modeling for control analysis

4.4.1 Actuated rotor

A state space model of the rotor-bearing system, accounting for an array of J actuators, is obtained from (4.8) as

$$\begin{bmatrix} \dot{x}_m \\ \ddot{x}_m \end{bmatrix} = \begin{bmatrix} 0_{2\times2} & I_{2\times2} \\ \Delta_m(\Omega) & \Sigma_m(\Omega) \end{bmatrix} \begin{bmatrix} x_m \\ \dot{x}_m \end{bmatrix} + \sum_{j=1}^{J} B_m(\phi_j^a)F_j \tag{4.10}$$

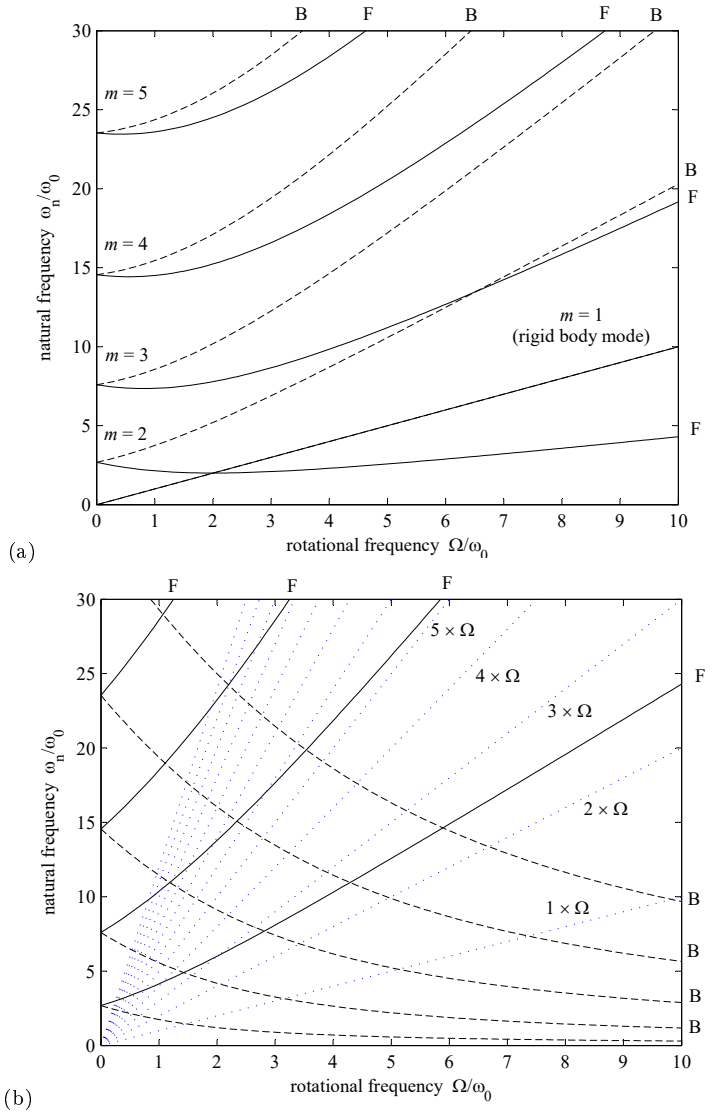

Figure 4.5: Campbell diagram for thin-walled rotor showing variation in natural frequencies for wall vibration with rotational speed: as observed in (a) rotating frame and (b) fixed frame. Each natural frequency relates to either a forward (F) or backward (B) traveling wave.

where the j^{th} actuator is located at angular position $\phi = \phi_j^a$. The radial displacement at the j^{th} actuator location is

$$u_j(t) = \sum_{m=1}^{\infty} p_m(t) \sin m\phi_j^a + q_m(t) \cos m\phi_j^a. \tag{4.11}$$

The radial displacement at sensor location ϕ_i^s is

$$y_i(t) = \sum_{m=1}^{\infty} p_m(t) \sin m\phi_i^s + q_m(t) \cos m\phi_i^s. \tag{4.12}$$

If each actuator has two-coils then, according to the model (4.1)-(4.2), the actuator force is

$$F_j = \frac{\mu_0 A_p (N_{1j} i_{1j} + N_{2j} i_{2j})^2}{(l_0 - 2u_j)^2} \tag{4.13}$$

where $l_0 = l_{iron}/\mu_r + 2s_0$ for equal gaps ($s_j = s_0$). A coil driving scheme with four drives, each used to power a series connection of a subset of coils with varying number of turns, may be considered as shown in Fig. 4.6. Suppose the currents produced by the four drives are specified by a differential scheme using a fixed bias current i_0 and two control currents i_{c1} and i_{c2} so that $i_1(t) = i_0 \pm i_{c1}(t)$ and $i_2(t) = i_0 \pm i_{c2}(t)$ (with the sign dependent on which drive is connected to the coil). Defining coil-turn parameters η_{1j} and η_{2j} that may take positive or negative values according to which drive is connected, but also satisfy $|\eta_{1j}| = N_{1j}$, $|\eta_{2j}| = N_{2j}$, the actuation force may be expressed

$$F_j = \frac{\mu_0 A_p (|\eta_{1j}| i_0 + \eta_{1j} i_{c1} + |\eta_{2j}| i_0 + \eta_{2j} i_{c2})^2}{(l_0 - 2u_j)^2}. \tag{4.14}$$

Linearizing about a given operating point, denoted E, gives

$$F_j \approx F_{0j} + a_{1j} i_{c1} + a_{2j} i_{c2} + h_j u_j \tag{4.15}$$

where

$$\begin{aligned}
a_{1j} &= \eta_{1j}(|\eta_{1j}| i_0 + \eta_{1j} i_{c1} + |\eta_{2j}| i_0 + \eta_{2j} i_{c2}) \frac{2\mu_0 A_p}{(l_0 - 2u_j)^2}\Big|_E, \\
a_{2j} &= \eta_{2j}(|\eta_{2j}| i_0 + \eta_{1j} i_{c1} + |\eta_{2j}| i_0 + \eta_{2j} i_{c2}) \frac{2\mu_0 A_p}{(l_0 - 2u_j)^2}\Big|_E, \\
h_j &= (|\eta_{1j}| i_0 + \eta_{1j} i_{c1} + |\eta_{2j}| i_0 + \eta_{2j} i_{c2})^2 \frac{4\mu_0 A_p}{(l_0 - 2u_j)^3}\Big|_E.
\end{aligned}$$

The parameters a_{1j}, a_{2j} are force/current gains for the actuator, while h_j is the force/displacement gain and acts as a destabilizing negative stiffness. The constant force components F_{0j} may cause some small distortion of the rotor, but can be neglected for dynamic analysis. Defining the block diagonal matrices $\Delta = diag(\Delta_1, \Delta_2, ..., \Delta_M)$, $\Sigma = diag(\Sigma_1, \Sigma_2, ..., \Sigma_M)$, the linearized state-space equation for the open-loop dynamics, retaining M modes, is obtained from (4.10) and (4.15) as

$$\begin{bmatrix} \dot{x} \\ \ddot{x} \end{bmatrix} = \begin{bmatrix} 0 & I \\ \Delta + \Delta^{neg} & \Sigma \end{bmatrix} \begin{bmatrix} x \\ \dot{x} \end{bmatrix} + \begin{bmatrix} 0 \\ B\Psi A \end{bmatrix} \begin{bmatrix} i_{c1} \\ i_{c2} \end{bmatrix} \tag{4.16}$$

where $\Delta^{neg} = B\Psi H \Psi^T$ and

$$B = diag(b_1, b_1, b_2, b_2, ..., b_M, b_M),$$

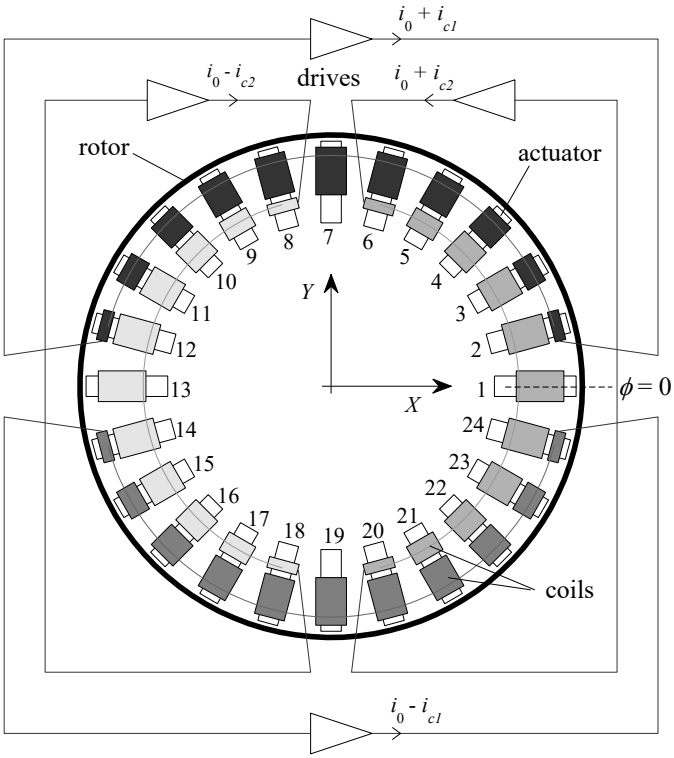

Figure 4.6: Coil winding and driving scheme for levitation control.

$$H = diag(h_1, h_2, ..., h_J),$$

$$\Psi = \begin{bmatrix} \sin\phi_1^a & \sin\phi_2^a & ... & \sin\phi_J^a \\ \cos\phi_1^a & \cos\phi_2^a & ... & \cos\phi_J^a \\ \sin 2\phi_1^a & \sin 2\phi_2^a & ... & \sin 2\phi_J^a \\ \cos 2\phi_1^a & \cos 2\phi_2^a & ... & \cos 2\phi_J^a \\ \vdots & \vdots & & \vdots \\ \sin M\phi_1^a & \sin M\phi_2^a & ... & \sin M\phi_J^a \\ \cos M\phi_1^a & \cos M\phi_2^a & ... & \cos M\phi_J^a \end{bmatrix},$$

$$A = \begin{bmatrix} a_{11} & a_{21} \\ a_{12} & a_{22} \\ \vdots & \vdots \\ a_{1J} & a_{2J} \end{bmatrix}.$$

4.4.2 Coil winding scheme

The aim now is to determine a coil configuration that will admit stabilizing control at a nominal operating point using feedback of measured rotor radial positions at discrete locations only. Standard non-contact displacement sensors may then be used, though preferably as few as is possible. A key issue is that, under these assumptions, there will always be actuators that are not collocated with sensors and so it can be anticipated that the stability of higher order modes will need to be considered when synthesizing an actuation/control scheme. The approach taken here is to adopt a winding scheme that (for a given operating point) decouples the net actuation forces from the flexural modes of

the rotor wall ($m > 1$). Such a decoupling requires that all but the first two rows of the matrix $B\Psi A$ appearing in (4.16) are zero. This requires

$$\begin{matrix} \sum_{j=1}^{J} \sin m\phi_j^a \, a_{qj} = 0 \\ \sum_{j=1}^{J} \cos m\phi_j^a \, a_{qj} = 0 \end{matrix} , \; m = 2, 3, ..., \infty, \; q = 1, 2. \tag{4.17}$$

Suppose the actuators are spaced evenly. These equations then hold if a_{qj} take values given by

$$a_{1j} = \alpha \sin \phi_j^a, \; a_{2j} = \alpha \cos \phi_j^a \tag{4.18}$$

for some constant α. The orthogonal rigid-body displacements p_1 and q_1 will then couple independently with i_{c1} and i_{c2} respectively. In this case, the applied distribution of actuation forces will have the form shown in Fig. 4.7 and can exactly oppose a rigid-body acceleration without exciting flexural modes or causing distortion of the rotor cross-section. Moreover, a feedback controller design can be undertaken by considering requirements for stable levitation of a rigid rotor, i.e. by considering the rigid body modes only, without concern for destabilization of the flexural modes.

To achieve modal decoupling for a disturbance-free operating point $i_{c1} = i_{c2} = u_j = 0$ requires

$$a_{1j} = \eta_{1j}(|\eta_{1j}| + |\eta_{2j}|)\frac{2i_0\mu_0 A_p}{l_0^2} = \alpha \sin \phi_j^a \tag{4.19}$$

$$a_{2j} = \eta_{2j}(|\eta_{1j}| + |\eta_{2j}|)\frac{2i_0\mu_0 A_p}{l_0^2} = \alpha \cos \phi_j^a \tag{4.20}$$

$$h_j = (|\eta_{1j}| + |\eta_{2j}|)^2 \frac{4i_0^2\mu_0 A_p}{l_0^3} = \text{constant}. \tag{4.21}$$

The equation (4.21) ensures that $\Psi H \Psi^T$ is a diagonal matrix and so the negative stiffness effects do not introduce cross-coupling of the rigid body and flexural modes. To achieve all three constraints (4.19)-(4.21), some extra design parameter (in addition to the coil's numbers of turns) would need to be adjusted for each actuator (such as the nominal air gap or pole face area). This will add considerable complexity to the manufacture and assembly of the system and so, for the bearing realization in this paper, the design is based on satisfying the first two constraints (4.19) and (4.20) only. The solution for the number of coil-turns is then

$$\eta_{1j} = \frac{N_0 \sin \phi_j^a}{\sqrt{|\sin \phi_j^a| + |\cos \phi_j^a|}}, \; \eta_{2j} = \frac{N_0 \cos \phi_j^a}{\sqrt{|\sin \phi_j^a| + |\cos \phi_j^a|}} \tag{4.22}$$

where N_0 is the maximum number of turns and some rounding will be necessary to get integer numbers. By substituting (4.22) in (4.19)-(4.21), it can be seen that $\alpha = 2N_0^2 i_0 \mu_0 A_p / l_0^2$ and the resulting negative stiffness for each actuator is given by

$$h_j = (|\sin \phi_j^a| + |\cos \phi_j^a|)\frac{4N_0^2 i_0^2 \mu_0 A_p}{l_0^3}. \tag{4.23}$$

4.4.3 Closed loop dynamics

A general PD-type feedback law using measured displacements and their derivatives has the form

$$\begin{bmatrix} i_{c1} & i_{c2} \end{bmatrix}^T = -K_p y - K_d \dot{y} \tag{4.24}$$

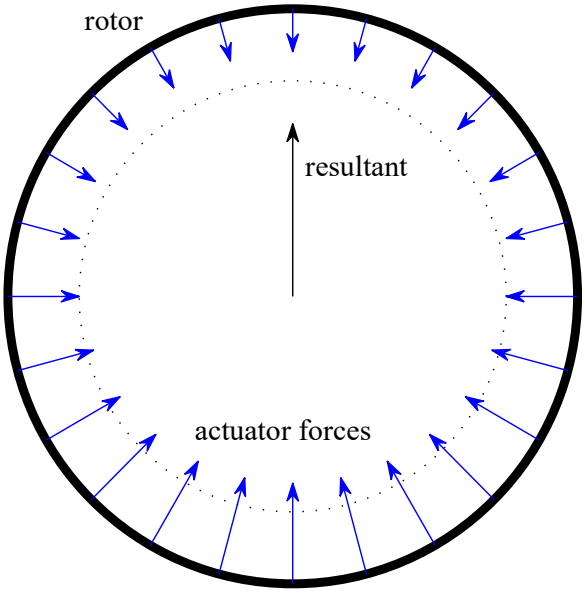

Figure 4.7: Actuator force distribution for rotor flexural mode decoupling.

where K_p and K_d are matrices with dimensions $2 \times N_s$ where N_s is the number of sensors. According to (4.12), the displacements may be expressed

$$y = \Psi_s^T x \tag{4.25}$$

where

$$\Psi_s = \begin{bmatrix} \sin\phi_1^s & \sin\phi_2^s & \dots & \sin\phi_{N_s}^s \\ \cos\phi_1^s & \cos\phi_2^s & \dots & \cos\phi_{N_s}^s, \\ \sin 2\phi_1^s & \sin 2\phi_2^s & \dots & \sin 2\phi_{N_s}^s \\ \cos 2\phi_1^s & \cos 2\phi_2^s & \dots & \cos 2\phi_{N_s}^s, \\ \vdots & \vdots & & \vdots \\ \sin M\phi_1^s & \sin M\phi_2^s & \dots & \sin M\phi_{N_s}^s \\ \cos M\phi_1^s & \cos M\phi_2^s & \dots & \cos M\phi_{N_s}^s \end{bmatrix}.$$

The linearized closed loop dynamics are then given by

$$\begin{bmatrix} \dot{x} \\ \ddot{x} \end{bmatrix} = \begin{bmatrix} 0 & I \\ \Delta + \Delta^{neg} + \Delta_p & \Sigma + \Sigma_d \end{bmatrix} \begin{bmatrix} x \\ \dot{x} \end{bmatrix} \tag{4.26}$$

where $\Delta_p = -B\Psi AK_p\Psi_s^T$ and $\Sigma_d = -B\Psi AK_d\Psi_s^T$ are matrices of size $2M \times 2M$ for which only the first two rows are non-zero (based on the decoupling condition previously defined).

Isolating the state equations for the rigid body dynamics ($m = 1$), we have

$$\begin{bmatrix} \dot{x}_1 \\ \ddot{x}_1 \end{bmatrix} = \begin{bmatrix} 0 & I \\ \Delta_1^{neg} - EK_p\Psi_{s1}^T & -EK_d\Psi_{s1}^T \end{bmatrix} \begin{bmatrix} x_1 \\ \dot{x}_1 \end{bmatrix} \tag{4.27}$$

where Ψ_{s1} is the first two rows of Ψ_s and

$$\Delta_1^{neg} = b_1 h_1 \begin{bmatrix} \sum_j \sin^2\phi_j^a & 0 \\ 0 & \sum_j \cos^2\phi_j^a \end{bmatrix}, \; E = b_1\alpha \begin{bmatrix} \sum_j \sin^2\phi_j^a & 0 \\ 0 & \sum_j \cos^2\phi_j^a \end{bmatrix}.$$

According to (4.27), a stabilizing controller may be obtained by selecting K_p and K_d such that $EK_p\Psi_{s1}^T$ and $EK_d\Psi_{s1}^T$ are symmetric matrices satisfying

$$EK_p\Psi_{s1}^T - \Delta_1^{neg} > 0, \quad EK_d\Psi_{s1}^T > 0. \tag{4.28}$$

Table 4.1: Rotor properties

parameter	symbol	value	units
rotor radius	r	111.0	mm
wall thickness	d	3.1	mm
material density	ρ	7740	kg/m^3
Young's modulus	E	2×10^{11}	N/m^2
characteristic frequency	ω_0	369	rad/s
axial length		51	mm
rotor mass		0.853	kg

Given that the number of sensors may be two or more, a control law that gives equal weighting to each sensor signal may be defined:

$$K_p = k_p(\Psi_{s1}\Psi_{s1}^T)^{-1}\Psi_{s1}, K_d = k_d(\Psi_{s1}\Psi_{s1}^T)^{-1}\Psi_{s1} \tag{4.29}$$

where k_p and k_d are positive scalars. From (4.27), the rigid body natural frequencies and damping ratios can be determined as

$$\omega_{nx} = \sqrt{b_1(\alpha k_p - h_1)\sum_j \cos^2\phi_j^a}, \tag{4.30}$$

$$\omega_{ny} = \sqrt{b_1(\alpha k_p - h_1)\sum_j \sin^2\phi_j^a}, \tag{4.31}$$

$$\zeta_x = \frac{b_1\alpha k_d}{2\omega_{nx}}\sum_j \cos^2\phi_j^a,\ \zeta_y = \frac{b_1\alpha k_d}{2\omega_{ny}}\sum_j \sin^2\phi_j^a. \tag{4.32}$$

An issue that must still be considered is that transmission of radial load through the bearing, typically due to the rotor weight or other quasi-static loading, will produce a change in operating point so that the decoupling condition (4.17) is no longer satisfied exactly. This will introduce additional non-zero entries in the matrix ΨA and hence a coupling of the flexible mode dynamics with the levitation control will arise. To quantify these effects and determine their impact on stability, a numerical study is undertaken in Section V.

4.5 Evaluation

4.5.1 System description

To evaluate the proposed AMB concept, the experimental prototype shown in Fig. 4.8 was created. The system comprises a short (51 mm length) rotor with diameter 222 mm. The ratio of wall thickness to radius is $d/r = 0.0279$. The rotor is made from a martensitic stainless steel (grade 420J2) with inner and outer surfaces finished by electric discharge machining. Full properties are given in Table 4.1. The internal bearing comprises a circular array of 24 actuators with E-shaped cores, having coils wound on the central claws. Key parameters for the actuator design are listed in Table 4.3. To reduce losses from eddy currents and help maintain actuator bandwidth, the actuator cores have been machined from a soft magnetic powder-sintered steel (Somaloy SPM). The actuator coils

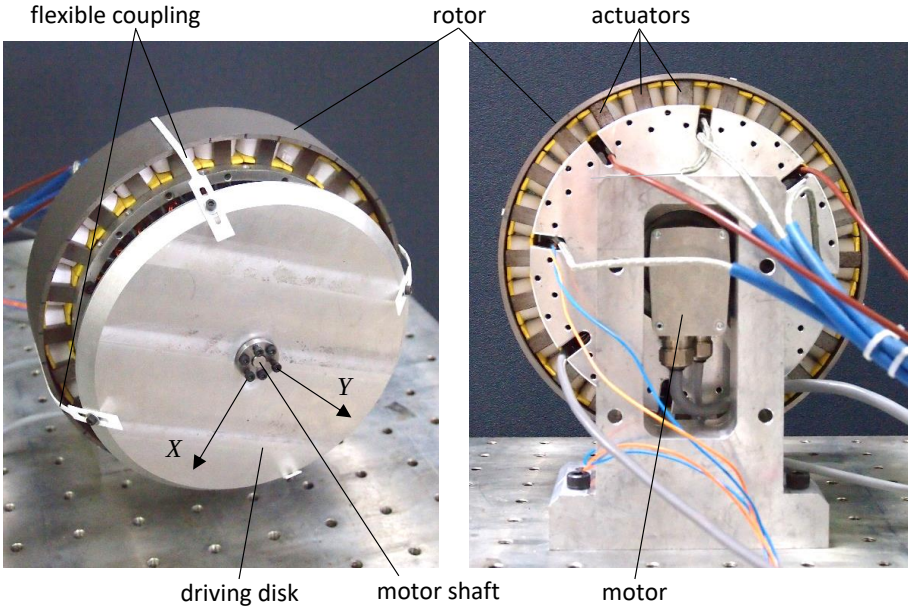

Figure 4.8: Experimental system: Active magnetic bearing with distributed actuation applied to a thin-walled cylindrical rotor.

Table 4.2: Actuator coil winding scheme.

actuator	1	2	3	4	5	6	7	8	9	10	11	12
N_1	0	16	30	42	52	61	70	61	52	42	30	16
N_2	70	61	52	42	30	16	0	16	30	42	52	61

actuator	13	14	15	16	17	18	19	20	21	22	23	24
N_1	0	16	30	42	52	61	70	61	52	42	30	16
N_2	70	61	52	42	30	16	0	16	30	42	52	61

Table 4.3: Actuator properties

parameter	symbol	value	units
number of actuators	J	24	
pole face area	A_p	100	mm^2
core flux path length	l_{iron}	100	mm
mean gap size	s_0	0.8	mm
core relative permeability	μ_r	300	
maximum number of turns	N_0	70	
bias current	i_0	2.2	A

are connected in series as four sets and driven by four d.c. servo drives, as shown in Fig. 4.6. The coil winding pattern is given by (4.22) with $N_0 = 70$, as detailed in Table 4.2.

The rotor is connected axially by four thin flexures to a disk driven by a brushless d.c. motor. This rotor-disk coupling was designed to constrain axial and tilting motion of the rotor and transmit driving/braking torque, but without significantly affecting the radial dynamics of the rotor and wall, as described by the theoretical model introduced in Section (4.3). Hence, stable levitation of the rotor can be achieved only by energizing the actuators based on feedback of rotor radial position, which is measured by non-contact inductance probes located internally. The radial stiffness of the coupling, which is approximately 500 N/m, makes a very small contribution to the overall radial stiffness of the bearing under feedback control. Small rollers may be fitted to the bearing hub to act as touch-down bearings and help avoid rotor-stator contact. These were not fitted for the photo in Fig. 4.8, but were deemed necessary for high speed operation in case of faults, failures or dynamic instability. The maximum operating speed is approximately 40 Hz due to power limitations of the driving motor.

The feedback control algorithm (4.24) was implemented digitally with PC-based hardware and with real-time code generation using MATLAB xPC Target software. The sampling frequency was set to 4000 Hz. The rotor velocity variables $\dot{y}$ were calculated from the position signals based on a first order difference equation with break frequency of 1000 rad/s.

4.5.2 Numerical analyses

Vibration and stability properties may be predicted using the reduced order closed-loop model with PD feedback control, as defined by (4.26) and (4.29). A PD control law is introduced with $k_p = 5700$ A/m and $k_d = 10$ As/m which, according to the theoretical model, results in a damped natural frequency of 25 Hz for rigid-body motion with damping at 32% of critical. The resulting net stiffness of the bearing is approximately 20,000 N/m. Low gain integral feedback may also be usefully applied to eliminate static positioning errors, but the effect on vibrational stability will be small. The effect of various perturbations can be investigated by modifying the operating point for linearization. This leads to a new system matrix in (4.26), the eigenvalues of which can be checked for stability. Although stable operation is predicted for an operating point involving zero load and uniform rotor-stator gaps, perturbation away from this operating point introduces dynamic coupling of the levitation control with the flexural dynamics. This impacts on damping and stability of flexible modes. The level of coupling, and whether it is destabilizing, depends on the number and location of the sensors.

Figure 4.9 shows stability boundaries in terms of static bearing load for two different sensor configurations. Any sensor configuration will provide stable operation for the zero-load operating point. It is seen that the two-sensor configuration (Fig. 4.9a) has an asymmetric stability zone, which necessitates that any loading must be suitably oriented with the sensor axes. Using the four-sensor configuration shown in Fig. 4.9b gives a more symmetric stability region. For both these cases, it is the first flexural mode ($m = 2$) that becomes unstable. This is because, for an equilibrium point that does not involve zero control currents, there is an imbalance of the actuator gains on opposing sides of the rotor. This gain imbalance introduces a feedback effect that may be stabilizing or destabilizing depending on the measured phasing of the modal response. The exact influence of sensor configuration (and other operating parameters) on stability is complex and difficult to predict without resorting to numerical calculations. It is found that the rotational speed does not have a large effect on these stability boundaries for the rotational frequency range considered in this study (0–40 Hz). However, levels of structural damping for the free rotor will depend on fluid/air effects, which are not accounted for in these calculations.

In gravity environments, using two sensors would be most appropriate for a horizontal axis rotor while the four-sensor configuration would be better suited to vertical axis systems. For the experiments reported in this paper, feedback control was based on two inductance probe sensors, oriented as shown in Fig. 4.9a. The system was set up with the rotation axis horizontal. To match the gravity load with the stability region, the bearing was positioned with the X and Y axes oriented at $\pm 45^\circ$ to the downwards direction, as shown in Fig. 4.8a. The static operating condition then corresponds to the point marked $\circ$ in Fig. 4.9a. The total weight of the rotor is 8.37 N.

4.5.3 Experimental results

The experiments reported here focus on steady-state rotordynamic response behavior for the levitated rotor. The Campbell diagram obtained from the closed loop model (Fig. 4.10) indicates the potential for excitation of both rigid body and flexural modes. Excitation of flexural modes may be significant if super-synchronous excitation arises due to asymmetry of the rotor structure, e.g. due to inhomogeneous material properties, non-uniform wall thickness or non-circularity of the rotor due to machining errors. These effects will share some similarities with classical mass-unbalance excitation but lead to more complex multi-harmonic response behavior.

The dynamic characteristics of the rotor-bearing system were assessed experimentally by frequency response measurements, undertaken at different rotational speeds. Excitation was achieved using small auxiliary coils wound on actuators 1 and 2 (in addition to the main levitation coils) which produced localized forcing of the rotor wall close to sensor 1. The results shown in Fig. 4.11 are for no rotation. For comparison, model-based predictions are also presented and these show good agreement with the experimental data: resonant frequencies for both rigid body and flexural modes are well-matched. Damping levels for flexural modes are dependent on the initial damping for the free rotor, which was set to 0.2 % of critical in the model. There are extra resonance peaks appearing in the experimental data which are associated with rigid body tilting and flexural twisting of the rotor. These modes are not captured by the theoretical model, for which wall deflection u is assumed to be independent of the axial coordinate z. It is believed that these extra modes are excited due to asymmetries introduced by the coupling at one end of the rotor. Figure 4.12 shows the measured frequency response for different rotational speeds (0, 15 and 27 Hz), from which the splitting of forward and backward mode natural frequencies with increasing rotational speed is evident. The theoretical predictions for modal frequen-

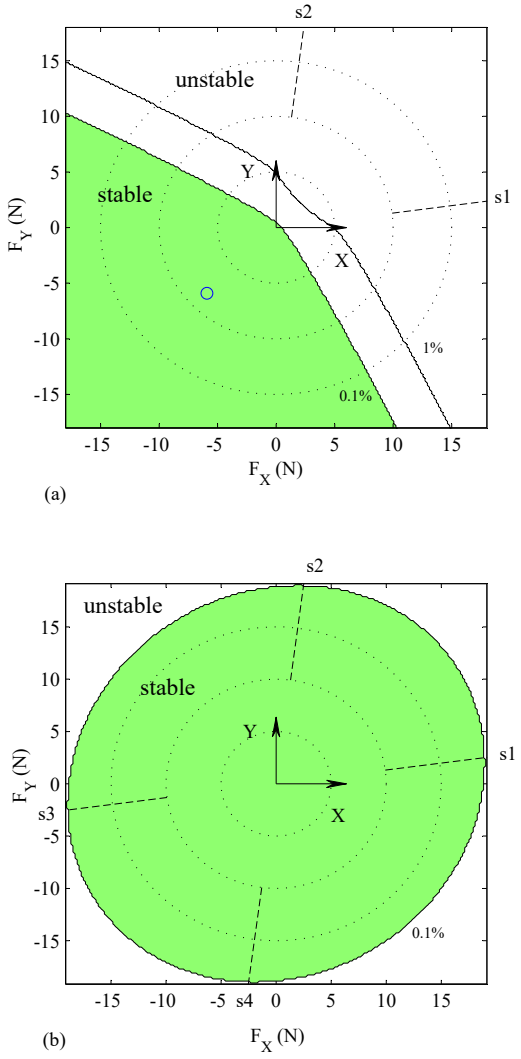

Figure 4.9: Stability regions for the experimental system in terms of static bearing force. Each map is for a different sensor configuration and shows stability regions for different initial levels of damping for rotor flexural modes (0.1% and 1% of critical). Sensor locations are indicated by s1, s2,...etc.

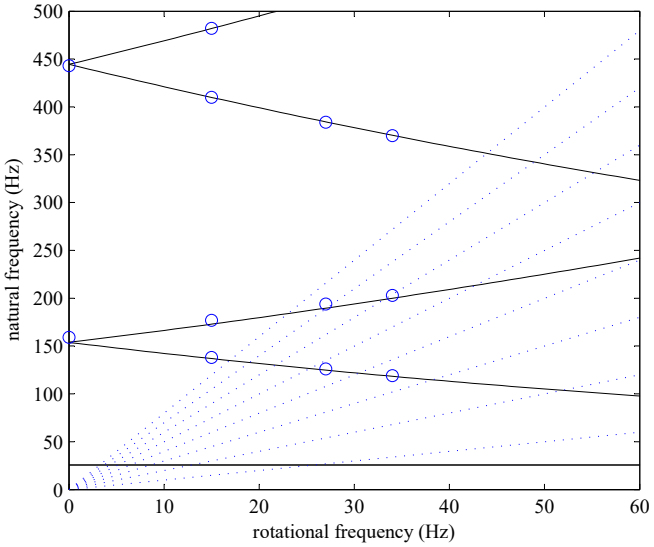

Figure 4.10: Campbell diagram for experimental system (levitated rotor) based on theoretical model. Experimentally determined natural frequencies are indicated by ∘.

cies based on thin-shell theory match well with these experimental results, as shown in Fig. 4.10. It is also notable that the twisting mode resonance (at 373 Hz) is suppressed during rotation.

Figure 4.13a shows measured signals during deceleration of the rotor from an initial rotational frequency of 34 Hz. A spectogram (short time Fourier transform) of the signal from sensor 1 is shown in Fig. 4.13b. The vibration involves many harmonic components with frequencies that are integer multiples of the rotational frequency. These arise due to asymmetry of the rotor shape and properties. The spectrogram shows that many different super-synchronous components excite the rigid body mode (at 25 Hz) during deceleration. Although non-circularity of the cross-section is within $\pm 50\,\mu$m (radial error), the rotor has a somewhat elliptical shape and this causes a dominant vibration component with frequency $2 \times \Omega$. There is only slight evidence of excitation of the $m = 2$ flexural modes from the spectogram (more so for the higher frequency forward mode). Given the low damping and highly resonant behavior seen in the direct frequency response measurements, the lack of flexural mode excitation during normal operation is significant. This can be at least partly attributed to the distributed actuation scheme, which has been designed to minimize excitation of the flexural modes through the bearing.

4.6 Chapter summary

This chapter has described a new active magnetic bearing design and control approach for supporting thin-walled rotor structures. The design embodies a distributed actuation scheme, synthesized from a theoretical description of rotor vibration with the aim of decoupling the levitation control system dynamics from the flexural dynamics of the rotor wall. The approach has been validated by both analytical and experimental studies focusing on stability and vibration behavior of a short-length rotor-bearing system. The results are encouraging and motivate further application of the distributed actuation approach to more complex thin-walled rotor systems, including those with multiple bearing units or multi-directional actuator distributions. This will facilitate new approaches to rotor-bearing system design and active vibration control for various machine types.

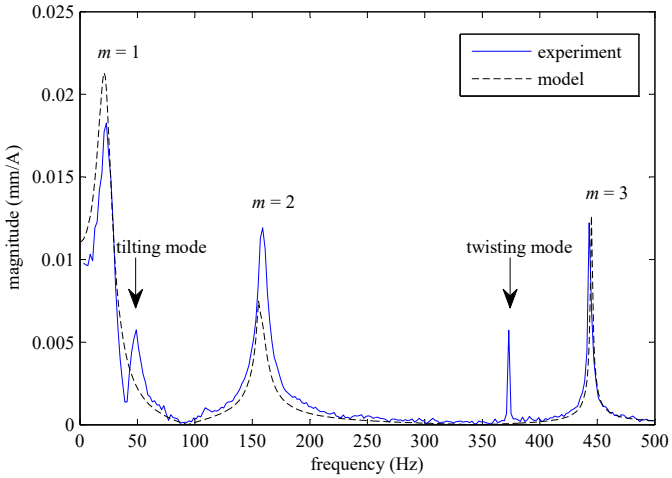

Figure 4.11: Frequency response data for excitation of levitated rotor using auxiliary actuation coils: Theory and experiment.

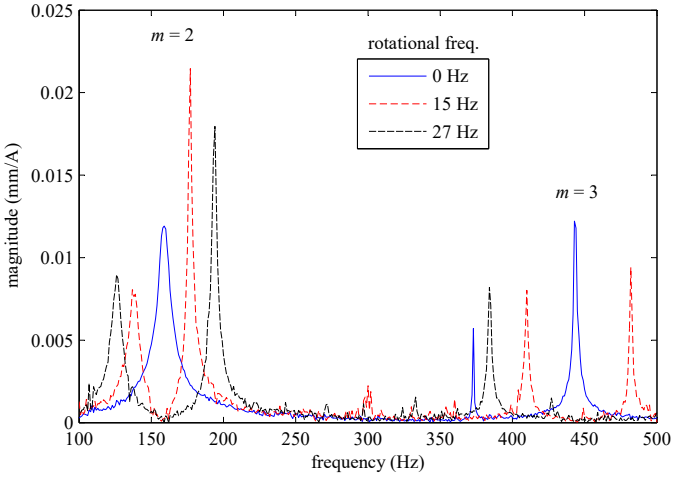

Figure 4.12: Frequency response measurements for different rotational frequencies.

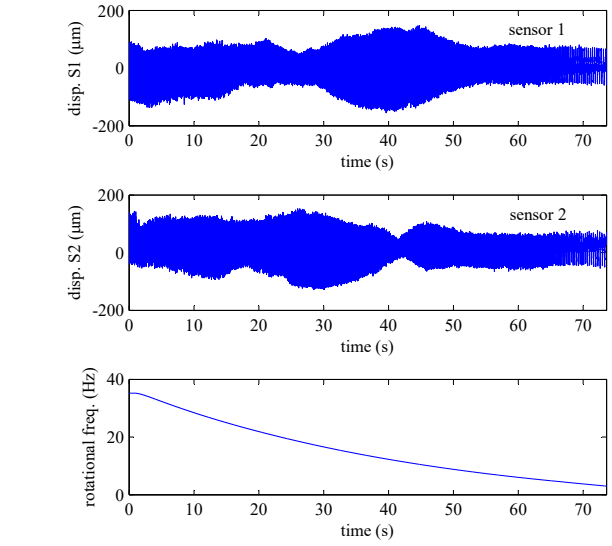

(a)

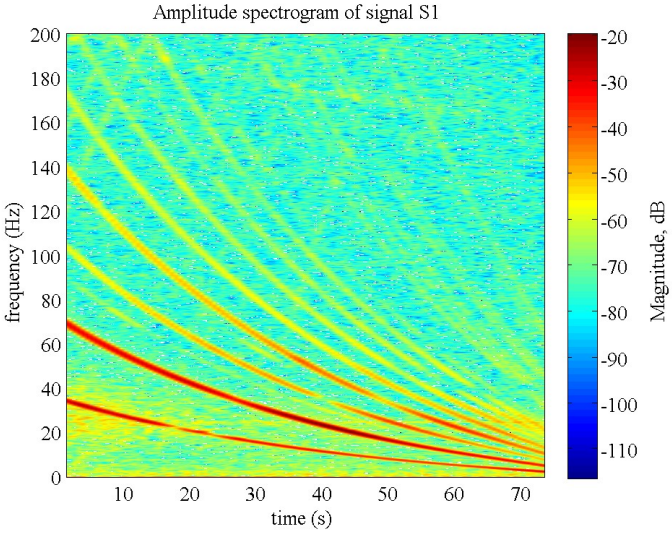

(b)

Figure 4.13: Rotor vibration response during coast-down: (a) measured signals (b) spectogram (short time Fourier transform) of displacement at sensor 1.

Chapter 5

Control methodology for a DAMB and thin-walled rotor subject to noncircularity

5.1 Introduction

Active magnetic bearings (AMBs) rely on feedback control of electromagnetic actuators to achieve stable levitation of a rotating shaft. The ability to apply forces to a rotor without contact eliminates wear and the need for lubrication and permits very high shaft speeds. Further advantages are derived from the capacity to actively control and suppress vibration within the structure of a machine [66]. Recently, the application of magnetic bearings has been considered for hollow thin-walled and annular rotors [13, 65, 50, 23]. In addition to specialized applications, thin-walled rotor topologies can play a significant role in future lightweight turbo-machine design [61, 58]. The development of control methods for a thin-walled rotor-AMB system with enhanced vibration suppression capabilities has not been previously considered and is the focus of this paper.

For solid-shaft rotors, discrepancy between the inertia axis and the geometric axis of the rotor causes harmonic vibration that is synchronous with rotation [27]. Early work on unbalance vibration control with AMBs considered strategies to minimize motion of the geometric axis of a rotor [52, 48, 41]. Various linear control methods such as repetitive control, adaptive disturbance rejection and notch filtering can be applied to this problem [30, 10, 19, 54]. Further advances have been made with strategies that can maintain stability during large-amplitude vibration subject to non-linear dynamics and contact with touchdown bearings [14, 8, 74, 12].

Although reducing rotor vibration is desirable to avoid contact or rub, it can cause unwanted transmission of vibration through the bearing to the machine housing. Furthermore, since unbalance forces are proportional to the square of rotational speed, actuator force saturation may occur when operating at high speed. Transmission of unbalance forces can be reduced by adjusting synchronous control forces until the rotor rotates around its inertia axis. This can be achieved by unbalance estimation methods or adaptive cancellation of synchronous current components [10, 11]. Such methods require that the rotor is well-balanced and are not appropriate when flexural dynamics dominate the response behavior.

Additional vibration excitation can arise with the use of proximity sensors for feedback control. Noncircularity of the rotor cross-section and/or non-homogeneous properties of the rotor material give rise to erroneous components in the measurement signals, commonly

referred to as run-out error. These are operated on by the feedback controller, causing unwanted control currents components that induce multi-frequency vibration of the rotor. Methods for periodic disturbance cancellation may be applied to reduce both synchronous and higher harmonic components of control currents [19, 79, 36]. Darbandi et al. employed sensor run-out identification using an integral adaptive observer [20] while Setiawan et al. proposed an adaptive algorithm for sensor run-out compensation achieving asymptotic stability of the rotor geometric center [67]. These papers focus on rotors that are effectively rigid and so dynamic models and stabilization schemes involve relatively simple parametric formulations.

Vibration control for flexible rotors with multiple excitation sources is more challenging [60]. The need for complex dynamic models may be avoided by using online identification routines to determine speed-dependent control influence coefficients. Optimized control can then be achieved even with complex multi-input multi-output dynamics [17, 51, 62]. For a thin-walled rotor, two main issues must be addressed in the controller design that do not arise for conventional solid-shaft rotor-AMB systems:

1. Flexural vibration modes involving radial distortion of the rotor wall can play a significant role in dynamic behavior and, without due consideration in control algorithm design, these lightly damped modes can easily destabilize. This is complicated by the fact that the natural frequencies undergo large changes in value due to speed-dependent Coriolis effects.

2. Multi-harmonic disturbances arise due to small noncircularity of the rotor cross-section. This differs to sensor run-out error as the variation in surface position is associated also with variation in mass distribution and gap size between the rotor and actuator, causing additional rotor disturbance effects.

An effective control strategy should achieve an acceptable balance of vibration attenuation and coil current levels irrespective of the exact operating conditions and state of rotor non-circularity. However, the presence of multi-harmonic vibration, arising through multiple excitation mechanisms, makes the problem challenging. This paper provides a detailed analysis of these issues and describes a novel control approach to suppress vibration of a thin-walled rotor with a distributed actuation magnetic bearing (DAMB).

5.2 DAMB design and control considerations

A distributed actuation magnetic bearing, designed to support a thin-walled rotor, is shown schematically in Fig. 5.1. An array of electromagnetic actuators (numbering N_A) is positioned, either internally or externally, around the rotor circumference with small uniform gaps between the pole faces and the rotor surface. Each actuator applies an attractive force to the rotor that varies with the gap size (dependent on rotor motion/vibration) and the currents within the actuator coils. To achieve a balanced contact-free support of the rotor, the position of the rotor surface is measured at two locations using proximity probes so that the center position may be calculated (subject to noncircularity error) and this information used in real-time for feedback control of the drives that power the actuator coils. The principle of operation is similar to a conventional active magnetic bearing. However, the large number of actuators and thin-walled rotor topology introduce new considerations in the design and operation of feedback controllers [13].

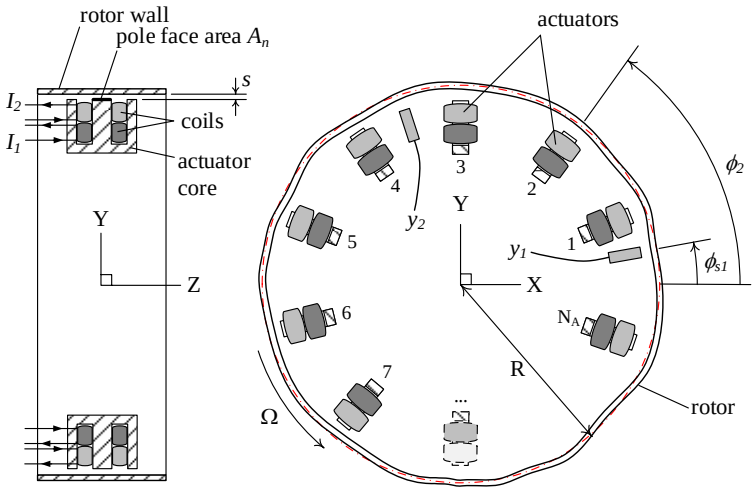

Figure 5.1: Thin-walled rotor with distributed actuation AMB support: Schematic diagram showing (exaggerated) noncircularity of rotor in bearing plane.

5.2.1 Multi-coil distributed actuation approach

A model of the bearing actuator forces for a driving scheme with four drives and up to four coils per actuator may be considered where the radial force applied to the rotor wall by the n^{th} actuator is

$$f_n = \mu_0 A_n \frac{(N_{1,n}I_1 + N_{2,n}I_2 + N_{3,n}I_3 + N_{4,n}I_4)^2}{(l_n/\mu_r + 2s_n - 2y_n)^2}, \quad n = 1, ..., N_A. \tag{5.1}$$

Here, A_n is the total pole face area, l_n is the flux path length through the iron (having relative permeability μ_r), the gap size for the equilibrium position is s_n and y_n is the radial displacement of the rotor wall local to the actuator. Suppose the coils, having number of turns $N_{k,n}$, are supplied currents with the same constant bias component I_0 so that $I_k(t) = I_0 + i_k(t)$ with i_k being the control feedback component. Combining all the actuator forces as single vector $f_A = [f_1\ f_2\ \ldots\ f_{N_A}]^T$ and linearizing Eqs (5.1) about a given operating point P gives an equation in the form

$$f_A = F_0 + \Gamma i_A + H y_A \tag{5.2}$$

where $i_A = [i_1\ i_2\ i_3\ i_4]^T$, $y_A = [y_1\ y_2\ \ldots\ y_{N_A}]^T$ and F_0 is the constant force components due to the bias currents. The elements of the actuator gain matrix Γ are the coefficients:

$$\gamma_{n,k} = \left.\frac{df_n}{di_k}\right|_{\mathrm{P}} = \left. 2\mu_0 A_n N_{k,n}(l_n - 2y_n)^{-2}(\sum_j N_{j,n}I_j)\right|_{\mathrm{P}} \tag{5.3}$$

and H is a diagonal matrix containing the negative stiffness coefficients

$$h_n = \left.\frac{df_n}{di_k}\right|_{\mathrm{P}} = \left. 4\mu_0 A_n (l_n - 2y_n)^{-3}(\sum_j N_{j,n}I_j)^2\right|_{\mathrm{P}} \tag{5.4}$$

For this topology, a coil-winding scheme based on flexural mode decoupling may be employed in order to maximize bearing load capacity and simplify the design of an initial

feedback controller that achieves stable levitation of the rotor [13]. In this case, a differential driving scheme with two control input variables in $i_C = [i_{C1}\, i_{C2}]^T$ is adopted, as for conventional AMBs:

$$i_A = T i_C, \quad T = \begin{bmatrix} 1 & 0 & -1 & 0 \\ 0 & 1 & 0 & -1 \end{bmatrix}^T. \tag{5.5}$$

5.2.2 Vibration control considerations

To define the vibration excitation problem, a mathematical description of the rotor geometry is introduced according to Fig. 5.1. The radial location of the outer (or inner) surface of the rotor is defined relative to the geometric center so that a Fourier series description of noncircularity has the form

$$r(\theta) = R + \sum_{j=2}^{\infty} a_j \cos(j(\theta - \psi_j)) \tag{5.6}$$

Due to rotation, the displacement measured at a fixed angular location ϕ_S will have a time-varying component that is not associated with rotor vibration. If the objective for control is to allow the the rotor to spin about its geometric center without distortion then the measured displacements should exactly match Eq. (5.6). For rotation at constant angular speed Ω this may be expressed

$$d_S(t) = y_S(\phi_S, t)|_{\text{no vib}} = \sum_{j=2}^{\infty} a_j \cos(j(\phi_S - \Omega t - \psi_j)) \tag{5.7}$$

To cancel the effect on control feedback signals, noncircularity may be treated in the same way as sensor run-out error. By using offline measurements of the rotor shape, the displacement due to non-circularity (Eq. (5.7)) can be constructed in real-tme and subtracted from the sensor readings. The resulting signal will correspond to the exact position of the rotor geometric center provided that no wall deformation occurs due to vibration. However, even if noncircularity can be measured accurately, there is still the possibility that the equilibrium shape of the rotor changes during operation e.g. due to thermal distortion or elastic deformation caused by centrifugal loading. Moreover, there are additional excitation effects associated with noncircularity, as well as other system disturbances, that cannot be exactly inferred from sensor readings. Section 3 gives a full analysis of non–circularity effects and their impact for vibration control based on a 2-d model of a thin-walled rotor with single DAMB.

5.3 Rotordynamic model

To obtain a representative model of rotordynamic behavior, the continuum equation for radial vibration of a thin rotating annulus may be considered in the form [23, 27, 22]:

$$\begin{aligned} \left(\frac{\partial^2 \ddot{u}}{\partial \phi^2} - \ddot{u}\right) + 2\Omega\left(\frac{\partial^3 \dot{u}}{\partial \phi^3} + \frac{\partial \dot{u}}{\partial \phi}\right) &+ \frac{Ed^2}{12\rho R^4}\left(\frac{\partial^6 u}{\partial \phi^6} + 2\frac{\partial^4 u}{\partial \phi^4} + \frac{\partial^2 u}{\partial^2 \phi}\right) \\ &= \frac{1}{\rho L d}\frac{\partial^2 F}{\partial \phi^2} + \Omega^2\left(\frac{\partial^4 u_0}{\partial \phi^4} + 3\frac{\partial^2 u_0}{\partial \phi^2}\right) \end{aligned} \tag{5.8}$$

where Ω is the constant angular speed, d is the wall thickness, L is the axial length and ρ and E are the material density and Young's modulus respectively. Motion is defined in

terms of the radial displacement $u(\phi,t)$ with ϕ being the angular position in the fixed frame, while $u_0(\phi,t)$ is the radial displacement associated with noncircularity. Applied forces are captured by a radial force distribution $F(\phi,t)$. The noncircularity may be represented by a truncated Fourier series from Eq. (5.6) so that, accounting also for rotation,

$$u_0(\phi,t) = \sum_{j=2}^{M} a_j \cos(j(\phi - \psi_j - \Omega t)) \tag{5.9}$$

Equation (5.9) defines the multi-harmonic forcing of the system. A solution to Eq. (5.8) can be approximated by a superposition of a finite number of modes:

$$u(\phi,t) \approx \sum_{m=1}^{M} [p_m(t)\sin m\phi + q_m(t)\cos m\phi] \tag{5.10}$$

where $\sin m\phi$ and $\cos m\phi$ are the mode shapes for free vibration and $p_m(t)$ and $q_m(t)$ are the m^{th} modal displacement coordinates, with m being the circumferential wavenumber (integer). Substituting Eq. (5.9) and (5.10) in Eq. (5.8) and evaluating the inner products with respect to $\sin m\phi$ and $\cos m\phi$ by integrating over ϕ leads to a set of $2M$ equations (for $m = 1, ..., M$):

$$\ddot{p}_m - \Omega g_m \dot{q}_m + k_m p_m = v_m \sum_{n=1}^{N} f_n \sin m\phi_n - \Omega^2 w_m [a_m \sin m(\Omega t - \psi_m)] \tag{5.11}$$

$$\ddot{q}_m + \Omega g_m \dot{p}_m + k_m q_m = v_m \sum_{n=1}^{N} f_n \cos m\phi_n - \Omega^2 w_m [a_m \cos m(\Omega t - \psi_m)] \tag{5.12}$$

where $f_n(t)$ is the radial actuator force applied at angular position ϕ_n. The constant coefficients are

$$k_m = \tfrac{Ed^2}{12\rho R^4}\tfrac{m^2(m^2-1)^2}{m^2+1},\ g_m = \tfrac{2m(m^2-1)}{m^2+1},\ v_m = \tfrac{m^2}{\rho\pi AR(m^2+1)},\ w_m = \tfrac{m^2(m^2-3)}{m^2+1}.$$

Accordingly, the zero-speed natural frequencies for flexural vibration are given by

$$\omega_m = \tfrac{d}{2R^2}\sqrt{\tfrac{E}{3\rho}}\tfrac{m(m^2-1)}{\sqrt{m^2+1}}\ .$$

By defining the noncircularity disturbance as $d_m(t) = a_m \left[\sin m(\Omega t - \psi_m)\ \cos m(\Omega t - \psi_m)\right]^T$, Eqs (5.11) and (5.12) may be expressed in first order matrix form

$$\frac{d}{dt}\begin{bmatrix} x_m \\ \dot{x}_m \end{bmatrix} = \begin{bmatrix} 0 & I \\ -K_m & -\Omega G_m \end{bmatrix}\begin{bmatrix} x_m \\ \dot{x}_m \end{bmatrix} + \begin{bmatrix} 0 \\ I \end{bmatrix}\left[V_m E_m^T f_A - \Omega^2 W_m d_m\right] \tag{5.13}$$

where $x_m = [p_m\ q_m]^T$, $K_m = k_m I$, $G_m = g_m J$, $V_m = v_m I$, $W_m = w_m I$ with I being the identity matrix and

$$J = \begin{bmatrix} 0 & 1 \\ -1 & 0 \end{bmatrix},\ E_m = \begin{bmatrix} \sin m\phi_1 & \cos m\phi_1 \\ \vdots & \vdots \\ \sin m\phi_N & \cos m\phi_N \end{bmatrix}.$$

Combining Eq. (5.13) for $m = 1, .., M$, and defining $x = [x_1^T\ x_2^T\ \cdots\ x_M^T]$ and $d = \left[d_1^T\ \cdots\ d_M^T\right]^T$ leads to

$$\frac{d}{dt}\begin{bmatrix} x \\ \dot{x} \end{bmatrix} = \begin{bmatrix} 0 & I \\ -K & -\Omega G \end{bmatrix}\begin{bmatrix} x \\ \dot{x} \end{bmatrix} + \begin{bmatrix} 0 \\ VE_A^T \end{bmatrix} f_A - \begin{bmatrix} 0 \\ \Omega^2 W \end{bmatrix} d \tag{5.14}$$

where $E_A = \begin{bmatrix} E_1 & E_2 & \cdots & E_M \end{bmatrix}$ and K, G, V and W are block diagonal matrices, in accordance with Eq. (5.13).

The radial location of the rotor surface is $y(\phi,t) = u(\phi,t) + u_0(\phi,t)$. Hence, the displacements at the sensor and actuator locations are given, respectively, by

$$y_S = E_S(x+d), \quad y_A = E_A(x+d) \tag{5.15}$$

where E_S is defined in the same way as E_A, but based on sensor angular locations. For sensor readings, we may define $d_S = E_S d$ such that for zero vibration ($x = 0$) we have $y_S = d_S$, as in Eq. (5.7). Substituting for y_A in the linearized AMB model (5.2) gives

$$f_A = F_0 + \Gamma_C i_C + HE_A(x+d) \tag{5.16}$$

where $\Gamma_C = \Gamma T$. According to equations (5.14)-(5.16) and the corresponding block diagram structure shown in Fig. 5.2, noncircularity excites the system through three mechanisms. Firstly, there is an inertia-related disturbance $\Omega^2 W d$ which acts as a direct forcing of the rotor. The synchronous $m = 1$ component of this disturbance is due to mass unbalance. However, the noncircularity-related components $m \geq 2$, are higher harmonics and have a forcing effect that tends to make the rotor more circular as Ω increases. Secondly, the noncircularity disturbance d has an additive contribution to the position of the rotor surface at the actuator locations. This impacts on actuator forces through feedback effects associated with the actuator stiffness coefficients (embedded in H). Thirdly, the noncircularity acts additively on the displacements measured by the sensors, which impacts on the feedback control signals and introduces additional multi-harmonic excitation that is dependent on the control algorithm.

A model of the plant suitable for control analysis/design follows from Eqs (5.13) and (5.14) as

$$\begin{array}{rcl} \dot{\eta} & = & A(\Omega)\eta + B_C i_C + B_d(\Omega) d \\ y_S & = & C_S \eta + E_S d \end{array} \tag{5.17}$$

where $\eta^T = [x^T \; \dot{x}^T]$ and

$$A(\Omega) = \begin{bmatrix} 0 & I \\ -K + K_A & -\Omega G \end{bmatrix}, \; B_C = \begin{bmatrix} 0 \\ V E_A^T \Gamma_C \end{bmatrix}, B_d(\Omega) = \begin{bmatrix} 0 \\ K_A - \Omega^2 W \end{bmatrix},$$
$$C_S = \begin{bmatrix} E_S & 0 \end{bmatrix}$$

The actuator negative stiffness matrix is $K_A = V E_A^T H E_A$. The transfer functions for the open-loop plant are $G_u(s,\Omega) = C_S(Is - A(\Omega))^{-1} B_C$ and $G_d(s,\Omega) = C_S(Is - A(\Omega))^{-1} B_d$. With the application of sensor-based noncircularity compensation, the signal used for feedback control may be defined as

$$\tilde{y}_S = y_S - \tilde{d}_S = C_S \eta + E_S d - \tilde{d}_S \tag{5.18}$$

where $\tilde{d}_S$ is a vector of compensation signals. For exact cancellation $\tilde{d}_S = E_S d = d_S$ (as in Eq. (5.7)).

5.4 Noncircularity vibration suppression

An approach for harmonic vibration control (HVC) suited to the noncircularity excitation problem is introduced here based on the control structure shown in Fig. 5.2. A feedback controller K_{act} is first implemented to achieve stable levitation of the rotor. This may be chosen as a standard PID controller that is tuned to achieve a targeted net stiffness for the bearing. However, the high frequency gain of K_{act} must be limited in order to avoid

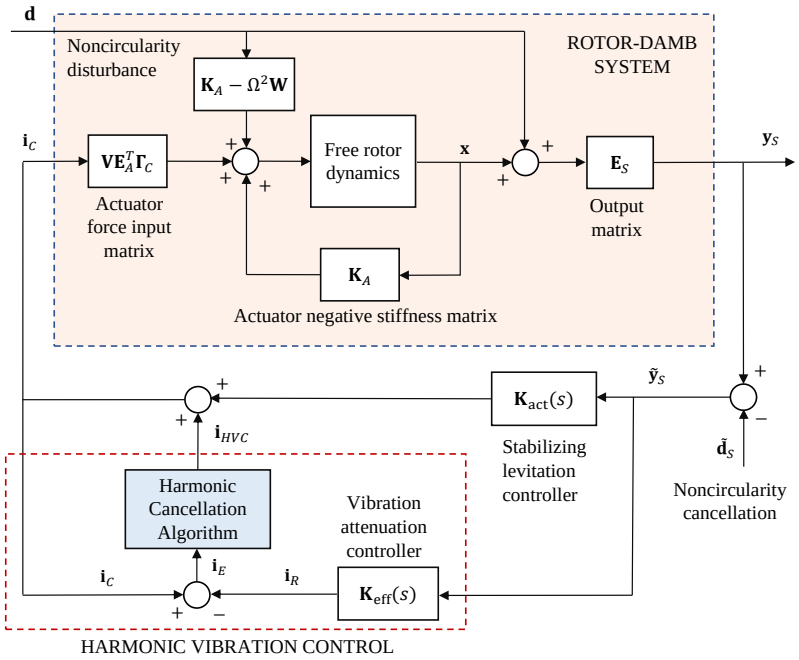

Figure 5.2: System structure for rotor vibration control.

problems of flexural mode destabilization and excessive noise excitation. Consequently, vibration suppression with the controller K_{act} is not optimal and unwanted resonances occur during operation. A different feedback compensation K_{eff} is therefore determined for which the closed-loop transfer function matrix $(I - G_u K_{\text{eff}})^{-1}$ has improved properties for vibration attenuation over the expected range of excitation frequencies (compared with $(I - G_u K_{\text{act}})^{-1}$). However, it is not necessary that K_{eff} can achieve satisfactory (stable and robust) levitation control if implemented on the actual system, only that it gives desired attenuation properties for the expected range of excitation frequencies.

According to Fig. 5.2, feedback stabilization is provided by K_{act}. The controller subsystem K_{eff} also operates on the sensor signals to provide a reference control signal i_R. The difference between the actual control input i_C and the reference signal is treated as an error signal $i_E = i_C - i_R$. The harmonic cancellation algorithm operates on i_E to generate the correction signal i_{HVC}. This algorithm, which is described in detail in Section 4.2, provides a multi-harmonic signal that adapts to eliminate the harmonic components of i_E such that, in steady state, the harmonic components of the control signal correspond to the output from K_{eff}. The result is that the steady-state disturbance attenuation then matches the characteristics of K_{eff}, but only for the discrete frequencies that are targeted within the cancellation algorithm.

5.4.1 System model for control analysis

A linear feedback controller $K(s) = C_K(Is - A_K)^{-1}B_K + D_K$ is considered having state space matrices $\{A_K, B_K, C_K, D_K\}$. Combining this with Eqs (5.17) and (5.18) gives a closed-loop system description as

$$\begin{aligned} \dot{z} &= \widehat{A}(\Omega)z + \widehat{B}_d(\Omega)d + \widehat{B}_S(E_S d - \tilde{d}_S) + \widehat{B}_C i_{HVC} \\ y_S &= \widehat{C}_S z + E_S d \end{aligned} \tag{5.19}$$

where $\widehat{C}_S = \begin{bmatrix} C_S & 0 \end{bmatrix}$ and

$$\widehat{A}(\Omega) = \begin{bmatrix} A(\Omega) + B_C D_K C_S & B_C C_K \\ B_K C_S & A_K \end{bmatrix}, \widehat{B}_C = \begin{bmatrix} B_C \\ 0 \end{bmatrix}, \widehat{B}_d(\Omega) = \begin{bmatrix} B_d(\Omega) \\ 0 \end{bmatrix},$$
$$\widehat{B}_S = \begin{bmatrix} B_C D_K \\ B_K \end{bmatrix}$$

The closed-loop transfer function matrix for the levitated rotor (from i_{HVC} to y_S) may be defined as $P(s,\Omega) = (I - G_u(s)K(s))^{-1}G_u(s) = \widehat{C}_S(Is - \widehat{A}(\Omega))^{-1}\widehat{B}_C$. Equation (5.19) can be used for the prediction of non-circularity excitation with feedback control only ($\tilde{d}_S = 0$), with non-circularity cancellation ($E_S d - \tilde{d}_S = 0$) and/or with operation of harmonic vibration control.

5.4.2 Harmonic Vibration Control algorithm

An alternative but equivalent representation of the control system structure, including HVC algorithm, is shown in Fig. 5.3, where the HVC algorithm operates on the additional feedback component i_E output from the subsystem $K_{\text{act}} - K_{\text{eff}}$. The subsystem $P_{\text{eff}} = (I - \widetilde{G}_u K_{\text{eff}})^{-1}\widetilde{G}_u$ is a speed-dependent model of the closed-loop dynamics, as given by Eq. (5.19) with the effective controller K_{eff}. This is included to provide dynamic cancellation for the effect of i_{HVC} on y_S. For this structure, the transfer function from i_{HVC} to i_E is identity if $\tilde{G}_u(s,\Omega) = G_u(s,\Omega)$, implying the effects of the plant dynamics on the HVC control loop are entirely compensated. This greatly simplifies the design of the HVC algorithm and allows fast convergence rates to be achieved. Note that, for this control structure, the dynamic compensation scheme involves the forward dynamics (rather than inverse dynamics) of the closed-loop system and this allows straightforward realization of a speed-dependent model, avoiding issues with implementation, noise amplification and stability that typically arise for disturbance cancellation schemes involving inverse models.

The harmonic cancellation algorithm involves a matrix-based discrete Fourier transform as shown in Fig. 5.4. The error signal i_E is down-sampled at regular intervals over the period of rotation to form a vector of N_s sample values. This vector is multiplied by the partial DFT matrix R_{FT} to give harmonic amplitudes (Fourier coefficients) for selected frequencies (e.g. the first eight harmonics of the rotational frequency):

$$R_{FT} = 2\begin{bmatrix} \text{Re}(w_2) \\ -\text{Im}(w_2) \\ \vdots \\ \text{Re}(w_8) \\ -\text{Im}(w_8) \end{bmatrix} \text{where} \begin{bmatrix} w_1 \\ w_2 \\ w_3 \\ \vdots \\ w_{N_s} \end{bmatrix} = \frac{1}{N_s}\begin{bmatrix} 1 & 1 & 1 & \cdots & 1 \\ 1 & r & r^2 & \cdots & r^{N_s-1} \\ 1 & r^2 & r^4 & \cdots & r^{2(N_s-1)} \\ \vdots & & & \ddots & \vdots \\ 1 & r^{N_s-1} & r^{2(N_s-1)} & \cdots & r^{(N_s-1)^2} \end{bmatrix}, r = e^{-2\pi j/N_s}$$

The calculated amplitudes then undergo discrete integration with updates every synchronous period (revolution) of the rotor. These control amplitudes are multiplied by the corresponding harmonic signals, which are summed to form the multi-harmonic control signal i_{HVC}. The control update involves a single gain parameter γ. The maximum value of γ for stable convergence is limited by errors in the system model used for dynamic compensation. Empirical tests can be used to select a value that gives acceptable convergence rates for all the targeted harmonic components.

5.5 Test case system

Evaluations were undertaken on a short thin-walled rotor with internal DAMB comprising a circular array of 24 actuators with E-shaped cores, as shown in Fig. 5.5. The experimental

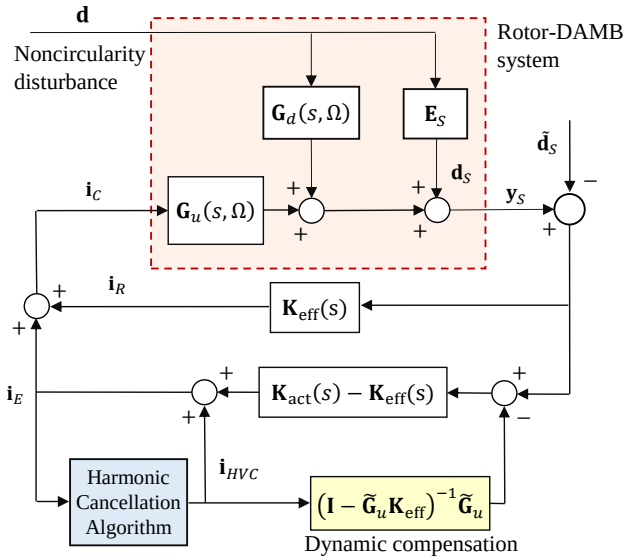

Figure 5.3: Equivalent structure for harmonic vibration control. Dynamic compensation is included so that, with an exact model $\tilde{G}_u = G_u$, the transfer function from i_{HVC} to i_E is identity.

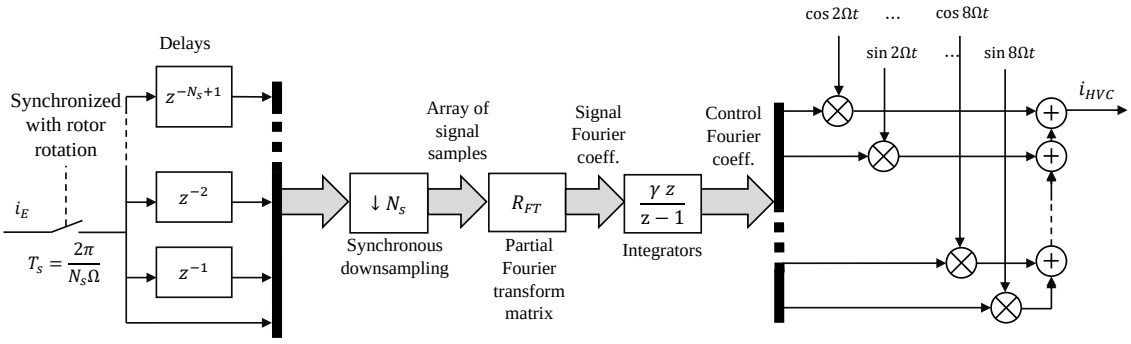

Figure 5.4: Efficient implementation of harmonic vibration cancellation algorithm based on synchronous down-sampling and integral feedback in Fourier coefficient domain.

rotor (radius $R = 111$ mm) was supported radially by the DAMB but also constrained axially by thin flexures connected to a driving disk coupled to a d.c. motor. The flexures prevent tilting and axial motion of the rotor but do not greatly affect the net radial stiffness of the bearing under feedback control. Further system characteristics are given in Table 5.1. The rotor wall thickness is $d = 3.1$ mm and the first flexural mode for wall vibration has a frequency of 155 Hz when $\Omega = 0$.

The actuator coils were connected in series as four sets, driven by four d.c. servo drives and operated with bias currents of $I_0 = 2.2$ A. The coil winding pattern and resulting actuator properties are shown in Fig. 5.6. The actuator force gains vary sinusoidally around the circumference of the bearing and this helps to decouple the actuator forces from the flexural modes of the rotor wall. The resulting negative stiffness distribution of the actuators exhibits a four-fold rotational symmetry. In reality, the effects of radial load and non-uniform clearances cause some deviation from the ideal characteristics shown. Under levitation, the mean gap size between the rotor and actuators was approximately 0.7 mm. For control testing purposes, the system was operated with rotational frequencies up to 30 Hz (1800 rpm).

A PD control law suitable to achieve stable levitation of the rotor was selected as

$$K_{\text{act}}(s) = \left(k_p + \frac{k_d s}{\tau s + 1}\right) I_{2\times 2} = \left(\frac{21s + 6000}{0.001s + 1}\right) I_{2\times 2}$$

A proportional gain of $k_p = 6000$ A/m yields a net bearing stiffness of 25 000 N/m and system natural frequency of 27 Hz for rigid-body motion (based on the theoretical model in Section 4.1). Even with a filtered derivative action ($\tau = 0.001$ s), the value of k_d must be limited to avoid excessive noise excitation and flexural modes destabilization. The chosen value $k_d = 15$ As/m produces damping at approximately 20 % of critical for the rigid body modes. To verify the theoretical model and system characteristics under closed loop control, experimental identification of the frequency response for $P_{\text{act}}(s, \Omega)$ was undertaken for zero speed ($\Omega = 0$). The results in Fig. 5.7 indicate a good level of agreement and confirm the suitability of the model for further analysis. A Campbell diagram showing speed dependency of the system natural frequencies is given in Fig. 5.8. Considering the first eight harmonic components of rotor noncircularity as possible excitation sources, this plot indicates at what speeds significant excitation of the rigid body mode ($m = 1$) and first flexural modes ($m = 2$) may be anticipated over the intended speed range of 0-30 Hz.

To suppress resonance while reducing transmission of bearing forces, the effective controller K_{eff} was chosen as a modified PD control law:

$$K_{\text{eff}}(s) = \left(\frac{29.5s + 4500}{0.001s + 1}\right) I_{2\times 2}$$

This controller (equivalent PD gains $k_p = 4500$ A/m and $k_d = 25$) would result in a very low bearing stiffness (approx. 1 800 N/m) if used directly for feedback control and would not achieve stable levitation. However, the frequency domain properties show much improved disturbance attenuation for the frequency range of concern, with near-elimination of resonances: Predicted frequency response characteristics for $P_{\text{eff}}(s, 0)$ are shown in Fig. 5.7. Further analysis of the vibration control performance with the HVC algorithm is given in Section 5.1, while experimental results are presented in Section 5.2.

5.6 Numerical analyses

Numerical predictions of steady state vibration response behavior were obtained for three different cases:

Table 5.1: Characteristics of experimental thin-walled rotor-DAMB system

Property	Symbol	Value	Units
Rotor radius	R	111.0	mm
Rotor length	L	51	mm
Rotor wall thickness	d	3.1	mm
Material density	ρ	7740	kgm^{-3}
Young's modulus	E	2×10^{11}	Nm^{-2}
First natural frequency for wall flexure	ω_2	155	Hz
Actuator pole-face area	A_n	100	mm^2
Core flux path length	l_n	100	mm
Core relative permeability	μ_r	300	–
Mean gap size	s_0	0.7	mm

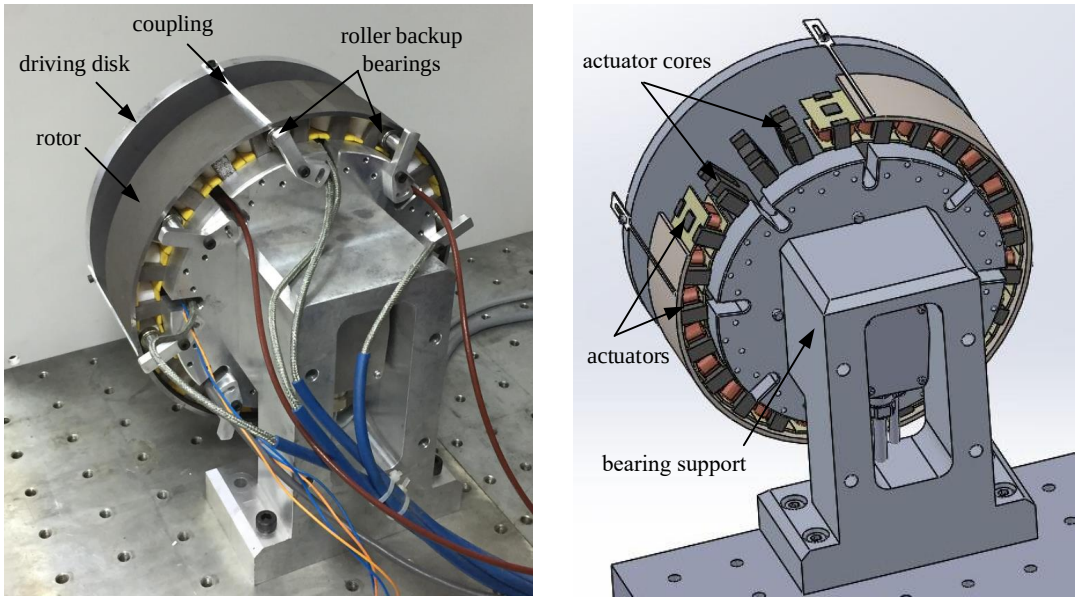

(a) (b)

Figure 5.5: Experimental distributed actuation magnetic bearing supporting a short annular rotor (a) photo (b) CAD model

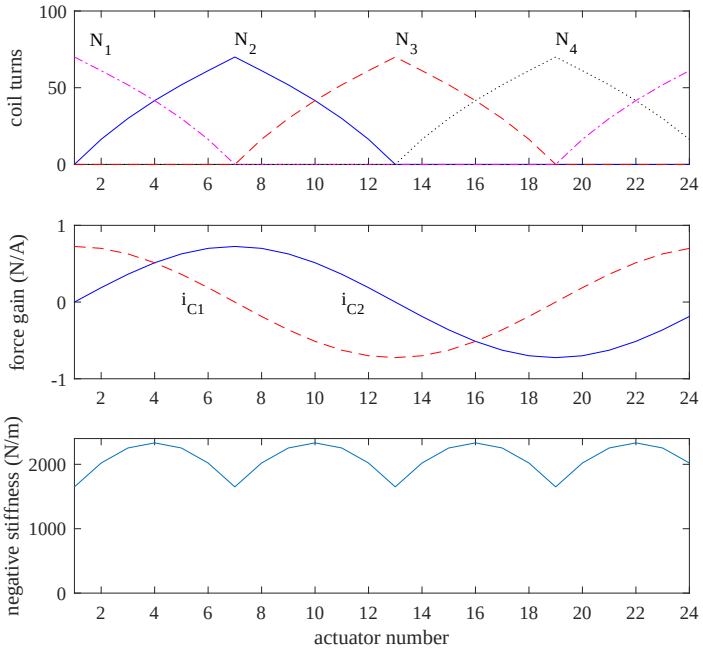

Figure 5.6: Actuator properties for experimental system for no-load operating condition.

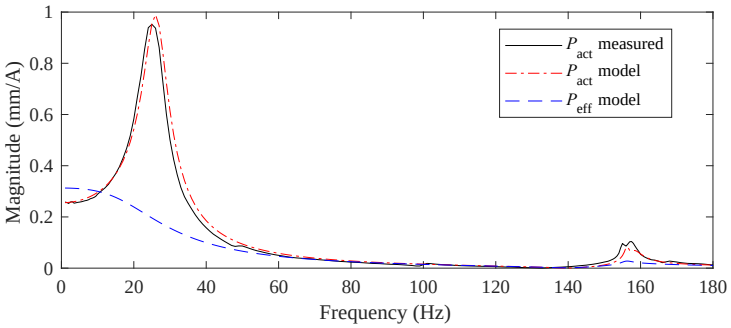

Figure 5.7: Frequency response characteristics for feedback controlled system P_{act} (from i_{HVC} to y_S) when $\Omega = 0$. Results are similar for x and y axis and so only x axis data is shown. The predicted response function P_{eff} with effective control K_{eff} is also shown.

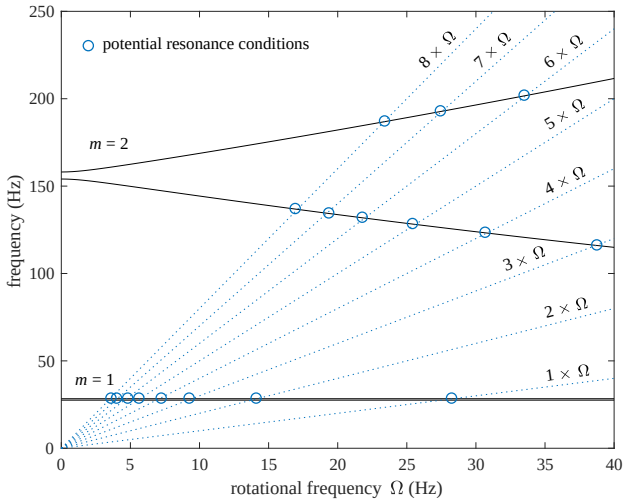

Figure 5.8: Campbell diagram showing variation in natural frequencies for rotor system with DAMB under closed-loop control.

1. Dynamic feedback of displacement sensor signals for bearing stabilization (controller K_{act} only).
2. Feedback with exact sensor-based noncircularity cancellation (controller K_{act} and $\tilde{d}_S = d_S$).
3. With HVC to achieve desired effective control action (controller K_{eff} and $\tilde{d}_S = 0$).

As these are reference cases, every harmonic component of the rotor noncircularity error was assigned an amplitude of $25\,\mu$m. The first harmonic component of vibration, which arises due to synchronous forcing rather than noncircularity error, is neglected. For case 1 shown in Fig. 5.9, every harmonic component exhibits a resonance corresponding to the natural frequency of 27 Hz. Resonance occurs whenever this natural frequency is an integer multiple of the rotational frequency. Both the noncircularity compensation scheme and the HVC algorithm (effective control K_{eff}) alleviate the resonance conditions. Flexural mode excitation remains quite low even without applying additional vibration control algorithms owing to the distributed actuation topology and optimized coil-winding pattern. Two additional cases for inexact noncircularity compensation ($\tilde{d}_S = 0.5 d_S$), both with and without HVC, are shown in Fig. 5.9 (as cases 4 and 5 respectively). It is seen that resonances still occur with inexact cancellation but can be suppressed effectively by the combined application of HVC.

5.7 Experimental results

Noncircularity of the experimental rotor was first determined by offline measurements. This data is shown in Fig. 5.10 with corresponding Fourier coefficients given in Table 5.2. Three different control methods were implemented and tested that correspond to the first three simulated cases described in Section 5.1:

1. Stabilizing feedback control K_{act} and synchronous vibration control only.
2. As case 1 but with additional sensor-based noncircularity compensation.
3. As case 1 but with additional HVC to achieve effective control K_{eff}.

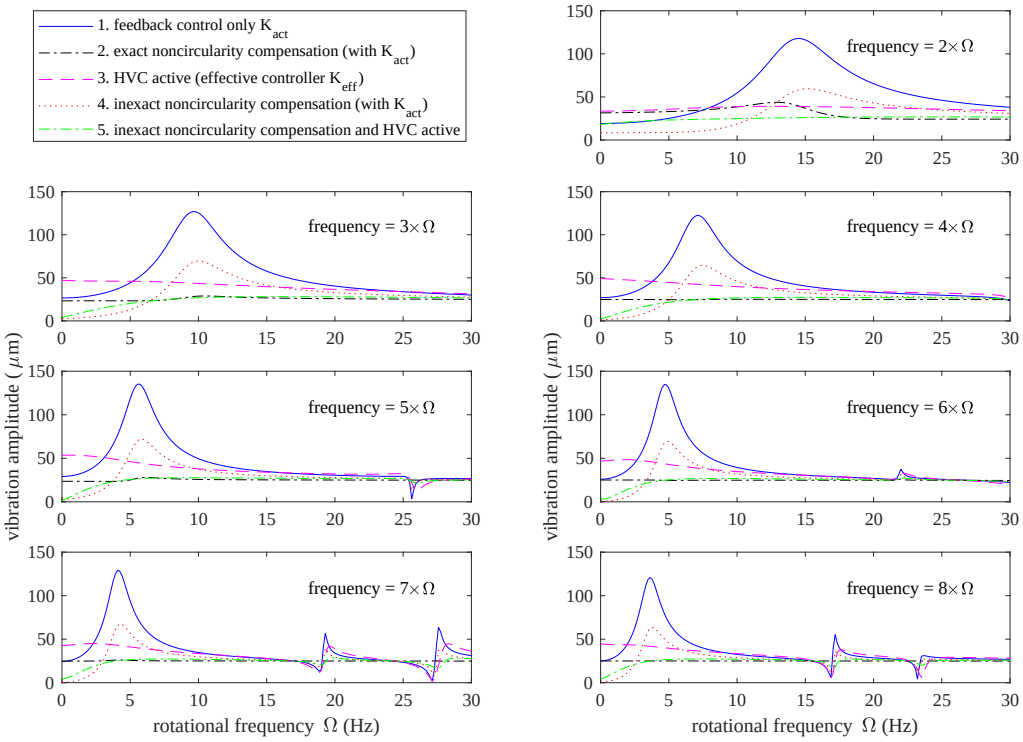

Figure 5.9: Predicted rotor excitation arising due to noncircularity: Amplitudes of harmonic components for displacement measurements.

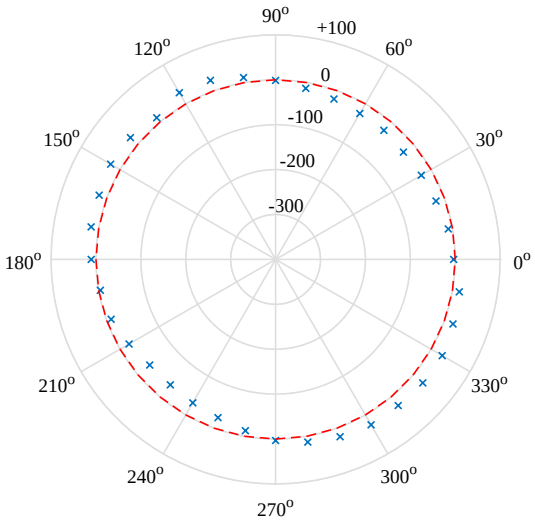

Figure 5.10: Measured noncircularity of experimental thin-walled rotor: inner surface location in sensor plane. Units: μm.

Table 5.2: Measured rotor noncircularity: Fourier coefficients for profile error

Harmonic j	Fourier coefficients	
	Amplitude a_j (μm)	Phase ψ_j (degree)
1	-	-
2	28.4	-85.96
3	3.1	18.26
4	3.4	24.41
5	2.5	42.27
6	2.1	89.29
7	1.0	48.86
8	1.5	-29.83

The first harmonic component of vibration, which arises due to synchronous disturbance forces, was suppressed by a synchronous control algorithm so that the amplitudes remained less than 50 μm for all three cases. The first six harmonic components of the (x-axis) sensor signal are shown in Fig. 5.11. The second ($2\times\Omega$) harmonic, which corresponds to the largest noncircularity component, was the dominant component of vibration. For case 1, a large resonance occurred when the rotational frequency was 14 Hz. Both the noncircularity compensation and the HVC algorithm were effective in suppressing this resonance.

With noncircularity compensation, some small resonances are still seen for the higher harmonics. This is due to errors in the run-out identification as well as residual excitation effects that are not associated with the position sensor signals. The overall behavior is consistent with the model-based predictions shown in Fig. 5.9. Note that, for the experimental system, the excitation of the $7 \times \Omega$ and $8 \times \Omega$ harmonics was too small to be clearly detected and, therefore, this data is not presented. Figure 5.11b shows that some noise effects were present for the higher harmonic components of the control currents with HVC applied, but the overall amplitudes remained low, at less than 0.2 A. Note also that vibration suppression and control stability was maintained even when the harmonic control frequencies pass through the flexural mode frequencies. This is possible due to the dynamic compensation scheme incorporating the flexible rotor model.

Transient behavior during convergence of the HVC algorithm is shown in Fig. 5.12. With the rotor operating at a constant rotational frequency of 13 Hz, multi-harmonic vibration was initially present with large magnitude. The amplitudes of the first two harmonic components were 48 and 35 μm respectively. Activation of the HVC algorithm gave steady attenuation over approximately 10 seconds. Although the rate of attenuation is quite fast, changes in rotor speed that are too rapid lead to a worsening in control performance. Small fluctuations in rotor speed can also prevent expected steady-state levels of vibration attenuation being achieved.

The best results were obtained when noncircularity compensation and HVC were applied together. In this case, the HVC algorithm deals with residual excitation and errors due to inexact knowledge of the noncircularity. The overall vibration attenuation performance was similar to when applying HVC alone, but control current amplitudes were reduced. The results in Fig. 5.13 show the residual sensor signal $y_S - \tilde{d}_S$ after non-circularity compensation. Initially, the system is operating with feedback of the raw sensor signals y_S when (after 5 seconds) the sensor-based noncircularity compensation is applied so that the feedback signal becomes $y_S - \tilde{d}_S$. After a further 10 seconds, the HVC algorithm is additionally operating. This produces a further reduction in vibration levels without noticeable change in control current levels.

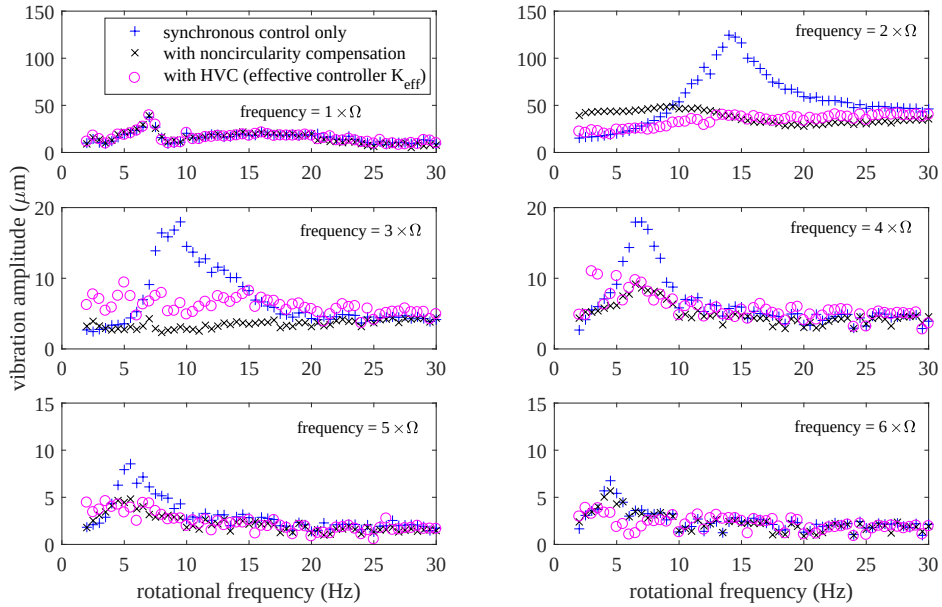

(a)

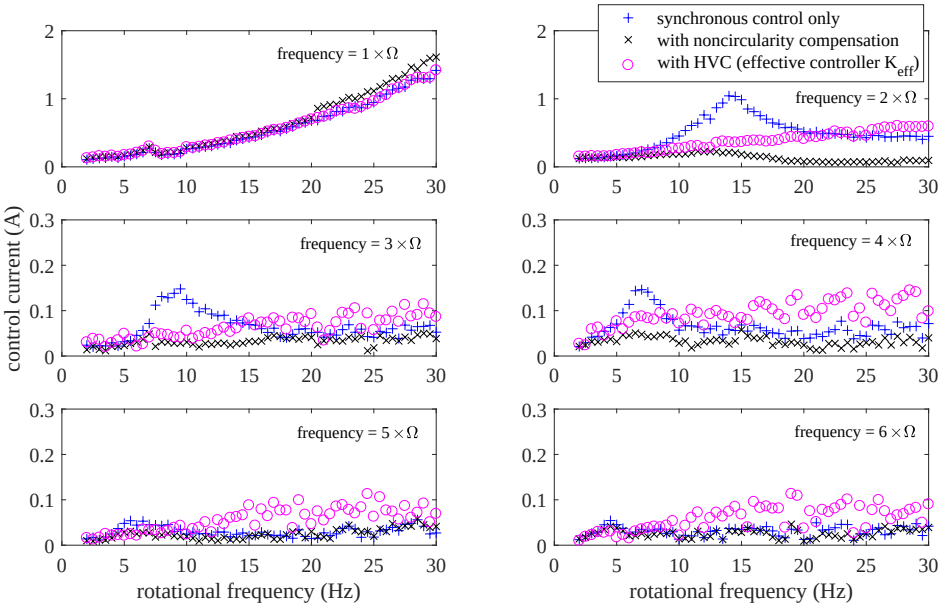

(b)

Figure 5.11: Rotor vibration components arising due to noncircularity excitation. Experimental data for (a) sensor measurements (b) control currents.

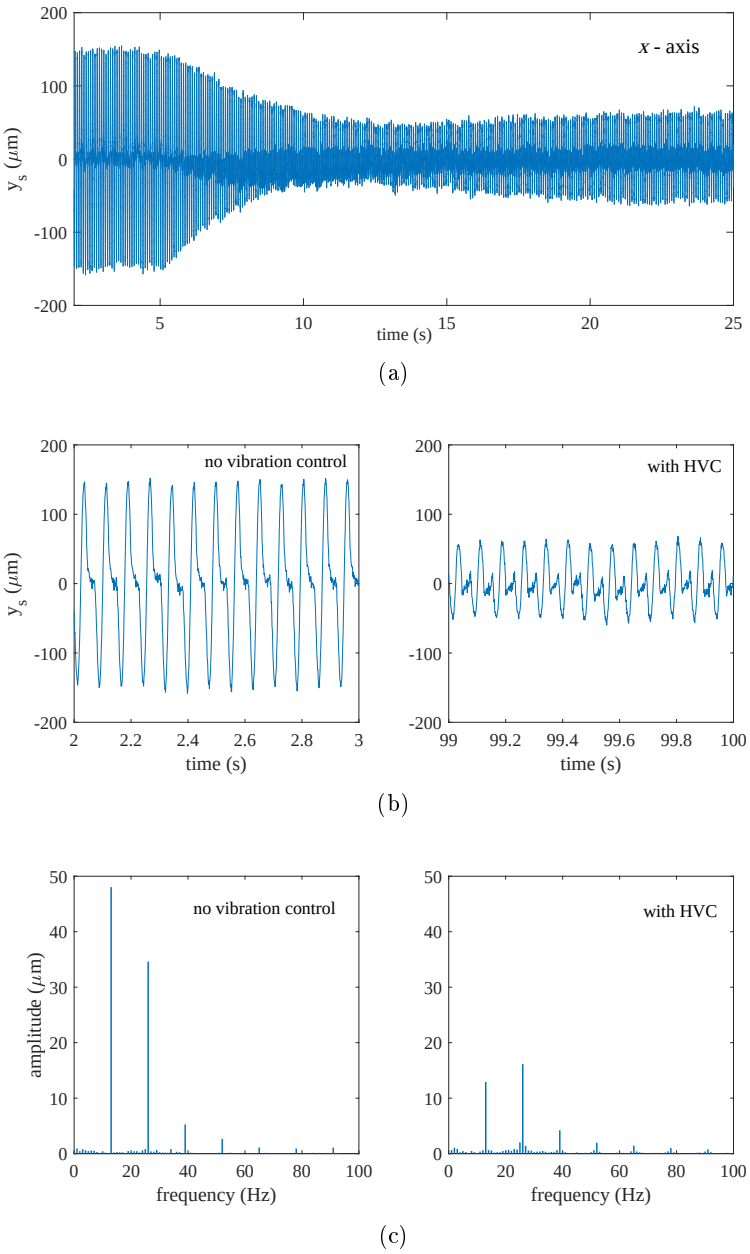

Figure 5.12: Rotor vibration measurements during controller activation $\Omega = 13$ Hz. (a) Transient behavior (b) Steady-state waveforms before and after HVC activation (c) Fourier transforms of steady-state waveforms.

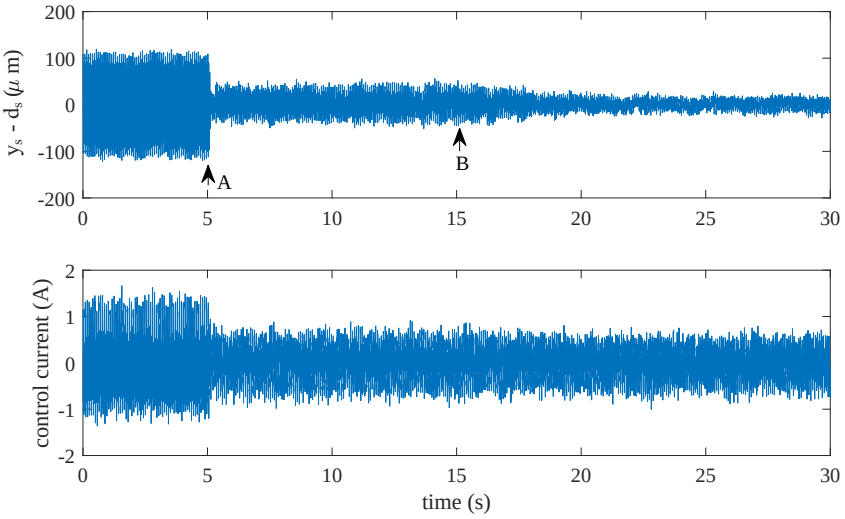

Figure 5.13: Residual vibration $y_S - \tilde{d}_S$ at $\Omega = 13$ Hz. After 5 seconds sensor-based noncircularity compensation is applied (A) and after 15 seconds HVC is additionally applied (B).

5.8 Chapter summary

A control approach has been developed for reducing the vibration of a flexible thin-walled rotor supported by a distributed actuation magnetic bearing. Although direct measurements of rotor noncircularity may be used to compensate its effect on position signals used for feedback control, multi-harmonic vibration may still arise due to measurement error and other excitation mechanisms. An approach for harmonic vibration control has therefore been introduced that achieves effective vibration suppression without requiring information on the rotor shape. The proposed algorithm adaptively modifies the harmonic components of the actuator control currents so that the system response and vibration attenuation performance match a targeted closed-loop system model. Experiments were conducted on a short thin-walled rotor with single DAMB to confirm the efficacy of the proposed methods in preventing resonance during operation. Combining sensor-based noncircularity compensation with harmonic vibration control is seen as a good practical solution as a reduction in vibration levels can be achieved even with imprecise knowledge of the rotor shape and with minimal bearing forces. In future work, extending the approach for application with longer thin-walled rotors having DAMB support in multiple planes will be considered.

Chapter 6

Experimental thin-walled rotor/DAMB system: vibration behviour and 3D model verification

6.1 Introduction

6.2 Experimental system

The experimental system is comprised of a horizontal cylindrical rotor of length 0.8 m with two radial magnetic bearings, as shown in Fig. 6.1. The rotor is a uniform steel tube with properties given in Table 2.1. The rotor has very high natural frequencies for beam bending modes (>1300 Hz) due to its thin-walled structure. The bearings are of a specialized design for thin-walled rotors and are based on a distributed actuation magnetic bearing (DAMB) topology [13]. Each bearing comprises a circular array of 24 small U-shape electromagnetic actuators that apply attractive forces around the periphery of the rotor. Using multiple compact actuators helps to avoid magnetic flux saturation within the rotor wall and thereby achieve high load capacity. The coil winding pattern and driving scheme are devised such that the orthogonal components of the net bearing force (X-Y axes) depend principally on two (X-Y) control current components within the two coils on each actuator. Hence, the bearing forces can be controlled using strategies similar to those applied with conventional AMBs. In open-loop configuration, the bearings are unstable due to the negative stiffness effects from coil bias currents. Stable support of the rotor can be achieved using feedback control of the coil currents based on the measured rotor position. Further details on the operation and modelling of the bearing are given in section 6.3.

The rotor is driven by a brushless d.c. motor connected via a flexible coupling. This

Table 6.1: Properties of magnetic bearing actuators

Parameter	Symbol	Value	Units
Pole face area	A	72	mm^2
Permeability of free space	μ_0	$4\pi \times 10^{-7}$	H/m^{-1}
Effective flux path length	l	1.2	mm
Maximum number of coil-turns	N_0	100	
Bias current	i_0	2.2	A

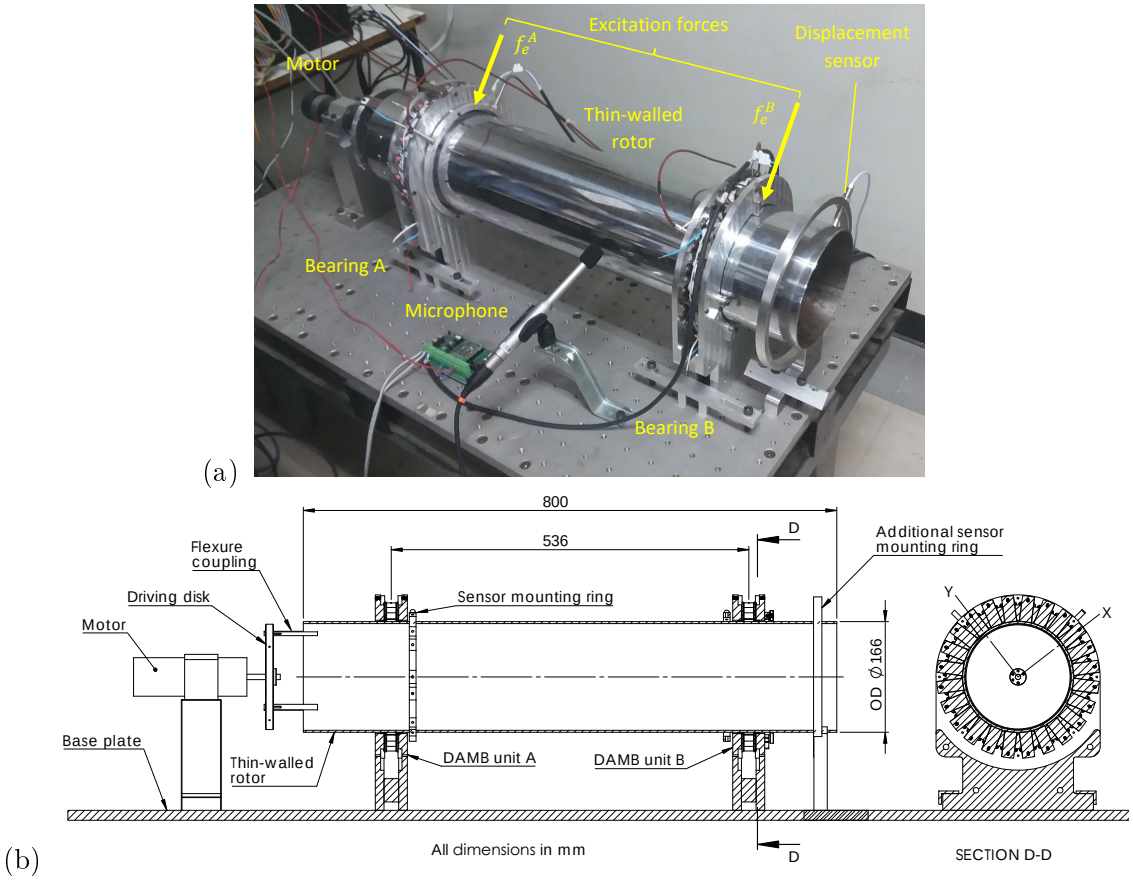

Figure 6.1: Experimental thin-walled cylindrical rotor supported by distributed actuation magnetic bearings (a) photograph (b) cross-section drawings

coupling comprises a disk mounted on the motor shaft with four foam rubber flexures (length 40 mm) that connect between the disk periphery and the end of the rotor. This coupling supports the transmission of a driving torque to the rotor but has negligible effect on the flexible mode dynamics of the rotor.

The system has two pairs of rotor position sensors located in two transverse planes adjacent to each bearing (see Fig. 6.1). These sensors are standard eddy current proximity probes and are used for feedback control of the bearings. In addition, a single high-sensitivity proximity probe is mounted on a movable ring that can be positioned to measure the radial vibration at any point on the rotor surface.

Each bearing has one actuator that is wound with an extra coil. The extra coils are used to apply localized excitation forces to the rotor wall that are aligned with the $+X$ axis direction, as shown in Fig. 6.1. The excitation forces couple strongly with the flexural dynamics of the rotor wall and so can be used for vibration response testing and modal identification of the overall structure during operation.

6.3 Active magnetic bearing model

For the DAMBs, the attractive force applied to the rotor wall by the j^{th} actuator at location (θ_j, z_j) may be described by a standard reluctance force model [66]:

$$P_{x,j}(t) = f_j(x_j, I_1, I_2, i_e) = -\mu_0 A \frac{(N_1 I_1 + N_2 I_2 + N_e i_e)^2}{(l + 2x_j)^2} \tag{6.1}$$

Here, A is the pole face area, l is the effective flux path length for the equilibrium position (accounting for the total reluctance including air gap) and $x_j = u(\theta_j, z_j, t)$ is the radial displacement of the rotor wall. Frictional forces may be neglected, and so $P_{y,j}(t) = P_{z,j}(t) = 0$. Physical values for the experimental system are given in Table 6.1. Two of the coils, having number of turns $N_1(\theta_j)$ and $N_2(\theta_j)$, are used for levitation control and are supplied currents I_1 and I_2 according to a differential driving mode with constant bias component i_0 and control currents i_1 and i_2 [66]. The excitation coil, having N_e turns, is supplied current i_e. This is used for excitation only and is powered separately to provide a localized forcing that can be utilized in dynamic response testing. For the levitation coils, the coil winding and driving scheme is defined by

$$N_1(\theta) = N_0 \frac{|\cos\theta|}{\sqrt{|\sin\theta| + |\cos\theta|}},\ N_2(\theta) = N_0 \frac{|\sin\theta|}{\sqrt{|\sin\theta| + |\cos\theta|}}$$

$$I_1(\theta, t) = i_0 + \operatorname{sgn}(\cos\theta) i_1(t),\ I_2(\theta_j, t) = i_0 + \operatorname{sgn}(\sin\theta) i_2(t)$$

where N_0 is the maximum number of coil turns. This scheme helps to decouple the levitation forces from the flexible mode dynamics and can be realized with just four current-controlled drives powering four sets of coils connected in series [13]. Linearizing Eq. (6.1) about the operating point E with $x_j = i_1 = i_2 = i_e = 0$ gives an equation in the form

$$f_j(t) = f_0 + k_a x_j + \sum_{k=1}^{2} \sigma_k i_k + \sigma_e i_e \tag{6.2}$$

where $f_0 = \mu_0 A l^{-2} i_0^2 (N_1 + N_2)^2$ and

$$k_a(\theta_j) = \left.\frac{df_j}{dx_j}\right|_E = 4\mu_0 A l^{-3} i_0^2 (N_1 + N_2)^2 \tag{6.3}$$

$$\sigma_k(\theta_j) = \left.\frac{df_j}{di_k}\right|_E = \mathrm{sgn}(g_k(\theta_j)) 2\mu_0 A N_k l^{-2} i_0 (N_1 + N_2) \tag{6.4}$$

$$\sigma_e(\theta_j) = \left.\frac{df_j}{di_e}\right|_E = \mathrm{sgn}(g_k(\theta_j)) 2\mu_0 A N_e l^{-2} i_0 (N_1 + N_2) \tag{6.5}$$

For the experimental system, the two identical radial bearings, A and B, have axial locations $z = -268$ mm and $z = 268$ mm respectively. Combining Eq. (6.2) for all 24 actuators, the bearing forces are expressed

$$F^{A,B} = F_0 + \mathbf{D}x^{A,B} + \mathbf{\Sigma}i^{A,B} + \mathbf{\Sigma}_e i_e^{A,B} \tag{6.6}$$

where $\mathbf{\Sigma}$ is a 24×2 matrix with coefficients $\Sigma_{jk} = \sigma_k(\theta_j)$, $i = 1, 2, ..., 24$, $k = 1, 2$, $\mathbf{\Sigma}_e$ is a 24×1 matrix with coefficients $\Sigma_{e,j} = \sigma_e(\theta_j)$, $j = 1, 2, ..., 24$ and $\mathbf{D}$ is a 24×24 diagonal matrix containing the negative stiffness coefficients $D_{j,j} = k_a(\theta_j)$.

To stabilize the bearings and give suitable stiffness and damping properties, feedback of the radial displacement of the rotor $y_s(t)$ measured at four locations is required. The combination of two bearings with an arbitrary linear feedback controller may be represented in state-space form as

$$\begin{aligned} \dot{x}_c &= \mathbf{A}_c x_c + \mathbf{B}_c y_s \\ i^{A,B} &= \mathbf{C}_c^{A,B} x_c \end{aligned} \tag{6.7}$$

where the matrices capture the dynamics of the feedback controller and drives. Combining Eqs (6.6) and (6.7) gives the complete linearized DAMB model as

$$\begin{aligned} \dot{x}_c &= \mathbf{A}_c x_c + \mathbf{B}_c y_s \\ F^{A,B} &= F_0 + \mathbf{D}x^{A,B} + \mathbf{\Sigma}\mathbf{C}_c^{A,B} x_c + \mathbf{\Sigma}_e i_e^{A,B} \end{aligned} \tag{6.8}$$

The DAMB and control system model may now be combined with the cylindrical rotor model, as defined by Eq. (6.8) in Chapter 2:

$$\mathbf{M}\ddot{\boldsymbol{\xi}} + (\mathbf{C} + 2\Omega\mathbf{J})\dot{\boldsymbol{\xi}} + \left(\mathbf{K} - \Omega^2\mathbf{K}_{\mathbf{\Omega}}\right)\boldsymbol{\xi} = \sum_j \mathbf{E}(\phi_j, z_j) P_j(t) \tag{6.9}$$

$$[u(\phi, z, t), v(\phi, z, t), w(\phi, z, t)]^T = \mathbf{E}^T(\phi, z)\boldsymbol{\xi}(t) \tag{6.10}$$

Combining the state variables for rotor vibration in Eq. (6.9) with the dynamic states in Eq. (6.8) and using $y_s(t) = \mathbf{E}_s^T \boldsymbol{\xi}(t)$ gives the complete system model in the form

$$\begin{aligned} \frac{d}{dt}\begin{bmatrix} \boldsymbol{\xi} \\ \dot{\boldsymbol{\xi}} \\ x_c \end{bmatrix} = & \\ \begin{bmatrix} \mathbf{0} & \mathbf{I} & \mathbf{0} \\ -\mathbf{M}^{-1}\left(\mathbf{K}_{cl} - \Omega^2\mathbf{K}_{\mathbf{\Omega}}\right) & -\mathbf{M}^{-1}(\mathbf{C} + 2\Omega\mathbf{J}) & \mathbf{M}^{-1}\left(\mathbf{E}_A\mathbf{\Sigma}^A\mathbf{C}_c^A + \mathbf{E}_{A,B}\mathbf{\Sigma}^B\mathbf{C}_c^B\right) \\ \mathbf{B}_c\mathbf{E}_s^T & \mathbf{0} & \mathbf{A}_c \end{bmatrix} \begin{bmatrix} \boldsymbol{\xi} \\ \dot{\boldsymbol{\xi}} \\ x_c \end{bmatrix} & \\ + \begin{bmatrix} \mathbf{0} & \mathbf{0} \\ \mathbf{M}^{-1}\mathbf{E}_A\mathbf{\Sigma}_e^A & \mathbf{M}^{-1}\mathbf{E}_B\mathbf{\Sigma}_e^B \\ \mathbf{0} & \mathbf{0} \end{bmatrix} \begin{bmatrix} f_e^A \\ f_e^B \end{bmatrix} & \end{aligned} \tag{6.11}$$

where $\mathbf{K}_{cl} = \mathbf{K} - \mathbf{E}_A\mathbf{D}^A\mathbf{E}_A^T - \mathbf{E}_B\mathbf{D}^B\mathbf{E}_B^T$ and the excitation forces are $f_e^A = \mathbf{\Sigma}_e^A i_e$, $f_e^B = \mathbf{\Sigma}_e^B i_e$.

6.4 Results

Frequency response testing was undertaken for a range of forcing conditions and rotational speeds. Radial excitation forces were applied to the wall of the levitated rotor using the two excitation coils located at bearings A and B, as shown in Fig. 6.1a. Two different forcing patterns were adopted involving symmetric ($f_e^A = f_e^B$) and anti-symmetric ($f_e^A = -f_e^B$) excitation. The first case predominantly excites modes with even values of n, while the second case excites modes with odd values of n. During testing, the DAMBs were operated with low gain PID feedback using a standard centralized control strategy to achieve decoupled control of parallel and conical rigid-body modes (see [66], Chapter 8). The resulting bearing forces produce very soft support charateristics and yield natural frequencies for rigid-body modes close to 30 Hz.

Tests were first performed without rotation and without attachment of the rotor coupling. Results are shown in Fig. 6.2. The data shown is for displacement measured by the sensor at the free end of the rotor. The model-based predictions show an agreement within 0.5 % for all natural frequencies within the testing range, with the maximum difference in natural frequency being 3.5 Hz for the $m = 3, n = 1$ mode (875 Hz). Non-uniformity of the cylindrical rotor due to machining error is a possible source of error, in addition to uncertainty in the DAMB properties. Note that the force gains for the two excitation coils are slightly different which leads to mixed excitation of symmetric and anti-symmetric modes for the two cases. Some extra resonances occur in the low frequency range (50 - 200 Hz) due to flexibility of the foundation structure on which the bearings are mounted.

For tests with rotation, imbalance excitation arose due to non-uniformity of the cylinder rotor. Disturbances from sensor run-out error and the flexible coupling were also present. These were suppressed by using a harmonic vibration control algorithm to generate disturbance-canceling forces, applied through the bearings [7]. This had negligible effect on the dynamic response characteristics of the system. Frequency response data for a rotational speed of 11.1 Hz ($\Omega = 70$ rad/s) are shown in Fig. 6.3. The numerical results are based on the parametric model for the speed-dependent dynamics, as described in section 2.3. The splitting of natural frequencies for forward and backward modes due to rotation effects is clearly evident for all flexible modes. A high level of agreement between the theoretical model and experimental data is seen. The small amplitude behaviour, which might reveal frequencies for anti-resonance, cannot be easily verified from the experimental data due to measurement errors from noise and electrical interference. This introduces a 'noise floor' for the sensitivity measurements which tends to increase with rotational speed, making accurate response testing more challenging for higher speeds.

By using acoustic signal measurements, the natural frequencies could be identified over a wider range than was possible with displacement signals alone. Tests were performed with short duration harmonic 'chirp' signals for excitation, with frequency sweep covering the range of interest. Example data is shown in Fig. 6.4. The FFT of the acoustic signal gives a clear indication of the natural frequencies within the target interval of 1000 to 2000 Hz. The complete set of experimental data is superimposed on the model-based Campbell diagram in Fig. 6.5. The experimental values for the natural frequencies show a high level of consistency with the model-based results. Even though, for certain modes, there is a visible offset error in the frequencies, the trend for changing rotational speed matches closely.

To perform tests at higher rotational speeds (>12 Hz), the rotor imbalance was reduced by the addition of small correction masses on the inner surface of the rotor. A partial balancing solution with masses of 45 g $\angle 10°$ at the driven end and 90 g $\angle 170°$ at the

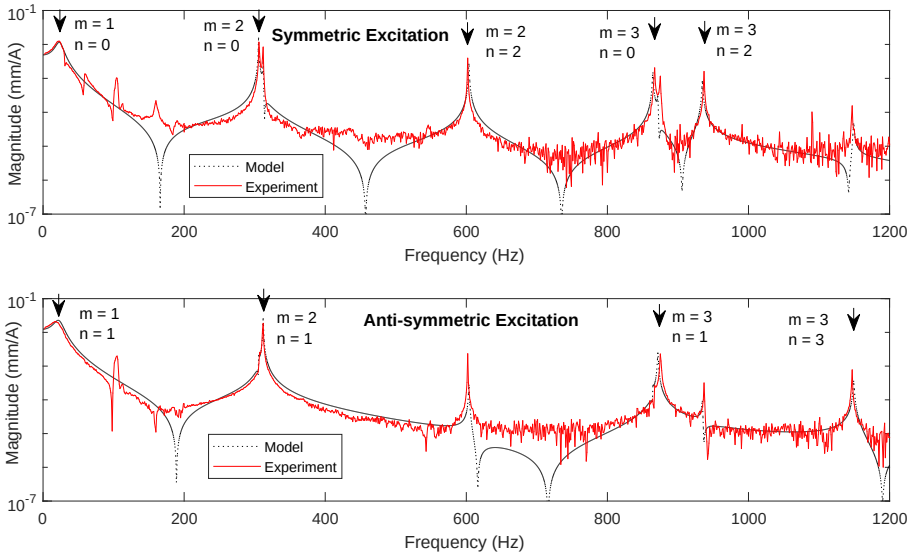

Figure 6.2: Frequency response data from experiment and theoretical modeling for no rotation

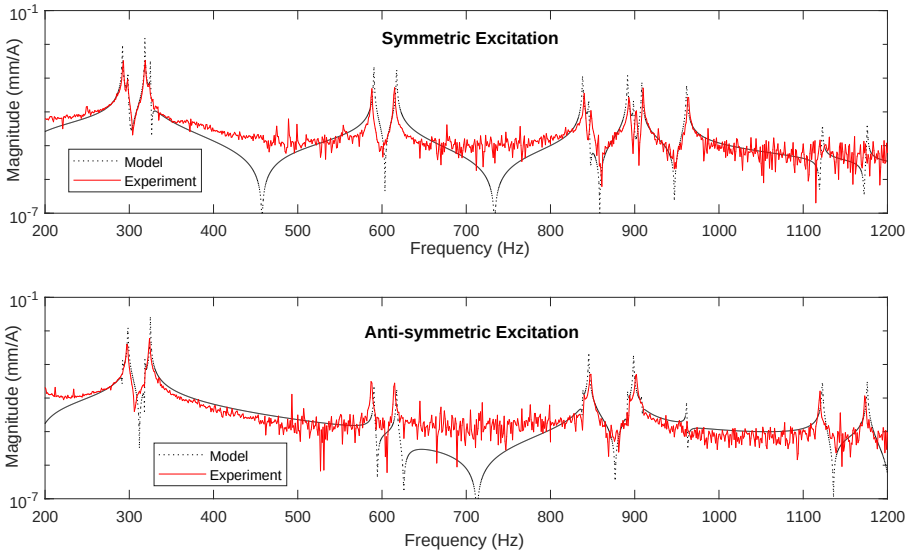

Figure 6.3: Frequency response data from experiment and theoretical modeling for rotation with $\Omega/2\pi = 11.1$ Hz

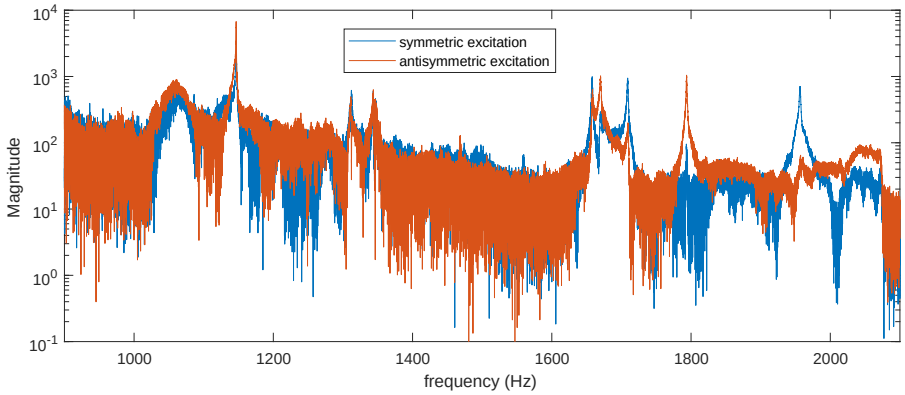

Figure 6.4: Example data for natural frequency identification over range 1000-2000 Hz: FFT of acoustic signal measurements

non-driven end was used. This resulted in a slight splitting of the degenerate mode natural frequencies, even at zero rotational speed, due to the asymmetry introduced by the added masses. For certain modes, the change in natural frequencies is quite evident, but the overall trend for higher speeds is consistent with the model-based results. The consistency between the experimental and theoretical results provides important validation for the described shell theory and for the use of the parametric forced-response model (Eq. (2.36)) in rotordynamic prediction.

6.5 Chapter summary

This chapter has defined and experimentally verified a 3-dimensional multi-mode model for the vibration behaviour of a thin-walled cylindrical rotor based on shell theory. Salient points from the study are that

1. The described model can provide a complete and accurate description of the vibrational dynamics of a thin-walled cylindrical rotor for a practical range of excitation types and rotational speeds.

2. The shown invariance properties of the mode-shapes allows the construction of a discrete model having a simple parametric dependency on rotational speed, with negligible impact on accuracy.

3. The parametric model for speed-dependent natural frequencies (Eq. (2.29)) indicates that, for the low order bending modes, the effect from circumferential extension is very small.

An implication of point 3 is that, even for experiments with higher rotational speeds, the correctness of the centripetal (Ω^2) terms in the equations of motion may not be exposed unless modes with significant in-surface extension are excited and identified.

The described theoretical model may be used to construct benchmark cases for validation of finite element codes for rotating shell structures. It also has good suitability for use in the design of active vibration control strategies. This will be considered in future work.

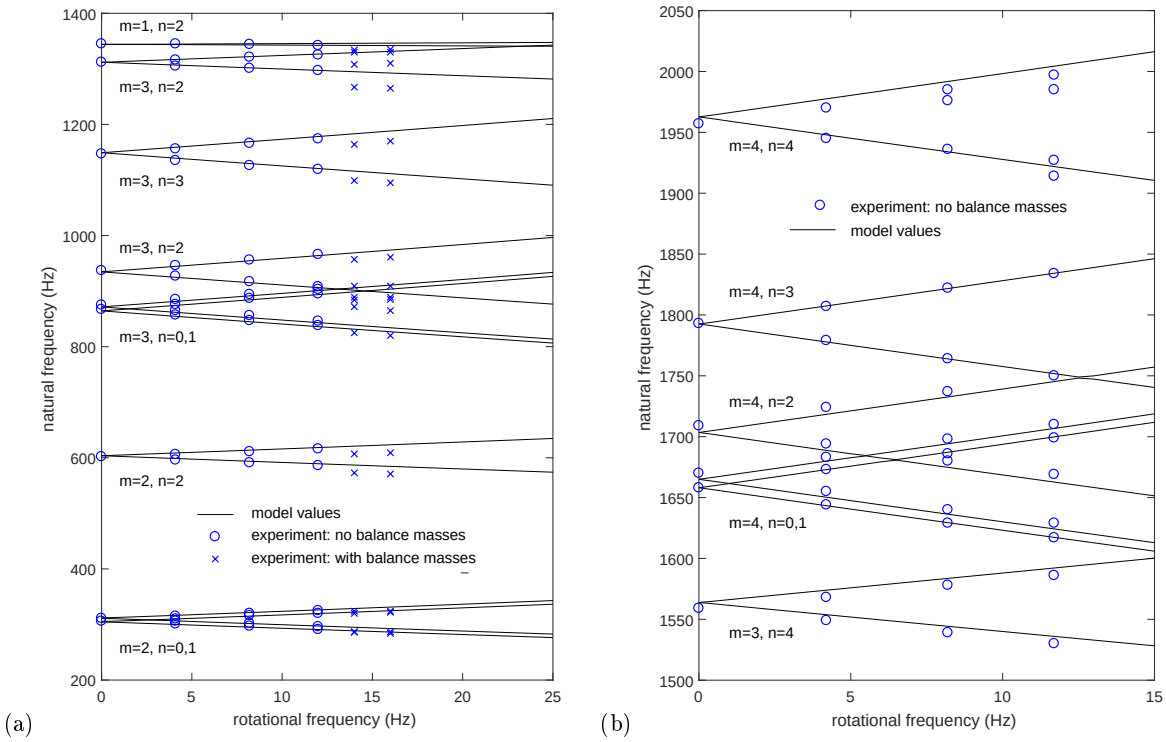

Figure 6.5: Campbell diagram for experimental system based on theoretical modeling. (a) low frequency modes (b) high frequency modes

Project Outputs

Publications

Published journal articles

J1 Cole, M.O.T., Chamroon, C., Keogh, P.S., 'H-infinity controller design for active magnetic bearings considering nonlinear vibrational rotordynamics,' *JSME Mechanical Engineering Journal*, Vol. 4, No. 5, 2017, pp. 16-00716.

J2 Fakkaew, W., Cole, M.O.T. 'Vibration due to non-circularity of a rotating ring having discrete radial supports - with application to thin-walled rotor/magnetic bearing systems,' *Journal of Sound and Vibration*, Vol. 423, No. 9, 2018, pp. 355–372.

J3 Cole, M.O.T., Fakkaew, W. 'An active magnetic bearing for thin-walled rotors: Vibrational dynamics and stabilizing control,' *IEEE/ASME Transactions on Mechatronics*, Vol. 23, No. 6, 2018, pp. 2859–2869.

J4 Chamroon, C., Cole M.O.T., Fakkaew, W. 'Model and control system development for a distributed actuation magnetic bearing and thin-walled rotor subject to noncircularity,' *ASME Journal of Vibration and Acoustics*, Vol. 141, No. 5, 2019, Art No. 051006.

Journal articles under review or under revision

J5 Fakkaew, W., Cole, M.O.T., Chamroon C, 'On the vibrational dynamics of thin-walled rotating cylinders: A theoretical and experimental study utilizing active magnetic bearings,' manuscript submitted to *International Journal of Mechanical Sciences* (under revision).

J6 Brand, Z., Cole, M.O.T., 'Controllability and actuator placement optimization for active damping of a thin rotating ring with piezo patch transducers,' manuscript submitted to *Journal of Sound and Vibration* (under review).

Conference papers

C1 Brand, Z., Cole, M.O.T., 'Results on active damping control of a thin-walled rotating cylinder with piezoelectric patch actuation and sensing,' in Proc. IEEE Conference on Control Technology and Applications, August 19-21, 2019, Hong Kong.

Other outputs

Patent application

P1 'Electromagnetic bearing incorporating an array of electromagnets for the support of plate and hollow shell structures' - in progress.

Bibliography

[1] N. Alujevic, N. Campillo-Davo, P. Kindt, W. Desmet, B. Pluymers, and S. Vercammen. Analytical solution for free vibrations of rotating cylindrical shells having free boundary conditions. *Engineering Structures*, 132:152–171, 2017.

[2] M. Amabili. A comparison of shell theories for large-amplitude vibrations of circular cylindrical shells: Lagrangian approach. *Journal of Sound and Vibration*, 264(5):1091 – 1125, 2003.

[3] Paolo Bisegna and Giovanni Caruso. Frequency split and vibration localization in imperfect rings. *Journal of Sound and Vibration*, 306(3):691 – 711, 2007.

[4] G. H. Bryan. On the beats in the vibrations of a revolving cylinder or bell. *Proceedings of the Cambridge Philosophical Society*, pages 101 – 111, 1890.

[5] S.V. Canchi and R.G. Parker. Effect of ring-planet mesh phasing and contact ratio on the parametric instabilities of a planetary gear ring. *ASME Journal of Mechanical Design*, 130(1):014501, 2008.

[6] GF Carrier. On the vibrations of the rotating ring. *Quarterly of Applied Mathematics*, 3(3):235–245, 1945.

[7] C. Chamroon, M.O T. Cole, and W. Fakkaew. Model and control system development for a distributed actuation magnetic bearing and thin-walled rotor subject to noncircularity. *ASME Journal of Vibration and Acoustics*, 141(5):051006, 2019.

[8] C. Chamroon, M.O.T. Cole, and T. Wongratanaphisan. An active vibration control strategy to prevent nonlinearly coupled rotor-stator whirl responses in multimode rotor-dynamic systems. *IEEE Trans. Contr. Syst. Technol.*, 22(3):1122–1129, 2014.

[9] E. Chatelet, F. D'Ambrosio, and G. Jacquet-Richardet. Toward global modelling approaches for dynamic analyses of rotating assemblies of turbomachines. *Journal of Sound and Vibration*, 282:163–178,, 2005.

[10] Q. Chen, G. Liu, and B. Han. Unbalance vibration suppression for amb system using adaptive notch filter. *Mechanical Systems and Signal Processing*, 93:136–150, 2017.

[11] Q. Chen, G. Liu, and S. Zheng. Suppression of imbalance vibration for ambs controlled driveline system using double-loop structure. *Journal of Sound and Vibration*, 337:1–13, 2015.

[12] M.O.T. Cole, C. Chamroon, and P.S. Keogh. H-infinity controller design for active magnetic bearings considering nonlinear vibrational rotordynamics. *JSME Mechanical Engineering Journal*, 4(5):16–00716., 2017.

[13] M.O.T. Cole and W. Fakkaew. An active magnetic bearing for thin-walled rotors: vibrational dynamics and stabilizing control. *IEEE/ASME Transactions on Mechatronics*, 23(6):2859–2869, 2018.

[14] M.O.T. Cole and P.S. Keogh. Rotor vibration with auxiliary bearing contact in magnetic bearing systems part 2: Robust synchronous control for rotor position recovery. *Proceedings of the Institute of Mechanical Engineers, Part C: Journal of Mechanical Engineeriung Science*, 217:393–409, 2003.

[15] M.O.T. Cole, P.S. Keogh, and C.R. Burrows. Vibration control of a flexible rotor/magnetic bearing system subject to direct forcing and base motion disturbances. *Proc. IMechE, Part C: Journal of Mechanical Engineering Science*, 212(7):535–546, 1998.

[16] M.O.T. Cole, P.S. Keogh, and C.R. Burrows. Control of multifrequency rotor vibration components. *Proc. IMechE, Part C: Journal of Mechanical Engineering Science*, 216(2):165–178, 2002.

[17] M.O.T. Cole, P.S. Keogh, C.R. Burrows, and M.N. Sahinkaya. Adaptive control of rotor vibration using compact wavelets. *ASME J. Vib. Acoust.*, 128:653–665, 2006.

[18] Christopher G. Cooley and Robert G. Parker. Vibration of high-speed rotating rings coupled to space-fixed stiffnesses. *Journal of Sound and Vibration*, 333(12):2631 – 2648, 2014.

[19] P. Cui, G. Zhao S. Li, and C. Peng. Suppression of harmonic current in active-passive magnetically suspended cmg using improved repetitive controller. *IEEE/ASME Trans. Mechatronics*, 21(4):2132–2141, 2016.

[20] S. M. Darbandi, A. Habibollahi, M. Behzad, and H. Salarieh. Sensor runout compensation in active magnetic bearings via an integral adaptive observer. *Control Eng. Practice*, 48:111–118, 2016.

[21] R.A. DiTaranto and M. Lessen. Coriolis acceleration effect on the vibration of a rotating thin-walled circular cylinder. *ASME Journal of Applied Mechanics*, 31(4):700–701, 1964.

[22] M. Endo, K. Hatamura, M. Sakata, and O. Taniguchi. Flexural vibration of a thin rotating ring. *Journal of Sound and Vibration*, 92(2):261 – 272, 1984.

[23] W. Fakkaew and M.O.T. Cole. Vibration due to non-circularity of a rotating ring having discrete radial supports - with application to thin-walled rotor/magnetic bearing systems. *Journal of Sound and Vibration*, 423:355 – 372, 2018.

[24] J. Fang, S. Zheng, and B. Han. Amb vibration control for structural resonance of double-gimbal control moment gyro with high-speed magnetically suspended rotor. *IEEE/ASME Trans. Mechatronics*, 18(18):32–43, 2013.

[25] K. Forsberg. Influence of boundary conditions on the modal characteristics of thin cylindrical shells. *American Institute of Aeronautics and Astronautics*, 2(12):2150 – 2157, 1964.

[26] C.H.J. Fox, R.S. Hwang, and S. McWilliam. The in-plane vibration of thin rings with in-plane profile variations part ii: application to nominally circular rings. *Journal of Sound and Vibration*, 220(3):517 – 539, 1999.

[27] Giancarlo Genta. *Dynamics of rotating systems.* Springer Science & Business Media, New York, 2007.

[28] Sunrong Gong. *A study of in-plane dynamics of tires.* PhD Thesis, Delft University of Technology, 1993.

[29] K. Gupta. Composite shaft rotor dynamics: An overview. *Mechanisms and Machine Science*, 23:79–94, 2015.

[30] R. Herzog, P. Buhler, C. Gahler, and R. Larsonneur. Unbalance compensation using generalized notch filters in the multivariable feedback of magnetic bearings. *IEEE Transactions on Control Systems Technology*, 4(5):580–586, 1996.

[31] L. Hua and K.Y. Lam. Frequency characteristics of a thin rotating cylindrical shell using the generalized differential quadrature method. *International Journal of Mechanical Sciences*, 40(5):443 – 459, 1998.

[32] L. Hua, K.Y. Lam, and T.Y. Ng. *Rotating Shell Dynamics.* Elsevier, 2005.

[33] S.C. Huang and W. Soedel. Response of rotating rings to harmonic and periodic loading and comparison with the inverted problem. *Journal of Sound and Vibration*, 118(2):253 – 270, 1987.

[34] R.S. Hwang, C.H.J. Fox, and S. McWilliam. The in-plane vibration of thin rings with in-plane profile variations part i: General background and theoretical formulation. *Journal of Sound and Vibration*, 220(3):497 – 516, 1999.

[35] R.S. Hwang, C.H.J. Fox, and S. McWillliam. Free vibrations of elliptical rings with circumferentially variable thickness. *Journal of Sound and Vibration*, 228(3):683 – 699, 1999.

[36] K. Jiang and C. Zhu. Multi-frequency periodic vibration suppressing in active magnetic bearing-rotor systems via response matching in frequency domain. *Mech. Syst. and Signal Process.*, 25:1417–1429, 2011.

[37] Jung-Hwan Kim and Ji-Hwan Kim. Thermoelastic dissipation of rotating imperfect micro-ring model. *International Journal of Mechanical Sciences*, 119:303 – 309, 2016.

[38] Y.-J Kim and J.S Bolton. Effects of rotation on the dynamics of a circular cylindrical shell with application to tire vibration. *Journal of Sound and Vibration*, 275(3):605 – 621, 2004.

[39] P. Kindt, P. Sas, and W. Desmet. Measurement and analysis of rolling tire vibrations. *Optics and Lasers in Engineering*, 47(3):443 – 453, 2009. Optical Measurements.

[40] F. Klocke, A. Klink, D. Veselovac, D.K. Aspinwall, S. Leung Soo, M. Schmidt, J. Schilp, G. Levy, and J. Kruth. Turbomachinery component manufacture by application of electrochemical, electro-physical and photonic processes. *CIRP Annals - Manufacturing Technology*, 63:703–726, 2014.

[41] C. Knospe, R. Hope, S. Fedigan, and R. Williams. Experiments in the control of unbalanced response using magnetic bearings. *Mechatronics*, 5:385–400, 1995.

[42] K.Y. Lam and C.T. Loy. Analysis of rotating laminated cylindrical shells by different thin shell theories. *Journal of Sound and Vibration*, 186(1):23 – 35, 1995.

[43] K.Y. Lam and C.T. Loy. Influence of boundary conditions for a thin laminated rotating cylindrical shell. *Composite Structures*, 41(3):215 – 228, 1998.

[44] Y. Le, J. Fang, and J. Sun. Design of a halbach array permanent magnet damping system for high speed compressor with large thrust load. *IEEE Transactions on Magnetics*, 51(1):1–9, 2015.

[45] A. E. H. Love. On the small free vibrations and deformations of elastic shells,. *Philosophical Trans. of the Royal Society (London), Series A*, 17:491–549, 1888.

[46] Augustus Edward Hough Love. *A treatise on the mathematical theory of elasticity, 4th Edition.* Dover Publication, New York, 1944.

[47] C.T. Loy and K.Y. Lam. Vibrations of rotating thin cylindrical panels. *Applied Acoustics*, 46(4):327 – 343, 1995.

[48] K.-Y. Lum, V.T. Coppola, and D.S. Bernstein. Adaptive autocentering control for an active magnetic bearing supporting a rotor with unknown mass imbalance. *IEEE Trans. Contr. Syst. Technol.*, 4(5):587–597, 1996.

[49] Z. Luo, Y. Zhu, N. Sun, Q. Han, and B. Wen. Approximate method in analyzing forced vibration response of rotating short thin-wall cylindrical shells in different boundary conditions. *Journal of Vibrational Engineering and Technologies*, 2:567–579, 2014.

[50] C. Lusty, N. Sahinkaya, and P. Keogh. A novel twin-shaft rotor layout with active magnetic couplings for vibration control. *Proc. IMechE, Part I: Journal of Systems and Control Engineering*, 230(3):266–276, 2016.

[51] D.W. Manchala, A.B. Palazzolo, A.K. Lin, A.K. Kasak, J. Montague, and G.V. Brown. Constrained quadratic programming active control of rotating mass imbalance. *J. Sound Vib.*, 205:561–580, 1997.

[52] A.M. Mohamed and I. Busch-Vishniac. Imbalance compensation and automation balancing in magnetic bearing systems using the q-parametrization theory. *IEEE Trans. Contr. Syst. Technol.*, 3(2):202–211, 1995.

[53] S. E. Mushi, Z. Lin, and P. E. Allaire. Design, construction, and modeling of a flexible rotor active magnetic bearing test rig. *IEEE/ASME Trans. Mechatronics*, 17(6):1170–1182, 2012.

[54] K. Nonami and Z. Liu. Adaptive unbalance vibration control of magnetic bearing system using frequency estimation for multiple periodic disturbances with noise. In *IEEE Conference on Control Applications - Proceedings, vol. 1*, pages 576–581, 1999.

[55] Y. Okada, K. Shimizu, and S. Ueno. Vibration control of flexible rotor by inclination control magnetic bearings with axial self-bearing motor. *IEEE/ASME Trans. Mechatronics*, 6(4):521–524, 2001.

[56] J. Padovan. Natural frequencies of rotating prestressed cylinders. *Journal of Sound and Vibration*, 31(4):469 – 482, 1973.

[57] A. B. Palazzolo, R. R. Lin, R. M. Alexander, A. F. Kascak, and J. J. Montague. Test and theory for piezoelectric actuator-active vibration control of rotating machinery. *ASME. J. Vib. Acoust.*, 113(2):167–175, 1991.

[58] D. Peters, C. Kaletsch, R. Nordmann, and B. Domes. Test rig for a supercritical rotor of an aero engine. *12th IFToMM World Congress, Proceedings (2007)*, 2007.

[59] G. Pinte, S. Devos, B. Stallaert, W. Symens, J. Swevers, and P. Sas. A piezo-based bearing for the active structural acoustic control of rotating machinery. *Journal of Sound and Vibration*, 329(9):1235–1253, 2010.

[60] Ch. Kannababu R. Siva Srinivas, R. Tiwari. Application of active magnetic bearings in flexible rotordynamic systems â a state-of-the-art review,. *Mech. Syst. and Signal Process.*, 106:537–572, 2018.

[61] J.M. Roche, D.T. Palac, J.E. Hunter, D.E. Myers, C.A. Snyder, D.N. Kosareo, D.R. McCurdy, and K.T. Dougherty. Investigation of exoskeletal engine propulsion system concept. Technical Report report NASA/TM-2005-213369, National Aeronautics and Space Adminstration, 2005.

[62] M. Sahinkaya, A.G. Abulrub, and C.R. Burrows. An adaptive multi-objective controller for flexible rotor and magnetic bearing systems. *ASME J. Dyn. Sys. Meas. Control*, 133(3):031003–031003–9, 2011.

[63] T. Saito and M. Endo. Vibration of finite length, rotating cylindrical shells. *Journal of Sound and Vibration*, 107(1):17 – 28, 1986.

[64] J. L. Sanders. An improved first-approximation theory for thin shells. *Langley Research Center, NASA Technical Report, NASA TR R-24*, 1959.

[65] T. Schneeberger, T. Nussbaumer, and J.W. Kolar. Magnetically levitated homopolar hollow-shaft motor. *IEEE/ASME Trans. Mechatronics*, 15(1):97–107, 2010.

[66] G. Schweitzer and E. H. Maslen. *Magnetic Bearings: Theory, Design, and Application to Rotating Machinery*. Springer-Verlag, Berlin, 2009.

[67] J.D. Setiawan, R. Mukherjee, and E.H. Maslen. Adaptive compensation of sensor runout for magnetic bearings with uncertain parameters: theory and experiments. *ASME J. Dyn. Sys. Meas. Control*, 123(2):211–218, 1999.

[68] J. L. Sewall and E.C. Naumann. An experimental and analytical vibration study of thin cylindrical shells with and without longitudinal stiffeners. *Langley Research Center, NASA Technical Note, NASA TN D-4705*, 1968.

[69] W. Soedel. *Vibrations of Shells and Plates*. Marcel Dekker Inc., 1981.

[70] A. V. Srinivasan and G.F. Lauterbach. Traveling waves in rotating cylindrical shells. *ASME Journal of Engineering for Industry*, 93(4):1229–1232, 1971.

[71] S. Sun, D. Cao, and S. Chu. Free vibration analysis of thin rotating cylindrical shells using wave propagation approach. *Archive of Applied Mechanics*, 83(4):521 – 531, 2013.

[72] S. Sun, D. Cao, and Q. Han. Vibration studies of rotating cylindrical shells with arbitrary edges using characteristic orthogonal polynomials in the rayleigh–ritz method. *International Journal of Mechanical Sciences*, 68:180 – 189, 2013.

[73] S. Sun, S. Chu, and D. Cao. Vibration characteristics of thin rotating cylindrical shells with various boundary conditions. *Journal of Sound and Vibration*, 331:4170–4186, 2012.

[74] M. Wang, M.O.T. Cole, and P.S. Keogh. New lmi based gain-scheduled control for recovering contact-free operation of a magnetically levitated rotor. *Mech. Syst. and Signal Process*, 96:104–124, 2017.

[75] J.D. Watkins and R.C. Clary. Vibrational characteristics of some thin-walled cylindrical and conical frustum shells. *Langley Research Center, NASA Technical Note, NASA TN D-2729*, 1965.

[76] Y.T. Wei, L. Nasdala, and H. Rothert. Analysis of forced transient response for rotating tires using ref models. *Journal of Sound and Vibration*, 320(1):145 – 162, 2009.

[77] Xionghua Wu and Robert G. Parker. Vibration of rings on a general elastic foundation. *Journal of Sound and Vibration*, 295(1 - 2):194 – 213, 2006.

[78] Yufeng Xing, Bo Liu, and Tengfei Xu. Exact solutions for free vibration of circular cylindrical shells with classical boundary conditions. *International Journal of Mechanical Sciences*, 75:178–188, 2013.

[79] X. Xu and S. Chen. Field balancing and harmonic vibration suppression in rigid amb-rotor systems with rotor imbalances and sensor runout. *Sensors*, 15:21876–21897, 2015.

[80] F. Y. Zeidan, L. San Andres, and J. M. Vance. Design and application of squeeze film dampers in rotating machinery. In *in Proceedings of the 25th Turbomachinery Symposium, Houston, TX, pp., 1996.*, pages 169–188, 1996.

[81] S. Zheng, B. Han, Y. Wang, and J. Zhou. Optimization of damping compensation for a flexible rotor system with active magnetic bearing considering gyroscopic effect. *IEEE/ASME Trans. Mechatronics*, 20(3):1130–1137, 2015.

[82] L. Zhou and L. Li. Modeling and identification of a solid-core active magnetic bearing including eddy currents. *IEEE/ASME Trans. Mechatronics*, 21(6):2784–2792, 2016.

.

Appendix: Paper publications

Journal of Sound and Vibration 423 (2018) 355–372

Contents lists available at ScienceDirect

Journal of Sound and Vibration

journal homepage: www.elsevier.com/locate/jsvi

Vibration due to non-circularity of a rotating ring having discrete radial supports - With application to thin-walled rotor/magnetic bearing systems

Wichaphon Fakkaew [a], Matthew O.T. Cole [b,*]

[a] School of Engineering, University of Phayao, Phayao, 56000, Thailand
[b] Department of Mechanical Engineering, Faculty of Engineering, Chiang Mai University, Chiang Mai, 50200, Thailand

ARTICLE INFO

Article history:
Received 4 September 2017
Revised 23 January 2018
Accepted 25 February 2018
Available online XXX

Keywords:
Rotating systems
Thin-walled structures
Hollow rotor
Magnetic bearing
Critical speeds

ABSTRACT

This paper investigates the vibration arising in a thin-walled cylindrical rotor subject to small non-circularity and coupled to discrete space-fixed radial bearing supports. A Fourier series description of rotor non-circularity is incorporated within a mathematical model for vibration of a rotating annulus. This model predicts the multi-harmonic excitation of the rotor wall due to bearing interactions. For each non-circularity harmonic there is a set of distinct critical speeds at which resonance can potentially arise due to flexural mode excitation within the rotor wall. It is shown that whether each potential resonance occurs depends on the multiplicity and symmetry of the bearing supports. Also, a sufficient number of evenly spaced identical supports will eliminate low order resonances. The considered problem is pertinent to the design and operation of thin-walled rotors with active magnetic bearing (AMB) supports, for which small clearances exist between the rotor and bearing and so vibration excitation must be limited to avoid contacts. With this motivation, the mathematical model is further developed for the case of a distributed array of electromagnetic actuators controlled by feedback of measured rotor wall displacements. A case study involving an experimental system with short cylindrical rotor and a single radial AMB support is presented. The results show that flexural mode resonance is largely avoided for the considered design topology. Moreover, numerical predictions based on measured non-circularity show good agreement with measurements of rotor wall vibration, thereby confirming the validity and utility of the theoretical model.

1. Introduction

The vibration behaviour of circular shell structures has been studied extensively over the last few decades as it is important for many conventional and emerging mechanical systems. In particular, current architectures in rotating machine design are evolving towards lightweight hollow rotor structures, including aero engines [1,2]. The vibration within the walls of a simple thin-walled rotor shares similarities with the in-plane vibrations of rings, for which Coriolis and centripetal accelerations give rise to rotational-speed-dependent splitting of natural frequencies for forward and backward circumferential waves [3,4]. The motivation for the present study was to better understand the underlying mechanism for vibrational excitation of a thin-walled rotor supported by active magnetic bearings. Vibration is seen to arise due to imperfect symmetry of the rotor cross-section and its accurate prediction may play an important role in machine design, manufacture and operation. A suitable dynamic model

* Corresponding author.
E-mail address: motcole@hotmail.com (M.O.T. Cole).

https://doi.org/10.1016/j.jsv.2018.02.055
0022-460X/

must incorporate mathematical descriptions of rotor non-circularity and space-fixed bearing elements in order to establish the forced vibration behaviour under rotation.

Limitations in manufacturing processes will cause profile variations in hollow cylindrical structures of nominally annular cross-section. Although a number of studies on the free vibration of imperfect rings can be found in the literature, these deal almost exclusively with non-rotating rings. Imperfections may be introduced as small initial displacements [5], or variation of the ring cross section [6,7], or perturbations of the uniform mass density and bending stiffness [8]. An elliptical ring has also been considered as a special case of an imperfect circular ring [9]. In most of these studies, the Rayleigh-Ritz approach has been used to determine the perturbations in natural frequencies and mode shapes for free vibration. The effect of uneven mass distribution for a spinning resonator ring in a MEMs device was studied in Ref. [10].

Machine rotor/shaft structures are usually supported by space-fixed bearing components with certain stiffness and damping characteristics. For a thin-walled rotor, bearing interactions occurring at discrete angular positions may result in significant changes in modal properties for wall vibration. The related problem of free vibration of a non-rotating thin ring on a general elastic foundations was solved in Ref. [11] via both perturbation and Galerkin methods. Similar behaviour is seen in models of vibration in meshing compliant gears which couple through space-fixed discrete stiffnesses [12,13].

The vibration of a rotating ring under forced conditions, both with and without constraints, was studied by Carrier [14] for a few special cases. Closed form solutions to the harmonic and periodic forced vibration of rotating rings have been reported by Huang and Soedel [15]. Response solutions for rotating tires based on rings with elastic foundations under various loading situations have also been published [16,17], while an experimental study on tire vibration can be found in Ref. [18].

Previous studies on forced vibration have been limited to the case of perfect rings subject to exogenous forcing. To the authors' knowledge, the mechanism for self-excitation due to imperfect geometry of a hollow cylindrical rotor with discrete supports has not previously been dealt with. In section 2 of this paper, a model is developed for vibration of a short thin-walled rotor where non-circularity is represented by an initial deflection of the rotor wall. Using a Fourier series description of non-circularity, a general model for the interaction of the rotor with space-fixed discrete supports is derived. Two types of bearing supports are considered:

1. An array of radial spring-damper bearing elements
2. An active bearing involving an array of compact electromagnetic actuators

In section 3, a numerical study is undertaken to investigate the influence of multiplicity and symmetry of discrete spring-damper supports on the resonance behaviour of the rotor. In section 4, an experimental investigation is described involving a prototype active magnetic bearing (AMB) with distributed actuation applied to a thin-walled rotor. Measurements of vibration excitation during operation are presented and compared with results from theoretical modelling. The final section draws conclusions.

2. Mathematical modelling

2.1. Equation of motion

The geometry of a thin-walled rotor with small non-circularity is shown in Fig. 1. The rotor has circumference length L_c and rectangular cross-section of depth d and length l. Uniform density ρ and modulus of elasticity E are assumed. The rotor is supported by space-fixed discrete bearing elements, shown here as radial spring-damper units. The XY axes are a fixed reference frame, while the reference frame $X'Y'$ rotates with the rotor at constant angular speed Ω about the fixed axis through O.

To derive the equations of motion we consider that non-circularity is introduced as an initial plastic deformation of a perfect circular ring so that its neutral plane is perturbed from a reference circle centred on the coordinate axes, as shown in Fig. 1a. Then, additional displacements arise under motion due to elastic deformation. The local reference frame for the displacement at a given point P is shown by axes x_0y_0 and the deformation frame is denoted by axes xy. The displacements of the cylinder wall in radial (x_0) direction and tangential (y_0) direction with respect to the reference circle are defined as

$$U(\theta,t) = u_{r0}(\theta) + u_r(\theta,t), \quad V(\theta,t) = v_{r0}(\theta) + v_r(\theta,t)$$

where $u_{r0}(\theta)$ and $v_{r0}(\theta)$ are the initial equilibrium displacements due to non-circularity and $u_r(\theta,t)$ and $v_r(\theta,t)$ are the displacements due to vibration. Under these assumptions we may apply an inextensibility condition to both the plastic and elastic components of the deformation:

$$u_r = v_r', \quad u_{r0} = v_{r0}' \tag{1}$$

Assuming that the cross-section planes remain plane after deformation, the angle between deformed and undeformed cross-section is $\varphi = \frac{1}{R}(U' + V)$, where the prime designates the partial derivative with respect to angle θ. The position vector for point P can be written as $\mathbf{r}_P = -(R-U)\mathbf{i}_0 + V\mathbf{j}_0$ and the acceleration as $\ddot{\mathbf{r}}_P = \ddot{r}_{0x}\mathbf{i}_0 + \ddot{r}_{0y}\mathbf{j}_0$ where $\ddot{r}_{0x} = \ddot{U} + 2\Omega\dot{V} + \Omega^2(R-U)$ and $\ddot{r}_{0y} = \ddot{V} - 2\Omega\dot{U} - \Omega^2 V$. Neglecting nonlinear terms, the acceleration with respect to the xy-frame is $\ddot{\mathbf{r}}_P = \ddot{r}_x\mathbf{i} + \ddot{r}_y\mathbf{j}$ where $\ddot{r}_x = \ddot{U} + 2\Omega\dot{V} + \Omega^2(R-U)$ and $\ddot{r}_y = \ddot{V} - 2\Omega\dot{U} + \Omega^2 U'$. Moreover, the inertia forces are $f_x = \rho dlR\ddot{r}_x d\theta$ and $f_y = \rho dlR\ddot{r}_y d\theta$. Hence, the equations of motion for a differential element with length $ds = Rd\theta$ may be obtained by resolving in the instantaneous

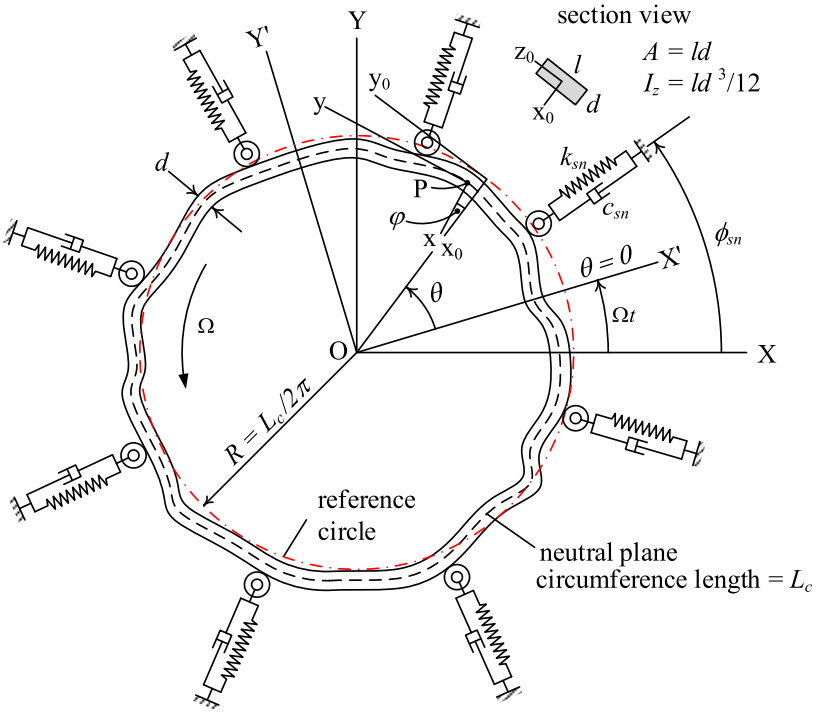

(a)

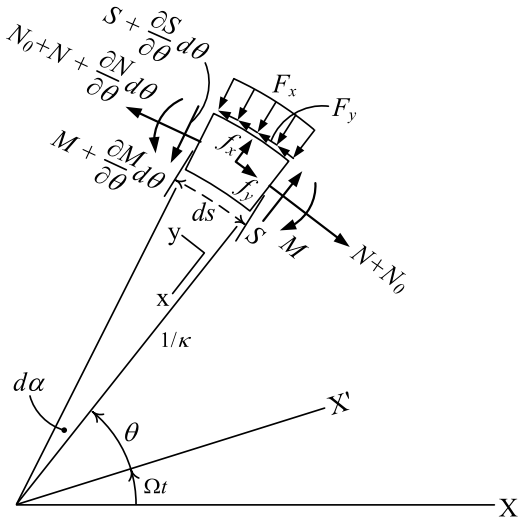

$$ds = Rd\theta$$
$$d\alpha = ds/(1/\kappa) = \kappa R d\theta$$

(b)

Fig. 1. (a) Schematic of a non-circular thin-walled cylindrical rotor with space-fixed discrete spring-damper modules (b) Rotor segment Free-Body-Diagram.

xy-frame (Fig. 1b) as

$$\frac{\partial S}{\partial \theta} + R(N_0 + N)\kappa + RF_x = \rho dlR\left(\ddot{U} + 2\Omega\dot{V} + \Omega^2(R - U)\right) \tag{2}$$

$$\frac{\partial N}{\partial \theta} - RS\kappa + RF_y = \rho dlR\left(\ddot{V} - 2\Omega\dot{U} + \Omega^2\frac{\partial U}{\partial \theta}\right) \tag{3}$$

$$\frac{\partial M}{\partial \theta} + RS = 0 \tag{4}$$

where F_x and F_y are externally applied force distributions (per unit length). The curvature of the element is given by

$$\kappa = \frac{1}{R} + \frac{1}{R^2}\left(\frac{\partial^2 U}{\partial \theta^2} + \frac{\partial V}{\partial \theta}\right) \tag{5}$$

Here, N_0 is a mean normal force which may be equated with the constant centripetal term on the right side of Eq. (2):

$$N_0 = \rho dlR^2\Omega^2 \tag{6}$$

The strain anywhere on the cross-section of the cylinder wall can be calculated from a linear strain-curvature relationship $\epsilon = \frac{1}{R}(v_r' - u_r) - x(\kappa - \kappa_0)$ where $\kappa_0 = \frac{1}{R} + \frac{1}{R^2}(u_{r0}'' + v_{r0}')$. To incorporate material damping we adopt a Kelvin-Voigt model where the stress-strain relation is $\sigma = E(1 + \tau\frac{d}{dt})\epsilon$ with τ being the characteristic relaxation time. The bending moment is then given by

$$M = \int x\sigma dA = \frac{Ed^3 l}{12}(\kappa - \kappa_0) + \tau\frac{Ed^3 l}{12}\frac{d}{dt}(\kappa - \kappa_0) \tag{7}$$

For low friction bearings, the external tangential forces will be negligible ($F_y = 0$).

Equations (2)–(4) may be combined to eliminate the normal force N and radial shear force S. Then, applying the inextensibility conditions Eq. (1) and (7) and neglecting nonlinear terms yields

$$\left(\frac{\partial^2 \ddot{v}_r}{\partial \theta^2} - \ddot{v}_r\right) + 4\Omega\frac{\partial \dot{v}_r}{\partial \theta} - \Omega^2\left(\frac{\partial^4 v_r}{\partial \theta^4} + 3\frac{\partial^2 v_r}{\partial \theta^2}\right) + \omega_0^2\left(1 + \tau\frac{d}{dt}\right)\left(\frac{\partial^6 v_r}{\partial \theta^6} + 2\frac{\partial^4 v_r}{\partial \theta^4} + \frac{\partial^2 v_r}{\partial \theta^2}\right)$$
$$-\frac{1}{\rho dl}\frac{\partial F_x}{\partial \theta} = \Omega^2\left(\frac{\partial^3 u_{r0}}{\partial \theta^4} + 3\frac{\partial u_{r0}}{\partial \theta}\right) \tag{8}$$

where $\omega_0^2 = \frac{Ed^2}{12\rho R^4}$.

The reduced (1–D) governing equation (Eq. (8)) is consistent with some previous studies [4,19]. However, the effect of damping and non-circularity in combination with space-fixed bearing supports, which are critical aspects for rotordynamic prediction, have not previously been considered. Endo et al. [4] showed experimentally that the (low order) natural frequencies for free vibration of a thin rotating ring corresponded well with the unforced version of this equation even though the inextensibility assumption is applied. For further comparison, two alternative but more complex models are given in the appendix that take account of circumferential extension and give further insight on the validity of Eq. (8). Note that the non-circularity terms on the right side are constant (time-independent) forcing terms that, for the free rotor, produce a deformation that tends to cancel the initial non-circularity as the rotational speed increases, i.e. an initially non-circular rotor becomes circular as the rotational speed tends to infinity. This behaviour, which is intuitively reasonable, is seen only when inextensibility is assumed for both the elastic and initial plastic deformation, as in Eq. (1). With the addition of discrete bearing supports, the impact of non-circularity on vibration is more complex.

2.2. Fixed-frame dynamics

To describe the rotor interaction with space-fixed bearing supports, it is convenient to express motion in terms of fixed-frame coordinates. For a given point on the rotor, the fixed-frame angular position is $\phi = \theta + \Omega t$. We define $u(\phi, t)$, $v(\phi, t)$, $u_0(\phi, t)$ and $F_x^*(\phi, t)$ as the radial and tangential displacement, non-circularity and distributed radial force as functions of ϕ, respectively. For each of these parameters, $y_r(\theta, t) = y(\phi(\theta, t), t)$ and so the following relations hold

$$\frac{\partial y_r}{\partial \theta} = \frac{\partial y}{\partial \phi}, \quad \dot{y}_r = \dot{y} + \Omega\frac{\partial y}{\partial \phi} \tag{9}$$

Using these transformations in Eq. (8) gives the equation of motion in stationary frame coordinates as

$$\left(\frac{\partial^2 \ddot{v}}{\partial \phi^2} - \ddot{v}\right) + 2\Omega\left(\frac{\partial^3 \dot{v}}{\partial \phi^3} + \frac{\partial \dot{v}}{\partial \phi}\right) + \omega_0^2\left(1 + \tau\Omega\frac{\partial}{\partial \phi} + \tau\frac{d}{dt}\right)\left(\frac{\partial^6 v}{\partial \phi^6} + 2\frac{\partial^4 v}{\partial \phi^4} + \frac{\partial^2 v}{\partial^2 \phi}\right) - \frac{1}{\rho dl}\frac{\partial F_x^*}{\partial \phi} = \Omega^2\left(\frac{\partial^3 u_0}{\partial \phi^3} + 3\frac{\partial u_0}{\partial \phi}\right) \tag{10}$$

2.3. Discrete model

The non-circularity can be approximated by a truncated Fourier series in the form

$$u_{r0}(\theta) = \sum_{j=1}^{M} \left[a_j \cos j\theta + b_j \sin j\theta\right] \tag{11}$$

where $a_j = \frac{1}{\pi}\int_0^{2\pi} u_{r0} \cos j\theta \, d\theta$ and $b_j = \frac{1}{\pi}\int_0^{2\pi} u_{r0} \sin j\theta \, d\theta$. The displacement component due to non-circularity $u_0(\phi, t) = u_{r0}(\phi - \Omega t)$ is then given by

$$u_0(\phi, t) = \sum_{j=1}^{M} \left(a_j \cos j\Omega t - b_j \sin j\Omega t\right) \cos j\phi + \sum_{j=1}^{M} \left(a_j \sin j\Omega t + b_j \cos j\Omega t\right) \sin j\phi \tag{12}$$

Since the $j = 1$ coefficients relate to the ring offset, the reference circle centre may be chosen such that a_1 and b_1 are zero, i.e. collocated with the mass-centre of the cylinder.

Discrete radial bearing forces $F_{sn}(t)$, applied at angular positions ϕ_{sn} and indexed by n, may be modelled by

$$F_x^*(\phi, t) = \frac{1}{R}\sum_{n=1}^{N_s} F_{sn}(t)\delta(\phi - \phi_{sn}) \tag{13}$$

where $\delta(.)$ denotes the Dirac delta function.

Suppose a solution to Eq. (10) can be approximated by

$$u(\phi, t) = \frac{\partial v(\phi, t)}{\partial \phi} \approx \sum_{m=1}^{M} \left[p_m(t)\sin m\phi + q_m(t)\cos m\phi\right] \tag{14}$$

where $\sin m\phi$ and $\cos m\phi$ are the mode shapes for undamped free vibration and $p_m(t)$ and $q_m(t)$ are the mth modal radial displacements, with m being the nodal index. Substituting Eqs (12)–(14) into Eq. (10) and exploiting the orthogonality properties of $\cos m\phi$ and $\sin m\phi$ yields a set of $2M$ equations:

$$\ddot{p}_m - \Omega g_m \dot{q}_m + \tau k_m \dot{p}_m + k_m p_m - \Omega\tau m k_m q_m - l_m \sum_{n=1}^{N_z} F_{sn} \sin m\phi_{sn} = -\Omega^2 h_m \left[a_m \sin m\Omega t + b_m \cos m\Omega t\right] \tag{15}$$

$$\ddot{q}_m + \Omega g_m \dot{p}_m + \tau k_m \dot{q}_m + k_m q_m + \Omega\tau m k_m p_m - l_m \sum_{n=1}^{N_z} F_{sn} \cos m\phi_{sn} = -\Omega^2 h_m \left[-b_m \sin m\Omega t + a_m \cos m\Omega t\right] \tag{16}$$

where $k_m = \omega_0^2 \frac{m^2(m^2-1)^2}{m^2+1}$, $h_m = \frac{m^2(m^2-3)}{m^2+1}$, $g_m = \frac{2m(m^2-1)}{m^2+1}$, $l_m = \frac{m^2}{\rho\pi dlR(m^2+1)}$.

By defining vectors $\mathbf{x} = \left[p_1 \; q_1 \; p_2 \; q_2 \cdots p_M \; q_M\right]^{\mathrm{T}}$ and $\mathbf{F}_s = \left[F_{s1} \; F_{s2} \; \cdots \; F_{sN_s}\right]^{\mathrm{T}}$, equations (15) and (16) can be rewritten in matrix form as

$$\ddot{\mathbf{x}} + (\tau\mathbf{C}_0 - \Omega\mathbf{C}_1)\dot{\mathbf{x}} + (\mathbf{K}_0 - \tau\Omega\mathbf{K}_1)\mathbf{x} - \mathbf{L}\mathbf{E}_s^T\mathbf{F}_s = -\Omega^2\mathbf{H}_0 \sum_{m=1}^{M} \left[\mathbf{W}_{2m-1} \sin m\Omega t + \mathbf{W}_{2m} \cos m\Omega t\right] \tag{17}$$

where the block-diagonal matrices involve submatrices

$$\mathbf{I}_2 = \begin{bmatrix} 1 & 0 \\ 0 & 1 \end{bmatrix}, \quad \mathbf{J}_2 = \begin{bmatrix} 0 & 1 \\ -1 & 0 \end{bmatrix}$$

and are given by

$$\mathbf{C}_0 = \mathrm{diag}\left(k_1\mathbf{I}_2, \; k_2\mathbf{I}_2, \; \ldots \; k_M\mathbf{I}_2\right),$$

$$\mathbf{C}_1 = \mathrm{diag}\left(g_1\mathbf{J}_2, \; g_2\mathbf{J}_2, \; \ldots \; g_M\mathbf{J}_2\right),$$

$$\mathbf{K}_0 = \mathrm{diag}\left(k_1\mathbf{I}_2, \; k_2\mathbf{I}_2, \; \ldots \; k_M\mathbf{I}_2\right),$$

$$\mathbf{K}_1 = \mathrm{diag}\left(k_1\mathbf{J}_2, \; 2k_2\mathbf{J}_2, \; \ldots \; Mk_M\mathbf{J}_2\right),$$

$$\mathbf{H}_0 = \mathrm{diag}\left(h_1\mathbf{I}_2, \; h_2\mathbf{I}_2, \; \ldots \; h_M\mathbf{I}_2\right),$$

$$\mathbf{L} = \mathrm{diag}\left(l_1\mathbf{I}_2,\ l_2\mathbf{I}_2,\ \ldots\ l_M\mathbf{I}_2\right),$$

$$\mathbf{W} = \mathrm{diag}\left((a_1\mathbf{I}_2 + b_1\mathbf{J}_2),\ (a_2\mathbf{I}_2 + b_2\mathbf{J}_2),\ \ldots\ (a_M\mathbf{I}_2 + b_M\mathbf{J}_2)\right)$$

Also, $\mathbf{W}_j$ denotes the jth column of $\mathbf{W}$. The matrix $\mathbf{E}_s$ is a force distribution matrix that introduces a modal coupling according to the support positions:

$$\mathbf{E}_s = \begin{bmatrix} \sin\phi_{s1} & \cos\phi_{s1} & \sin 2\phi_{s1} & \cos 2\phi_{s1} & \cdots & \sin M\phi_{s1} & \cos M\phi_{s1} \\ \sin\phi_{s2} & \cos\phi_{s2} & \sin 2\phi_{s2} & \cos 2\phi_{s2} & \cdots & \sin M\phi_{s2} & \cos M\phi_{s2} \\ \vdots & \vdots & \vdots & \vdots & & \vdots & \vdots \\ \sin\phi_{sN_s} & \cos\phi_{sN_s} & \sin 2\phi_{sN_s} & \cos 2\phi_{sN_s} & \cdots & \sin M\phi_{sN_s} & \cos M\phi_{sN_s} \end{bmatrix}$$

A set of radial displacements $\mathbf{y} = \left[y(\phi_1, t)\ y(\phi_2, t)\cdots y(\phi_K, t)\right]^{\mathrm{T}}$ may be defined for a general set of fixed angular positions $\phi_1, \ldots, \phi_K$. These will equal the summation of the displacements due to elastic deflection and the initial non-circularity, as given respectively by Eqs (12) and (14):

$$\mathbf{y} = \mathbf{u} + \mathbf{u}_0 = \mathbf{E}\left(\mathbf{x} + \sum_{m=1}^{M}\left(\mathbf{W}_{2m-1}\sin m\Omega t + \mathbf{W}_{2m}\cos m\Omega t\right)\right) \tag{18}$$

where

$$\mathbf{E} = \begin{bmatrix} \sin\phi_1 & \cos\phi_1 & \sin 2\phi_1 & \cos 2\phi_1 & \cdots & \sin M\phi_1 & \cos M\phi_1 \\ \sin\phi_2 & \cos\phi_2 & \sin 2\phi_2 & \cos 2\phi_2 & \cdots & \sin M\phi_2 & \cos M\phi_2 \\ \vdots & \vdots & \vdots & \vdots & & \vdots & \vdots \\ \sin\phi_K & \cos\phi_K & \sin 2\phi_K & \cos 2\phi_K & \cdots & \sin M\phi_K & \cos M\phi_K \end{bmatrix}.$$

In practice, the vibration of the rotor wall may be observed by measuring the rotor surface position using non-contact sensors such as proximity probes or laser vibrometers.

2.4. Discrete space-fixed spring-damper supports

For a discrete radial bearing unit with linear stiffness and damping properties (with coefficients k_{sn} and c_{sn}, respectively), the applied force is given by

$$F_{sn}(t) = F_{0n} + c_{sn}\dot{y}(\phi_{sn}, t) + k_{sn}y(\phi_{sn}, t) \tag{19}$$

where F_{0n} is a preload. From Eq. (18), the bearing forces may be expressed in matrix form as

$$\mathbf{F}_s = \mathbf{F}_0 + \mathbf{C}_s\mathbf{E}_s\dot{\mathbf{x}} + \mathbf{K}_s\mathbf{E}_s\mathbf{x} + \left(\Omega\mathbf{C}_s\mathbf{E}_s\mathbf{S} + \mathbf{K}_s\mathbf{E}_s\right)\sum_{m=1}^{M}\left(\mathbf{W}_{2m-1}\cos m\Omega t + \mathbf{W}_{2m}\sin m\Omega t\right) \tag{20}$$

where

$$\mathbf{C}_s = \mathrm{diag}\left(c_{s1},\ c_{s2},\ \ldots\ c_{sN_s}\right),$$

$$\mathbf{K}_s = \mathrm{diag}\left(k_{s1},\ k_{s2},\ \ldots\ k_{sN_s}\right),$$

$$\mathbf{S} = \mathrm{diag}\left(\mathbf{J}_2,\ 2\mathbf{J}_2,\ \ldots\ M\mathbf{J}_2\right)$$

Substituting Eq. (20) in Eq. (17) and rearranging yields

$$\ddot{\boldsymbol{x}} + \mathbf{C}_\Omega\dot{\mathbf{x}} + \mathbf{K}_\Omega x = \mathbf{f}_0 + \mathbf{H}_\Omega\sum_{m=1}^{M}\left(\mathbf{W}_{2m-1}\sin m\Omega t + \mathbf{W}_{2m}\cos m\Omega t\right) \tag{21}$$

where

$$\mathbf{C}_\Omega = \tau\mathbf{C}_0 + \mathbf{L}\mathbf{E}_s^{\mathrm{T}}\mathbf{C}_s\mathbf{E}_s - \Omega\mathbf{C}_1$$

$$\mathbf{K}_\Omega = \mathbf{K}_0 + \mathbf{L}\mathbf{E}_s^{\mathrm{T}}\mathbf{K}_s\mathbf{E}_s - \tau\Omega\mathbf{K}_1$$

$$\mathbf{H}_\Omega = -\Omega^2\mathbf{H} - \Omega\mathbf{L}\mathbf{E}_s^{\mathrm{T}}\mathbf{C}_s\mathbf{E}_s\mathbf{S} - \mathbf{L}\mathbf{E}_s^{\mathrm{T}}\mathbf{K}_s\mathbf{E}_s$$

$$\mathbf{f}_0 = -\mathbf{L}\mathbf{E}_s^{\mathrm{T}}\mathbf{F}_0$$

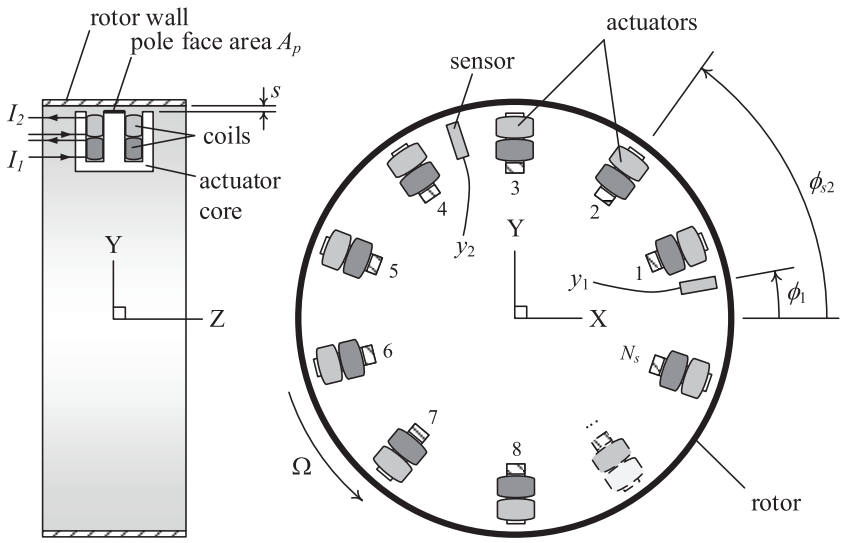

Fig. 2. Thin-walled rotor with active magnetic bearing supports: schematic.

Equation (21) describes the forced response behaviour due to non-circularity, where the mechanism for excitation is embodied via the time-dependent terms on the right side of the equation. The excitation behaviour depends critically on the matrices $\mathbf{E}_s^{\mathrm{T}}\mathbf{K}_s\mathbf{E}_s$ and $\mathbf{E}_s^{\mathrm{T}}\mathbf{C}_s\mathbf{E}_s$, which depend on the bearing unit characteristics and locations. To reveal the nature of this influence, numerical results are presented in Section 3.

2.5. Active magnetic bearing supports

Consider now the case of a thin-walled rotor, supported radially by a distribution of electromagnetic actuators, as shown schematically in Fig. 2. Further details of a prototype system and experimental results will be given in Section 4. Levitation of the rotor is achieved through electromagnetic forces generated by the actuators using a coil-winding scheme where each actuator has two independently powered coils having number of turns N_1 and N_2 and regulated currents I_1 and I_2. A standard model for the attractive force between the actuator and rotor may be adopted [20]:

$$F_{sn} = \frac{\mu_0 A_p (N_{1n} I_{1n} + N_{2n} I_{2n})^2}{\left(l_{iron}/\mu_r + 2s_n\right)^2}, \quad n = 1,\ 2,\ \ldots, N_s \tag{22}$$

where μ_0 is the permeability of free space, μ_r is the relative permeability for the core material, A_p is the pole-face area, l_{iron} is the mean flux path length through the actuator core and s is the size of the air gap between the rotor and actuator.

Suppose that the coil currents are produced by four powering drives and are given by $I_1(t) = i_0 \pm i_1(t)$ and $I_2(t) = i_0 \pm i_2(t)$ where i_0 is a fixed bias current and i_1, i_2 are two control currents, with the sign $\pm$ dependent on which of the four drives is connected to the coil. The air gap s may be expressed as $s_n(t) = s_0 - y(\phi_{sn}, t)$. Linearizing about a given operating point $s = s_0$ and $I_{1,2} = i_0$ gives the attractive force at each actuator as

$$F_{sn}(t) \approx F_{0n} - d_{0n} y(\phi_{sn}, t) + d_{1n} i_1(t) + d_{2n} i_2(t), \quad n = 1, \ldots, N_s \tag{23}$$

where

$$F_{0n} = \frac{\mu_0 A_p (N_{1n} i_0 + N_{2n} i_0)^2}{\left(l_{iron}/\mu_r + 2s_0\right)^2}, \qquad d_{0n} = \frac{4\mu_0 A_p (N_{1n} i_0 + N_{2n} i_0)^2}{\left(l_{iron}/\mu_r + 2s_0\right)^3},$$

$$d_{1n} = \pm\frac{2\mu_0 A_p N_{1n} (N_{1n} i_0 + N_{2n} i_0)}{\left(l_{iron}/\mu_r + 2s_0\right)^2}, \quad d_{2n} = \pm\frac{2\mu_0 A_p N_{2n} (N_{1n} i_0 + N_{2n} i_0)}{\left(l_{iron}/\mu_r + 2s_0\right)^2}.$$

Equation (23) may be combined in matrix form as

$$\mathbf{F}_s = \mathbf{F}_0 + \mathbf{D}_1\mathbf{i} - \mathbf{D}_0\mathbf{E}_s\left(\mathbf{x} - \sum_{m=1}^{M}\left(\mathbf{W}_{2m-1}\sin m\Omega t + \mathbf{W}_{2m}\cos m\Omega t\right)\right) \tag{24}$$

where

$$\mathbf{F}_0 = \begin{bmatrix} F_{01} & F_{02} & \dots & F_{0N_s} \end{bmatrix}^{\mathrm{T}},$$

$$\mathbf{i} = \begin{bmatrix} i_1 & i_2 \end{bmatrix}^{\mathrm{T}}, \quad \mathbf{D}_0 = \mathrm{diag}\left(d_{01}, \ d_{02}, \ \dots \ d_{0N_s} \right),$$

$$\mathbf{D}_1 = \begin{bmatrix} d_{11} & d_{12} & \dots & d_{1N_s} \\ d_{21} & d_{22} & \dots & d_{2N_s} \end{bmatrix}^{\mathrm{T}}$$

For levitation control, a general PD-type feedback law may be employed:

$$\mathbf{i} = -\mathbf{K}_P \mathbf{y} - \mathbf{K}_D \dot{\mathbf{y}} \tag{25}$$

where $\mathbf{y}$ is the rotor wall positions, as measured by two proximity probes, which may be expressed as in Eq. (18). The controller gain matrices $\mathbf{K}_P$ and $\mathbf{K}_D$ have dimensions $2 \times N_s$. The fixed-frame discrete model of a thin-wall rotor with active magnetic bearing support follows from Eqs (17), (24) and (25) as

$$\ddot{\mathbf{x}} + \mathbf{C}_\Omega^* \dot{\mathbf{x}} + \mathbf{K}_\Omega^* \mathbf{x} = \mathbf{f}_0^* + \mathbf{H}_\Omega^* \sum_{m=1}^{M} \left(\mathbf{W}_{2m-1} \sin m\Omega t + \mathbf{W}_{2m} \cos m\Omega t \right) \tag{26}$$

where

$$\mathbf{C}_\Omega^* = \tau \mathbf{C}_0 + \mathbf{L}\mathbf{E}_s^{\mathrm{T}} \mathbf{D}_1 \mathbf{K}_D \mathbf{E} - \Omega \mathbf{C}_1$$

$$\mathbf{K}_\Omega^* = \mathbf{K}_0 - \mathbf{L}\mathbf{E}_s^{\mathrm{T}} \mathbf{D}_0 \mathbf{E}_s + \mathbf{L}\mathbf{E}_s^{\mathrm{T}} \mathbf{D}_1 \mathbf{K}_P \mathbf{E} - \tau \Omega \mathbf{K}_1$$

$$\mathbf{H}_\Omega^* = -\Omega^2 \mathbf{H} - \Omega \mathbf{L}\mathbf{E}_s^{\mathrm{T}} \mathbf{D}_1 \mathbf{K}_D \mathbf{E}\mathbf{S} - \mathbf{L}\mathbf{E}_s^{\mathrm{T}} \left(-\mathbf{D}_0 \mathbf{E}_s + \mathbf{D}_1 \mathbf{K}_P \mathbf{E} \right)$$

$$\mathbf{f}_0^* = -\mathbf{L}\mathbf{E}_s^{\mathrm{T}} \mathbf{F}_0$$

Some important differences between this case and that of the spring-damper supports is that the actuators behave like negative stiffness springs, as modelled by the matrix $\mathbf{E}_s^{\mathrm{T}} \mathbf{D}_0 \mathbf{E}_s$. This effect is compensated by feedback, which produces a stabilizing stiffness matrix $\mathbf{E}_s^{\mathrm{T}} \mathbf{D}_1 \mathbf{K}_P \mathbf{E}$ and damping matrix $\mathbf{E}_s^{\mathrm{T}} \mathbf{D}_1 \mathbf{K}_D \mathbf{E}$. Note also that $\mathbf{D}_1$ depends on the coil winding pattern and this can be exploited in order to minimize the excitation of flexural modes through the bearing.

2.6. Steady-state solution

It may be assumed, based on linearity, that the solution for steady-state vibration takes the form

$$\mathbf{x}(t) = \mathbf{A}_0 + \sum_{m=1}^{M} \left(\mathbf{A}_m(\Omega) \sin m\Omega t + \mathbf{B}_m(\Omega) \cos m\Omega t \right) \tag{27}$$

where $\mathbf{A}_m, \mathbf{B}_m \in \mathcal{R}^{2M \times 1}$. After substituting Eq. (27) in Eq. (21) and using the method of undetermined coefficients, we obtain

$$\mathbf{A}_0 = \mathbf{K}_{\Omega=0} \mathbf{f}_0 \tag{28}$$

$$\begin{bmatrix} \mathbf{A}_m \\ \mathbf{B}_m \end{bmatrix} = \begin{bmatrix} \mathbf{K}_\Omega - (m\Omega)^2 \mathbf{I} & -m\Omega \mathbf{C}_\Omega \\ m\Omega \mathbf{C}_\Omega & \mathbf{K}_\Omega - (m\Omega)^2 \mathbf{I} \end{bmatrix}^{-1} \begin{bmatrix} \mathbf{H}_\Omega \mathbf{W}_{2m-1} \\ \mathbf{H}_\Omega \mathbf{W}_{2m} \end{bmatrix} \tag{29}$$

where $\mathbf{I} \in \mathcal{R}^{2M \times 2M}$ is the identity matrix. Equations in the same form can be obtained for the AMB model (Eq. (26)).

From a practical point of view, it is useful to be able to predict the vibration of the rotor wall that would be observed at a fixed point in the stationary frame. This is important when the rotor has finite clearances with surrounding components that are fixed in space. It will also correspond to the vibration that would be measured by surface proximity sensors. The solution can be obtained by substituting Eq. (27) into Eq. (18):

$$\mathbf{y} = -\mathbf{E}\mathbf{A}_0 - \mathbf{E} \sum_{m=1}^{M} \left[(\mathbf{A}_m + \mathbf{W}_{2m-1}) \sin m\Omega t + (\mathbf{B}_m + \mathbf{W}_{2m}) \cos m\Omega t \right] \tag{30}$$

Table 1
Rotor properties.

Parameter	Symbol	Value	Units
Rotor radius	R	111.0	mm
Wall thickness	d	3.1	mm
Material density	ρ	7740	kg m^{-3}
Young's modulus	E	2×10^{11}	N m^{-2}
Axial length	l	51	mm

3. Numerical study

To investigate the vibration behaviour of a thin-walled rotor for cases with spring-damper supports, a numerical study has been undertaken. The considered properties correspond to an experimental rotor with length 51 mm, radius 111 mm and wall thickness to radius ratio $d/R = 5/179$. The rotor was manufactured by electric discharge machining from martensitic stainless steel (grade 420 J). Further properties are given in Table 1. Table 2 shows the natural frequencies for free vibration of the rotor obtained from the inextensible ring model Eq. (8) and from 2–D thin-shell models, as detailed in the appendix. The difference between the inextensible case and full 2–D model is very small, as expected for the given d/R value. With the classical DMV assumptions for thin shells there are significant differences. Importantly, the neglected terms result in an erroneous imbalance of internal forces and so the natural frequency for the rigid body modes ($m = 1$) is non-zero. Such errors are unacceptable for combined rotor-bearing system modelling where the modified dynamics, including rigid body modes, must be captured accurately.

Firstly, the case of unsymmetrical two-spring supports will be presented to show the basic behaviour predicted by the proposed model (Eq. (21)). Cases with symmetrical and unsymmetrical bearing supports will then be compared to examine the effects from symmetry and multiplicity.

3.1. Unsymmetrical two-spring supports

Two orthogonal supports are considered with the following properties

$$\phi_{s1} = 0 \text{ rad}, k_{s1} = 90 \text{ kN m}^{-1}, c_{s1} = 9 \text{ N s m}^{-1}$$

$$\phi_{s2} = \pi/2 \text{ rad}, k_{s2} = 22.5 \text{ kN m}^{-1}, c_{s2} = 2.25 \text{ N s m}^{-1}$$

Zero preload is assumed ($\mathbf{f}_0 = 0$). The material relaxation time is 0.1 μs. All calculations are based on a 24th order model ($M = 24$) for the rotor in Table 1.

For presentation of the results, the non-circularity is considered with coefficients $a_m = 0$ μm and $b_m = 1$ μm, $m = 1, 2, \ldots, 24$. For observation at a single location, and in accordance with Eq. (30), the vibration response may be defined in terms of the following amplitude/phase parameters:

$$\left.\begin{aligned} &\alpha_m(\Omega) = -\mathbf{E}(\mathbf{A}_m + \mathbf{W}_{2m-1}), \quad \beta_m(\Omega) = -\mathbf{E}(\mathbf{B}_m + \mathbf{W}_{2m}), \\ &Y_m(\Omega) = \sqrt{\alpha_m^2 + \beta_m^2}, \quad \psi_m(\Omega) = \tan^{-1}(\beta_m/\alpha_m) \end{aligned}\right\} \tag{31}$$

The observed vibration can then be expressed

$$y_1(t) = \sum_{m=1}^{M} Y_m(\Omega)\sin\left(m\Omega t + \psi_m(\Omega)\right) \tag{32}$$

Equation (21) shows that, for a given speed Ω, the forcing frequencies are $\omega = \Omega,\ 2\Omega,\ 3\Omega, \ldots,\ 24\Omega$. The response amplitudes $Y_m(\Omega)$ may be evaluated for each harmonic frequency $m\Omega$ based on Eqs. (29) and (31).

Suppose that the observation of vibration is made at angular position $\phi_1 = \pi/24$ rad. A plot of the amplitude of each harmonic component of the vibration over the $(\Omega, m\Omega)$ plane is shown in Fig. 3. For illustration, harmonic amplitudes for a rotational

Table 2
Theoretical natural frequencies (in Hz) for flexural vibration of free non-rotating rotor.

Model	m				
	1	2	3	4	5
1–D Inextensible ring model (Eq. (8))	0	157.673	445.965	855.099	1382.88
2–D thin-shell model (Eq. (A.4))	0	157.659	445.918	855.001	1382.71
2–D model with DMV assumptions (Eq. (A.6))	41.550	210.226	501.698	912.080	1440.46

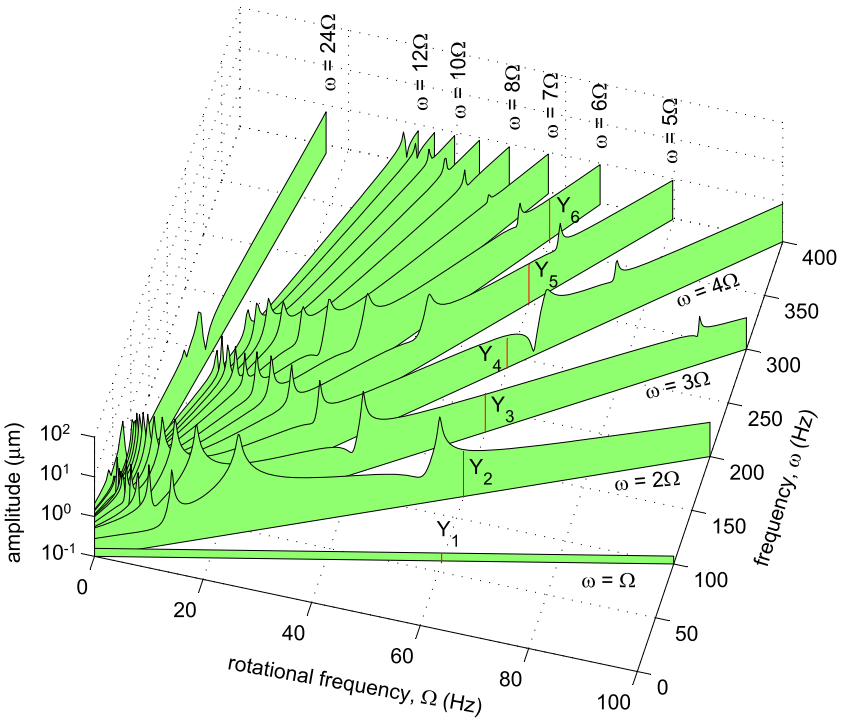

Fig. 3. Response amplitudes due to non-circularity excitation.

frequency of 60 Hz are highlighted as vertical lines at points (60, 60 m) Hz having height Y_m. For varying rotational speed, the frequency response due to the mth non-circularity component is defined in the domain $\omega = m\Omega$.

The Campbell diagram shown in Fig. 4a was constructed from the numerical eigensolutions for Eq. (21) for a set of discrete Ω values. The resonant peaks in Fig. 3 align with the natural frequencies shown in the Campbell diagram. Note that some splitting of the natural frequencies occurs at zero speed due to the asymmetry of the discrete supports. The 'front' view of Y_4 as a function of Ω is shown in Fig. 4b. Resonance conditions are observed for Y_4 at the intersections of the line $\omega = 4\Omega$ and the natural frequency lines in the Campbell diagram. Clearly, if the rotor has high order non-circularity then many resonance conditions can arise during spin-up or spin-down.

3.2. Effect of symmetry and number of supports

To show the effects from symmetry and multiplicity of supports, four different cases are considered, as detailed in Table 3. Equal support stiffness and damping $k_s = 17\,450$ N m^{-1}, $c_s = 1.7450$ N s m^{-1} are assigned for the 3-support cases and $k_s = 4131$ N m^{-1}, $c_s = 0.413$ N s m^{-1} for the 12-support cases.

The Campbell diagrams for the cases with non-symmetrical supports are shown in Fig. 5a, and the harmonic response amplitudes $Y_{2,\ldots,5}$ shown in Fig. 5b and c. The natural frequencies of the two rigid body modes are split for these cases. The flexible mode natural frequencies depend on the stiffness of the supports but are not affected significantly by the symmetry or number of supports, as the support stiffness is relatively low. Resonant peaks are seen at all crossing points of the lines $\omega = m\Omega$ and the natural frequency lines in the Campbell diagram.

For the symmetrical cases with equally spaced supports, the Campbell diagrams are shown in Fig. 6a, and the response amplitude $Y_{2,\ldots,5}$ for each case shown in Fig. 6b and c. For these cases, a resonance occurs at only some crossing points. Also resonance is not seen at all if there is a sufficient number of supports (see Fig. 6c).

These phenomena can be related to the structure of the matrix $\mathbf{H}_\Omega$ in Eq. (21), as this matrix determines the coupling of each excitation harmonic with each mode. The dominant term in $\mathbf{H}_\Omega$ is $\mathbf{L}\mathbf{E}_s^{\mathrm{T}}\mathbf{K}_s\mathbf{E}_s$. The 2×2 submatrices that make up $\mathbf{E}_s^{\mathrm{T}}\mathbf{K}_s\mathbf{E}_s$ are given by

$$K_{ij} = k_s \sum_{n=1}^{N_s} \begin{bmatrix} \sin i\phi_{sn} \sin j\phi_{sn} & \sin i\phi_{sn} \cos j\phi_{sn} \\ \cos i\phi_{sn} \sin j\phi_{sn} & \cos i\phi_{sn} \cos j\phi_{sn} \end{bmatrix}. \tag{33}$$

This matrix determines the excitation of the mode with nodal index i by the jth non-circularity harmonic. From the numerical study, it is found that if the off-diagonal submatrices ($i \neq j$) are non-zero then one or more resonances are observed. For non-

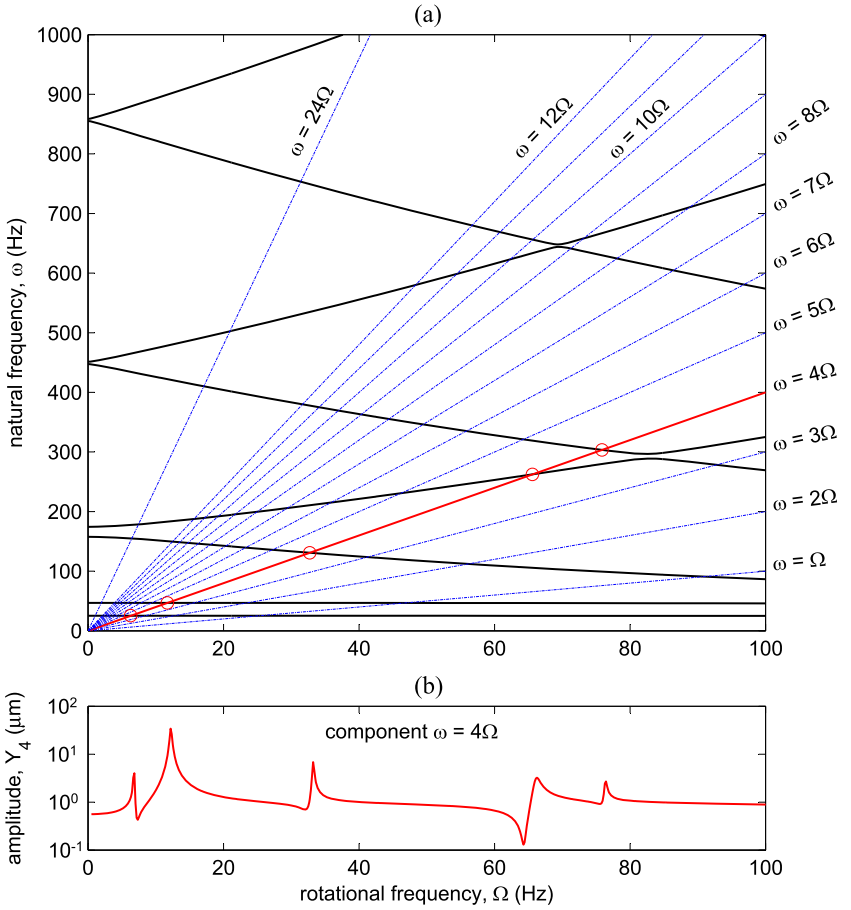

Fig. 4. (a) Campbell diagram (b) Response amplitude in domain $\omega = 4\Omega$.

Table 3
Cases with different numbers and positions of supports.

Supports	Support positions
3 symmetrical	$0, \frac{2\pi}{3}, \frac{4\pi}{3}$
3 non-symmetrical	$0, \frac{8\pi}{9}, \frac{23\pi}{18}$
12 symmetrical	$0, \frac{\pi}{6}, \frac{2\pi}{6}, \frac{3\pi}{6}, \ldots, \frac{11\pi}{6}$
12 non-symmetrical	$0, \frac{\pi}{21}, \frac{2\pi}{21}, \frac{4\pi}{21}, \frac{6\pi}{21}, \frac{9\pi}{21}, \frac{12\pi}{21}, \frac{16\pi}{21}, \frac{20\pi}{21}, \frac{25\pi}{21}, \frac{30\pi}{21}, \frac{36\pi}{21}$

symmetrical supports, $K_{ij} \neq 0$ for $i \neq j$, and this leads to a coupling of every non-circularity excitation harmonic with every rotor mode. In the case of symmetrical supports, $K_{ij} = 0$ for all $i \neq j$ and $i + j < N_s$ and so resonance is only observed for some crossings involving sufficiently high nodal index and non-circularity harmonic. In addition, if the number of supports N_s is larger than the model order then $\mathbf{E}_s^{\mathrm{T}}\mathbf{K}_s\mathbf{E}_s$ becomes a diagonal matrix and no resonance is observed. Physically, with many identical supports, a given location fixed on the rotor does not experience any variation in loading from the supports and, therefore, there is no excitation from non-circularity.

Clearly, the resonance of a rotating non-circular ring interacting with space-fixed support can be avoided by having a sufficient number of identical evenly spaced supports. An alternative approach to avoid resonance with active magnetic bearing supports is to generate a distribution of actuation forces that couples only with the rigid body modes (by satisfying an orthogonality condition with respect to the flexural mode shapes). A system design based on this scheme has been tested, and results are described in the following section.

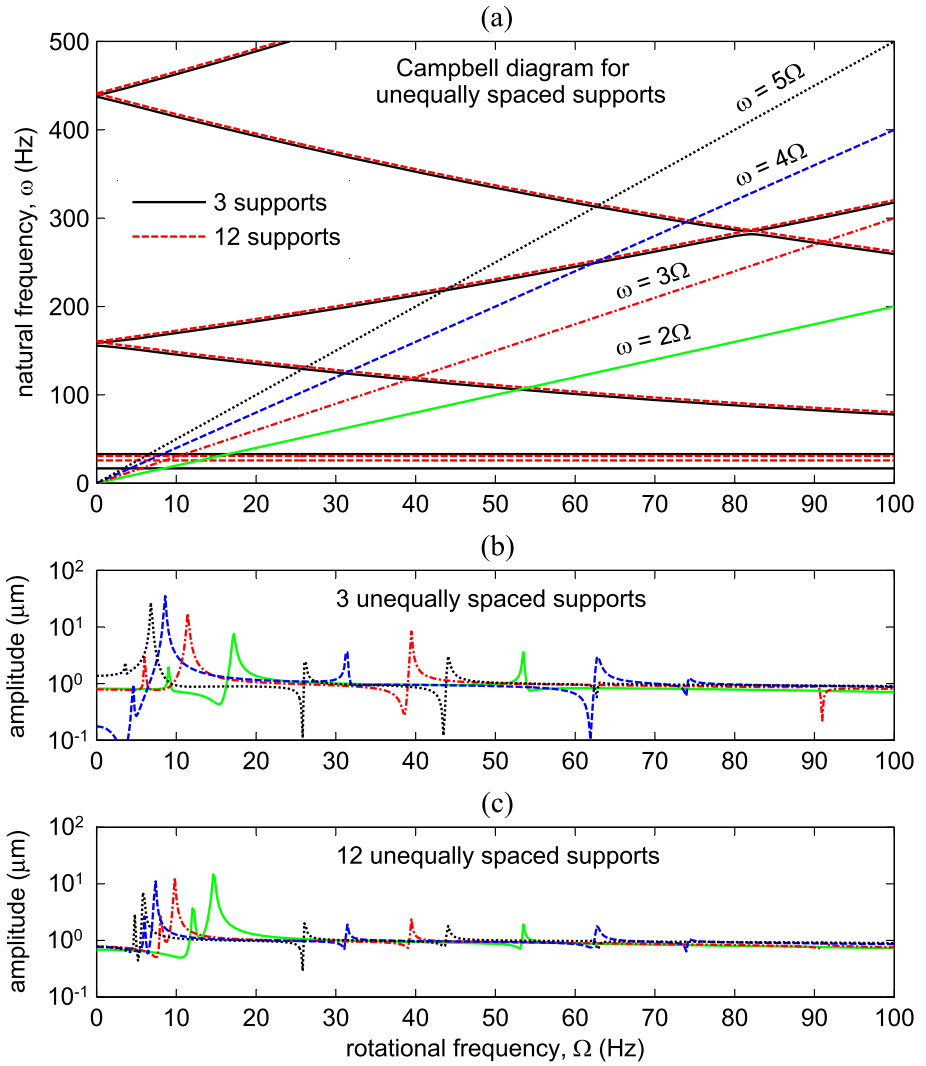

Fig. 5. (a) Campbell diagram for unequally spaced supports (b) Response harmonic amplitudes $Y_{2,\ldots,5}$ for 3 supports (c) Response harmonic amplitudes $Y_{2,\ldots,5}$ for 12 supports.

4. Experimental study

4.1. Experimental setup

In this section, vibration of a rotor with active magnetic bearing support will be studied by experiment and results compared with theoretical predictions. Fig. 7 shows the experimental system, which comprises a thin-walled rotor with internal magnetic bearing constructed as a circular array of 24 identical actuators having E-shaped cores. The rotor properties were previously described in section 3, with details given in Table 1. The coil-winding scheme for the actuators is given in Table 4 and the coils connect with drives supplying currents as follows:

$$I_{1n} = \begin{cases} i_0 + i_1, & n = 1,\ 2,\ \ldots,\ 12 \\ i_0 - i_1, & n = 13,\ 14,\ \ldots,\ 24 \end{cases} \tag{34}$$

$$I_{2n} = \begin{cases} i_0 + i_2, & n = 7,\ 8,\ \ldots,\ 18 \\ i_0 - i_2, & n = 1,\ 2,\ \ldots,\ 6, 19,\ 20,\ \ldots,\ 24 \end{cases} \tag{35}$$

Key parameters for the actuator design are listed in Table 5. The rotor is connected by four flexible couplings to a disk driven by a DC motor, as shown in Fig. 7. The rotor is levitated without contact during operation under feedback control and the mean

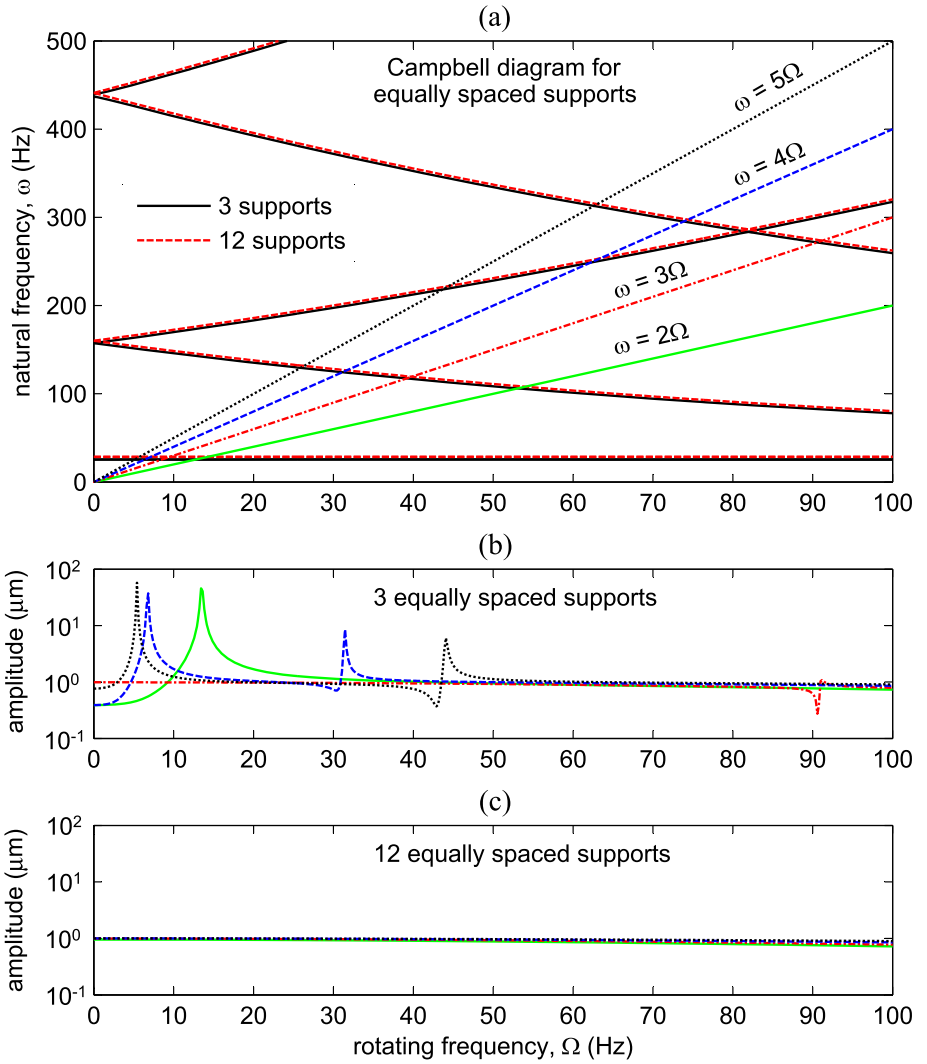

Fig. 6. (a) Campbell diagram for equally spaced supports (b) Response harmonic amplitudes $Y_{2,\ldots,5}$ for 3 supports (c) Response harmonic amplitudes $Y_{2,\ldots,5}$ for 12 supports.

air-gap size between the rotor and stator (actuator poles) is approximately 0.8 mm.

Two proximity sensors are installed at positions $\phi = \pi/12$ and $\phi = 11\pi/12$. The PD-feedback gains, as defined for Eq. (25), are

$$\mathbf{K}_P = k_p \begin{bmatrix} -0.135 & 1.026 \\ 1.026 & -0.135 \end{bmatrix}, \quad \mathbf{K}_D = k_d \begin{bmatrix} -0.135 & 1.026 \\ 1.026 & -0.135 \end{bmatrix} \tag{36}$$

where $k_p = 5700$ A m^{-1} and $k_d = 8.5$ A s m^{-1}.

4.2. Experimental results

The non-circularity of the rotor was determined by measuring the inside radius for evenly spaced points with angular separation $\pi/5$ rad. Fourier series coefficients were then determined as reported in Table 6. The coefficients a_1 and b_1 are negligible for a well aligned coupling.

The theoretical model of the rotor with active magnetic bearing supports (Eq. (26)) was first validated experimentally by frequency response measurements, undertaken for various rotational speeds. The rotor was excited by small auxiliary coils wound on actuators 1 and 2, which produce localized forcing of the rotor wall close to the sensor location. The results shown in Fig. 8a are for rotational speeds of 0, 15, 27 and 34 Hz. The comparison between theoretical natural frequencies and the resonance frequencies observed from experiment are shown in Fig. 8b. Generally, a good level of agreement is seen,

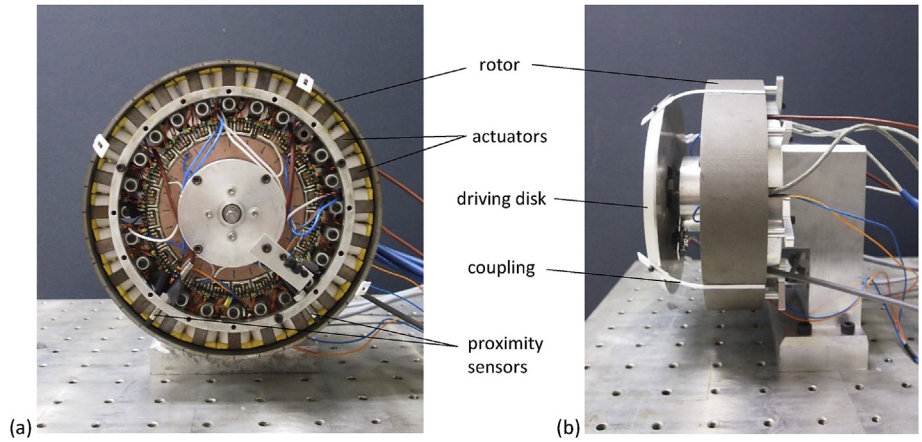

Fig. 7. Experimental system: Active magnetic bearing applied to a thin-walled cylindrical rotor (a) internal bearing actuator array (driving disk removed) (b) side view.

Table 4
Coil winding scheme for AMB actuators.

Actuator no.	1	2	3	4	5	6	7	8	9	10	11	12
N_1(turns)	0	16	30	42	52	61	70	61	52	42	30	16
N_2(turns)	70	61	52	42	30	16	0	16	30	42	52	61
Actuator No.	13	14	15	16	17	18	19	20	21	22	23	24
N_1(turns)	0	16	30	42	52	61	70	61	52	42	30	16
N_2(turns)	70	61	52	42	30	16	0	16	30	42	52	61

though there are extra resonance peaks appearing in the experimental data in Fig. 8a. These are due to modes involving out-of-plane rigid body tilting and flexural twisting and are believed to be excited due to the effect of the attached coupling. These modes cannot be captured by the theoretical model because any dependency of $u(\theta, t)$ on the axial z coordinate is neglected.

These experimental findings are aligned with those of Endo et al. [4] for a thin spinning ring and confirm that the rotating ring model based on shell theory can accurately describe the vibration of a thin-walled rotor, at least for small values of nodal index.

To evaluate steady-state vibration excitation, the rotor was operated at constant rotational frequency and the vibration of the rotor wall recorded using the proximity sensor at $\phi = \pi/24$ rad. The rotational frequency was varied from 2 Hz, increasing in steps of 0.5 Hz up to 36 Hz, which was the maximum limit for the driving motor.

Table 5
Actuator properties.

Parameter	Symbol	Value	Units
Pole face area	A_p	100	mm^2
Core flux path length	l_{iron}	100	mm
Mean gap size	s_0	0.8	mm
Permeability of free space	μ_0	$4\pi \times 10^{-7}$	H m^{-1}
Core relative permeability	μ_r	350	–
Bias current	i_0	2.2	A

Table 6
Non-circularity measurements for experimental rotor.

Harmonic j	2	3	4	5	6	7	8	9	10
a_j(μm)	−33.3	−1.7	4.0	−1.1	1.3	−0.8	0.4	−0.4	0
b_j(μm)	−4.5	−3.0	−1.3	1.7	1.1	−1.1	0.8	−0.2	0.2

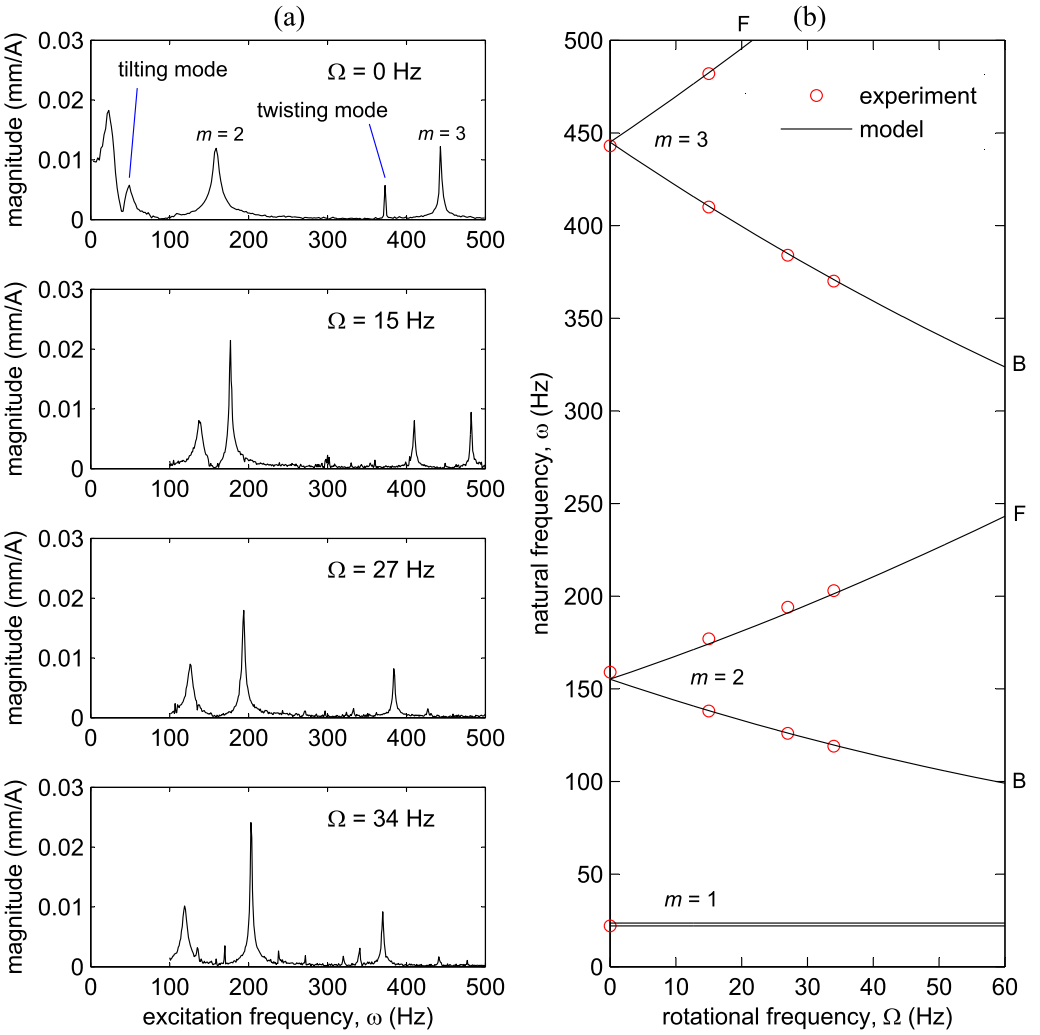

Fig. 8. (a) Frequency response data for excitation of levitated rotor for different rotational frequencies (b) Campbell diagram: forward (F) and backward (B) modes are indicated, with experimental measurements shown by ○.

Fig. 9 shows the measured displacement signal and harmonic components for rotational frequencies of $\Omega = 9.96$ Hz and $\Omega = 20.05$ Hz. The harmonic component amplitudes were determined by a discrete Fourier transform approach. The harmonic component Y_1 is predicted to be zero by the theoretical model but arises due to synchronous forcing (rather than non-circularity), notionally due to coupling offset and/or inhomogenous properties of the rotor.

The harmonic component amplitudes for a range of rotational frequencies are shown in Fig. 10 and compared with theoretical predictions based on the model Eq. (26) and the measured non-circularity. These results indicate there is a good level of agreement between the model-based prediction and the actual behaviour. For higher order harmonics, the vibration amplitudes become very small (< 10 μm) and so their measured values are perturbed by uncontrollable effects, including electrical noise, quantization and small fluctuations in rotational speed. The most significant resonances are due to excitation of the rigid body modes, and the associated amplitude variations are captured well by the model. The resonant peaks associated with the rotor flexural modes are very small, partly due to the distributed actuation topology, which has been designed to minimize coupling of the bearing forces with the flexural modes. Nonetheless, small resonances can be detected in the experimental data that are consistent with the model-based predictions. It is also seen in Fig. 10 that, for each harmonic, there is an anti-resonance close to the rigid body resonance, when the excitation frequency is approximately 38 Hz. The anti-resonance is associated with tilting mode vibration and, therefore, cannot be captured by the model. Importantly, the modelling approach can be used to determine permissible levels of non-circularity such that contact between the rotor and stator is avoided.

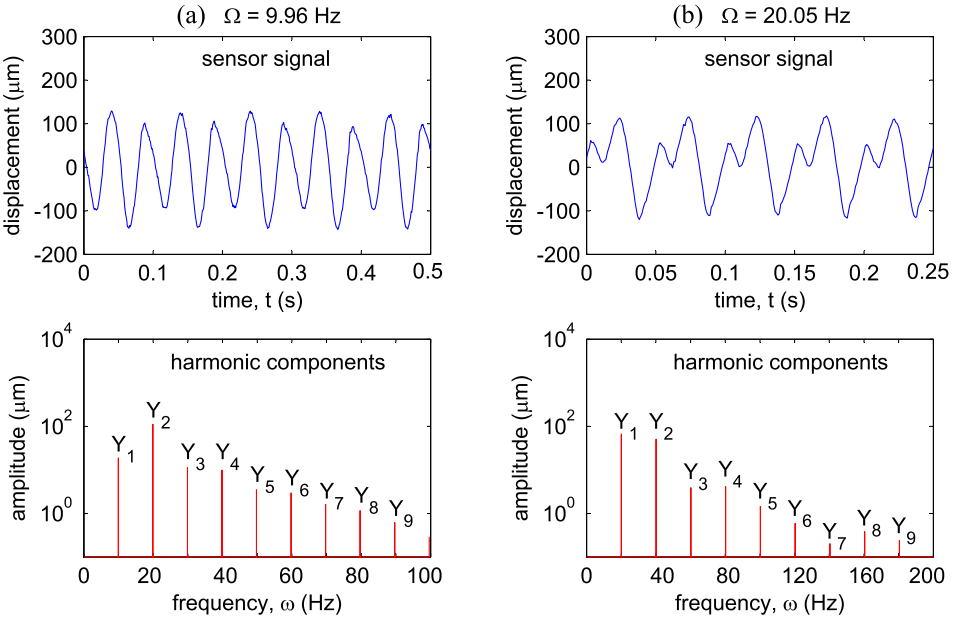

Fig. 9. Measured vibration and harmonic components for steady rotation of levitated rotor at (a) rotational frequency of 9.96 Hz and (b) rotational frequency of 20.05 Hz.

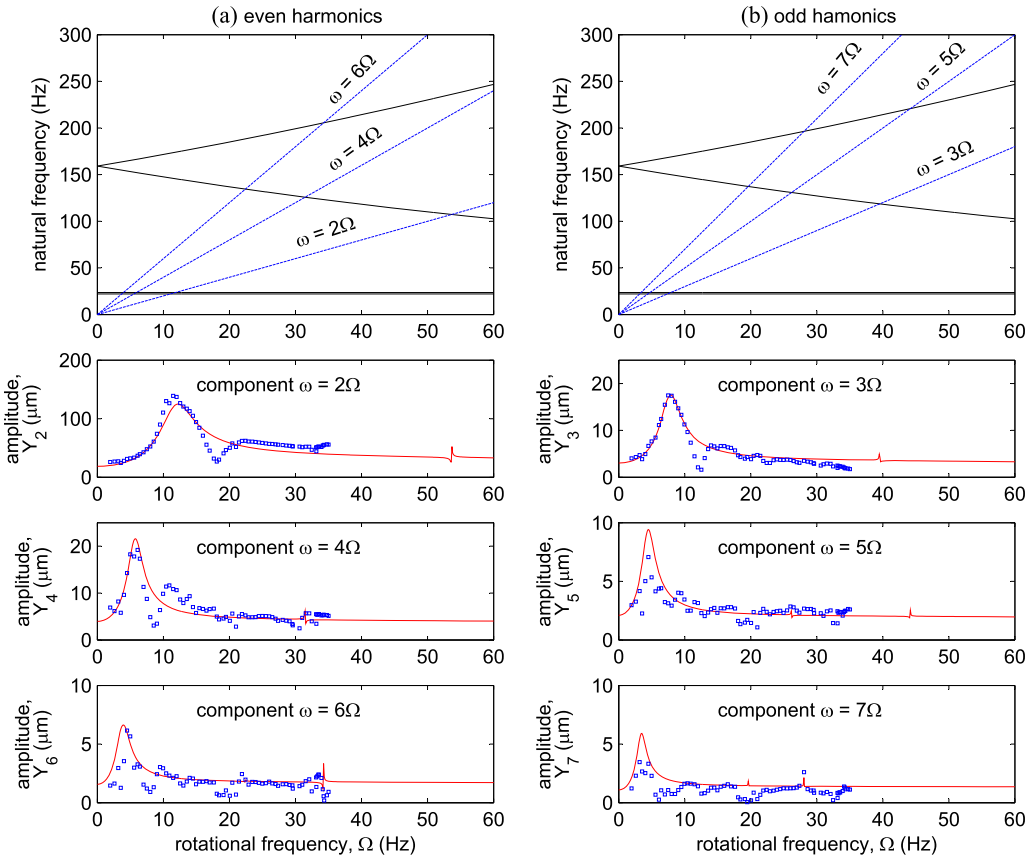

Fig. 10. Campbell diagrams and non-circularity response for levitated rotor considering (a) even harmonics and (b) odd harmonics. Theoretical predictions of the amplitude of vibration are based on the measured rotor non-circularity. Experimental data is shown by □ symbols.

5. Conclusions

This paper has introduced a mathematical model for the vibration of a thin-walled cylindrical rotor subject to small non-circularity and coupled to space-fixed bearing supports. Rotor non-circularity has been shown to give rise to multi-harmonic excitation of the rotor-bearing structure. Whether a resonance occurs at a predicted critical speed depends on the multiplicity and symmetry of the bearing supports. Generally, a large number of evenly spaced identical supports will eliminate the possibility of low order resonance conditions. The modelling approach can also be applied to thin-walled rotor-AMB systems by accounting for feedback controlled electromagnetic actuators within the formulation. The experimental results for an AMB-supported rotor showed that significant flexural mode resonance could be avoided for the considered distributed actuation topology. Also, numerical predictions based on measured non-circularity showed good agreement with measurements of vibration of the rotor wall, thereby confirming the validity and utility of the theoretical modelling. A limitation of the work, at present, is that axial variation in wall deformation was not addressed by the modelling. Extending the work in this way will be important for vibration prediction for longer thin-walled rotors with axial distributions of bearing components.

Acknowledgements

This work was supported by the Thailand Research Fund and Chiang Mai University [grant number BRG5980013].

Appendix. 2–D cylindrical shell models

This appendix describes alternative models based on shell theories that yield useful comparative results for free vibration behaviour.

2–D model without inextensibility assumption

A two-dimensional model for vibration of a thin rotating annulus may be obtained from Eqs (2)–(4) without the inextensibility assumption by applying $N = \frac{Edl}{R}(v_r' - u_r)$, yielding rotating frame equations of motion as

$$\frac{E}{\rho R^2}(v_r' - u_r) - \frac{Ed^2}{12\rho R^4}(u_r'''' + v_r''') + \Omega^2(u_r'' + v_r' + u_r) = \ddot{u}_r + 2\Omega\dot{v}_r \tag{A.1}$$

$$\frac{E}{\rho R^2}(v_r'' - u_r') + \frac{Ed^2}{12\rho R^4}(u_r''' + v_r'') + \Omega^2 u_r' = \ddot{v}_r - 2\Omega\dot{u}_r \tag{A.2}$$

These equations are consistent with Love's approximation theory for thin shells [21]. Substituting the free vibration solution in the form

$$\begin{bmatrix} u_r \\ v_r \end{bmatrix} = \begin{bmatrix} Ae^{j(m\theta+\omega t)} \\ jBe^{j(m\theta+\omega t)} \end{bmatrix} \tag{A.3}$$

leads to the following eigenvalue problem for natural frequencies ω:

$$\begin{bmatrix} -1-\delta m^4-(m^2-1)\overline{\Omega}^2+\overline{\omega}^2 & -m-\delta m^3-m\overline{\Omega}^2+2\overline{\Omega}\overline{\omega} \\ -m-\delta m^3-m\overline{\Omega}^2+2\overline{\Omega}\overline{\omega} & -(1+\delta)m^2+\overline{\omega}^2 \end{bmatrix} \begin{bmatrix} A \\ B \end{bmatrix} = 0 \tag{A.4}$$

where $\overline{\Omega} = \Omega R\sqrt{\rho/E}, \overline{\omega} = \omega R\sqrt{\rho/E}$ and $\delta = d^2/12R^2$. The characteristic equation is thus quartic in $\overline{\omega}$ and (for each value of m) yields four natural frequencies. The two lower frequencies relate to predominantly flexural modes (for which $u_r \approx v_r'$) while the two higher frequencies are extensional modes. Under the assumption $\delta m^2 \ll 1$, the natural frequencies (for $\Omega = 0$) follow as

$$\omega_f = \pm\omega_0 \frac{m(m^2-1)}{\sqrt{m^2+1}}, \quad \omega_e = \pm\omega_0 \frac{2R}{d}\sqrt{3(m^2+1)} \tag{A.5}$$

The first frequency matches that for the inextensible ring model Eq. (8), thereby confirming its validity for cases where $dm \ll 2\sqrt{3}\,R$. The exact value from (A.4) will be somewhat lower, however.

2–D shell model with DMV approximations

A possible simplification for thin-shell cylinders is to neglect the radial shear stress term in the tangential acceleration Eq. (A.2). A further approximation made in Donnell-Mushtari-Vlasov (DMV) theory, is that the contribution of the tangential displacement to the bending strain is negligible [22]. Under these assumptions, Eq. (A.4) simplifies to

$$\begin{bmatrix} -1-\delta m^4-(m^2-1)\overline{\Omega}^2+\overline{\omega}^2 & -m-m\overline{\Omega}^2+2\overline{\Omega}\overline{\omega} \\ -m-m\overline{\Omega}^2+2\overline{\Omega}\overline{\omega} & -m^2+\overline{\omega}^2 \end{bmatrix} \begin{bmatrix} A \\ B \end{bmatrix} = 0 \tag{A.6}$$

Although commonly applied, the validity of this model for a thin-walled rotor-bearing system should be verified by comparison with the results from Eq. (A.4).

References

[1] D. Peters, C. Kaletsch, R. Nordmann, B. Domes, Test rig for a supercritical rotor of an aero engine, in: 12th IFToMM World Congress, Proceedings, 2007.
[2] V.I. Gulyaev, P.Z. Lugovoi, I.L. Solov'ev, Elastic vibrations of a single-support thin-walled rotor (compound shell) during complex rotation, Int. Appl. Mech. 39 (8) (2003) 969–975, https://doi.org/10.1023/A:1027420900937.
[3] G. Genta, Dynamics of Rotating Systems, Springer Science & Business Media, New York, 2007.
[4] M. Endo, K. Hatamura, M. Sakata, O. Taniguchi, Flexural vibration of a thin rotating ring, J. Sound Vib. 92 (2) (1984) 261–272, https://doi.org/10.1016/0022-460X(84)90560-1.
[5] M. Amabili, A comparison of shell theories for large-amplitude vibrations of circular cylindrical shells: Lagrangian approach, J. Sound Vib. 264 (5) (2003) 1091–1125, https://doi.org/10.1016/S0022-460X(02)01385-8.
[6] R. Hwang, C. Fox, S. McWilliam, The in-plane vibration of thin rings with in-plane profile variations part i: general background and theoretical formulation, J. Sound Vib. 220 (3) (1999) 497–516, https://doi.org/10.1006/jsvi.1998.1963.
[7] C. Fox, R. Hwang, S. McWilliam, The in-plane vibration of thin rings with in-plane profile variations part ii: application to nominally circular rings, J. Sound Vib. 220 (3) (1999) 517–539, https://doi.org/10.1006/jsvi.1998.1962.
[8] P. Bisegna, G. Caruso, Frequency split and vibration localization in imperfect rings, J. Sound Vib. 306 (3) (2007) 691–711, https://doi.org/10.1016/j.jsv.2007.06.027.
[9] R. Hwang, C. Fox, S. McWillliam, Free vibrations of elliptical rings with circumferentially variable thickness, J. Sound Vib. 228 (3) (1999) 683–699, https://doi.org/10.1006/jsvi.1999.2421.
[10] J.-H. Kim, J.-H. Kim, Thermoelastic dissipation of rotating imperfect micro-ring model, Int. J. Mech. Sci. 119 (2016) 303–309, https://doi.org/10.1016/j.ijmecsci.2016.10.024.
[11] X. Wu, R.G. Parker, Vibration of rings on a general elastic foundation, J. Sound Vib. 295 (1–2) (2006) 194–213, https://doi.org/10.1016/j.jsv.2006.01.007.
[12] C.G. Cooley, R.G. Parker, Vibration of high-speed rotating rings coupled to space-fixed stiffnesses, J. Sound Vib. 333 (12) (2014) 2631–2648, https://doi.org/10.1016/j.jsv.2014.01.005.
[13] S.V. Canchi, R.G. Parker, Effect of ring-planet mesh phasing and contact ratio on the parametric instabilities of a planetary gear ring, ASME J. Mech. Design 130 (1) (2008) 014501, https://doi.org/10.1115/1.2803716.
[14] G. Carrier, On the vibrations of the rotating ring, Q. Appl. Math. 3 (3) (1945) 235–245.
[15] S. Huang, W. Soedel, Response of rotating rings to harmonic and periodic loading and comparison with the inverted problem, J. Sound Vib. 118 (2) (1987) 253–270, https://doi.org/10.1016/0022-460X(87)90524-4.
[16] Y. Wei, L. Nasdala, H. Rothert, Analysis of forced transient response for rotating tires using ref models, J. Sound Vib. 320 (1) (2009) 145–162, https://doi.org/10.1016/j.jsv.2008.07.007.
[17] Y.-J. Kim, J. Bolton, Effects of rotation on the dynamics of a circular cylindrical shell with application to tire vibration, J. Sound Vib. 275 (3) (2004) 605–621, https://doi.org/10.1016/j.jsv.2003.06.003.
[18] P. Kindt, P. Sas, W. Desmet, Measurement and analysis of rolling tire vibrations, Optic Laser. Eng. 47 (3) (2009) 443–453, https://doi.org/10.1016/j.optlaseng.2008.06.017.
[19] S. Gong, A Study of In-plane Dynamics of Tires, (PhD Thesis), Delft University of Technology, 1993.
[20] G. Schweitzer, E.H. Maslen, Magnetic Bearings: Theory, Design, and Application to Rotating Machinery, Springer-Verlag, Berlin, 2009.
[21] A.E.H. Love, A Treatise on the Mathematical Theory of Elasticity, fourth ed., Dover Publication, New York, 1944.
[22] Y. Xing, B. Liu, T. Xu, Exact solutions for free vibration of circular cylindrical shells with classical boundary conditions, Int. J. Mech. Sci. 75 (4) (2013) 178–188, https://doi.org/10.1016/j.ijmes.2013.06.005.

An Active Magnetic Bearing for Thin-Walled Rotors: Vibrational Dynamics and Stabilizing Control

Matthew O. T. Cole and Wichaphon Fakkaew

***Abstract*—This paper describes a novel active magnetic bearing with distributed actuation, designed for contact-free support of a thin-walled rotor. A full-dynamic analysis, control formulation, and experimental evaluation are presented. Important aspects of the bearing operation include the vibration excitation of the rotor wall due to asymmetries in manufacture and assembly, and the limits of stable operation with respect to static loading of the bearing. For the proposed design, the vibratory dynamics for flexure of the rotor wall are accounted for explicitly in the actuator coil-winding and driving scheme so that the coupling of the levitation control with the wall dynamics is minimized. This enables the selection of control feedback laws based on rigid-body dynamic considerations alone. Dynamic performance is investigated by theoretical and experimental study involving a prototype rotor-bearing system. The operating principles are validated and the dynamic behavior is shown to align well with the theoretical predictions.**

***Index Terms*—Active magnetic bearing (AMB), hollow rotor, rotordynamics, thin-walled structure, vibration control.**

I. Introduction

IN ROTATING machine design, achieving a high stiffness-to-mass ratio for rotating parts is often a key requirement for extending envelops of operation and performance. This has led to the introduction of hollow shaft rotor designs for several machine types, including turbomachines [1]–[3]. Modern additive manufacturing methods such as metal deposition and optimized composite shell fabrication will further support the creation of more complex thin-walled rotor structures [4], [5].

For all rotating machinery, vibration phenomena arise from the interaction of rotating parts with fixed bearing components. Classical rotordynamic considerations deal primarily with the lateral vibration of rotors due to asymmetries arising in manufacture and installation, such as rotor unbalance or component misalignments [6], [7]. A key issue is that the natural modes of vibration for the rotor-bearing structure give rise to critical speeds at which resonance occurs during operation. Damping of rotor flexible modes to allow supercritical operation can be achieved with passive components, such as magnetic or squeeze-film dampers [8], [9], or by active techniques, e.g., with actuated bearings [10], [11]. For systems with active magnetic bearings (AMBs), optimized feedback controller designs can be usefully applied [12]–[15]. Active control methods that involve direct vibration cancellation are also possible, e.g., those based on adaptive cancellation [16]–[18], notch-filtering of feedback signals [19], or repetitive control methods [20].

For hollow rotors, the natural frequencies for vibration due to lateral bending will become much higher than the rotational frequency range if the wall-thickness-to-radius ratio is sufficiently small. However, excitation of vibration within the wall of the rotor then becomes a new concern. Further issues may relate to stress-concentration that occurs where the rotor wall connects with supporting bearing components. One possible approach to overcome these issues is through the use of distributed AMB elements that can support a rotating component by applying forces over a larger surface area than is possible with mechanical bearings. The potential to apply control forces to actively suppress vibration within the wall structure of the rotor is also significant.

This paper introduces a new design topology and control approach for the integration of a distributed AMB with a thin-walled rotor. Although AMB designs for hollow cylinders and ring-like rotors had been previously reported, the rotor walls were sufficiently thick that their distortion could be neglected, and so control considerations focused on rigid-body dynamics [21] or vibration due to lateral bending [22]. In this paper, a hollow rotor is considered for which the walls are so thin that their flexibility cannot be neglected in the actuation and control strategy. Although the results here involve analysis and experimentation on a short cylindrical rotor, an applicability to more complex rotor structures is foreseen and may be evaluated fully in subsequent work.

II. Conceptual Approach

A concept for active bearing interfacing with a thin-walled rotor structure is exemplified by the circular array of

Manuscript received July 31, 2017; revised January 20, 2018; accepted October 18, 2018. Date of publication October 24, 2018; date of current version December 13, 2018. Recommended by Technical Editor J.-Y. (James) Chang. The work was supported in part by the Thailand Research Fund and in part by Chiang Mai University under Grant BRG5980013. *(Corresponding author: Matthew Cole.)*

M. O. T. Cole is with the Department of Mechanical Engineering, Faculty of Engineering, Chiang Mai University, Chiang Mai 50200, Thailand (e-mail: motcole@hotmail.com).

W. Fakkaew is with the School of Engineering, University of Phayao, Phayao 56000, Thailand (e-mail: wichaphon_me@hotmail.com).

Color versions of one or more of the figures in this paper are available online at http://ieeexplore.ieee.org.

Digital Object Identifier 10.1109/TMECH.2018.2877777

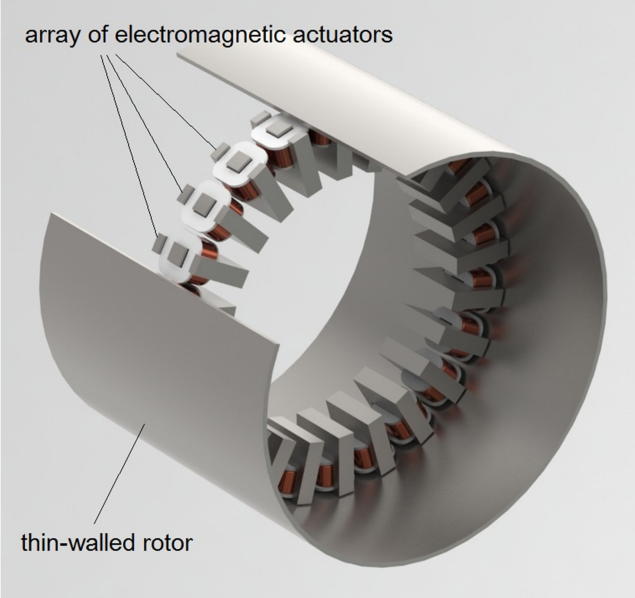

Fig. 1. Multiactuator radial AMB concept for interfacing with a thin-walled cylindrical rotor (cutaway).

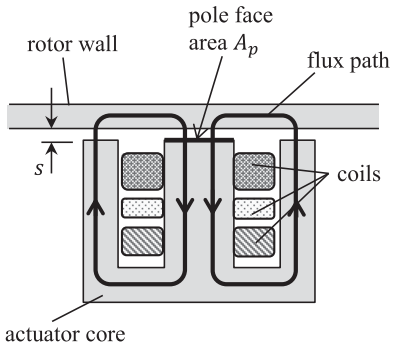

Fig. 2. Compact E-core actuator geometry.

electromagnetic actuators shown in Fig. 1. This topology would be appropriate for an internal radial bearing applied to a hollow rotor/shaft system. Similar concepts for internal/external radial, thrust, and combination bearings can also be envisaged. For reasons that will become clear, the jth actuator has a number of independently powered coils (indexed by k) with the number of turns N_{kj} and regulated current $i_{kj}(t)$. Neglecting the eddy current (EC) and saturation effects, the magnetic field strength B_j within the actuator core is given by (see [23])

$$B_j = \frac{\mu_0}{l_{\text{iron}}/\mu_r + 2s_j} \sum_k N_{kj} i_{kj} \tag{1}$$

where l_{iron} is the mean flux path length through the actuator core and rotor wall, s_j is the size of the air gap between the rotor and actuator, μ_0 is the permeability of free space, and μ_r is the relative permeability of the core material. The geometry of an archetypal E-shaped actuator is shown in Fig. 2. With a further assumption of uniform magnetic field, the attractive force between the actuator and rotor is

$$F_j = \frac{A_p}{\mu_0} B_j^2 \tag{2}$$

where A_p is the pole-face area.

A main difference between the proposed topology and that of a standard AMB is the number and size of the electromagnets. The potential utility of any AMB is dependent on the load capacity for a given axial length of bearing. The specific load capacity (force per unit area) is fundamentally limited only by magnetic flux saturation, which is material-dependent. Therefore, downsizing of the actuator to match the wall thickness should have little effect on the overall capacity if the total pole-face area is preserved. Rather, the main issue that arises is that the same current-turns must be realized with a smaller coil volume, and this introduces more localized heat generation and stringent cooling requirements. For the tested realization of the concept introduced in this paper, the actuators were operated sufficiently below the maximum capacity so that heat generation could be managed by passive cooling.

The state of the art for AMB control is to use dc servo amplifiers to achieve a controlled variation of the coil currents around a mean "bias" value [7]. Although this causes the uncontrolled bearing to have unstable negative stiffness properties, it allows the design of feedback control algorithms based on linearized models. To make effective use of a large array of actuators, the current in every coil should be varied according to real-time measurements of rotor motion. It is beneficial, for reasons of cost, reliability, weight, and size, if this can be achieved with the minimum possible number of drives and sensors.

For industrial applications, it is also desirable that feedback control strategies can be designed using simple models or test procedures, at least to achieve initial levitation and stable operation of a rotor. It is with this motivation that an actuation strategy is proposed (in Section IV) for flexural mode decoupling such that the consideration of rigid-body dynamics and proportional-derivative (PD) gain tuning is sufficient to achieve stable operation with acceptable vibration behavior during rotation. The expectation is that more sophisticated model-based feedback control or vibration suppression algorithms may then be designed and implemented as add-on controllers to improve the overall performance with regard to flexible-mode damping and vibration suppression. However, such extensions are outside the scope of this paper.

III. Dynamic Behavior of a Thin-Walled Rotor

A. Wall Vibration

To understand the interaction of rotor wall vibration with AMB operation, a mathematical model is first developed based on the established shell theory for vibration of thin-walled cylinders [24], but with modifications that take into account rotational effects [6], [25]. According to Fig. 3, a reference frame (X', Y', Z) rotates with the rotor at a constant angular speed Ω about the fixed axis OZ, which is the axis of symmetry for the undeformed rotor. The deformation of the cylinder walls in the radial x-direction is given by $u(t, \theta)$ and the deformation

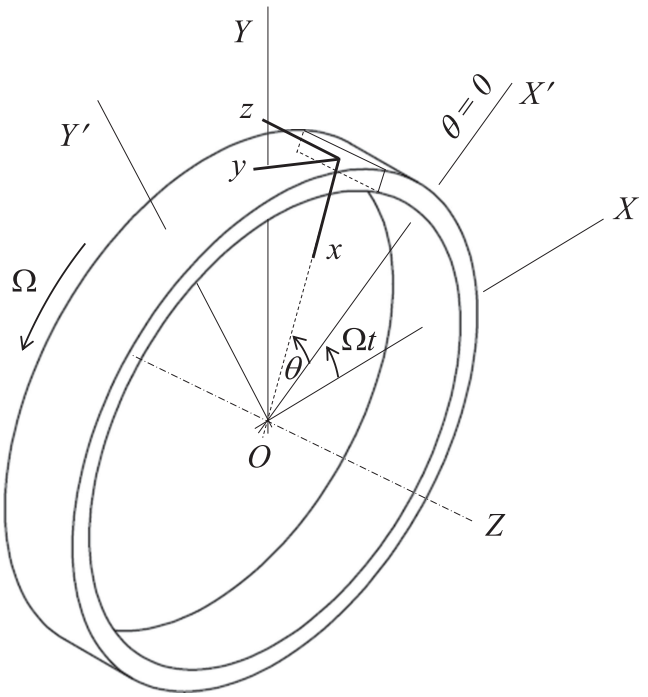

Fig. 3. Local (x, y, z) and fixed global (X, Y, Z) coordinate systems for describing the vibration of a hollow cylindrical rotor.

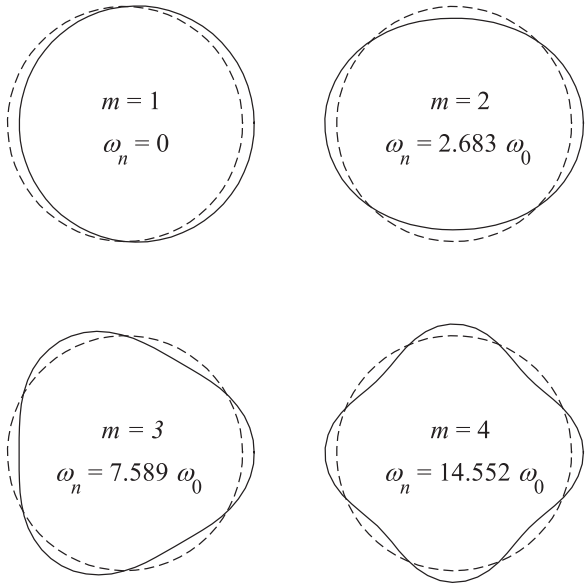

Fig. 4. Mode shapes for vibration of the walls of a hollow rotor. Natural frequencies are shown for a nonrotating case.

in the tangential y-direction is given by $v(t, \theta)$, where θ is the angular position defined relative to the reference line OX', fixed in the rotating frame. The equations of motion for a differential element with cross-sectional area A and length $rd\theta$ may be expressed in terms of the internal forces f_x and f_y in the normal and radial (shear) directions, respectively, and the moment about the z-axis m_z [6] as

$$\frac{\partial f_x}{\partial \theta} + r f_y \kappa_z + r L_x = r\rho A \left[\ddot{u} + 2\Omega\dot{v} + \Omega^2(r-u)\right] \quad (3)$$

$$\frac{\partial f_y}{\partial \theta} - r f_x \kappa_z = r\rho A \left[\ddot{v} - 2\Omega\dot{u} + \Omega^2 \frac{\partial u}{\partial \theta}\right] \quad (4)$$

$$\frac{\partial m_z}{\partial \theta} + r f_x = 0. \quad (5)$$

Here, κ_z is the curvature of the neutral plane about the axis of rotation. The variable $L_x(\theta)$ is an applied force distribution (per unit length) in the radial direction. The moment–strain relation for bending is

$$m_z = EI_z(\kappa_z - 1/r) + \tau EI_z \frac{d\kappa_z}{dt} \quad (6)$$

where E is Young's modulus, I_z is the second moment of area, and $\tau = \frac{\eta}{E}$ is the material relaxation time, as appropriate for a Kelvin–Voigt material model. The curvature may be expressed as

$$\kappa_z = \frac{1}{r^2}\left(r + v^{(1)} + u^{(2)}\right) \quad (7)$$

where, for brevity, the notation $u^{(n)} = \partial^n u/\partial\theta^n$ is adopted. A mean normal force may be associated with the constant (centripetal acceleration) term on the right-hand side of (3) and is given by $f_{y0} = \rho A\Omega^2 r^2$. Substituting (6) and (7) into (3)–(5) and retaining only first-order terms gives

$$\frac{\partial f_x}{\partial \theta} + \frac{f_{y0}}{r}(v^{(1)} + u^{(2)}) + \tilde{f}_y + rL_x = r\rho A[\ddot{u} + 2\Omega\dot{v} + \Omega^2(r-u)] \quad (8)$$

$$\frac{\partial \tilde{f}_y}{\partial \theta} - f_x = r\rho A[\ddot{v} - 2\Omega\dot{u} + \Omega^2 u^{(1)}] \quad (9)$$

$$\frac{EI_z}{r^2}(v^{(2)} + u^{(3)}) + \frac{\tau EI_z}{r^2}(v^{(2)} + u^{(3)}) + r f_x = 0 \quad (10)$$

where $\tilde{f}_y = f_y - f_{y0}$. Eliminating f_x and $\tilde{f}_y$ from (8)–(10) gives

$$\omega_0^2\left[v^{(6)} + 2v^{(4)} + v^{(2)} + \tau\frac{d}{dt}(v^{(6)} + 2v^{(4)} + v^{(2)})\right] + \frac{d^2}{dt^2}\left(v^{(2)} - v\right) + 4\Omega\frac{d}{dt}(v^{(1)}) - \Omega^2\left(v^{(4)} + 3v^{(2)}\right) = \frac{1}{\rho A}\frac{\partial L_x}{\partial \theta} \quad (11)$$

where $\omega_0 = \sqrt{EI_z/\rho r^4 A}$, and the assumption of circumferential inextensibility $u = \partial v/\partial\theta$ has been applied [24].

Solutions to (11) can be obtained in the form of $u_m(t, \theta) = P_m(t)\sin m\theta + Q_m(t)\cos m\theta$, where m is the nodal index and corresponds to the (integer) number of wavelengths that fit within the rotor circumference. The corresponding mode shapes for the first four modes are shown in Fig. 4. Substituting this solution into (11) and exploiting the orthogonality properties of

$\cos m\theta$ and $\sin m\theta$ leads to

$$\begin{aligned}&(m^2+1)\ddot{P}_m + 4\Omega m\dot{Q}_m + \tau\omega_0^2 m^2(m^2-1)^2\dot{P}_m \\ &+ \left[\Omega^2 m^2(m^2-3) + \omega_0^2 m^2(m^2-1)^2\right]P_m \\ &= \frac{m^2\sin m\theta_F}{\pi\rho r A}F \qquad (12)\\ &(m^2+1)\ddot{Q}_m - 4\Omega m\dot{P}_m + \tau\omega_0^2 m^2(m^2-1)^2\dot{Q}_m \\ &+ \left[\Omega^2 m^2(m^2-3) + \omega_0^2 m^2(m^2-1)^2\right]Q_m \\ &= \frac{m^2\cos m\theta_F}{\pi\rho r A}F. \qquad (13)\end{aligned}$$

Here, a force F from a single bearing actuator has been accounted for by assuming the force is applied in the radial x-direction at position $\theta = \theta_F$ so that $L_x = \delta(\theta - \theta_F)F/r$. Equations (12) and (13) can be expressed in the first-order matrix form as

$$\dot{X}_m = A_m^R X_m + B_m(\theta_F)F, \quad m = 1, \ldots, \infty \qquad (14)$$

where $X_m = [P_m \; Q_m \; \dot{P}_m \; \dot{Q}_m]^T$ and

$$A_m^R = \begin{bmatrix} 0 & 0 & 1 & 0 \\ 0 & 0 & 0 & 1 \\ -k_m - \Omega^2 d_m & 0 & -\tau k_m & -\Omega g_m \\ 0 & -k_m - \Omega^2 d_m & \Omega g_m & -\tau k_m \end{bmatrix}$$

$$B_m(\theta) = b_m \begin{bmatrix} 0 & 0 & \sin m\theta & \cos m\theta \end{bmatrix}^T$$

with

$$d_m = \frac{m^2(m^2-3)}{m^2+1}, \quad k_m = \omega_0^2\frac{m^2(m^2-1)^2}{m^2+1}$$

$$g_m = \frac{4m}{m^2+1}, \quad b_m = \frac{m^2}{\pi\rho r A(m^2+1)}.$$

The solution for wall vibration is given by

$$u(t,\theta) = \sum_{m=1}^{\infty} u_m(t,\theta) = \sum_{m=1}^{\infty} P_m(t)\sin m\theta + Q_m(t)\cos m\theta \qquad (15)$$

where $P_m(t)$ and $Q_m(t)$ satisfy (14).

B. Fixed-Frame Dynamics

A transformation to stationary-frame coordinates may be undertaken by defining the fixed-frame angular position as $\phi = \theta + \Omega t$. Then, the radial displacement is $u_m(t,\phi) = P_m(t)\sin m(\phi - \Omega t) + Q_m(t)\cos m(\phi - \Omega t) = p_m(t)\sin m\Omega t + q_m(t)\cos m\Omega t$, where p_m and q_m are fixed-frame modal displacement variables. This transformation involves a rotation matrix

$$\begin{bmatrix} P_m \\ Q_m \end{bmatrix} = \begin{bmatrix} \cos m\Omega t & -\sin m\Omega t \\ \sin m\Omega t & \cos m\Omega t \end{bmatrix}\begin{bmatrix} p_m \\ q_m \end{bmatrix}.$$

By substituting this expression into (14) and assuming the force F is applied at a fixed angular position ϕ_F in the stationary frame, so that $\theta_F = \phi_F - \Omega t$, we can finally derive the fixed-frame state-space equations describing the vibratory dynamics of the free rotor as

$$\begin{bmatrix} \dot{x}_m \\ \ddot{x}_m \end{bmatrix} = \begin{bmatrix} 0_{2\times 2} & I_{2\times 2} \\ \Delta_m(\Omega) & \Sigma_m(\Omega) \end{bmatrix}\begin{bmatrix} x_m \\ \dot{x}_m \end{bmatrix} + B_m(\phi_F)F$$

$$m = 1, \ldots, \infty \qquad (16)$$

where $x_m = [p_m \; q_m]^T$ and

$$\Delta_m(\Omega) = \begin{bmatrix} -k_m & m\Omega\tau k_m \\ -m\Omega\tau k_m & -k_m \end{bmatrix}$$

$$\Sigma_m(\Omega) = \begin{bmatrix} -\tau k_m & -\Omega g_m + 2m\Omega \\ \Omega g_m - 2m\Omega & -\tau k_m \end{bmatrix}.$$

The deflection of the rotor wall at angular position ϕ is

$$u(t,\phi) = \sum_{m=1}^{\infty} p_m(t)\sin m\phi + q_m(t)\cos m\phi. \qquad (17)$$

The natural frequencies for free vibration, and the variation in their values with rotational speed, are important for the rotordynamic behavior. These may be determined from the eigenmodes of (14) and (16) for observation in the rotating frame and fixed frame, respectively. For each integer value of the nodal index m, there are two natural modes. For a nonzero rotational speed, their natural frequencies are distinct due to the Coriolis terms $\pm\Omega g_m$ in (14). For flexural vibration ($m > 1$), the lower frequency mode corresponds to a forward-traveling wave, while the higher frequency mode is a backward-traveling wave. The $m = 1$ mode involves rigid-body translation, and both natural frequencies are equal to the rotational frequency (for rotating-frame observation). Campbell diagrams for the free rotor are shown in Fig. 5.

To assess the potential for the excitation of these modes, the natural frequencies should also be evaluated in the fixed frame [see Fig. 5(b)]. It may be observed from the eigenvectors of A_m^F that, for each value of the nodal index $m > 1$, the natural frequency for the forward-traveling wave (which is now the higher value) increases monotonically with increasing rotational speed. For the backward-traveling waves, the observed frequency decreases with increasing speed, converging toward zero. The potential for resonance may be anticipated due to excitation sources having frequencies that are harmonics of the rotational frequency, as also shown in Fig. 5(b). The presence of higher harmonics could lead to many resonance conditions during spin-up/spin-down, as indicated by the crossing points in Fig. 5(b). These would arise due to unwanted asymmetries associated with the rotor geometry (noncircularity) or material properties. These characteristics are examined more closely for the experimental rotor-bearing system under closed loop control in Section V.

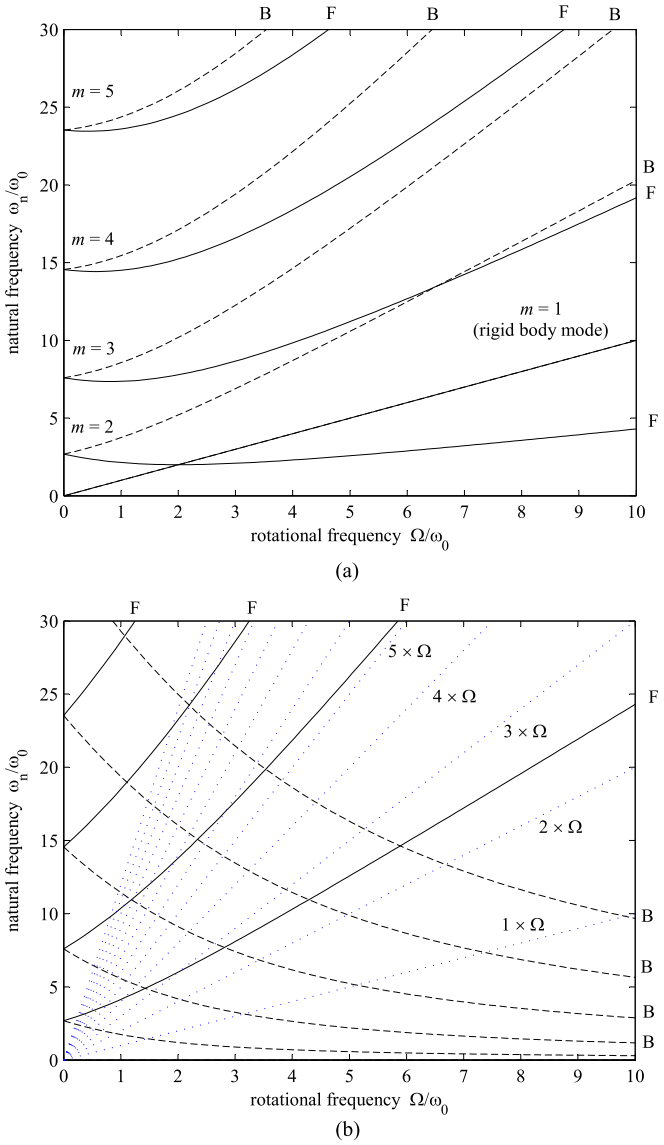

Fig. 5. Campbell diagram for a thin-walled rotor showing variation in natural frequencies for wall vibration with rotational speed as observed in a (a) rotating frame and a (b) fixed frame. Each natural frequency relates to either a forward (F) or backward (B) traveling wave.

IV. System Modeling for Control Analysis

A. Actuated Rotor

A state-space model of the rotor-bearing system, accounting for an array of J actuators, is obtained from (16) as

$$\begin{bmatrix} \dot{x}_m \\ \ddot{x}_m \end{bmatrix} = \begin{bmatrix} 0_{2\times 2} & I_{2\times 2} \\ \Delta_m(\Omega) & \Sigma_m(\Omega) \end{bmatrix} \begin{bmatrix} x_m \\ \dot{x}_m \end{bmatrix} + \sum_{j=1}^{J} B_m(\phi_j^a) F_j \tag{18}$$

where the jth actuator is located at angular position $\phi = \phi_j^a$. The radial displacement at the jth actuator location is

$$u_j(t) = \sum_{m=1}^{\infty} p_m(t) \sin m\phi_j^a + q_m(t) \cos m\phi_j^a . \tag{19}$$

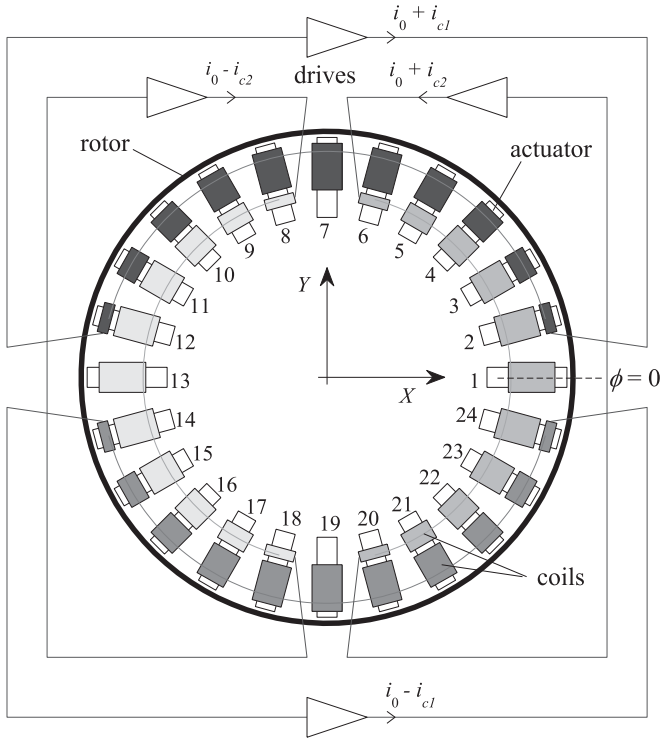

Fig. 6. Coil winding and driving scheme for levitation control.

The radial displacement at sensor location ϕ_i^s is

$$y_i(t) = \sum_{m=1}^{\infty} p_m(t) \sin m\phi_i^s + q_m(t) \cos m\phi_i^s . \tag{20}$$

If each actuator has two coils, then, according to the model (1)–(2), the actuator force is

$$F_j = \frac{\mu_0 A_p (N_{1j} i_{1j} + N_{2j} i_{2j})^2}{(l_0 - 2u_j)^2} \tag{21}$$

where $l_0 = l_{\text{iron}}/\mu_r + 2s_0$ for equal gaps ($s_j = s_0$). A coil-driving scheme with four drives, each used to power a series connection of a subset of coils with a varying number of turns, may be considered as shown in Fig. 6. Suppose the currents produced by the four drives are specified by a differential scheme using a fixed bias current i_0 and two control currents i_{c1} and i_{c2} so that $i_1(t) = i_0 \pm i_{c1}(t)$ and $i_2(t) = i_0 \pm i_{c2}(t)$ (with the sign dependent on the drive connected to the coil). Defining coil-turn parameters η_{1j} and η_{2j}, which may take positive or negative values depending on the drive connected, but also satisfy $|\eta_{1j}| = N_{1j}$, $|\eta_{2j}| = N_{2j}$, the actuation force may be expressed as

$$F_j = \frac{\mu_0 A_p (|\eta_{1j}| i_0 + \eta_{1j} i_{c1} + |\eta_{2j}| i_0 + \eta_{2j} i_{c2})^2}{(l_0 - 2u_j)^2} . \tag{22}$$

Linearizing about a given operating point, denoted E, gives

$$F_j \approx F_{0j} + a_{1j} i_{c1} + a_{2j} i_{c2} + h_j u_j \tag{23}$$

where

$$a_{1j} = \eta_{1j}(|\eta_{1j}|i_0 + \eta_{1j}i_{c1} + |\eta_{2j}|i_0 + \eta_{2j}i_{c2})\frac{2\mu_0 A_p}{(l_0 - 2u_j)^2}\Big|_E$$

$$a_{2j} = \eta_{2j}(|\eta_{2j}|i_0 + \eta_{1j}i_{c1} + |\eta_{2j}|i_0 + \eta_{2j}i_{c2})\frac{2\mu_0 A_p}{(l_0 - 2u_j)^2}\Big|_E$$

$$h_j = (|\eta_{1j}|i_0 + \eta_{1j}i_{c1} + |\eta_{2j}|i_0 + \eta_{2j}i_{c2})^2\frac{4\mu_0 A_p}{(l_0 - 2u_j)^3}\Big|_E.$$

The parameters a_{1j}, a_{2j} are force/current gains for the actuator, while h_j is the force/displacement gain and acts as a destabilizing negative stiffness. The constant force components F_{0j} may cause some small distortion of the rotor, but can be neglected for dynamic analysis. Defining the block diagonal matrices $\Delta = \text{diag}(\Delta_1, \Delta_2, \ldots, \Delta_M)$, $\Sigma = \text{diag}(\Sigma_1, \Sigma_2, \ldots, \Sigma_M)$, the linearized state-space equation for the open-loop dynamics, retaining M modes, is obtained from (18) and (23) as

$$\begin{bmatrix}\dot{x}\\ \ddot{x}\end{bmatrix} = \begin{bmatrix}0 & I\\ \Delta + \Delta^{\text{neg}} & \Sigma\end{bmatrix}\begin{bmatrix}x\\ \dot{x}\end{bmatrix} + \begin{bmatrix}0\\ B\Psi A\end{bmatrix}\begin{bmatrix}i_{c1}\\ i_{c2}\end{bmatrix} \tag{24}$$

where $\Delta^{\text{neg}} = B\Psi H\Psi^T$ and

$$B = \text{diag}(b_1, b_1, b_2, b_2, \ldots, b_M, b_M)$$

$$H = \text{diag}(h_1, h_2, \ldots, h_J)$$

$$\Psi = \begin{bmatrix}\sin\phi_1^a & \sin\phi_2^a & \cdots & \sin\phi_J^a\\ \cos\phi_1^a & \cos\phi_2^a & \cdots & \cos\phi_J^a\\ \sin 2\phi_1^a & \sin 2\phi_2^a & \cdots & \sin 2\phi_J^a\\ \cos 2\phi_1^a & \cos 2\phi_2^a & \cdots & \cos 2\phi_J^a\\ \vdots & \vdots & & \vdots\\ \sin M\phi_1^a & \sin M\phi_2^a & \cdots & \sin M\phi_J^a\\ \cos M\phi_1^a & \cos M\phi_2^a & \cdots & \cos M\phi_J^a\end{bmatrix}$$

$$A = \begin{bmatrix}a_{11} & a_{21}\\ a_{12} & a_{22}\\ \vdots & \vdots\\ a_{1J} & a_{2J}\end{bmatrix}.$$

B. Coil-Winding Scheme

The aim now is to determine a coil configuration that will admit stabilizing control at a nominal operating point using the feedback of measured rotor radial positions at discrete locations only. Standard noncontact displacement sensors may then be used, though preferably as few as is possible. A key issue is that, under these assumptions, there will always be actuators that are not collocated with sensors and so it can be anticipated that the stability of higher order modes will need to be considered when synthesizing an actuation/control scheme. The approach taken here is to adopt a winding scheme that (for a given operating point) decouples the net actuation forces from the flexural modes of the rotor wall ($m > 1$). Such a decoupling requires that all but the first two rows of the matrix $B\Psi A$ appearing in (24) are zero. This requires

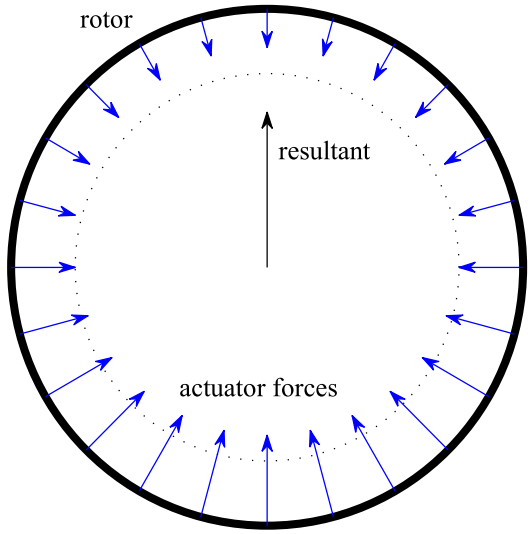

Fig. 7. Actuator force distribution for rotor flexural-mode decoupling.

$$\begin{matrix}\sum_{j=1}^{J}\sin m\phi_j^a\, a_{qj} = 0\\ \sum_{j=1}^{J}\cos m\phi_j^a\, a_{qj} = 0\end{matrix}, \quad m = 2, 3, \ldots, \infty,\ q = 1, 2. \tag{25}$$

Suppose the actuators are evenly spaced. These equations then hold if a_{qj} take values given by

$$a_{1j} = \alpha\sin\phi_j^a,\ a_{2j} = \alpha\cos\phi_j^a \tag{26}$$

for some constant α. The orthogonal rigid-body displacements p_1 and q_1 will then couple independently with i_{c1} and i_{c2}, respectively. In this case, the applied distribution of actuation forces will have the form shown in Fig. 7 and can exactly oppose a rigid-body acceleration without exciting flexural modes or causing distortion of the rotor cross section. Moreover, a feedback controller design can be undertaken by considering requirements for stable levitation of a rigid rotor, i.e., by considering only the rigid-body modes, without any concern for destabilization of the flexural modes.

To achieve modal decoupling for a disturbance-free operating point $i_{c1} = i_{c2} = u_j = 0$ requires

$$a_{1j} = \eta_{1j}(|\eta_{1j}| + |\eta_{2j}|)\frac{2i_0\mu_0 A_p}{l_0^2} = \alpha\sin\phi_j^a \tag{27}$$

$$a_{2j} = \eta_{2j}(|\eta_{1j}| + |\eta_{2j}|)\frac{2i_0\mu_0 A_p}{l_0^2} = \alpha\cos\phi_j^a \tag{28}$$

$$h_j = (|\eta_{1j}| + |\eta_{2j}|)^2\frac{4i_0^2\mu_0 A_p}{l_0^3} = \text{constant}. \tag{29}$$

Equation (29) ensures that $\Psi H\Psi^T$ is a diagonal matrix and so the negative stiffness effects do not introduce cross-coupling of the rigid-body and flexural modes. To achieve all three constraints (27)–(29), some extra design parameter (in addition to the number of turns of coil) needs to be adjusted for each actuator (such as the nominal air gap or pole-face area). This will add considerable complexity to the manufacture and assembly

of the system, and so, for the bearing realization in this paper, the design is based on satisfying only the first two constraints (27) and (28). The solution for the number of coil turns is then

$$\eta_{1j} = \frac{N_0 \sin\phi_j^a}{\sqrt{|\sin\phi_j^a| + |\cos\phi_j^a|}}, \; \eta_{2j} = \frac{N_0 \cos\phi_j^a}{\sqrt{|\sin\phi_j^a| + |\cos\phi_j^a|}} \tag{30}$$

where N_0 is the maximum number of turns, and some rounding will be necessary to get integer numbers. By substituting (30) into (27)–(29), it can be seen that $\alpha = 2N_0^2 i_0 \mu_0 A_p / l_0^2$, and the resulting negative stiffness for each actuator is given by

$$h_j = (|\sin\phi_j^a| + |\cos\phi_j^a|)\frac{4N_0^2 i_0^2 \mu_0 A_p}{l_0^3}. \tag{31}$$

C. Closed-Loop Dynamics

A general PD-type feedback law using measured displacements and their derivatives has the form

$$\begin{bmatrix} i_{c1} \; i_{c2} \end{bmatrix}^T = -K_p y - K_d \dot{y} \tag{32}$$

where K_p and K_d are matrices with dimensions $2 \times N_s$, where N_s is the number of sensors. According to (20), the displacements may be expressed as

$$y = \Psi_s^T x \tag{33}$$

where

$$\Psi_s = \begin{bmatrix} \sin\phi_1^s & \sin\phi_2^s & \dots & \sin\phi_{N_s}^s \\ \cos\phi_1^s & \cos\phi_2^s & \dots & \cos\phi_{N_s}^s, \\ \sin 2\phi_1^s & \sin 2\phi_2^s & \dots & \sin 2\phi_{N_s}^s \\ \cos 2\phi_1^s & \cos 2\phi_2^s & \dots & \cos 2\phi_{N_s}^s, \\ \vdots & \vdots & & \vdots \\ \sin M\phi_1^s & \sin M\phi_2^s & \dots & \sin M\phi_{N_s}^s \\ \cos M\phi_1^s & \cos M\phi_2^s & \dots & \cos M\phi_{N_s}^s \end{bmatrix}.$$

The linearized closed-loop dynamics are then given by

$$\begin{bmatrix} \dot{x} \\ \ddot{x} \end{bmatrix} = \begin{bmatrix} 0 & I \\ \Delta + \Delta^{\text{neg}} + \Delta_p & \Sigma + \Sigma_d \end{bmatrix} \begin{bmatrix} x \\ \dot{x} \end{bmatrix} \tag{34}$$

where $\Delta_p = -B\Psi A K_p \Psi_s^T$ and $\Sigma_d = -B\Psi A K_d \Psi_s^T$ are matrices of size $2M \times 2M$ for which only the first two rows are nonzero (based on the decoupling condition previously defined).

Isolating the state equations for the rigid-body dynamics ($m = 1$), we have

$$\begin{bmatrix} \dot{x}_1 \\ \ddot{x}_1 \end{bmatrix} = \begin{bmatrix} 0 & I \\ \Delta_1^{\text{neg}} - EK_p\Psi_{s1}^T & -EK_d\Psi_{s1}^T \end{bmatrix} \begin{bmatrix} x_1 \\ \dot{x}_1 \end{bmatrix} \tag{35}$$

where Ψ_{s1} is the first two rows of Ψ_s and

$$\Delta_1^{\text{neg}} = b_1 h_1 \begin{bmatrix} \sum_j \sin^2\phi_j^a & 0 \\ 0 & \sum_j \cos^2\phi_j^a \end{bmatrix}$$

$$E = b_1 \alpha \begin{bmatrix} \sum_j \sin^2\phi_j^a & 0 \\ 0 & \sum_j \cos^2\phi_j^a \end{bmatrix}.$$

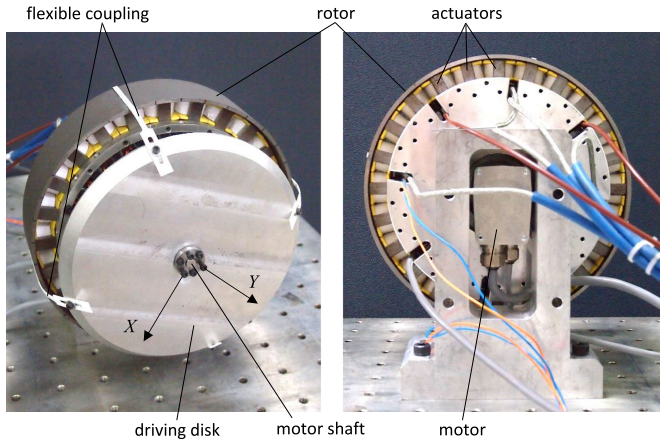

Fig. 8. Experimental system: AMB with distributed actuation applied to a thin-walled cylindrical rotor.

According to (35), a stabilizing controller may be obtained by selecting K_p and K_d such that $EK_p\Psi_{s1}^T$ and $EK_d\Psi_{s1}^T$ are symmetric matrices satisfying

$$EK_p\Psi_{s1}^T - \Delta_1^{\text{neg}} > 0, \quad EK_d\Psi_{s1}^T > 0. \tag{36}$$

Given that the number of sensors may be two or more, a control law that gives equal weighting to each sensor signal may be defined as

$$K_p = k_p(\Psi_{s1}\Psi_{s1}^T)^{-1}\Psi_{s1}, K_d = k_d(\Psi_{s1}\Psi_{s1}^T)^{-1}\Psi_{s1} \tag{37}$$

where k_p and k_d are positive scalars. From (35), the rigid-body natural frequencies and damping ratios can be determined as

$$\omega_{nx} = \sqrt{b_1(\alpha k_p - h_1)\sum_j \cos^2\phi_j^a} \tag{38}$$

$$\omega_{ny} = \sqrt{b_1(\alpha k_p - h_1)\sum_j \sin^2\phi_j^a} \tag{39}$$

$$\zeta_x = \frac{b_1\alpha k_d}{2\omega_{nx}}\sum_j \cos^2\phi_j^a, \; \zeta_y = \frac{b_1\alpha k_d}{2\omega_{ny}}\sum_j \sin^2\phi_j^a. \tag{40}$$

An issue that must still be considered is that transmission of radial load through the bearing, typically due to the rotor weight or other quasi-static loading, will produce a change in operating point so that the decoupling condition (25) is no longer exactly satisfied. This will introduce additional nonzero entries in the matrix ΨA and, hence, a coupling of the flexible-mode dynamics with the levitation control will arise. To quantify these effects and determine their impact on stability, a numerical study is undertaken in Section V.

V. Evaluation

A. System Description

To evaluate the proposed AMB concept, the experimental prototype shown in Fig. 8 was created. The system comprises a short (51-mm-length) rotor with diameter 222 mm. The ratio of wall thickness to radius is $d/r = 0.0279$. The rotor is made from martensitic stainless steel (grade 420J2) with inner and

TABLE I
ROTOR PROPERTIES

parameter	symbol	value	units
rotor radius	r	111.0	mm
wall thickness	d	3.1	mm
material density	ρ	7740	$\mathrm{kg/m^3}$
Young's modulus	E	2×10^{11}	$\mathrm{N/m^2}$
axial length		51	mm

TABLE II
ACTUATOR COIL-WINDING SCHEME

actuator	1	2	3	4	5	6	7	8	9	10	11	12
N_1	0	16	30	42	52	61	70	61	52	42	30	16
N_2	70	61	52	42	30	16	0	16	30	42	52	61

actuator	13	14	15	16	17	18	19	20	21	22	23	24
N_1	0	16	30	42	52	61	70	61	52	42	30	16
N_2	70	61	52	42	30	16	0	16	30	42	52	61

TABLE III
ACTUATOR PROPERTIES

parameter	symbol	value	units
number of actuators	J	24	
pole face area	A_p	100	$\mathrm{mm^2}$
core flux path length	l_{iron}	100	mm
mean gap size	s_0	0.8	mm
core relative permeability	μ_r	300	
maximum number of turns	N_0	70	
bias current	i_0	2.2	A

outer surfaces finished by electric discharge machining. Full properties are given in Table I. The internal bearing comprises a circular array of 24 actuators with E-shaped cores, having coils wound on the central claws. Key parameters for the actuator design are listed in Table III. To reduce losses from EC and help maintain the actuator bandwidth, the actuator cores have been machined from soft magnetic powder-sintered steel (Somaloy Prototyping Material). The actuator coils are connected in series as four sets and driven by four dc servo drives, as shown in Fig. 6. The coil-winding pattern is given by (30) with $N_0 = 70$, as detailed in Table II.

The rotor is connected axially by four thin flexures to a disk driven by a brushless dc motor. This rotor–disk coupling was designed to constrain the axial and tilting motion of the rotor and transmit a driving/braking torque, but without significantly affecting the radial dynamics of the rotor and wall, as described by the theoretical model introduced in Section III. Hence, stable levitation of the rotor can be achieved only by energizing the actuators based on the feedback of rotor radial position, which is measured by noncontact inductance probes located internally. The radial stiffness of the coupling, which is approximately 500 N/m, makes a very small contribution to the overall radial stiffness of the bearing under feedback control. Small rollers may be fitted to the bearing hub to act as touch-down bearings and help avoid rotor–stator contact. These were not installed for the photograph in Fig. 8, but were deemed necessary for high-speed operation in the case of faults, failures, or dynamic instability. The maximum operating speed is approximately 40 Hz due to power limitations of the driving motor.

The feedback control algorithm (32) was implemented digitally with PC-based hardware and with real-time code generation using the MATLAB xPC Target software. The sampling frequency was set to 4000 Hz. The rotor velocity variables $\dot{y}$ were calculated from the position signals based on a first-order difference equation with a break frequency of 1000 rad/s.

B. Numerical Analyses

Vibration and stability properties may be predicted using the reduced-order closed-loop model with PD feedback control, as defined by (34) and (37). A PD control law is introduced with $k_p = 5700$ A/m and $k_d = 10$ As/m, which, according to the theoretical model, results in a damped natural frequency of 25 Hz for rigid-body motion with damping at 32% of critical. The resulting net stiffness of the bearing is approximately 20 000 N/m. Low-gain integral feedback may also be usefully applied to eliminate static positioning errors, but the effect on vibrational stability will be small. The effect of various perturbations can be investigated by modifying the operating point for linearization. This leads to a new system matrix in (34), the eigenvalues of which can be checked for stability. Although stable operation is predicted for an operating point involving zero load and uniform rotor–stator gaps, perturbation away from this operating point introduces dynamic coupling of the levitation control with the flexural dynamics. This impacts on the damping and stability of flexible modes. The level of coupling, and whether it is destabilizing, depends on the number and location of the sensors.

Fig. 9 shows stability boundaries in terms of static bearing load for two different sensor configurations. Any sensor configuration will provide stable operation for the zero-load operating point. It is seen that the two-sensor configuration [see Fig. 9(a)] has an asymmetric stability zone, which necessitates that any loading must be suitably oriented with the sensor axes. Using the four-sensor configuration shown in Fig. 9(b) gives a more symmetric stability region. For both these cases, it is the first flexural mode ($m = 2$) that becomes unstable. This is because, for an equilibrium point that does not involve zero control currents, there is an imbalance of the actuator gains on opposing sides of the rotor. This gain imbalance introduces a feedback effect that may be stabilizing or destabilizing depending on the measured phasing of the modal response. The exact influence of sensor configuration (and other operating parameters) on stability is complex and difficult to predict without resorting to numerical calculations. It is found that the rotational speed does not have a large effect on these stability boundaries for the rotational frequency range considered in this study (0–40 Hz). However, levels of structural damping for the free rotor will depend on fluid/air effects, which are not accounted for in these calculations.

In gravity environments, using two sensors would be most appropriate for a horizontal axis rotor, while the four-sensor configuration would be better suited for vertical-axis systems. For the experiments reported in this paper, feedback control

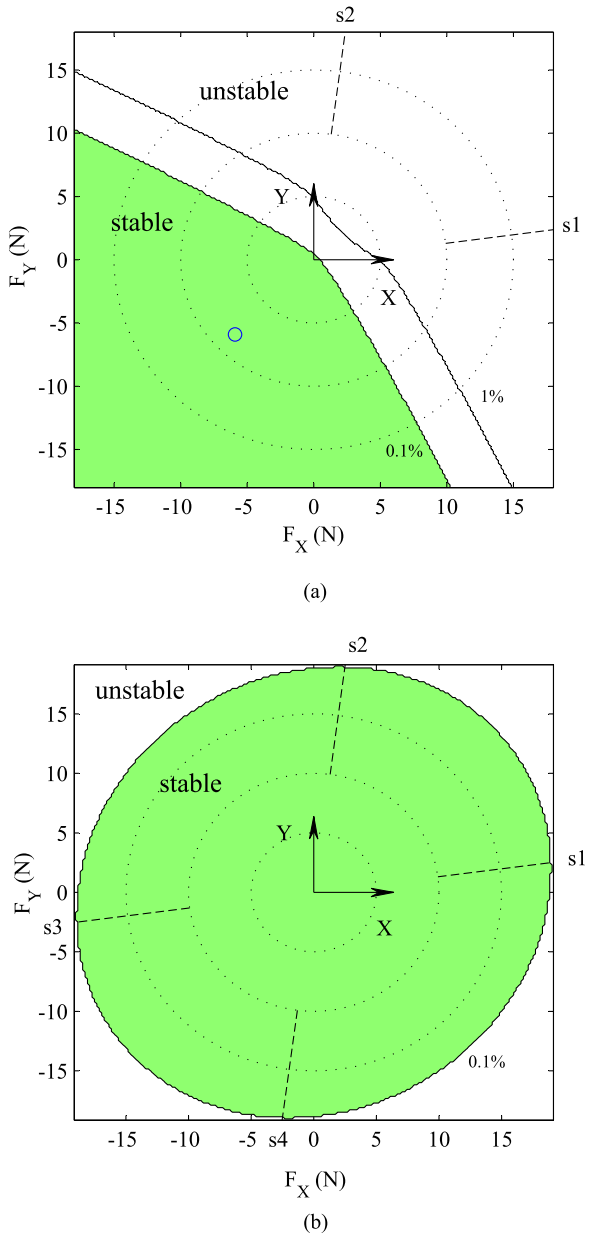

Fig. 9. Stability regions for the experimental system in terms of static bearing force. Each map is for a different sensor configuration and shows stability regions for different initial levels of damping for rotor flexural modes (0.1% and 1% of critical). Sensor locations are indicated by $s1, s2, \ldots$, etc.

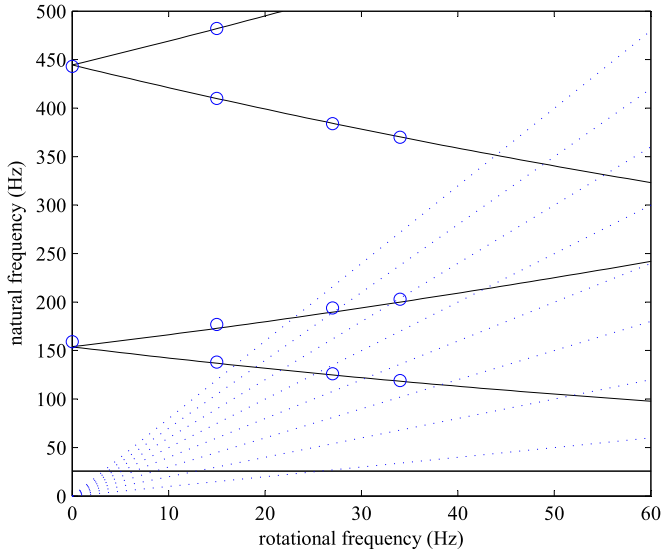

Fig. 10. Campbell diagram for an experimental system (levitated rotor) based on the theoretical model. Experimentally determined natural frequencies are indicated by ○.

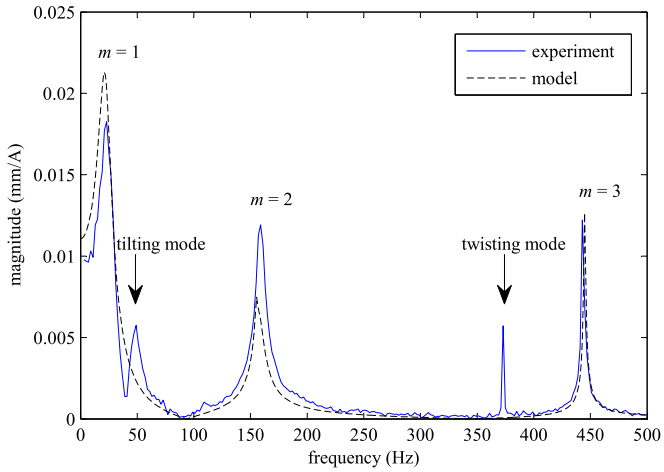

Fig. 11. Frequency response data for the excitation of levitated rotor using auxiliary actuation coils: theory and experiment.

was based on two inductance probe sensors, oriented as shown in Fig. 9(a). The system was set up with the rotation axis horizontal. To match the gravity load with the stability region, the bearing was positioned with the X and Y axes oriented at $\pm 45°$ in the downward direction, as shown in Fig. 8(a). The static operating condition then corresponds to the point marked ○ in Fig. 9(a). The total weight of the rotor is 8.37 N.

C. Experimental Results

The experiments reported here focus on steady-state rotordynamic response behavior for the levitated rotor. The Campbell diagram obtained from the closed-loop model (Fig. 10) indicates the potential for the excitation of both rigid-body and flexural modes. Excitation of flexural modes may be significant if super-synchronous excitation arises due to asymmetry of the rotor structure, e.g., due to inhomogeneous material properties, nonuniform wall thickness, or noncircularity of the rotor due to machining errors. These effects will share some similarities with classical mass-unbalance excitation but lead to more complex multiharmonic response behavior.

The dynamic characteristics of the rotor–bearing system were assessed experimentally by frequency response measurements, undertaken at different rotational speeds. Excitation was achieved using small auxiliary coils wound on actuators 1 and 2 (in addition to the main levitation coils), which produced localized forcing of the rotor wall close to sensor 1. The results shown in Fig. 11 are for no rotation. For comparison, model-based predictions are also presented, and these show good agreement with the experimental data: resonant

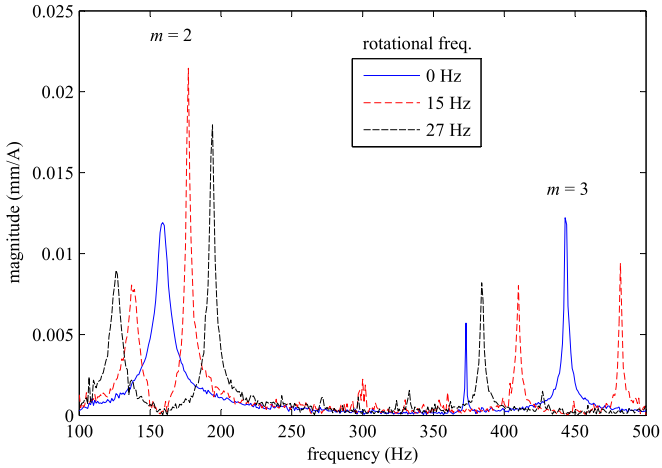

Fig. 12. Frequency response measurements for different rotational frequencies.

frequencies for both rigid-body and flexural modes are well-matched. Damping levels for flexural modes are dependent on the initial damping for the free rotor, which was set to 0.2% of critical in the model. There are extra resonance peaks appearing in the experimental data, which are associated with rigid-body tilting and flexural twisting of the rotor. These modes are not captured by the theoretical model, for which wall deflection u is assumed to be independent of the axial coordinate z. It is believed that these extra modes are excited due to asymmetries introduced by the coupling at one end of the rotor. Fig. 12 shows the measured frequency response for different rotational speeds (0, 15, and 27 Hz), from which the splitting of forward- and backward-mode natural frequencies with increasing rotational speed is evident. The theoretical predictions for modal frequencies based on thin-shell theory match well with these experimental results, as shown in Fig. 10. It is also notable that the twisting-mode resonance (at 373 Hz) is suppressed during rotation.

Fig. 13(a) shows measured signals during the deceleration of the rotor from an initial rotational frequency of 34 Hz. A spectogram (short-time Fourier transform) of the signal from sensor 1 is shown in Fig. 13(b). The vibration involves many harmonic components with frequencies that are integer multiples of the rotational frequency. These arise due to asymmetry of the rotor shape and properties. The spectrogram shows that many different super-synchronous components excite the rigid-body mode (at 25 Hz) during deceleration. Although the noncircularity of the cross section is within $\pm 50\ \mu$m (radial error), the rotor has a somewhat elliptical shape, and this causes a dominant vibration component with frequency $2 \times \Omega$. There is only slight evidence of excitation of the $m = 2$ flexural modes from the spectogram (more so for the higher frequency forward mode). Given the low damping and highly resonant behavior seen in the direct frequency response measurements, the lack of flexural-mode excitation during normal operation is significant. This can be at least partly attributed to the distributed actuation scheme, which has been designed to minimize the excitation of the flexural modes through the bearing.

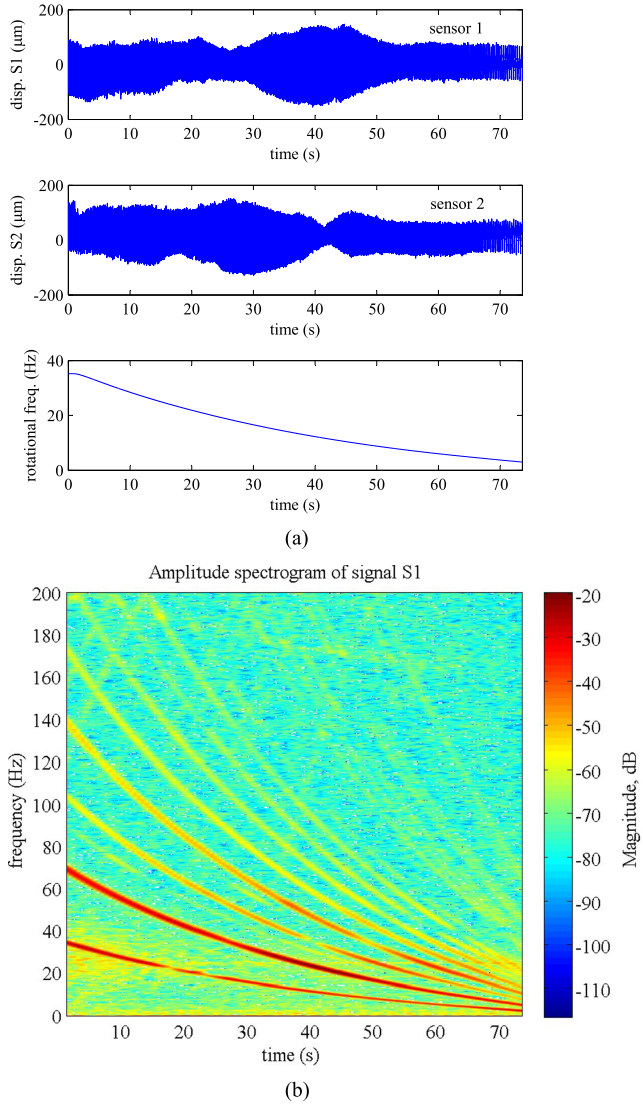

Fig. 13. Rotor vibration response during coast-down. (a) Measured signals. (b) Spectogram (short-time Fourier transform) of displacement at sensor 1.

VI. Conclusion

This paper has described a new AMB design and control approach for supporting thin-walled rotor structures. The design embodies a distributed actuation scheme, synthesized from a theoretical description of rotor vibration with the aim of decoupling the levitation control system dynamics from the flexural dynamics of the rotor wall. The approach has been validated by both analytical and experimental studies focusing on the stability and vibration behavior of a short-length rotor–bearing system. The results are encouraging and motivate further application of the distributed actuation approach to more complex thin-walled rotor systems, including those with multiple bearing units or multidirectional actuator distributions. This will facilitate new approaches to rotor–bearing system design and active vibration control for various machine types.

REFERENCES

[1] D. Peters, C. Kaletsch, R. Nordmann, and B. Domes, "Test rig for a supercritical rotor of an aero engine," in *Proc. 12th IFToMM World Congr.,* Besancon, France, 2007, pp. 180–187.

[2] E. Chatelet, F. D'Ambrosio, and G. Jacquet-Richardet, "Toward global modelling approaches for dynamic analyses of rotating assemblies of turbomachines," *J. Sound Vib.*, vol. 282, pp. 163–178, 2005.

[3] K. Gupta, "Composite shaft rotor dynamics: An overview," *Mechanisms Mach. Sci.*, vol. 23, pp. 79–94, 2015.

[4] F. Klocke *et al.*, "Turbomachinery component manufacture by application of electrochemical, electro-physical and photonic processes," *CIRP Ann. - Manuf. Technol.*, vol. 63, no. 2, pp. 703–726, 2014.

[5] M. S. Darlow and J. Creonte, "Optimal design of composite helicopter power transmission shafts with axially varying fiber lay-up," *J. Amer. Helicopter Soc.*, vol. 40, no. 2, pp. 50–56, 1995.

[6] G. Genta, *Dynamics of Rotating Systems*. New York, NY: Springer Science+Business Media, Inc., 2009.

[7] G. Schweitzer and E. H. Maslen, Eds, *Magnetic Bearings: Theory, Design, and Application to Rotating Machinery*. Berlin, Germany: Springer-Verlag, 2009.

[8] Y. Le, J. Fang, and J. Sun, "Design of a Halbach array permanent magnet damping system for high speed compressor with large thrust load," *IEEE Trans. Mag.*, vol. 51, no. 1, pp. 1–9, Jan. 2015.

[9] F. Y. Zeidan, L. San Andres, and J. M. Vance, "Design and application of squeeze film dampers in rotating machinery," in *Proc. 25th Turbomachinery Symp.*, Houston, TX, 1996, pp. 169–188.

[10] A. B. Palazzolo, R. R. Lin, R. M. Alexander, A. F. Kascak, and J. J. Montague, "Test and theory for piezoelectric actuator-active vibration control of rotating machinery," *ASME. J. Vib. Acoust.*, vol. 113, no. 2, pp. 167–175, 1991.

[11] G. Pinte, S. Devos, B. Stallaert, W. Symens, J. Swevers, and P. Sas, "A piezo-based bearing for the active structural acoustic control of rotating machinery," *J. Sound Vib.*, vol. 329, no. 9, pp. 1235–1253, 2010.

[12] M. O. T. Cole, P. S. Keogh, and C. R. Burrows, "Vibration control of a flexible rotor/magnetic bearing system subject to direct forcing and base motion disturbances," *Proc. IMechE, Part C: J. Mech. Eng. Sci.*, vol. 212, no. 7, pp. 535–546, 1998.

[13] Y. Okada, K. Shimizu, and S. Ueno, "Vibration control of flexible rotor by inclination control magnetic bearings with axial self-bearing motor," *IEEE/ASME Trans. Mechatronics*, vol. 6, no. 4, pp. 521–524, 2001.

[14] S. E. Mushi, Z. Lin, and P. E. Allaire, "Design, construction, and modeling of a flexible rotor active magnetic bearing test rig," *IEEE/ASME Trans. Mechatronics*, vol. 17, no. 6, pp. 1170–1182, 2012.

[15] S. Zheng, B. Han, Y. Wang, and J. Zhou, "Optimization of damping compensation for a flexible rotor system with active magnetic bearing considering gyroscopic effect," *IEEE/ASME Trans. Mechatronics*, vol. 20, no. 3, pp. 1130–1137, 2015.

[16] K. Nonami and Z. Liu, "Adaptive unbalance vibration control of magnetic bearing system using frequency estimation for multiple periodic disturbances with noise," in *Proc. IEEE Conf. Control Appl.*, 1999, vol. 1, pp. 576–581.

[17] M. O. T. Cole, P. S. Keogh, and C. R. Burrows, "Control of multifrequency rotor vibration components," *Proc. IMechE, Part C: J. Mech. Eng. Sci.*, vol. 216, no. 2, pp. 165–178, 2002.

[18] J. Fang, S. Zheng, and B. Han, "AMB vibration control for structural resonance of double-gimbal control moment gyro with high-speed magnetically suspended rotor," *IEEE/ASME Trans. Mechatronics*, vol. 18, no. 18, pp. 32–43, Feb. 2013.

[19] R. Herzog, P. Buhler, C. Gahler, and R. Larsonneur, "Unbalance compensation using generalized notch filters in the multivariable feedback of magnetic bearings," *IEEE Trans. Control Syst. Technol.*, vol. 4, no. 5, pp. 580–586, Sep. 1996.

[20] P. Cui, S. Li, G. Zhao, and C. Peng, "Suppression of harmonic current in active-passive magnetically suspended CMG using improved repetitive controller," *IEEE/ASME Trans. Mechatronics*, vol. 21, no. 4, pp. 2132–2141, Aug. 2016.

[21] T. Schneeberger, T. Nussbaumer, and J. W. Kolar, "Magnetically levitated homopolar hollow-shaft motor," *IEEE/ASME Trans. Mechatronics*, vol. 15, no. 1, pp. 97–107, Feb. 2010.

[22] C. Lusty, N. Sahinkaya, and P. Keogh, "A novel twin-shaft rotor layout with active magnetic couplings for vibration control," *Proc. IMechE, Part I: J. Syst. Control Eng.*, vol. 230, no. 3, pp. 266–276, 2016.

[23] L. Zhou and L. Li, "Modeling and identification of a solid-core active magnetic bearing including eddy currents," *IEEE/ASME Trans. Mechatronics*, vol. 21, no. 6, pp. 2784–2792, Dec. 2016.

[24] A. Love, *A Treatise on the Mathematical Theory of Elasticity*, Cambridge, U.K.: Cambridge Univ. Press, 1906.

[25] M. Endo, K. Hatamura, M. Sakata, and O. Taniguchi, "Flexural vibration of a thin rotating ring," *J. Sound Vib.*, vol. 92, no. 2, pp. 261–272, 1984.

Matthew O. T. Cole was born in Leamington Spa, Warwickshire, U.K., in 1971. He received the M.A. degree in natural sciences from the University of Cambridge, Cambridge, U.K., in 1995, and the M.Sc. and Ph.D. degrees in mechanical engineering from the University of Bath, Bath, U.K., in 1995 and 1999, respectively.

He has been a faculty member at Chiang Mai University, Chiang Mai, Thailand since 2003 and is currently an Associate Professor with the Department of Mechanical Engineering. He has authored or co-authored more than 90 articles on these topics in research journals and conference proceedings. His research interests include mathematical modeling, control, and signal processing techniques for machine systems with a particular focus on rotating machinery, magnetic bearings, active vibration control systems, and high-precision robotics.

Wichaphon Fakkaew was born in Phayao, Thailand, in 1977. He received the B.Eng. and M.Eng. degrees from the Department of Mechanical Engineering, Chiang Mai University, Chiang Mai, Thailand, in 2000 and 2005 respectively, and the Ph.D. degree from Chiang Mai University in 2015, all in mechanical engineering.

He is currently a Lecturer with the School of Engineering, University of Phayao, Phayao, Thailand. His research interests include modeling and control system design for mechanical systems.

Model and Control System Development for a Distributed Actuation Magnetic Bearing and Thin-Walled Rotor Subject to Noncircularity

Chakkapong Chamroon
School of Engineering,
University of Phayao,
Phayao 56000, Thailand
e-mail: chakkapong.ch@up.ac.th

Matthew O. T. Cole[1]
Department of Mechanical Engineering,
Center for Mechatronic Systems and Innovation,
Chiang Mai University,
Chiang Mai 50200, Thailand
e-mail: motcole@dome.eng.cmu.ac.th

Wichaphon Fakkaew
School of Engineering,
University of Phayao,
Phayao 56000, Thailand
e-mail: wichaphon.fa@up.ac.th

This paper considers the problem of controlling the vibration of a lightweight thin-walled rotor with a distributed actuation magnetic bearing (DAMB). A theoretical flexible rotor model is developed that shows how multiharmonic vibration arises due to small noncircularity of the rotor cross section. This model predicts a series of resonance conditions that occur when the rotational frequency matches a subharmonic of a system natural frequency. Rotor noncircularity can be measured offline, and the measurement data used to cancel its effect on the position sensor signals used for feedback control. A drawback of this approach is that noncircularity is difficult to measure exactly and may vary over time due to changing thermal or elastic state of the rotor. Moreover, any additional multiharmonic excitation effects will not be compensated. To overcome these issues, a harmonic vibration control algorithm is applied that adaptively modifies the harmonic components of the actuator control currents to match a target vibration control performance, but without affecting the stabilizing feedback control loops. Experimental results for a short thin-walled rotor with a single DAMB are presented, which show the effectiveness of the techniques in preventing resonance during operation. By combining sensor-based noncircularity compensation with harmonic vibration control, a reduction in vibration levels can be achieved without precise knowledge of the rotor shape and with minimal bearing forces.
[DOI: 10.1115/1.4043510]

Keywords: magnetic bearing, thin-walled structure, flexible rotor, vibration control, sensor run-out

1 Introduction

Active magnetic bearings (AMBs) incorporate electromagnetic actuators with a feedback control system to maintain contact-free support of a rotor. This eliminates wear and the need for lubrication and permits very high shaft speeds. Further advantages are derived from the capacity to actively control and suppress vibration within the structure of a machine [1]. Recently, the application of the magnetic bearings has been considered for the hollow thin-walled and annular rotors [2–5]. In addition to the specialized applications, thin-walled rotor topologies can play a significant role in lightweight turbomachine design [6,7]. The development of control methods for a thin-walled rotor-AMB system with enhanced vibration suppression capabilities has not been previously considered and is the focus of this paper.

For a solid-shaft rotor, the discrepancy between the inertial and geometric axes causes harmonic vibration that is synchronous with rotation [8]. Early work on unbalance vibration control with AMBs involved strategies to minimize motion of the geometric axis of a rotor [9–11]. Various linear control methods such as repetitive control, adaptive disturbance rejection, and notch filtering can be applied to this problem [12–15]. Further advances have been made with strategies that can maintain stability during large-amplitude vibration subject to nonlinear dynamics and contact with touchdown bearings [16–19].

Although reducing rotor vibration is desirable to avoid contact and rub, it tends to cause increased transmission of vibration through the bearing to the machine housing. Furthermore, since unbalance forces are proportional to the square of rotational speed, actuator force saturation may occur when operating at a high speed. Transmission of unbalance forces can be reduced by adjusting synchronous control forces until the rotor rotates around its inertia axis. This can be achieved by unbalance estimation methods or adaptive cancellation of synchronous current components [15,20]. Such methods require that the rotor is well-balanced and are not appropriate when flexural dynamics dominates the response behavior.

Additional vibration excitation is associated with the use of proximity sensors. Noncircularity of the rotor cross section and/or nonhomogeneous properties of the rotor material give rise to erroneous components in the measurement signals, commonly referred to as run-out error. These are operated on by the feedback controller, causing unwanted control currents components that induce multifrequency vibration of the rotor. Methods for periodic disturbance cancellation may be applied to reduce both synchronous and higher harmonic components of control currents [13,21,22]. Darbandi et al. employed sensor run-out identification using an integral adaptive observer [23], while Setiawan et al. proposed an adaptive algorithm for sensor run-out compensation achieving asymptotic stability of the rotor geometric center [24]. These papers focus on rotors that are effectively rigid, and so, dynamic models and stabilization schemes involve relatively simple parametric formulations.

Vibration control of flexible rotors with multiple excitation sources presents additional challenges [25]. The need for dynamic models may be circumvented by using online identification routines

[1]Corresponding author.

Contributed by the Technical Committee on Vibration and Sound of ASME for publication in the Journal of Vibration and Acoustics. Manuscript received November 25, 2018; final manuscript received April 3, 2019; published online May 22, 2019. Assoc. Editor: Costin Untaroiu.

to determine speed-dependent control influence coefficients, allowing optimized control even with complex multi-input multi-output dynamics [26–28]. For thin-walled rotors, two key issues must be addressed in the controller design, which do not arise for conventional solid-shaft AMB systems:

(1) Flexural vibration modes involving radial distortion of the rotor wall can play a significant role in the dynamic behavior, and without due consideration in the control algorithm design, these modes are prone to destabilization. This is complicated by the fact that the natural frequencies undergo large changes in value due to speed-dependent Coriolis effects.
(2) Multiharmonic disturbances arise due to small noncircularity of the rotor cross section. This differs to sensor run-out error as the variation in surface position is associated also with variation in the mass distribution and the gap size between the rotor and actuator, which cause additional rotor disturbance effects.

An effective control strategy must achieve an acceptable balance of vibration attenuation and coil current levels irrespective of the operating conditions and exact state of rotor noncircularity. The presence of multiharmonic vibration, arising through multiple excitation mechanisms, makes this challenging. This paper provides a detailed analysis of these issues and describes a novel control approach to suppress vibration of a thin-walled rotor with a distributed actuation magnetic bearing (DAMB).

2 DAMB Design and Control Considerations

A distributed actuation magnetic bearing supporting a thin-walled rotor is shown schematically in Fig. 1. An array of electromagnetic actuators (numbering N_A) is positioned internally (or externally) around the rotor circumference with small uniform gaps between the pole faces and the rotor surface. Each actuator applies an attractive force to the rotor that varies with the gap size (dependent on rotor motion/vibration) and the currents within the coils. To achieve stable contact-free support, the position of the rotor surface is measured at two locations using proximity probes so that the center position may be calculated (subject to noncircularity error), and this information used in real-time for feedback control of the drives that power the actuator coils. The principle of operation is similar to a conventional AMB. However, the larger number of actuators and thin-walled rotor topology introduce new considerations in the design and operation of feedback controllers [4].

2.1 Multicoil Distributed Actuation Approach. A model of the bearing actuator forces for a driving scheme with four drives and up to four coils per actuator may be considered where the radial force applied to the rotor wall by the nth actuator is

$$f_n = \mu_0 A_n \frac{(N_{1,n}I_1 + N_{2,n}I_2 + N_{3,n}I_3 + N_{4,n}I_4)^2}{(l_n/\mu_r + 2s_n - 2y_n)^2}, \quad n = 1, \ldots, N_A \tag{1}$$

Here, A_n is the total pole-face area, l_n is the flux path length through the iron (having a relative permeability μ_r), s_n is the gap size for the equilibrium position, and y_n is the radial displacement of the rotor wall local to the actuator. Suppose the coils, having a number of turns $N_{k,n}$, are supplied currents with the same constant bias component I_0 so that $I_k(t) = I_0 + i_k(t)$ with i_k being the control feedback component. Combining all the actuator forces as a single vector $\mathbf{f}_A = [f_1\ f_2 \cdots f_{N_A}]^T$ and linearizing Eq. (1) about a given operating point P gives an equation in the form

$$\mathbf{f}_A = \mathbf{F}_0 + \Gamma \mathbf{i}_A + \mathbf{H}\mathbf{y}_A \tag{2}$$

where $\mathbf{i}_A = [i_1\ i_2\ i_3\ i_4]^T$, $\mathbf{y}_A = [y_1\ y_2 \cdots y_{N_A}]^T$, and $\mathbf{F}_0$ is the constant force components due to the bias currents. The elements of the actuator gain matrix Γ are the coefficients:

$$\gamma_{n,k} = \left.\frac{df_n}{di_k}\right|_P = 2\mu_0 A_n N_{k,n}(l_n - 2y_n)^{-2}\left(\sum_j N_{j,n}I_j\right)\Bigg|_P \tag{3}$$

and $\mathbf{H}$ is a diagonal matrix containing the negative stiffness coefficients

$$h_n = \left.\frac{df_n}{di_k}\right|_P = 4\mu_0 A_n (l_n - 2y_n)^{-3}\left(\sum_j N_{j,n}I_j\right)^2\Bigg|_P \tag{4}$$

For this topology, a coil-winding scheme based on the flexural mode decoupling may be employed in order to maximize bearing load capacity and simplify the design of an initial feedback controller that achieves stable levitation of the rotor [4]. A differential driving scheme with two control input variables $\mathbf{i}_C = [i_{C,1}\ i_{C,2}]^T$ is then adopted, as for conventional AMBs:

$$\mathbf{i}_A = \mathbf{T}\mathbf{i}_C, \quad \mathbf{T} = \begin{bmatrix} 1 & 0 & -1 & 0 \\ 0 & 1 & 0 & -1 \end{bmatrix}^T \tag{5}$$

2.2 Vibration Control Considerations. To define the vibration excitation problem, a mathematical description of the rotor geometry is introduced according to Fig. 1. The radial location of the outer (or inner) surface of the rotor is defined relative to the geometric center so that a Fourier series description of noncircularity has the form

$$r(\theta) = R + \sum_{j=2}^{\infty} a_j \cos(j(\theta + \psi_j)) \tag{6}$$

Due to rotation, the displacement measured at a fixed angular location ϕ_S will have a time-varying component that is not associated with the rotor vibration. If the objective for control is to allow the rotor to spin about its geometric center without distortion, then the measured displacements should exactly match Eq. (6). For rotation at constant angular speed Ω, this may be expressed as

$$d_S(t) = r(\phi_S - \Omega t) - R = \sum_{j=2}^{\infty} a_j \cos(j(\phi_S - \Omega t + \psi_j)) \tag{7}$$

To cancel the effect on control feedback signals, noncircularity may be treated in the same way as sensor run-out error. Using offline measurements of the rotor shape, the displacement due to noncircularity (Eq. (7)) can be constructed in real-time and subtracted from the sensor readings. The resulting signal will correspond to the exact position of the rotor geometric center provided that no wall deformation occurs due to vibration.

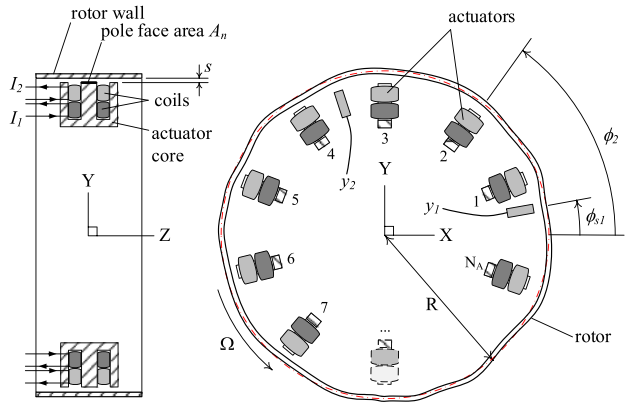

Fig. 1 Thin-walled rotor with distributed actuation AMB support: schematic diagram showing (exaggerated) noncircularity of the rotor in the bearing plane

In practice, it is difficult to measure noncircularity of the rotor in-situ as measurements are always affected by the bearing operation. Also, even if noncircularity can be measured accurately, there is still the possibility that the equilibrium shape of the rotor changes during operation, e.g., due to thermal distortion or elastic deformation caused by centrifugal loading. Moreover, there are additional excitation effects associated with noncircularity, as well as other system disturbances, which cannot be exactly inferred from sensor readings. Section 3 gives a full analysis of noncircularity effects and their impact for vibration control based on a 2D model of a thin-walled rotor with single DAMB.

3 Rotordynamic Model

To obtain a representative model of rotordynamic behavior, the continuum equation for radial vibration of a thin rotating annulus may be considered in the form [5,8,29]:

$$\left(\frac{\partial^2 \ddot{u}}{\partial \phi^2} - \ddot{u}\right) + 2\Omega\left(\frac{\partial^3 \dot{u}}{\partial \phi^3} + \frac{\partial \dot{u}}{\partial \phi}\right) + \frac{Ed^2}{12\rho R^4}\left(\frac{\partial^6 u}{\partial \phi^6} + 2\frac{\partial^4 u}{\partial \phi^4} + \frac{\partial^2 u}{\partial^2 \phi}\right) = \frac{1}{\rho L d}\frac{\partial^2 F}{\partial \phi^2} + \Omega^2\left(\frac{\partial^4 u_0}{\partial \phi^4} + 3\frac{\partial^2 u_0}{\partial \phi^2}\right) \tag{8}$$

where Ω is the constant angular speed, d is the wall thickness, L is the axial length, and ρ and E are the material density and Young's modulus, respectively. Motion is defined in terms of the radial displacement $u(\phi, t)$ with ϕ being the angular position in the fixed frame, while $u_0(\phi, t)$ is the radial displacement associated with noncircularity. Applied forces are captured by a radial force distribution $F(\phi, t)$. The noncircularity may be represented by a truncated Fourier series from Eq. (6) so that accounting also for rotation

$$u_0(\phi, t) = \sum_{j=2}^{M} a_j \cos\left(j(\phi - \Omega t + \psi_j)\right) \tag{9}$$

Equation (9) defines the multiharmonic forcing of the system. A solution to Eq. (8) can be approximated by a superposition of a finite number of modes:

$$u(\phi, t) \approx \sum_{m=1}^{M}\left[p_m(t)\sin m\phi + q_m(t)\cos m\phi\right] \tag{10}$$

where $\sin m\phi$ and $\cos m\phi$ are the mode shapes for free vibration and $p_m(t)$ and $q_m(t)$ are the mth modal displacement coordinates, with m being the circumferential wavenumber (integer). Substituting Eqs. (9) and (10) in Eq. (8) and evaluating the inner products with respect to $\sin m\phi$ and $\cos m\phi$ by integrating over ϕ leads to a set of $2M$ equations (for $m = 1, \ldots, M$):

$$\ddot{p}_m - \Omega g_m \dot{q}_m + k_m p_m = v_m \sum_{n=1}^{N} f_n \sin m\phi_n - \Omega^2 w_m\left[a_m \sin m(\Omega t - \psi_m)\right] \tag{11}$$

$$\ddot{q}_m + \Omega g_m \dot{p}_m + k_m q_m = v_m \sum_{n=1}^{N} f_n \cos m\phi_n - \Omega^2 w_m\left[a_m \cos m(\Omega t - \psi_m)\right] \tag{12}$$

where $f_n(t)$ is the radial actuator force applied at angular position ϕ_n. The constant coefficients are

$$k_m = \frac{Ed^2}{12\rho R^4}\frac{m^2(m^2-1)^2}{m^2+1}, \quad g_m = \frac{2m(m^2-1)}{m^2+1}, \quad v_m = \frac{m^2}{\rho\pi AR(m^2+1)}, \quad w_m = \frac{m^2(m^2-3)}{m^2+1}$$

Accordingly, the zero-speed natural frequencies for the flexural vibration are given by $\omega_m = \sqrt{k_m}$.

By defining the noncircularity disturbance as $\mathbf{d}_m(t) = a_m\left[\sin m(\Omega t - \psi_m)\cos m(\Omega t - \psi_m)\right]^T$, Eqs. (11) and (12) may be expressed in the first-order matrix form

$$\frac{d}{dt}\begin{bmatrix}\mathbf{x}_m \\ \dot{\mathbf{x}}_m\end{bmatrix} = \begin{bmatrix}\mathbf{0} & \mathbf{I} \\ -\mathbf{K}_m & -\Omega\mathbf{G}_m\end{bmatrix}\begin{bmatrix}\mathbf{x}_m \\ \dot{\mathbf{x}}_m\end{bmatrix} + \begin{bmatrix}\mathbf{0} \\ \mathbf{I}\end{bmatrix}\left[\mathbf{V}_m\mathbf{E}_m^T\mathbf{f}_A - \Omega^2\mathbf{W}_m\mathbf{d}_m\right] \tag{13}$$

where $\mathbf{x}_m = [p_m\ q_m]^T$, $\mathbf{K}_m = k_m\mathbf{I}$, $\mathbf{G}_m = g_m\mathbf{J}$, $\mathbf{V}_m = v_m\mathbf{I}$, and $\mathbf{W}_m = w_m\mathbf{I}$ with $\mathbf{I}$ being the identity matrix and

$$\mathbf{J} = \begin{bmatrix}0 & 1 \\ -1 & 0\end{bmatrix}, \quad \mathbf{E_m} = \begin{bmatrix}\sin m\phi_1 & \cos m\phi_1 \\ \vdots & \vdots \\ \sin m\phi_N & \cos m\phi_N\end{bmatrix}$$

Combining Eq. (13) for $m = 1, \ldots, M$ and defining $\mathbf{x} = [\mathbf{x}_1^T\ \mathbf{x}_2^T\ \ldots\ \mathbf{x}_M^T]^T$ and $\mathbf{d} = \left[\mathbf{d}_1^T\ \ldots\ \mathbf{d}_M^T\right]^T$ leads to

$$\frac{d}{dt}\begin{bmatrix}\mathbf{x} \\ \dot{\mathbf{x}}\end{bmatrix} = \begin{bmatrix}\mathbf{0} & \mathbf{I} \\ -\mathbf{K} & -\Omega\mathbf{G}\end{bmatrix}\begin{bmatrix}\mathbf{x} \\ \dot{\mathbf{x}}\end{bmatrix} + \begin{bmatrix}\mathbf{0} \\ \mathbf{V}\mathbf{E}_A^T\end{bmatrix}\mathbf{f}_A - \begin{bmatrix}\mathbf{0} \\ \Omega^2\mathbf{W}\end{bmatrix}\mathbf{d} \tag{14}$$

where $\mathbf{E}_A = [\mathbf{E}_1\ \mathbf{E}_2 \cdots \mathbf{E}_M]$ and $\mathbf{K}$, $\mathbf{G}$, $\mathbf{V}$, and $\mathbf{W}$ are block diagonal matrices, in accordance with Eq. (13).

The radial location of the rotor surface is $y(\phi, t) = u(\phi, t) + u_0(\phi, t)$. Hence, the displacements at the sensor and actuator locations are given, respectively, by

$$\mathbf{y}_S = \mathbf{E}_S(\mathbf{x} + \mathbf{d}), \quad \mathbf{y}_A = \mathbf{E}_A(\mathbf{x} + \mathbf{d}) \tag{15}$$

where $\mathbf{E}_S$ is defined in the same way as $\mathbf{E}_A$, but based on sensor angular locations. For sensor readings, we may define $\mathbf{d}_S = \mathbf{E}_S\mathbf{d}$ such that for zero vibration ($\mathbf{x} = 0$), we have $\mathbf{y}_S = \mathbf{d}_S$, as in Eq. (7). Substituting for $\mathbf{y}_A$ in the linearized AMB model (2) gives

$$\mathbf{f}_A = \mathbf{F}_0 + \Gamma_C\mathbf{i}_C + \mathbf{H}\mathbf{E}_A(\mathbf{x} + \mathbf{d}) \tag{16}$$

where $\Gamma_C = \Gamma\mathbf{T}$. According to Eqs. (14)–(16) and the corresponding block diagram structure shown in Fig. 2, noncircularity excites the system through three mechanisms. First, there is an inertia-related disturbance $\Omega^2\mathbf{W}\mathbf{d}$ that acts as a direct forcing of the rotor. The synchronous $m = 1$ component is due to mass unbalance. However, the noncircularity-related components $m \geq 2$ are higher harmonics and have a forcing effect that tends to make the rotor more circular as Ω increases. Second, the noncircularity disturbance $\mathbf{d}$ has an additive contribution to the position of the rotor surface at the actuator locations. This impacts on actuator forces through feedback effects associated with the actuator stiffness coefficients (embedded in $\mathbf{H}$). Third, the noncircularity acts additively on the displacements measured by the sensors, which impacts on the feedback control signals and introduces additional multiharmonic excitation that is dependent on the control algorithm.

A model of the plant suitable for control analysis/design follows from Eqs. (14)–(16) as

$$\begin{aligned}\dot{\eta} &= \mathbf{A}(\Omega)\eta + \mathbf{B}_C\mathbf{i}_C + \mathbf{B}_d(\Omega)\mathbf{d} \\ \mathbf{y}_S &= \mathbf{C}_S\eta + \mathbf{E}_S\mathbf{d}\end{aligned} \tag{17}$$

where $\eta^T = [\mathbf{x}^T\ \dot{\mathbf{x}}^T]$ and

$$\mathbf{A}(\Omega) = \begin{bmatrix}\mathbf{0} & \mathbf{I} \\ -\mathbf{K} + \mathbf{K}_A & -\Omega\mathbf{G}\end{bmatrix}, \quad \mathbf{B}_C = \begin{bmatrix}\mathbf{0} \\ \mathbf{V}\mathbf{E}_A^T\Gamma_C\end{bmatrix}, \quad \mathbf{B}_d(\Omega) = \begin{bmatrix}\mathbf{0} \\ \mathbf{K}_A - \Omega^2\mathbf{W}\end{bmatrix}, \quad \mathbf{C}_S = [\mathbf{E}_S\ \mathbf{0}]$$

The actuator negative stiffness matrix is $\mathbf{K}_A = \mathbf{V}\mathbf{E}_A^T\mathbf{H}\mathbf{E}_A$. The transfer functions for the open-loop plant are $\mathbf{G}_u(s, \Omega) = \mathbf{C}_S(\mathbf{I}s - \mathbf{A}(\Omega))^{-1}\mathbf{B}_C$ and $\mathbf{G}_d(s, \Omega) = \mathbf{C}_S(\mathbf{I}s - \mathbf{A}(\Omega))^{-1}\mathbf{B}_d$. With the application of the sensor-based noncircularity compensation, the signal used

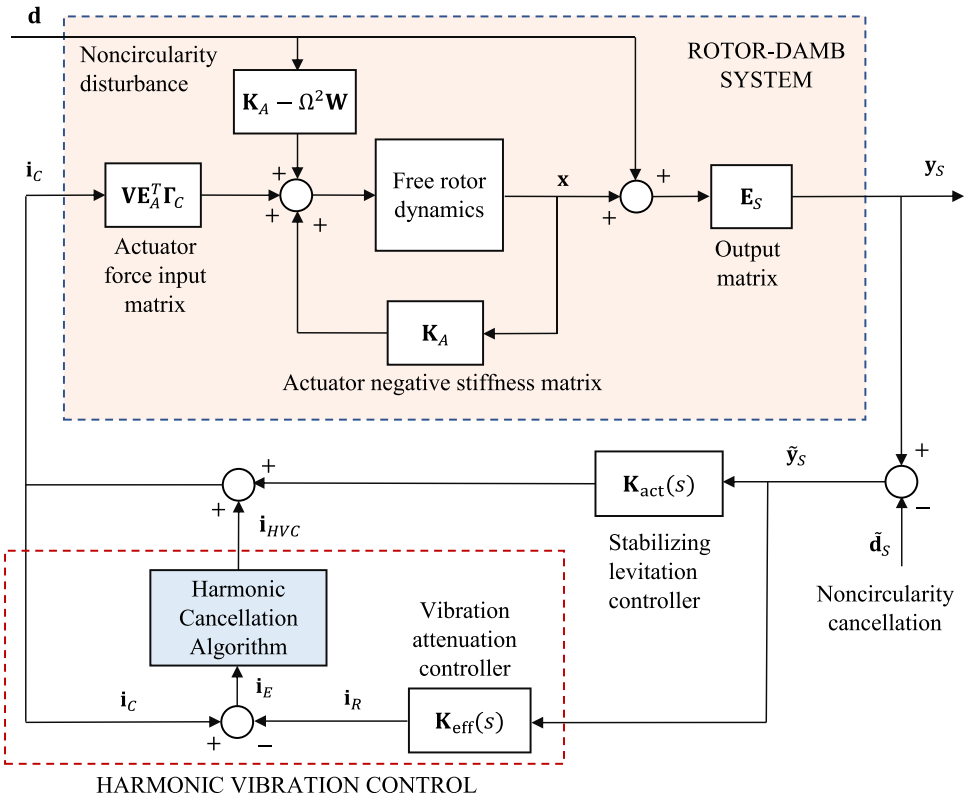

Fig. 2 System block diagram for rotor vibration control

for the feedback control may be defined as

$$\tilde{\mathbf{y}}_S = \mathbf{y}_S - \tilde{\mathbf{d}}_S = \mathbf{C}_S\eta + \mathbf{E}_S\mathbf{d} - \tilde{\mathbf{d}}_S \tag{18}$$

where $\tilde{\mathbf{d}}_S$ is a vector of compensation signals. For exact cancellation $\tilde{\mathbf{d}}_S = \mathbf{E}_S\mathbf{d} = \mathbf{d}_S$ (as in Eq. (7)).

4 Noncircularity Vibration Suppression

An approach for harmonic vibration control (HVC) suited to the noncircularity excitation problem is introduced here based on the control structure shown in Fig. 2. A feedback controller $\mathbf{K}_{\text{act}}$ is first implemented to achieve stable levitation of the rotor. This may be chosen as a standard proportional-integral-derivative controller that is tuned to achieve a targeted net stiffness for the bearing. However, the high-frequency gain of $\mathbf{K}_{\text{act}}$ must be limited in order to avoid problems of flexural mode destabilization and excessive noise excitation. Consequently, vibration suppression with the controller $\mathbf{K}_{\text{act}}$ is not optimal and unwanted resonances occur during operation. A different feedback compensation $\mathbf{K}_{\text{eff}}$ is therefore determined for which the closed-loop transfer function matrix $(\mathbf{I} - \mathbf{G}_u\mathbf{K}_{\text{eff}})^{-1}$ has improved properties for vibration attenuation over the expected range of excitation frequencies (compared with $(\mathbf{I} - \mathbf{G}_u\mathbf{K}_{\text{act}})^{-1}$). However, it is not necessary that K_{eff} can achieve satisfactory (stable and robust) levitation control if implemented on the actual system, only that it gives desired attenuation properties for the expected range of excitation frequencies.

According to Fig. 2, the feedback stabilization is provided by $\mathbf{K}_{\text{act}}$. The controller subsystem $\mathbf{K}_{\text{eff}}$ also operates on the sensor signals to provide a reference control signal $\mathbf{i}_R$. The difference between the actual control input $\mathbf{i}_C$ and the reference signal is treated as an error signal $\mathbf{i}_E = \mathbf{i}_C - \mathbf{i}_R$. The harmonic cancellation algorithm operates on $\mathbf{i}_E$ to generate the correction signal $\mathbf{i}_{HVC}$. This algorithm, which is described in detail in Sec. 4.2, provides a multiharmonic signal that adapts to eliminate the harmonic components of $\mathbf{i}_E$ such that, in steady-state, the harmonic components of the control signal correspond to the output from $\mathbf{K}_{\text{eff}}$. The result is that the steady-state disturbance attenuation then matches the characteristics of $\mathbf{K}_{\text{eff}}$, but only for the discrete frequencies that are targeted within the cancellation algorithm.

4.1 System Model for Control Analysis. A linear feedback controller $\mathbf{K}(s) = \mathbf{C}_K(\mathbf{I}s - \mathbf{A}_K)^{-1}\mathbf{B}_K + \mathbf{D}_K$ is considered, which, when combined with Eqs. (17) and (18), gives closed-loop system dynamics described by

$$\begin{aligned} \dot{\mathbf{z}} &= \widehat{\mathbf{A}}(\Omega)z + \widehat{\mathbf{B}}_d(\Omega)\mathbf{d} + \widehat{\mathbf{B}}_S(\mathbf{E}_S\mathbf{d} - \tilde{\mathbf{d}}_S) + \widehat{\mathbf{B}}_C\mathbf{i}_{HVC} \\ \mathbf{y}_S &= \widehat{\mathbf{C}}_S\mathbf{z} + \mathbf{E}_S\mathbf{d} \end{aligned} \tag{19}$$

where $\widehat{\mathbf{C}}_S = [\mathbf{C}_S \;\; \mathbf{0}]$ and

$$\widehat{\mathbf{A}}(\Omega) = \begin{bmatrix} \mathbf{A}(\Omega) + \mathbf{B}_C\mathbf{D}_K\mathbf{C}_S & \mathbf{B}_C\mathbf{C}_K \\ \mathbf{B}_K\mathbf{C}_S & \mathbf{A}_K \end{bmatrix}, \quad \widehat{\mathbf{B}}_C = \begin{bmatrix} \mathbf{B}_C \\ \mathbf{0} \end{bmatrix},$$
$$\widehat{\mathbf{B}}_d(\Omega) = \begin{bmatrix} \mathbf{B}_d(\Omega) \\ \mathbf{0} \end{bmatrix}, \quad \widehat{\mathbf{B}}_S = \begin{bmatrix} \mathbf{B}_C\mathbf{D}_K \\ \mathbf{B}_K \end{bmatrix}$$

The closed-loop transfer function matrix for the levitated rotor (from $\mathbf{i}_{HVC}$ to $\mathbf{y}_S$) may be defined as $\mathbf{P}(s, \Omega) = (\mathbf{I} - \mathbf{G}_u(s)\mathbf{K}(s))^{-1}\mathbf{G}_u(s) = \widehat{\mathbf{C}}_S(\mathbf{I}s - \widehat{\mathbf{A}}(\Omega))^{-1}\widehat{\mathbf{B}}_C$. Equation (19) can be used for the prediction of noncircularity excitation with feedback control only ($\tilde{\mathbf{d}}_S = 0$), with noncircularity cancellation ($\mathbf{E}_S\mathbf{d} - \tilde{\mathbf{d}}_S = 0$) and/or with operation of harmonic vibration control.

4.2 Harmonic Vibration Control Algorithm. An alternative but an equivalent representation of the control system structure is shown in Fig. 3, where the HVC algorithm operates on the additional feedback component $\mathbf{i}_E$ output from the subsystem $\mathbf{K}_{\text{act}} - \mathbf{K}_{\text{eff}}$. The subsystem $\mathbf{P}_{\text{eff}} = (\mathbf{I} - \widetilde{\mathbf{G}}_u K_{\text{eff}})^{-1}\widetilde{\mathbf{G}}_u$ is a speed-dependent model of the closed-loop dynamics, as given by Eq. (19), with the effective

controller. This is included to provide dynamic cancellation for the effect of $\mathbf{i}_{HVC}$ on $\mathbf{y}_S$. For this structure, the transfer function from $\mathbf{i}_{HVC}$ to $\mathbf{i}_E$ is identity if $\tilde{\mathbf{G}}_u(s, \Omega) = \mathbf{G}_u(s, \Omega)$, implying the effects of the plant dynamics on the HVC control loop are entirely compensated. This greatly simplifies the design of the HVC algorithm and allows fast convergence rates to be achieved. Note that, for this control structure, the dynamic compensation scheme involves the forward dynamics (rather than inverse dynamics) of the closed-loop system, and this allows straightforward realization of a speed-dependent model, avoiding issues with implementation, noise amplification, and stability that typically arise for disturbance cancellation schemes involving inverse models.

The harmonic cancellation algorithm involves a matrix-based discrete Fourier transform as shown in Fig. 4. The error signal $\mathbf{i}_E$ is down-sampled at regular intervals over the period of rotation to form a vector of N_s sample values. This vector is multiplied by the partial DFT matrix $\mathbf{R}_{FT}$ to give harmonic amplitudes (Fourier coefficients) for selected frequencies (e.g., the first eight harmonics of the rotational frequency):

$$\mathbf{R}_{FT} = 2\begin{bmatrix} \mathrm{Re}(\mathbf{w}_2) \\ -\mathrm{Im}(\mathbf{w}_2) \\ \vdots \\ \mathrm{Re}(\mathbf{w}_8) \\ -\mathrm{Im}(\mathbf{w}_8) \end{bmatrix}, \text{ where } \begin{bmatrix} \mathbf{w}_1 \\ \mathbf{w}_2 \\ \mathbf{w}_3 \\ \vdots \\ \mathbf{w}_{N_s} \end{bmatrix} = \frac{1}{N_s}\begin{bmatrix} 1 & 1 & 1 & \cdots & 1 \\ 1 & r & r^2 & \cdots & r^{N_s-1} \\ 1 & r^2 & r^4 & \cdots & r^{2(N_s-1)} \\ \vdots & & & \ddots & \vdots \\ 1 & r^{N_s-1} & r^{2(N_s-1)} & \cdots & r^{(N_s-1)^2} \end{bmatrix}, \quad r = e^{-2\pi j/N_s}$$

The calculated amplitudes then undergo discrete integration with updates every synchronous period (revolution) of the rotor. These control amplitudes are multiplied by the corresponding harmonic signals, which are summed to form the multiharmonic control signal $\mathbf{i}_{HVC}$. The control update involves a single gain parameter γ. The maximum value of γ for stable convergence is limited by errors in the system model used for dynamic compensation. Empirical tests can be used to select a value that gives acceptable convergence rates for all the targeted harmonic components.

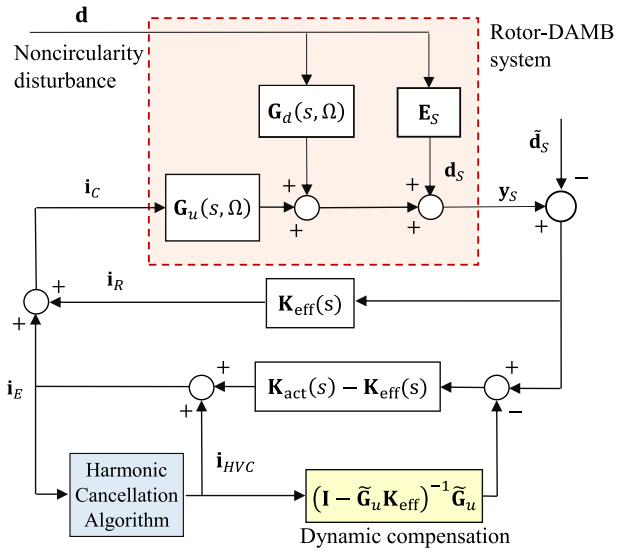

Fig. 3 Block diagram for harmonic vibration control. The structure is exactly equivalent to that in Fig. 2, except additional dynamic compensation is included so that, with an exact model $\tilde{G}_u = G_u$, the transfer function from i_{HVC} to i_E is identity.

5 Evaluations

Evaluations were undertaken on a short thin-walled rotor with internal DAMB comprising a circular array of 24 actuators with E-shaped cores, as shown in Fig. 5. The experimental rotor (radius $R = 111$ mm) was supported radially by the DAMB but also constrained axially by thin flexures connected to a driving disk coupled to a direct current motor. The flexures prevent tilting and axial motion of the rotor but do not greatly affect the net radial stiffness of the bearing under feedback control. Further system characteristics are given in Table 1. The rotor wall thickness is $d = 3.1$ mm, and the first flexural mode for wall vibration has a frequency of 155 Hz when $\Omega = 0$.

The actuator coils were connected in series as four sets, driven by four direct current servo drives and operated with bias currents of $I_0 = 2.2$ A. The coil-winding pattern and resulting actuator properties are shown in Fig. 6. The actuator force gains vary sinusoidally around the circumference of the bearing, and this helps to decouple the actuator forces from the flexural modes of the rotor wall. The resulting negative stiffness distribution of the actuators exhibits a four-fold rotational symmetry. In reality, the effects of radial load

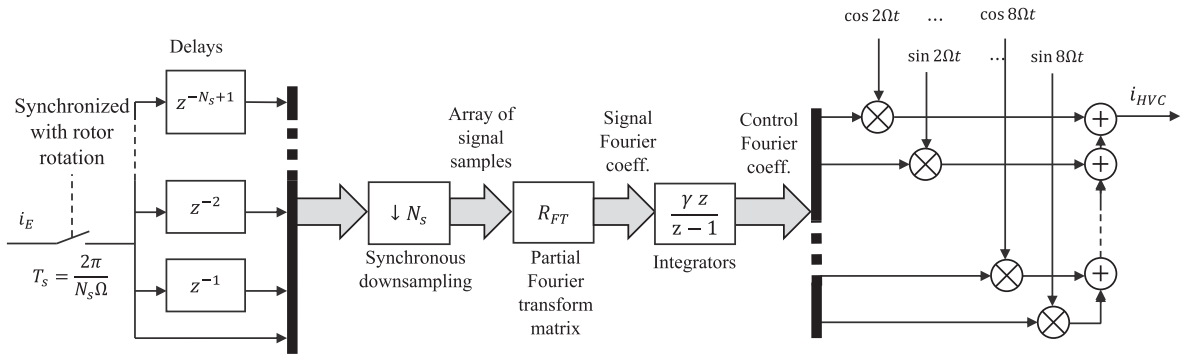

Fig. 4 Efficient implementation of harmonic vibration cancellation algorithm based on synchronous down-sampling and integral feedback in Fourier coefficient domain

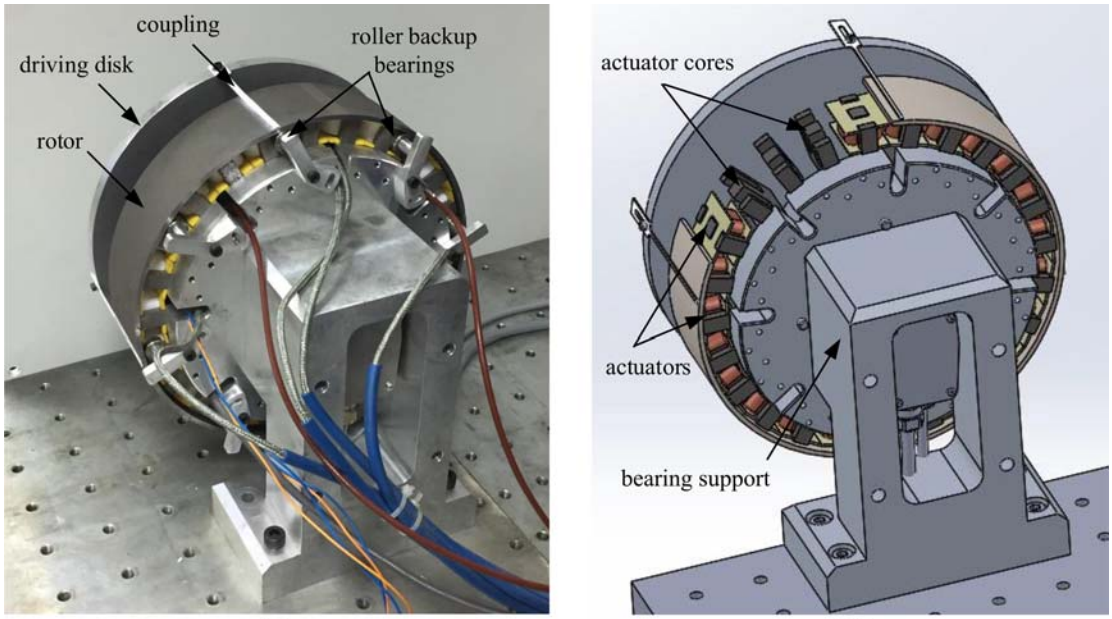

Fig. 5 Experimental distributed actuation magnetic bearing supporting a short annular rotor: (*a*) photo and (*b*) computer-aided design model

Table 1 Characteristics of an experimental thin-walled rotor-DAMB system

Property	Symbol	Value	Units
Rotor radius	R	111.0	mm
Rotor length	L	51	mm
Rotor wall thickness	d	3.1	mm
Material density	ρ	7740	kg m^{-3}
Young's modulus	E	2×10^{11}	Nm^{-2}
First flexural natural frequency	ω_2	155	Hz
Actuator pole-face area	A_n	100	mm^2
Core flux path length	l_n	100	mm
Core relative permeability	μ_r	300	–
Mean gap size	s_0	0.8	mm

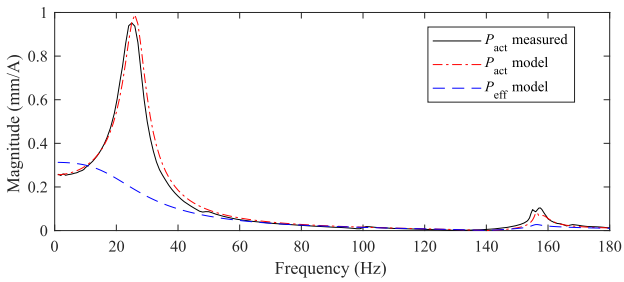

Fig. 7 Frequency response characteristics for a feedback controlled system P_{act} (from i_{HVC} to y_S) when $\Omega = 0$. Results are for *x*-axis only as *y*-axis data were similar. The predicted response function P_{eff} with effective control K_{eff} is also shown.

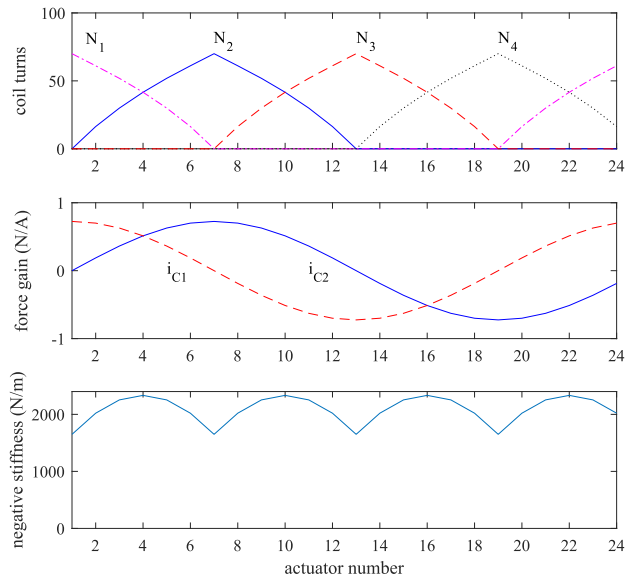

Fig. 6 Actuator properties for the experimental system for no-load operating condition

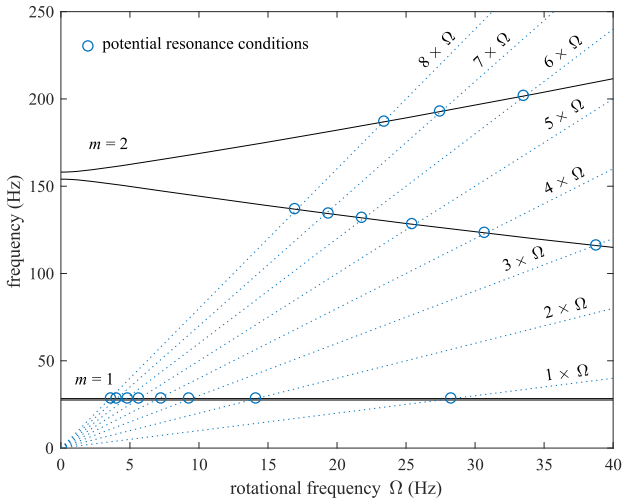

Fig. 8 Campbell diagram showing variation in natural frequencies for rotor system with DAMB under closed-loop control

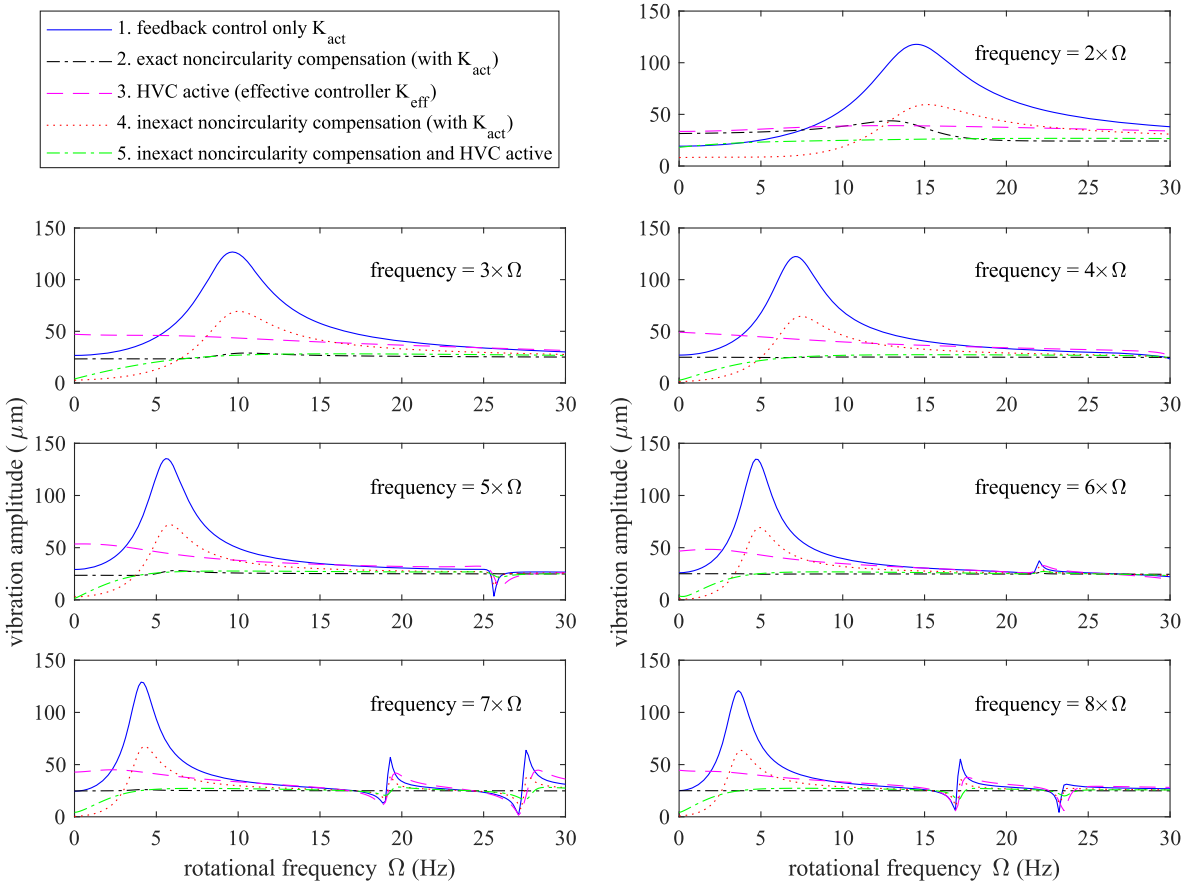

Fig. 9 Predicted rotor excitation arising due to noncircularity: amplitudes of harmonic components for displacement measurements

and nonuniform clearances cause some deviation from the ideal characteristics shown. Under levitation, the mean gap size between the rotor and actuators was approximately 0.8 mm. For control testing purposes, the system was operated with rotational frequencies up to 30 Hz (1800 rpm).

A proportional-derivative (PD) control law suitable to achieve stable levitation of the rotor was selected as

$$\mathbf{K}_{\text{act}}(s) = -\left(k_p + \frac{k_d s}{\tau s + 1}\right)\mathbf{I}_{2\times 2} = -\left(\frac{21s + 6000}{0.001s + 1}\right)\mathbf{I}_{2\times 2}$$

A proportional gain of $k_p = 6000$ A/m yields a net bearing stiffness of 25,000 N/m and system natural frequency of 27 Hz for rigid-body motion (based on the theoretical model in Sec. 4.1). Even with a filtered derivative action ($\tau = 0.001$ s), the value of k_d must be limited to avoid excessive noise excitation and flexural modes destabilization. The chosen value $k_d = 15$ As/m produces damping at approximately 20% of critical for the rigid-body modes. To verify the theoretical model and system characteristics under the closed-loop control, experimental identification of the frequency response for $\mathbf{P}_{\text{act}}(s, \Omega)$ was undertaken for zero speed ($\Omega = 0$). The results in Fig. 7 indicate a good level of agreement and confirm the suitability of the model for further analysis. A Campbell diagram showing speed dependency of the system natural frequencies is given in Fig. 8. Considering the first eight harmonic components of rotor noncircularity as possible excitation sources, this plot indicates at what speeds significant excitation of the rigid-body mode ($m = 1$) and first flexural modes ($m = 2$) may be anticipated over the intended speed range of 0–30 Hz.

To suppress resonance while reducing transmission of bearing forces, the effective controller was chosen as a modified PD control law:

$$\mathbf{K}_{\text{eff}}(s) = -\left(\frac{29.5s + 4500}{0.001s + 1}\right)\mathbf{I}_{2\times 2}$$

This controller (equivalent PD gains $k_p = 4500$ A/m and $k_d = 25$) would result in a very low bearing stiffness (approx. 1800 N/m) if

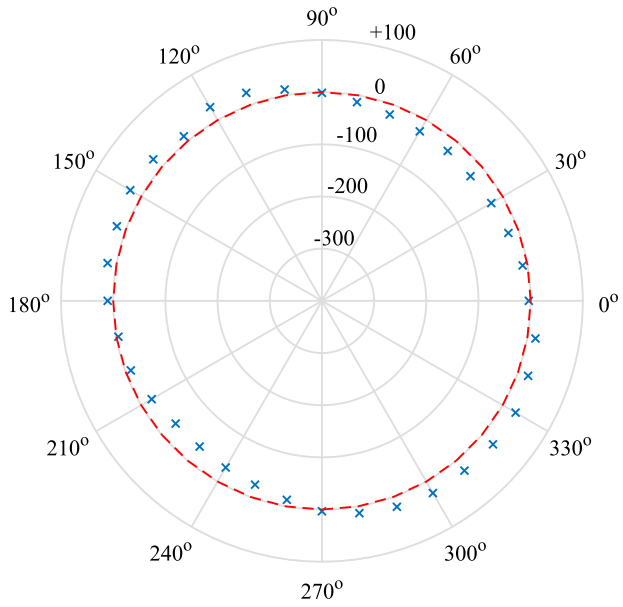

Fig. 10 Measured noncircularity of an experimental thin-walled rotor: inner surface location in sensor plane (units: μm)

Table 2 Measured rotor noncircularity: Fourier coefficients for profile error

	Fourier coefficients	
Harmonic j	Amplitude a_j (μm)	Phase ψ_j (deg)
2	28.4	−85.96
3	3.1	18.26
4	3.4	24.41
5	2.5	42.27
6	2.1	89.29
7	1.0	48.86
8	1.5	−29.83

used directly for the feedback control and would not achieve stable levitation. However, the frequency domain properties show much improved disturbance attenuation for the frequency range of concern, with near-elimination of resonances: Predicted frequency response characteristics for $\mathbf{P}_{\text{eff}}(s, 0)$ are shown in Fig. 7. Further analysis of the vibration control performance with the HVC algorithm is given in Sec. 5.1, while experimental results are presented in Sec. 5.2.

5.1 Numerical Analyses. Numerical predictions of steady-state vibration response behavior were obtained for three different cases:

(1) Dynamic feedback of displacement sensor signals for bearing stabilization (controller $\mathbf{K}_{\text{act}}$ only).
(2) Feedback with exact sensor-based noncircularity cancellation (controller $\mathbf{K}_{\text{act}}$ and $\tilde{\mathbf{d}}_S = \mathbf{d}_S$).
(3) With HVC to achieve desired effective control action (controller $\mathbf{K}_{\text{eff}}$ and $\tilde{\mathbf{d}}_S = 0$).

As these are reference cases, every harmonic component of the rotor noncircularity error was assigned an amplitude of 25 μm. The first harmonic component of the vibration, which arises due to synchronous forcing rather than noncircularity error, is neglected. For case 1 shown in Fig. 9, every harmonic component exhibits a

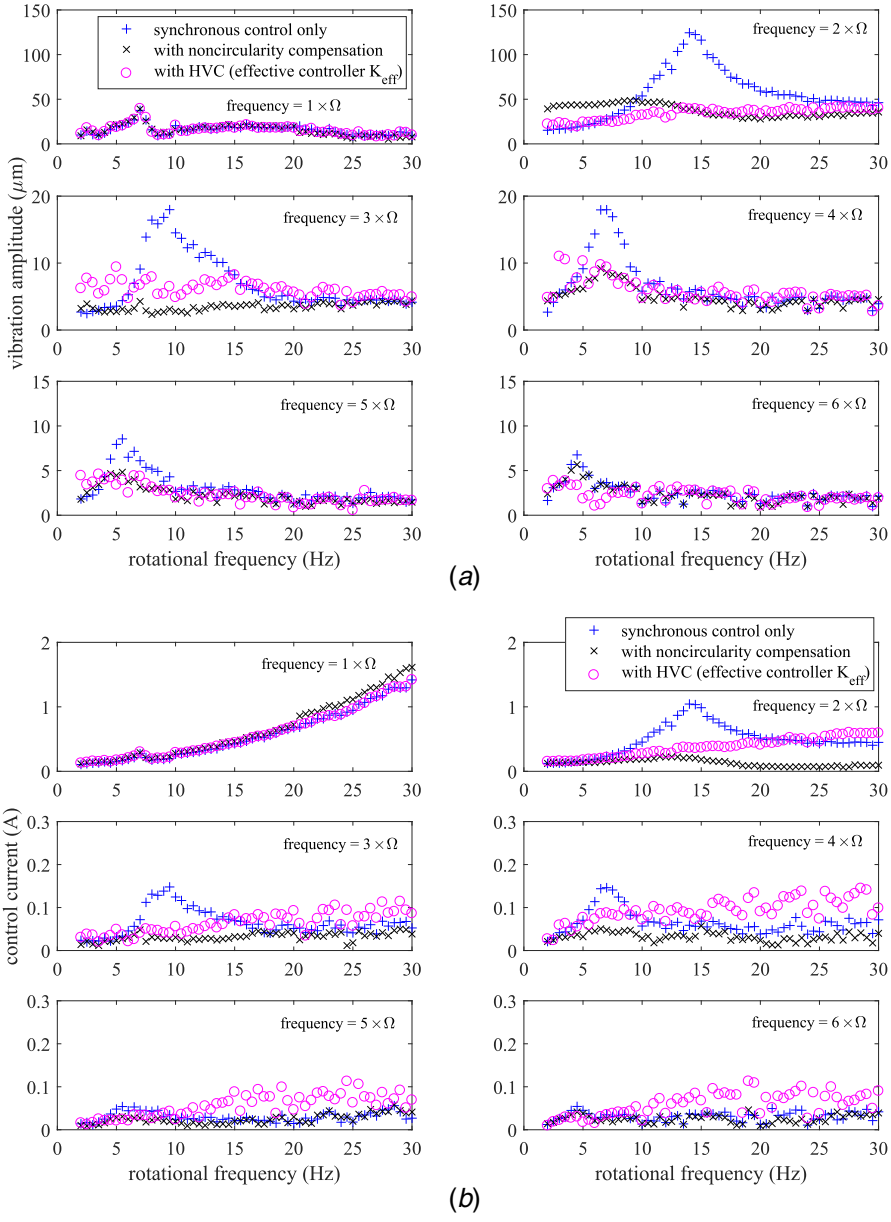

Fig. 11 Rotor vibration components arising due to noncircularity excitation. Experimental data for (*a*) sensor measurements and (*b*) control currents.

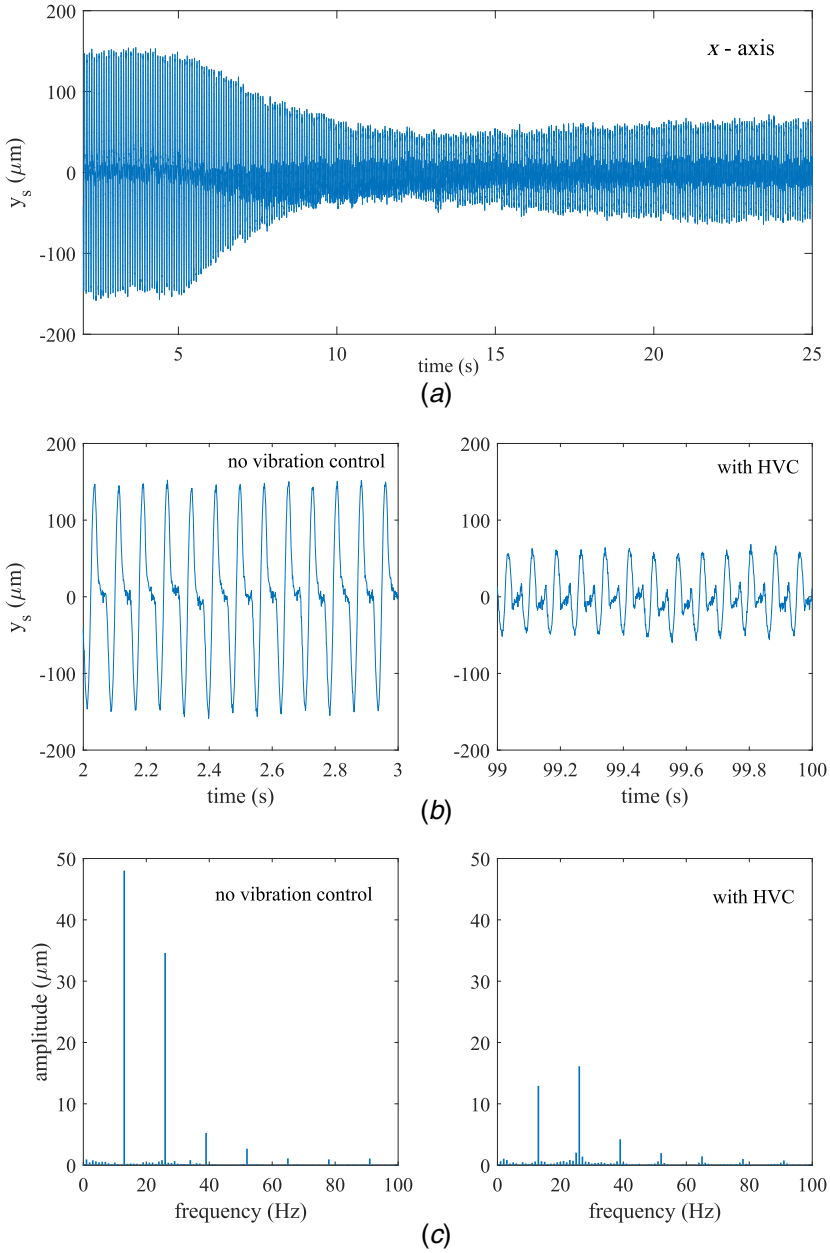

Fig. 12 Rotor vibration measurements during controller activation $\Omega = 13$ Hz: (*a*) transient behavior, (*b*) steady-state waveforms before and after HVC activation, and (c) Fourier transforms of steady-state waveforms

resonance corresponding to the natural frequency of 27 Hz. Resonance occurs whenever this natural frequency is an integer multiple of the rotational frequency. Both the noncircularity compensation scheme and the HVC algorithm (effective control $\mathbf{K}_{\text{eff}}$) alleviate the resonance conditions. Flexural mode excitation remains quite low even without applying additional vibration control algorithms owing to the distributed actuation topology and optimized coil-winding pattern. Two additional cases for inexact noncircularity compensation ($\tilde{\mathbf{d}}_S = 0.5\mathbf{d}_S$), both with and without HVC, are shown in Fig. 9 (as cases 4 and 5, respectively). It is seen that resonances still occur with inexact cancellation but can be suppressed effectively by the combined application of HVC.

5.2 Experimental Results. Noncircularity of the experimental rotor was first determined offline by mounting the rotor on a turntable and measuring the surface position under slow-rotation. These data are shown in Fig. 10, with corresponding Fourier coefficients given in Table 2. Three different control methods were implemented and tested that correspond to the first three simulated cases described in Sec. 5.1:

(1) Stabilizing feedback control $\mathbf{K}_{\text{act}}$ and synchronous vibration control only.
(2) As case 1 but with additional sensor-based noncircularity compensation.
(3) As case 1 but with additional HVC to achieve effective control $\mathbf{K}_{\text{eff}}$.

In all cases, the first harmonic component of vibration was suppressed by a synchronous control algorithm so that the amplitudes remained less than 50 μm for all three cases. The first six harmonic components of the (x-axis) sensor signal are shown in Fig. 11. The second ($2 \times \Omega$) harmonic, which corresponds to the largest noncircularity component, was the dominant component of vibration. For case 1, a large resonance occurred when the rotational

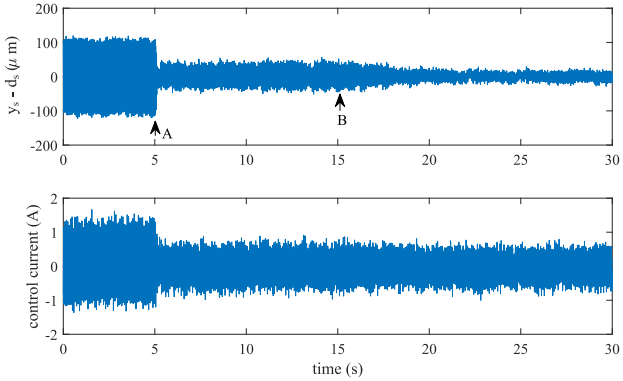

Fig. 13 Residual vibration $\mathbf{y}_S - \tilde{\mathbf{d}}_S$ at $\Omega = 13$ Hz. After 5 s, sensor-based noncircularity compensation is applied (A), and after 15 s, HVC is additionally applied (B).

frequency was 14 Hz. Both the noncircularity compensation and the HVC algorithm were effective in suppressing this resonance.

With noncircularity compensation, some small resonances are still seen for the higher harmonics. This is due to the errors in the run-out identification as well as residual excitation effects that are not associated with the position sensor signals. The overall behavior is consistent with the model-based predictions shown in Fig. 9. Note that, for the experimental system, the excitation of the $7\times\Omega$ and $8\times\Omega$ harmonics was too small to be clearly detected, and therefore, these data are not presented. Figure 11(*b*) shows that some noise effects were present for the higher harmonic components of the control currents with HVC applied, but the overall amplitudes remained low, at less than 0.2 A. Note also that vibration suppression and control stability were maintained even when the harmonic control frequencies pass through the flexural mode frequencies. This is possible due to the dynamic compensation scheme incorporating the flexible rotor model.

Convergence behavior of the HVC algorithm is shown in Fig. 12. With the rotor operating at a rotational frequency of 13 Hz, high levels of multiharmonic vibration were initially present. The amplitudes of the first two harmonic components were 48 μm and 35 μm, respectively. Activation of the HVC algorithm gave steady attenuation over approximately 10 s.

Although attenuation occurs quickly, changes in the rotor speed that are too rapid lead to a worsening in control performance. Small fluctuations in rotor speed can also prevent expected steady-state levels of vibration attenuation being achieved.

The best results were obtained when noncircularity compensation and HVC were applied together. In this case, the HVC algorithm deals with residual excitation and errors due to inexact knowledge of the noncircularity. The overall vibration attenuation performance was similar to when applying HVC alone, but control current amplitudes were reduced. Figure 13 shows the *x*-component of the residual sensor signal $\mathbf{y}_S - \tilde{\mathbf{d}}_S$ after noncircularity compensation. Initially, the system is operating with feedback of the raw sensor signals $\mathbf{y}_S$ when (after 5 s) the sensor-based noncircularity compensation is applied so that the feedback signal becomes $\mathbf{y}_S - \tilde{\mathbf{d}}_S$. After a further 10 s, the HVC algorithm is additionally operating. This produces a further reduction in vibration levels without noticeable change in control current levels.

6 Conclusions

To reduce the multiharmonic vibration of a flexible thin-walled rotor supported by a distributed actuation magnetic bearing, a control algorithm has been devised that adaptively modifies the harmonic components of the actuator control currents so that the vibration attenuation matches a targeted closed-loop system model. The approach avoids the need for information on the state of rotor noncircularity, yet achieves effective suppression of vibration due to multiple complex excitation mechanisms. Experiments conducted on a short thin-walled rotor with single DAMB confirmed the efficacy of the methods in preventing resonance during operation. Combining sensor-based noncircularity compensation with the harmonic vibration control algorithm is seen to be a good practical solution as a reduction in vibration levels can be achieved without precise knowledge of the rotor shape, and with minimal bearing forces. Future work will aim to extend the approach for application with longer thin-walled rotors having DAMB support in multiple planes.

Funding Data

- Thailand Research Fund (10.13039/501100004396) (Grant No. BRG5980013).
- Chiang Mai University (10.13039/501100002842).

References

[1] Schweitzer, G., and Maslen, E. H., eds., 2009, *Magnetic Bearings, Theory, Design, and Application to Rotating Machinery*, Springer-Verlag, Berlin.

[2] Schneeberger, T., Nussbaumer, T., and Kolar, J. W., 2010, "Magnetically Levitated Homopolar Hollow-Shaft Motor," IEEE/ASME Trans. Mechatron., **15**(1), pp. 97–107.

[3] Lusty, C., Sahinkaya, M. N., and Keogh, P. S., 2016, "A Novel Twin-Shaft Rotor Layout With Active Magnetic Couplings for Vibration Control," Proc. Inst. Mech. Eng., Part I: J. Syst. Control Eng., **230**(3), pp. 266–276.

[4] Cole, M. O. T., and Fakkaew, W., 2018, "An Active Magnetic Bearing for Thin-Walled Rotors: Vibrational Dynamics and Stabilizing Control," IEEE/ASME Trans. Mechatron., **23**(6), pp. 2859–2869.

[5] Fakkaew, W., Cole, M. O. T., 2018, "Vibration Due To Noncircularity of a Rotating Ring Having Discrete Radial Supports—With Application to Thin-Walled Rotor/Magnetic Bearing Systems," J. Sound Vib., **423**, pp. 355–372.

[6] Roche, J. M., Palac, D. T., Hunter, J. E., Myers, D. E., Snyder, C. A., Kosareo, D. N., McCurdy, D. R., and Dougherty, K. T., 2005, "Investigation of Exoskeletal Engine Propulsion System Concept," NASA Report No. NASA–2005-213369.

[7] Peters, D., Kaletsch, C., Nordmann, R., and Domes, B., "Test Rig for a Supercritical Rotor of an Aero Engine," Proceedings of the 12th IFToMM World Congress, Besançon, France, June 17–21, 2007.

[8] Genta, G., 2005, *Dynamics of Rotating Systems*, Springer, New York.

[9] Mohamed, A. M., and Busch-Vishniac, I., 1995, "Imbalance Compensation and Automation Balancing in Magnetic Bearing Systems Using the Q-Parametrization Theory," IEEE Trans. Control Syst. Technol., **3**(2), pp. 202–211.

[10] Lum, K.-Y., Coppola, V. T., and Bernstein, D. S., 1996, "Adaptive Autocentering Control for an Active Magnetic Bearing Supporting a Rotor With Unknown Mass Imbalance," IEEE Trans. Control Syst. Technol., **4**(5), pp. 587–597.

[11] Knospe, C., Hope, R., Fedigan, S., and Williams, R., 1995, "Experiments in the Control of Unbalanced Response Using Magnetic Bearings," Mechatronics, **5**(1), pp. 385–400.

[12] Herzog, R., Buhler, P., Gahler, C., and Larsonnoeur, R., 1996, "Unbalance Compensation Using Generalized Notch Filters in the Multivariable Feedback of Magnetic Bearings," IEEE Trans. Control Syst. Technol., **4**(5), pp. 581–586.

[13] Cui, P., Li, S., Zhao, G., and Peng, C., 2016, "Suppression of Harmonic Current in Active-Passive Magnetically Suspended CMG Using Improved Repetitive Controller," IEEE/ASME Trans. Mechatron., **21**(4), pp. 2132–2141.

[14] Nonami, K., and Liu, Z., "Adaptive Unbalance Vibration Control of Magnetic Bearing System Using Frequency Estimation for Multiple Periodic Disturbances with Noise," Proceedings of IEEE Conference on Control Applications, Kohala Coast, HI, Aug. 22–27, 1999. IEEE, Piscataway, NJ.

[15] Chen, Q., Liu, G., and Han, B., 2017, "Unbalance Vibration Suppression for AMB System Using Adaptive Notch Filter," Mech. Syst. Signal Process., **93**, pp. 136–150.

[16] Cole, M. O. T., and Keogh, P. S., 2003, "Rotor Vibration With Auxiliary Bearing Contact in Magnetic Bearing Systems. Part 2: Robust Synchronous Control for Rotor Position Recovery," Proc. Inst. Mech. Eng., Part C: J. Mech. Eng. Sci., **217**(4), pp. 393–409.

[17] Chamroon, C., Cole, M. O. T., and Wongratanaphisan, T., 2014, "An Active Vibration Control Strategy to Prevent Nonlinearly Coupled Rotor-Stator Whirl Responses in Multimode Rotor-Dynamic Systems," IEEE Trans. Control Syst. Technol., **22**(3), pp. 1122–1129.

[18] Wang, M., Cole, M. O. T., and Keogh, P. S., 2017, "New LMI Based Gain-Scheduled Control for Recovering Contact-Free Operation of a Magnetically Levitated Rotor," Mech. Syst. Signal Process., **96**, pp. 104–124.

[19] Cole, M. O. T., Chamroon, C., and Keogh, P. S., 2017, "H-Infinity Controller Design for Active Magnetic Bearings Considering Nonlinear Vibrational Rotordynamics," JSME Mech. Eng. J., **4**(5), 16-00716.

[20] Chen, Q., Liu, G., and Zheng, S., 2015, "Suppression of Imbalance Vibration for AMB Controlled Driveline System Using Double-Loop Structure," J. Sound Vib., **337**, pp. 1–13.

[21] Xu, X., and Chen, S., 2015, "Field Balancing and Harmonic Vibration Suppression in Rigid AMB-Rotor Systems with Rotor Imbalances and Sensor Runout," Sensors, **15**(9), pp. 21876–21897.

[22] Jiang, K., Zhu, C., 2011, "Multi-Frequency Periodic Vibration Suppressing in Active Magnetic Bearing-Rotor Systems Via Response Matching in Frequency Domain," Mech. Syst. Signal Process., **25**, pp. 1417–1429.
[23] Darbandi, S. M., Habibollahi, A., Behzad, M., and Salarieh, H., 2016, "Sensor Runout Compensation in Active Magnetic Bearings Via an Integral Adaptive Observer," Control Eng. Pract., **48**, pp. 111–118.
[24] Setiawan, J. D., Mukherjee, R., and Maslen, E. H., 1999, "Adaptive Compensation of Sensor Runout for Magnetic Bearings With Uncertain Parameters: Theory and Experiments," ASME J. Dyn. Syst. Meas. Control, **123**(2), pp. 211–218.
[25] Siva Srinivas, R., Tiwari, R., and Kannababu, Ch., 2018, "Application of Active Magnetic Bearings in Flexible Rotordynamic Systems–A State-of-The-Art Review," Mech. Syst. Signal Process., **106**, pp. 537–572.
[26] Cole, M. O. T., Keogh, P. S., Burrows, C. R., and Sahinkaya, M. N., 2006, "Adaptive Control of Rotor Vibration Using Compact Wavelets," ASME J. Vib. Acoust., **128**(5), pp. 653–665.
[27] Manchala, D. W., Palazzolo, A. B., Lin, A. K., Kasak, A. K., Montague, J., and Brown, G. V., 1997, "Constrained Quadratic Programming Active Control of Rotating Mass Imbalance," J. Sound Vib., **205**(5), pp. 561–580.
[28] Sahinkaya, M., Abulrub, A. G., and Burrows, C. R., 2011, "An Adaptive Multi-Objective Controller for Flexible Rotor and Magnetic Bearing Systems," ASME J. Dyn. Syst. Meas. Control, **133**(3), p. 031003.
[29] Endo, M., Hatamura, K., Sakata, M., and Taniguchi, O., 1984, "Flexural Vibration of a Thin Rotating Ring," J. Sound Vib., **92**(2), pp. 261–272.

Bulletin of the JSME Vol.4, No.5, 2017
Mechanical Engineering Journal

H-infinity controller design for active magnetic bearings considering nonlinear vibrational rotordynamics

Matthew O. T. COLE*, Chakkapong CHAMROON** and Patrick S. KEOGH***
*Department of Mechanical Engineering, Chiang Mai University,
239 Huay Gaew Rd, Chiang Mai 50200, Thailand.
E-mail: motcole@hotmail.com
**School of Engineering, University of Phayao
19 Maeka, Phayao 56000, Thailand.
***Department of Mechanical Engineering, University of Bath,
Bath BA2 7AY, UK.

Received: 28 December 2016; Revised: 4 May 2017; Accepted: 10 August 2017

Abstract
This paper deals with optimal controller design for active magnetic bearing (AMB) systems for which nonlinear rotordynamic behavior is evident, and so vibration predicted by operating point linearization differs from that which occurs in actuality. Nonlinear H-infinity control theory is applied with a rotordynamic model involving nonlinear stiffness and/or damping terms. The associated Hamilton-Jacobi-Isaacs (HJI) equation is formulated and solved to obtain a state feedback control law achieving specified vibration attenuation performance in terms of the peak L_2 gain of the nonlinear system. The method is applied in case study to a flexible rotor/AMB system that exhibits nonlinear stiffness properties owing to rotor interaction with a clearance bearing. Simulations are performed to quantify RMS vibration due to harmonic disturbances and the results compared with the norm-bound values embedded in the HJI equations. A feedback controller design method is then presented that is similar in approach to the standard loop-shaping/mixed-sensitivity methods used for linear systems, and involves augmenting the system model with weighting transfer functions. Experiments are undertaken to compare controller performance for designs based on nonlinear and linearized models. The results highlight the shortcomings of applying linear optimal control methods with rotor systems exhibiting nonlinear stiffness properties as large amplitude vibration and loss of rotordynamic stability can occur. Application of the described nonlinear H-infinity control method is shown to overcome these problems, albeit at the expense of vibration attenuation performance for operation in linear regimes.

Keywords : Rotor vibration, Magnetic bearings, H-infinity control, Nonlinear dynamics

1. Introduction

The successful application of modern optimal and robust control methodologies with AMB/rotor systems has been widely reported. For frequency domain analysis and design, industry standards have now been established that fit well within the framework of linear H-infinity control (Schweitzer and Maslen, 2009). In this framework, specifications for rotor vibration attenuation are defined using system norm-bound criteria, which can directly account for external disturbances having specified sources and spectral characteristics, e.g. sensor noise, rotor unbalance and external motions. The limitations of a linear design may be exposed, however, when large amplitude vibration occurs, or when the rotor equilibrium position varies significantly during operation, as nonlinear effects can then become important.

Previous work on active control of vibration in nonlinear rotordynamic systems covers quite diverse aspects. Unbalance compensation for a single-disk rotor with nonlinear supports was considered by Inoue et al. (2009). Control of synchronous vibration for a rotor supported by magnetic bearings when contacting with clearance bearings was investigated by Cole and Keogh (2003) and Chamroon et al., (2014), while active clearance bearings have also been

Paper No.16-00716
J-STAGE Advance Publication date: 24 August, 2017
[DOI: 10.1299/mej.16-00716]

proposed for a similar purpose in (Cade et al., 2010). In other work, destabilizing nonlinear effects have been accounted for in controller designs via linear approximations (Simon and Flowers, 2008, El-Shafai and Dimitri 2010, Karkoub, 2011). Nonlinear H-infinity control methods have been applied previously with magnetic bearings to deal with nonlinear properties of the AMBs (rather than rotordynamics) as, for example, by Sinha and Pechov (2005).

According to standard definitions, an optimal H-infinity controller for a nonlinear system achieves a minimum value for the peak RMS gain, i.e. minimizes the induced L_2 to L_2 norm of the closed loop system. The solution can be found by solving a partial differential equation known as the Hamilton-Jacobi-Isaacs (HJI) equation (Van der Schaft, 1992, Isidori and Alstofi 1992). This is usually a difficult task, due to nonlinearity of the HJI equation and non-uniqueness of the solution in the suboptimal case. It is shown here that, for rotordynamic models incorporating nonlinear stiffness and/or damping effects, a solution to the HJI equation (in inequality form) can be obtained by numerical optimization if a certain form of Lyapunov function is adopted. The main aim of this paper is to investigate whether the obtained solutions are practically useful for enhancing vibration suppression qualities of AMB control for rotors that exhibit significant nonlinear dynamic behavior.

2. Nonlinear rotordynamic model

Vibration of a nonlinear rotordynamic system subject to disturbance forces d and magnetic bearing control forces u, applied directly to the rotor, may be described by a matrix equation in the form

$$M\ddot{s} + G\dot{s} + Ks = E_f f(s,\dot{s}) + E_u u + E_d d \tag{1}$$

The vector f comprises a set of internal forces that vary as nonlinear functions of a subset of velocity and/or displacement states, which will be denoted z. Defining the state vector $x^T = [s^T\ \dot{s}^T]$, a state space representation is

$$\dot{x} = Ax + B_f f(z) + B_d d + B_u u \tag{2}$$

$$z = Cx \tag{3}$$

$$A = \begin{bmatrix} 0 & I \\ -M^{-1}K & -M^{-1}G \end{bmatrix},\ B_u = \begin{bmatrix} 0 \\ M^{-1}E_u \end{bmatrix}, B_d = \begin{bmatrix} 0 \\ M^{-1}E_d \end{bmatrix}, B_f = \begin{bmatrix} 0 \\ M^{-1}E_f \end{bmatrix} \tag{4}$$

A linearized model for the equilibrium point $x = 0$ is given by Eq. (2) with $f = 0$. For the purpose of controller design, it is appropriate to further define a set of output variables for inclusion in a cost function. These may be expressed as a linear function of x and u:

$$y = C_y x + D_u u \tag{5}$$

3. Existence of H-infinity controllers

The peak L_2 gain for a nonlinear system described by Eqs (2)-(5) may be defined as

$$Peak\ Gain_{L_2} = \sup_{d\neq 0} \frac{\|y\|_2}{\|d\|_2} \tag{6}$$

where $\|.\|_2$ denotes the signal L_2-norm: $\|y\|_2 = \left(\int_{-\infty}^{\infty} y(t)^2 dt\right)^{\frac{1}{2}}$. It is well known that for linear systems the peak L_2 gain is a time-domain version of the H-infinity norm. According to standard theory, under the assumptions $D_u^T C_y = 0$ and $D_u^T D_u = I$, if there exists a positive semi-definite function $V(x) \geq 0$ with bounded Jacobian $V_x(x) = dV/dx$ satisfying the Hamiltonian-Jacobi-Isaacs equation given by

$$V_x\left(Ax + B_f f(z)\right) + x^T C_y^T C_y x + \frac{1}{4}\gamma^{-2} V_x B_d B_d^T V_x^T - \frac{1}{4} V_x B_u B_u^T V_x^T = 0 \tag{7}$$

then, the control law $u = -\frac{1}{2}B_u^T V_x^T$ renders the controlled system stable with $Peak\ Gain_{L_2} < \gamma$ (see Isidori and Astolfi, 1992). In general, it is difficult to solve Eq. (7) unless some assumptions are made about the form of $V(x)$. Although methods based on multi-dimensional Taylor series expansions can be used (Sinha and Pechev, 2004; Abu-Khalaf et al., 2006) the numerical complexity for high order systems is prohibitive. For this study, a quadratic function is considered with additional higher order terms in the nonlinear variables z only. This can be expressed

$$V(x) = x^T P x + 2g(z) \tag{8}$$

where $P = P^T > 0$. Given that $V_x = 2x^T P + 2g_z C$, where $g_z = dg/dz$, the HJI equation becomes

[DOI: 10.1299/mej.16-00716]

$$x^T\left(PA + A^TP + C_y^TC_y\right)x + \gamma^{-2}x^TPB_dB_d^TPx - x^TPB_uB_u^TPx + 2g_z(z)CB_ff(z) + 2\left(f(z)^TB_f^TP + g_z(z)CA\right)x = 0 \quad (9)$$

If no assumptions are made about how f depends on z, the first three quadratic terms in x and remaining nonlinear terms must sum independently to zero. This requires $CB_f = 0$ and $f(z)^TB_f^TP + g_z(z)CA = [0]$. By choosing

$$g_z(z) = f(z)^T\Sigma \quad (10)$$

it then follows that equation (9) will hold if Σ and P satisfy

$$B_f^TP + \Sigma CA = [0] \quad (11)$$

$$PA + A^TP + C_y^TC_y + \gamma^{-2}PB_dB_d^TP - PB_uB_u^TP = [0] \quad (12)$$

From Eq. (10),

$$V(x) = x^TPx + 2\int_0^{Cx} f(z)^T\Sigma\, dz \geq 0$$

Hence, the requirement that $V(x)$ is positive semi-definite imposes further restrictions on the allowed values of Σ. Nonetheless, if a solution (P, Σ) to equations (11) and (12) can be found which is feasible (in the sense $V(x) \geq 0$) then this provides the nonlinear state feedback control law

$$u = -\tfrac{1}{2}B_u^TV_x^T = -B_u^TPx - B_u^TC^T\Sigma^Tf(z) \quad (13)$$

which renders $Peak\ Gain_{L_2} < \gamma$ for the controlled system.

A less strict condition than that imposed by Eqs. (11) and (12) can be derived when the nonlinear force function $f(z)$ is a conservative vector field and is known to satisfy a quadratic constraint in the form

$$f^Tf - f^TNz - z^TMz \leq 0 \quad (14)$$

In this case, a sufficient condition for a solution to Eq. (9) to exist is that there exists feasible (P, Σ) such that

$$x^T\left(PA + A^TP + C_y^TC_y + \gamma^{-2}PB_dB_d^TP - PB_uB_u^TP\right)x + 2f^{\mathrm{T}}\Sigma CB_ff + 2f^T\left(B_f^TP + \Sigma CA\right)x < 0 \quad (15)$$

This inequality must hold only for values of f satisfying (14). Via application of the so-called *S*-procedure (Boyd et al., 1994), the constraints (14) and (15) can be combined, leading to the following sufficient condition in matrix inequality form:

There exists $P = P^T > 0$, $\Sigma = \Sigma^T \geq 0$ *and scalar* $\mu > 0$ *satisfying*

$$\begin{bmatrix} A^TP + PA - PB_uB_u^TP + \mu 2CMC^T & PB_f + A^TC^T\Sigma^T + C^TN^T\mu & PB_d & C_y^T \\ B_f^TP + \Sigma CA + \mu NC & -2\mu I + \Sigma CB_f + B_f^TC^T\Sigma^T & 0 & 0 \\ B_d^TP & 0 & -\gamma^2 I & 0 \\ C_y & 0 & 0 & -I \end{bmatrix} < 0 \quad (16)$$

The controller is again given by Eq. (13).

An important case for rotordynamic systems, and particularly those with AMBs, is when the non-linear force is associated with rotor-stator interaction. This may be due to bearings with internal clearances, direct contact between a rotor and stator over a clearance space, seals with clearances, or more complex bearing characteristics. To apply the method described here, it must be possible to determine matrices N and M such that $f(z)$ will satisfy (14). In what follows, the focus will be on a situation where rotor-stator interaction involves a radial interaction force F (scalar) that depends only on the radial displacement $|z|$ where $z = [z_X\ z_Y]^T$ includes orthogonal displacement variables for the rotor in a lateral plane. The orthogonal components for the interaction force are then defined by $f = [f_X\ f_Y]^T$ with

$$f_X = \tfrac{z_X}{|z|}F(|z|),\ f_Y = \tfrac{z_Y}{|z|}F(|z|) \quad (17)$$

Suppose that $F(|z|)$ is a nonlinear function satisfying $0 \leq F(|z|)/|z| \leq \bar{\kappa}$ where $F(|z|)/|z|$ may be considered as the equivalent linear stiffness for a given value of $|z|$. The following equation can then be shown to hold:

$$f^T(f - \bar{\kappa}z) \leq 0, \quad \bar{\kappa} = sup\tfrac{F(|z|)}{|z|} \quad (18)$$

Comparing Eq. (18) with Eq. (14), it can be seen that the H-infinity controller solution may be found by solving Eq.

[DOI: 10.1299/mej.16-00716]

(16) with $N = \bar{\kappa}I$ and $M = 0$. Specifically, the following feasibility problem must be solved for a given γ value:

Find $P = P^T > 0$, $\Sigma \geq 0$ *and scalar* $\mu > 0$ *satisfying*

$$\Phi(P,\Sigma,\mu) = \begin{bmatrix} A^TP + PA - PB_uB_u^TP & PB_f + A^TC^T\Sigma^T + C^T\bar{\kappa}\mu & PB_d & C_y^T \\ B_f^TP + \Sigma CA + \mu\bar{\kappa}C & -2\mu I + \Sigma CB_f + B_f^TC^T\Sigma^T & 0 & 0 \\ B_d^TP & 0 & -\gamma^2 I & 0 \\ C_y & 0 & 0 & -I \end{bmatrix} < 0 \tag{19}$$

To convert Eq. (16) (or Eq. (19)) to a linear matrix inequality (LMI) problem that can be solved using standard convex optimization routines, some transformations must be applied, as shown in the Appendix. To find a solution giving minimum norm value, the value of γ must also be minimized.

It should be remarked that for systems with nonlinear stiffness effects (as in Eq. (17)) the output matrix C will be orthogonal to the input matrices B_u and B_f and so $CB_f = CB_u = 0$. In consequence, the feedback control law (Eq. (13)) no longer involves f and is a linear state feedback law (as for the linear H-infinity solution), although the gains will be optimized for the nonlinear dynamics. For the linear H-infinity controller, synthesis may be undertaken (for the linearized system with $f = 0$) by solving the LMI problem Eq. (19) with the second row and column omitted from Φ. This case will be considered for comparison purpose in the experimental study.

4. Vibration analysis and controller design for a flexible rotor

4.1 System description

The described nonlinear H-infinity control approach was applied to the experimental rotor-AMB system shown in Fig. 1. The rotor is constructed from a steel shaft of length 700 mm and diameter 10 mm supported by ball bearings at each end. Two disks are fixed on the shaft. Disk 1 has mass 0.36 kg and forms the hub of the AMB. A backup bearing with radial clearance of 1 mm is also installed within the AMB. Disk 2, which has a mass 1.12 kg, is surrounded by a clearance ring which is compliantly supported by a force-sensing unit comprising four cantilever supports (stator unit), as shown in Fig. 1c. The ring may contact with a lubricated aluminium ring fixed to the rotor disk and having a radial clearance of 0.4 mm. Pairs of non-contact probes measure lateral displacement in orthogonal directions at both disks. The AMB was initially operated under PD feedback control. Large amplitude vibration leads to contact interaction between disk 2 and the surrounding ring and this contributes a nonlinear stiffness effect on rotordynamic behavior.

To model the system, the state vector may be partitioned according to X and Y axis coordinates: $x^T = [x_X^T\ x_Y^T]$. The system inputs are the AMB forces applied at disk 1, $u = [u_X\ u_Y]^T$, the non-linear interaction force acting at disk 2, $f = [f_X\ f_Y]^T$, and external (unbalance) force disturbances represented by $d = [d_X\ d_Y]^T$. A model of rotor vibration may be defined in the form of Eqs (2) and (3) with

$$A = \begin{bmatrix} A_{XX} & A_{XY} \\ A_{YX} & A_{YY} \end{bmatrix},\ B_f = \begin{bmatrix} B_2 & 0 \\ 0 & B_2 \end{bmatrix},\ B_u = B_d = \begin{bmatrix} B_1 & 0 \\ 0 & B_1 \end{bmatrix},\ C = \begin{bmatrix} C_2 & 0 \\ 0 & C_2 \end{bmatrix}, \tag{20}$$

where B_1 and B_2 are appropriate for input forces applied at disk 1 and disk 2, respectively. Similarly, C_2 is the output matrix appropriate to displacement at disk 2. For this system definition, the disturbance force d acts in the same plane as the control force u (at disk 1). For the nominal rotational speed range of 0-200 rad/s, which includes the first critical speed, gyroscopic coupling between *X*-*Z* and *Y*-*Z* planes is negligible and hence $A_{XY} = A_{YX} = 0$.

A system identification approach was used to obtain values for the system matrices in Eq. (20) based on frequency response measurements for small-amplitude vibration. The system behaviour was found to be quite linear if contact at the clearance ring was avoided. Note that the control forces u act in addition to the feedback components from the PD controller, which is already accounted for within the model. The state sub-vectors $x_{X,Y}$ each have four states that capture the first two natural modes for vibration in lateral planes. The PD control was implemented with a low-pass filter. However, the filter dynamics did not significantly affect the system response over the bandwidth for vibration control (<1000 rads/s) and hence a fourth order model was appropriate. The PD controller gains were set to give only moderate stiffness and damping from the bearing so that the response characteristics are similar to those for the rotor without the AMB operating. Hence, the main control effects will be derived from the optimized control component u.

[DOI: 10.1299/mej.16-00716]

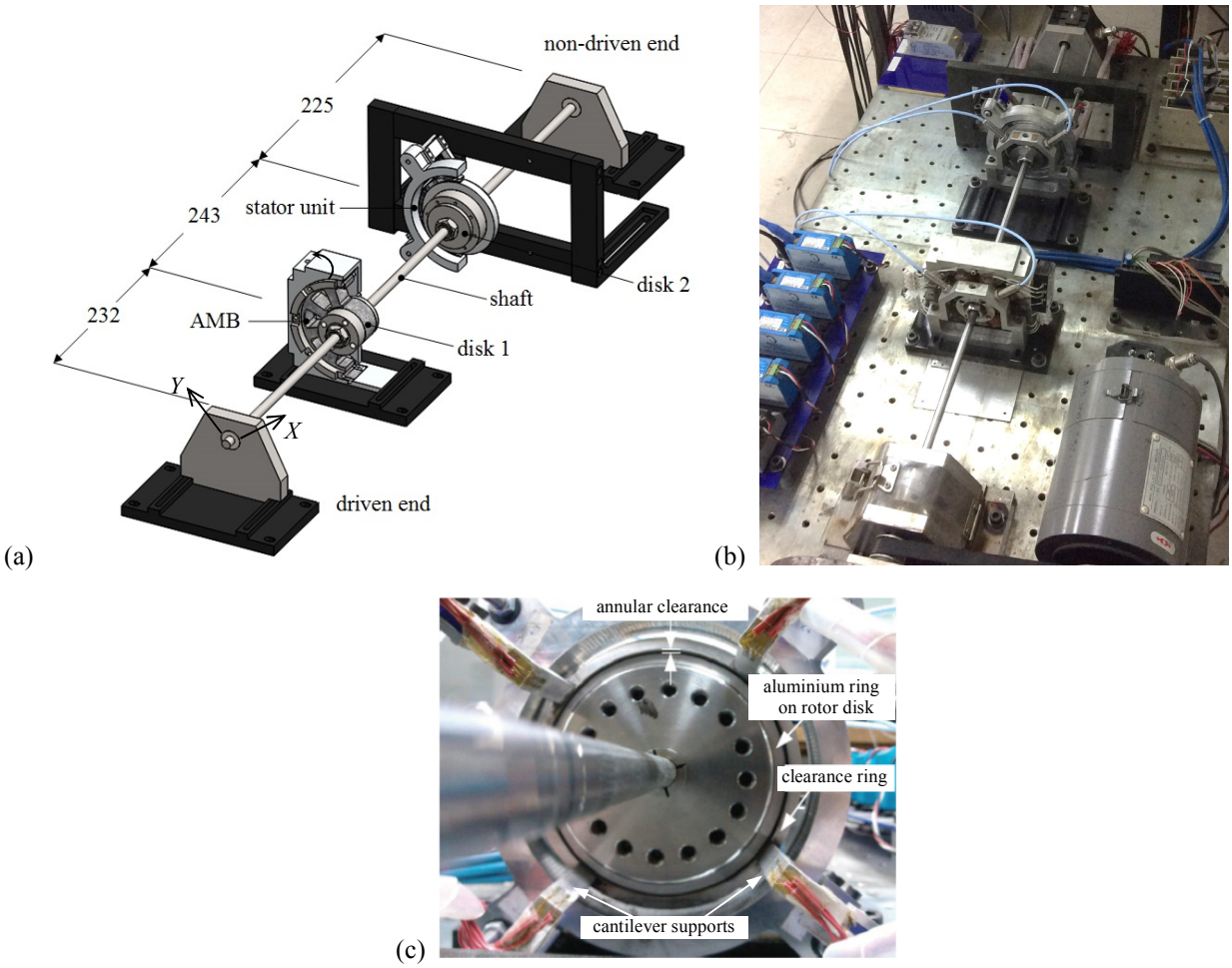

Fig. 1 Experimental flexible rotor-AMB system: (a) CAD model, (b) test bench, (c) rotor and clearance ring

4.2 Nonlinear vibration analysis via LMIs

Prior to undertaking the controller design, a numerical study was performed where the LMI analysis results (norm-bound values) were compared with the system L_2 gain characteristics obtained from simulations. For this study, the PD-controlled system was considered (without the optimized control input u). The system disturbance for simulation involved harmonic forcing in a single direction at disk 1: $d_X(t) = m_e\Omega^2 \cos\Omega t$, $d_Y(t) = 0$. A nonlinear radial rotor-stator interaction force was applied according to Eq. (17) with a cubic nonlinear function $F(|z|) = \beta\,|z|^3$. This function was chosen as a bench-mark case similar to a Duffing term, as defined for single degree of freedom nonlinear oscillators. It is also representative of the experimental system in that it imposes a stiffening effect that increase with vibration amplitude. The system output for the L_2 gain evaluation was defined according to Eq. (5) with $u = 0$ and

$$C_y = \begin{bmatrix} C_2 & 0 \\ 0 & C_2 \end{bmatrix} \tag{21}$$

such that the output y is the lateral displacements at disk 2.

Time-step integration of the system equations defined by Eqs. (2), (3) and (5) with $u = 0$ and with the model matrices defined by Eq. (20) and (21) was performed for a range of values of forcing frequency Ω and nonlinear parameter β. For each simulation run the L_2 gain was calculated as $\|y\|_2/\|d\|_2$. The results are shown as scattered points in Fig. 2. For the linear case ($\beta = 0$), two resonant peaks are clearly evident and are associated with the first and second natural modes for lateral vibration of the flexible rotor. For larger values of β, constraining effects due to the nonlinear stiffness tend to reduce the amplitude of vibration but also extend the frequency range for resonance for the first natural mode. There are large disparities between the magnitude of vibration occurring in the linear and nonlinear

[DOI: 10.1299/mej.16-00716]

cases for a frequency range 140-250 rad/s and it is this frequency range that will be a focus for controller design and testing.

For the LMI analysis, the system described by Eqs (20) and (21) was combined with an input weighting function, as shown in Fig. 3. The transfer function $W_1(s)$ is a stable approximation of the forcing function $\cos\Omega t$ given by

$$W_1(s) = \frac{2\zeta\Omega s}{s^2+2\zeta\Omega s+\Omega^2} \tag{22}$$

This resonant filter is used to probe the L_2 gain characteristics for harmonic forcing. If ζ is chosen sufficiently small then, for a stable linear system ($f = 0$), we have

$$Peak\ Gain_{L_2} = \sup_{\tilde{d}\neq 0} \frac{\|y_1\|_2}{\|\tilde{d}\|_2} = \left\|W_1(s)G_{yd}(s)\right\|_\infty = \sup_\omega \bar{\sigma}\left(W_1(j\omega)G_{yd}(j\omega)\right) \approx \bar{\sigma}\left(G_{yd}(j\Omega)\right) \tag{23}$$

For the nonlinear case, this frequency domain interpretation is no longer valid. Nonetheless, the value of the peak L_2 gain provides a useful bound on the magnitude of vibration (in the sense of the L_2 norm) under conditions of harmonic forcing. An upper bound on the value of the peak gain can be obtained by solving the LMI Eq. (19) with the smallest possible value of γ. Values for the peak-gain bound obtained by solving the LMI problem for a range of values of Ω are shown in Fig. 2. Note that for this analysis $B_u = 0$ as the PD controller is already accounted for within the model and no additional control is being applied. For the LMI analysis, the forcing amplitude is not accounted for directly but is implicit in the choice of $\bar{\kappa}$. Larger forcing amplitude is associated with larger values of $\beta\,|z|^3$ and hence, a larger value of $\bar{\kappa} = \sup_t(F(t)/|z(t)|) = \beta\sup_t(|z(t)|^2)$. For the results shown in Fig. 2, the LMI gain-bound was obtained using the actual value of $\bar{\kappa}$ from each simulation run. The gain-bound from the LMI analysis is seen to be sufficiently 'tight' to warrant its further application in the controller synthesis problem – which seeks to reduce the gain bound through application of an optimized feedback control law.

4.3 Robust feedback control synthesis

For controller synthesis, the augmented plant structure shown in Fig. 4 was considered. Here, the output weighting $W_1(s)$ reflects the expected characteristics of the disturbance signals (as for the analysis case in Fig. 3). Note that $W_1(s)$ is now applied at the output of the plant so that, for implementation, the states of $W_1(s)$ can be reconstructed from measurement of y. In the case study, we consider rotating unbalance as the main source of vibration excitation and seek to minimize vibration at disk 1 only. Hence, we may anticipate nonlinear behavior due to large amplitude vibration at disk 2. The weighting function W_1 is therefore chosen to penalize y over a frequency range corresponding to rotational speeds 0-200 rad/s, but emphasizing a nominal operating speed of 190 rad/s.

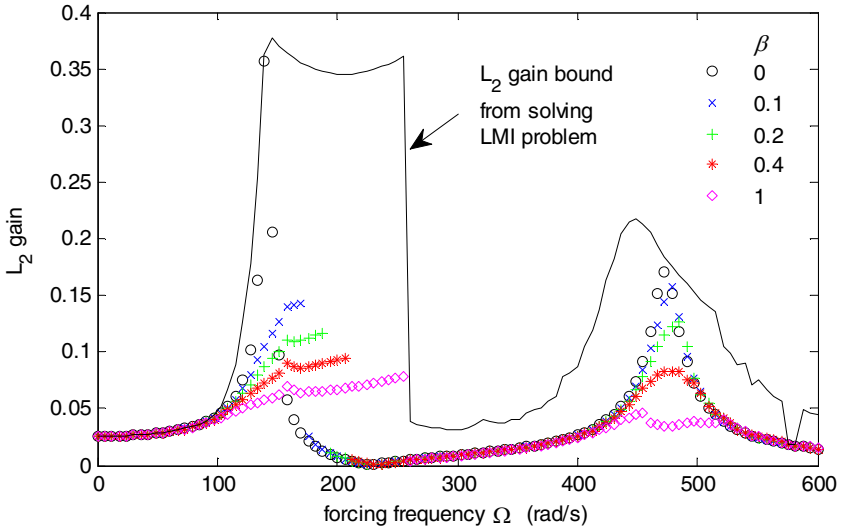

Fig. 2 L_2 gain calculated from simulation runs with harmonic forcing: results are shown for a selection of values for the non-linear parameter β. The peak L_2 gain-bound obtained by solving LMI problem Eq. (16) is also shown

[DOI: 10.1299/mej.16-00716]

For linear controller design, the weighting function W_2 would be chosen so that $|W_2(j\omega)|$ exceeds the multiplicative uncertainty in the plant (frequency response) model. According to the small gain theorem, if the closed loop system model T_{ud} (from d to u) satisfies $\|W_2 T_{ud}\|_\infty < 1$, the actual closed loop system will then always be stable. Strictly, these arguments are appropriate for linear systems only. Nonetheless, limiting the peak L_2 gain of the nonlinear system $W_2 T_{ud}$ helps to create a controller that is more robust to model error (although an appropriate choice of W_2 to guarantee stability is harder to deduce). Note also that T_{ud} must be interpreted as an operator (signal-to-signal mapping) in this context rather than a transfer function. The synthesis problem then is to obtain a control law such that the peak L_2 gain of the closed loop system is less than one. This is a nonlinear version of an H-infinity control problem, similar to the mixed sensitivity design paradigm, with the objective to achieve a closed loop system satisfying

$$\|T_{\tilde{y}d}\|_\infty = \left\| \begin{matrix} W_1 T_{yd} \\ W_2 T_{ud} \end{matrix} \right\|_\infty < 1 \tag{24}$$

A controller for which Eq. (24) holds will provide vibration attenuation performance with robust stability. The state-space model for the augmented plant has the same form as Eqs (2)-(5) but with new state vector $\tilde{x}$, which combines the rotor states x with weighting states x_1 and x_2 according to $\tilde{x}^T = [x^T \quad x_1^T \quad x_2^T]$, as shown in Fig. 4.

Figure 5 shows the frequency response characteristics (singular values) for the linearized closed loop dynamics T_{yd} and T_{ud}, together with the inverse of the weighting functions W_1^{-1} and W_2^{-1}. The inverse weighting functions exceed the maximum singular values over all frequencies, which agrees with Eq. (24). Hence, the required H-infinity performance and robustness properties are confirmed for the linearized system dynamics.

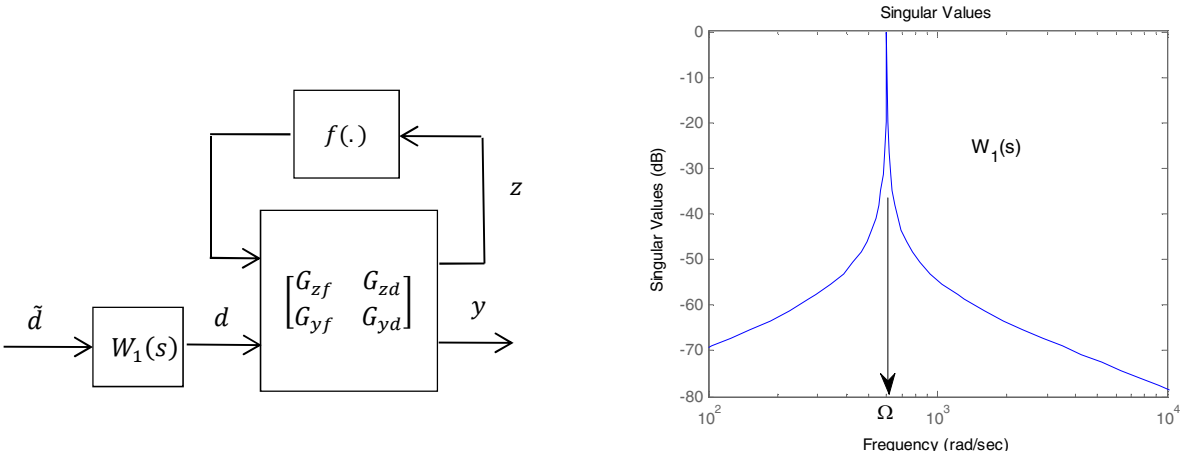

Fig. 3 The nonlinear rotordynamic model is augmented with a weighting function (disturbance model) for analytical determination of the L_2 gain under conditions of harmonic excitation

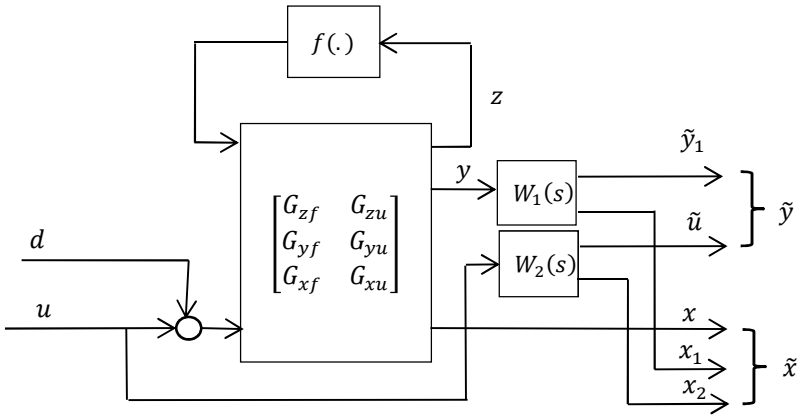

Fig. 4 Augmented plant for nonlinear H-infinity controller synthesis

[DOI: 10.1299/mej.16-00716]

5. Experimental results

Nonlinear H-infinity controllers were implemented and tested on the experimental system described in section 4.1. The designs and implementations were based on the system under initial PD feedback control. For comparison, a linear H-infinity controller was synthesized using the LMI formulation with the reduced version of matrix Φ in Eq. (19). The same weighting functions were used for both types of controller (although scaling factors were adjusted to obtain controllers giving similar levels of linear performance). It was found that the linear H-infinity controllers generally had good vibration attenuation characteristics over a low frequency range (0-200 rad/s), even for nonlinear operation. This can be explained by the increased damping for the first flexural mode. However, for certain choices of W_1, closed loop stability was not maintained when rotor interaction with the clearance ring occurred at disk 2. In contrast, the nonlinear H-infinity controller could maintain stability over the full range of linear and nonlinear operating conditions. It thus became clear that, for linear controller design, stability under nonlinear operation was difficult to ensure and sensitive to the exact choice of weighting functions. So, the approach of dealing with nonlinear effects explicitly was clearly advantageous.

For a given feedback control system that is known to be stable for linear (small amplitude) vibration it may also be possible to check for potential instability using frequency response data. An alternative to the LMI analysis approach is to apply the Popov stability criterion (see Khalil (2000)). Strictly, this is appropriate only for scalar (single-input/single-output) nonlinear functions that satisfy a sector-bound condition. However, it may still be applied to the nonlinear rotor-stator interaction model given by Eqs (17) and (18) if rotordynamic coupling between axes is sufficiently weak. Then X and Y axes may be considered separately and the Nyquist plot of the linear system (considering f_X or f_Y as input and z_X or z_Y as output) used to assess stability. These plots are shown for the test case system in Fig. 6. For the linear H-infinity controller design, the Nyquist curve crosses the negative real axis at $a = -0.26$ and so, according to the Popov criterion, stability cannot be ensured if the nonlinear force function is such that $f_X/z_X > -a^{-1} = 3.85$ N/mm. Conversely, to guarantee stable vibration, the nonlinear function must satisfy the sector-bound condition $0 \leq f_X/z_X \leq -a^{-1}$. For the nonlinear H-infinity controller the Nyquist curve does not cross the negative real axis and so stability of the system is always ensured, at least for the nominal model.

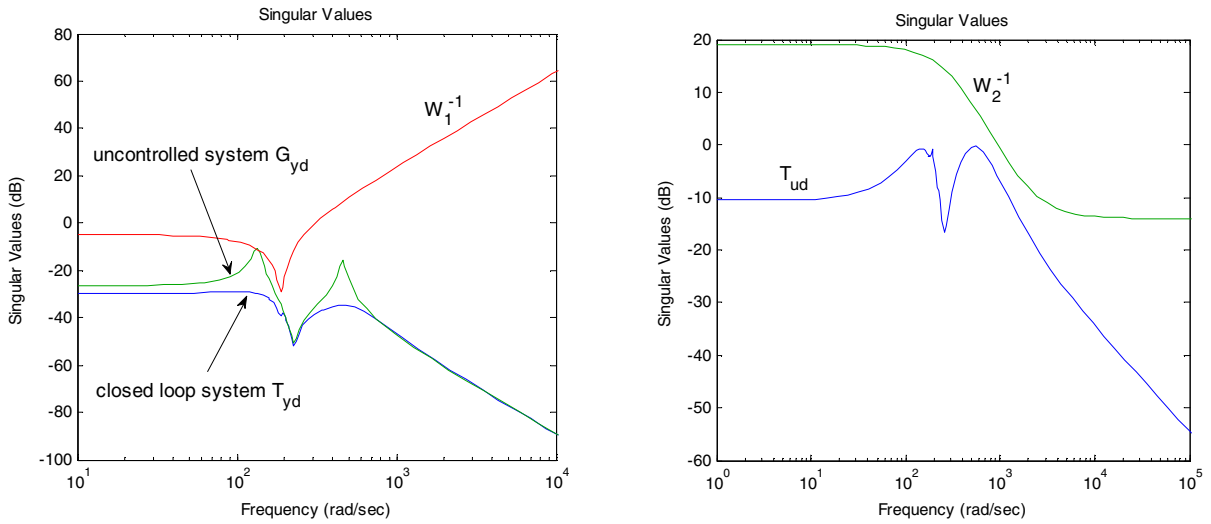

(a) (b)

Fig. 5 Results of nonlinear H-infinity controller design. Plots show frequency response characteristics for the linearized closed loop system: (a) vibration attenuation performance (b) robust stability

[DOI: 10.1299/mej.16-00716]

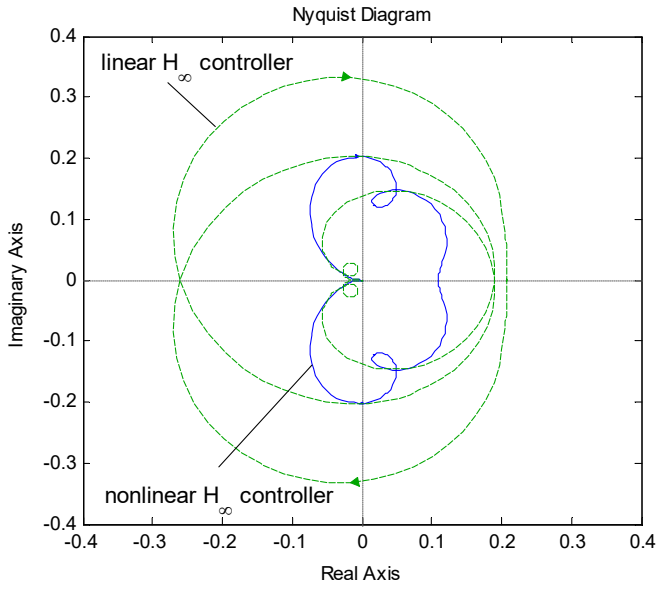

Fig. 6 Nyquist plots for linearized closed loop systems: transfer functions from input f_X to output z_X

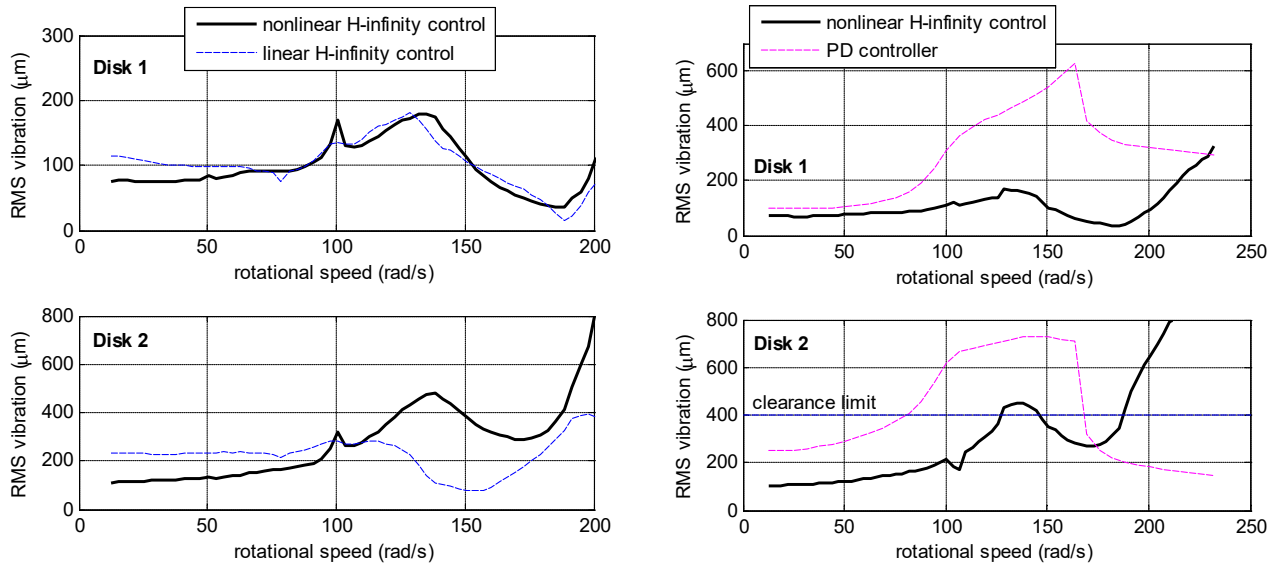

(a) linear operation (without clearance ring) (b) nonlinear operation (with clearance ring)

Fig. 7 Rotor vibration during steady speed rotation: (a) no rotor-stator contact interaction (linear case) (b) with rotor-stator contact interaction (nonlinear case)

Figure 7 shows rotor vibration levels for constant rotational speed, quantified in terms of the RMS displacements measured at disks 1 and 2. Figure 7a shows results for both linear and nonlinear H-infinity designs under linear operation (with no clearance ring fitted). The controllers gave similar results in terms of RMS vibration at disk 1, although the linear controller design gave reduced vibration for the nominal operating speed of 190 rad/s. The response behavior reflects the overall form and scaling of W_1 (see Fig. 5a). The vibration at disk 2, which is not included in the cost function, is noticeably different for the two controllers. Figure 7b shows results for nonlinear operation, with installation of the clearance ring at disk 2. The nonlinear H-infinity controller was effective for the full range of running speeds and unbalance conditions tested. The unbalance condition of the rotor was such that hard interaction with the clearance ring only occurred for higher speeds (>180 rad/s). For the linear H-infinity controller, the risk of

[DOI: 10.1299/mej.16-00716]

destabilization due to rotor contact with the clearance ring prevented a full set of results being obtained. Although light rubs resulted in limit-cycle response, sustained rubbing led to severe vibration requiring immediate controller shut down. Results for the base-level PD controller are also shown in Fig. 7b for comparison. Figure 8 shows orbit plots for a rotational speed of 95 rad/s for all three controllers. For this speed, the sizes of the contact-free orbit were similar for both the linear and nonlinear controllers and were just large enough to initiate a light rub at the contact disk. However, for the linear H-infinity controller, the vibration quickly grew to a limit cycle instability with hard contact at the clearance ring, as evident in Fig. 8c.

6. Conclusions

It has been shown how, for a rotordynamic model incorporating nonlinear effects, an H-infinity controller solution can be obtained by using numerical optimization to solve the HJI equation (in matrix inequality form). This leads to a suboptimal linear state feedback controller for the nonlinear rotordynamic system. For the test case investigated, controllers were designed to achieve rotor vibration suppression for a rotational frequency range including the first critical speed for rotor flexure. Although linear and nonlinear controllers had similar vibration suppression qualities over a low frequency range, linear designs were prone to lose stability during large amplitude vibration. The nonlinear H-infinity controller maintained stability while giving comparable vibration suppression qualities - when assessed by metrics used for the controller design optimization. Further work should develop the design approach for systems having more than one AMB and with rotordynamic models having multiple nonlinear terms, for example due to multiple clearance/backup bearings. This could validate the approach for typical AMB/rotor configurations and applications.

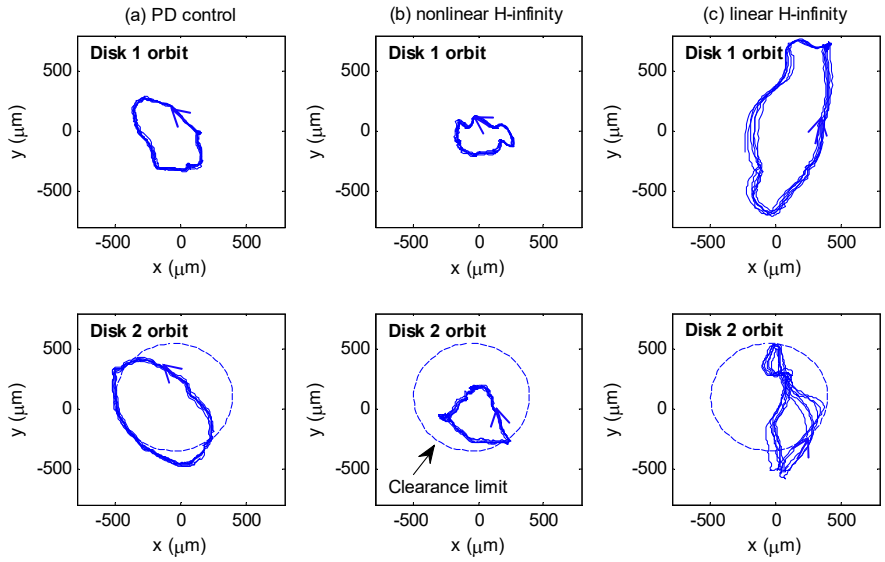

Fig. 8 Measured rotor orbits involving nonlinear rotor vibration for rotational speed of 95 rad/s

Acknowledgement

The authors gratefully acknowledge financial support for this work from the Thailand Research Fund and Chiang Mai University under grant BRG5980013.

References

Abu-Khalaf, M., Huang, J., and Lewis, F.L. Nonlinear H2/H∞ Constrained Feedback Control, (2006), Springer-Verlag, London, ISBN: 1-84628-349-3.

Boyd, S., Feron, E., Ghaoui L. E.and Balakrishnan, V., Linear Matrix Inequalities in System and Control Theory, (1994), Pennsylvania: SIAM.

[DOI: 10.1299/mej.16-00716]

Cade I. S., Sahinkaya, M. N., Burrows, C. R. and Keogh, P. S. An active auxiliary bearing control strategy to reduce the onset of asynchronous periodic contact modes in rotor/magnetic bearing systems, Trans. ASME, J. Eng. Gas Turbines and Power, Vol. 132, (2010), Art. No. 052502.

Chamroon, C., Cole, M.O.T. and Wongratanaphisan, T., An active vibration control strategy to prevent nonlinearly coupled rotor-stator whirl responses in multimode rotor-dynamic systems, IEEE Transactions on Control Systems Technology, Vol. 22, No. 3, (2014), pp. 1122-1129.

Cole, M.O.T. and Keogh, P.S. Rotor vibration with auxiliary bearing contact in magnetic bearing systems, Part 2: Robust synchronous control to restore rotor position, Proc. Instn. Mech. Engrs, Part C, Journal of Mechanical Engineering Science, Vol. 217, No. 4 (2003), pp. 393-409.

El-Shafai, A., Dimitri, A.S., Controlling journal bearing instability using active magnetic bearings, ASME J. Eng. Gas Turbines Power, Vol. 132, No. 1, (2010), art. no. 012502.

Inoue, T. Liu, J. Ishida Y. and Yoshimura, Y., Vibration control and unbalance estimation of a nonlinear rotor system using disturbance observer, ASME J. Vibr. Acoust., Vol. 131, (2009), Art. No. 031010.

Isidori, A. and Astolfi, A. Disturbance attenuation and H∞ control via measurement feedback in nonlinear systems, IEEE Transactions on Automatic Control, Vol. 37, No.9, (1992), pp. 1283-1293.

Karkoub, M. Robust control of the elastodynamic vibration of flexible rotor system with discontinuous friction, ASME J. Vib. Acoust., Vol. 133, (2011) art. no. 034501.

Khalil, H.K. Nonlinear Systems, 3rd edition. (2000) Pearson Education.

Schweitzer, G., Maslen, E. (Eds.), Magnetic Bearings: Theory, Design and Application to Rotating Machinery, Chapter 12, (2009), Springer, Berlin, ISBN: 978-3-642-00496-4.

Simon, A. and Flowers, G.T., Adaptive disturbance rejection and stabilisation for rotor system with internal damping, International Journal of Acoustics and Vibrations, Vol. 13, No. 2, (2008), pp. 73-81.

Sinha, P. K. and Pechev, A. N. Nonlinear H∞ controllers for electromagnetic suspension systems, IEEE Transactions on Automatic Control, Vol. 49, No. 4, (2004), pp. 563-568.

Van der Schaft, A.J. L2-Gain analysis of nonlinear systems and nonlinear state feedback H∞ control, IEEE Transactions on Automatic Control, Vol. 37, No. 6, (1992), pp. 770-784.

Appendix

Applying a congruency transformation with $diag(P^{-1}, \mu^{-1}I, I, I)$ to Eq. (16) followed by a change of variables $Q = P^{-1}$, $\theta = \mu^{-1}$ and $\hat{\Sigma} = \Sigma\mu^{-1}$ yields

$$\begin{bmatrix} QA^T + AQ - B_u B_u^T + \theta^{-1} 2QCMC^T Q & B_f\theta + QA^T C^T\hat{\Sigma} + QC^T N^T & B_d & QC_y^T \\ \mu^{-1}B_f^T + \Sigma CAQ + \mu NCQ & -2\theta I + \theta\hat{\Sigma}CB_f + \theta B_f^T C^T\hat{\Sigma} & 0 & 0 \\ B_d^T & 0 & -\gamma^2 I & 0 \\ C_y Q & 0 & 0 & -I \end{bmatrix} < 0 \quad \text{(A1)}$$

By Schur complements (see Boyd et al., 1994), this is equivalent to

$$\begin{bmatrix} QA^T + AQ - B_u B_u^T & B_f\theta + QA^T C^T\hat{\Sigma} + QC^T N^T & B_d & QC_y^T & QC \\ \mu^{-1}B_f^T + \Sigma CAQ + \mu NCQ & -2\theta I + \hat{\Sigma}CB_f\theta + \theta B_f^T C^T\hat{\Sigma}^T & 0 & 0 & 0 \\ B_d^T & 0 & -\gamma^2 I & 0 & 0 \\ C_y Q & 0 & 0 & -I & 0 \\ C^T Q & 0 & 0 & 0 & -\frac{1}{2}\theta M^{-1} \end{bmatrix} < 0 \quad \text{(A2)}$$

It can be seen that this inequality still has bilinear terms involving $\hat{\Sigma}$. Although techniques for solving bilinear matrix inequalities (which are non-convex) can be used, the method used for this paper was to set $\hat{\Sigma} = \sigma I$ and solve Eq. (A2) for selected values of the scalar σ. Repeatedly solving the LMI problem with a line-search over σ allowed a solution yielding the minimum value of γ to be obtained.

[DOI: 10.1299/mej.16-00716]

On the vibrational dynamics of thin-walled rotating cylinders: A theoretical and experimental study utilizing active magnetic bearings

Wichaphon Fakkaew[a], Matthew O. T. Cole[b,*], Chakkapong Chamroon[a]

[a] *School of Engineering, University of Phayao, Phayao 56000, Thailand*
[b] *Department of Mechanical Engineering, Chiang Mai University, Chiang Mai 50200, Thailand*

Abstract

This paper describes a theoretical and experimental study to establish the vibrational dynamics of a thin-walled rotating cylinder with radial bearing supports. The main focus is on the prediction of forced response, and on the variation in response behaviour with rotational speed. A shell theory analysis is shown to provide a very complete description of rotordynamic behaviour that predicts various types of natural mode for free vibration. These include in-surface torsional and extensional modes, out-of-surface wall bending modes, as well as the classical beam bending modes exhibited by long flexible rotors. For exact solution of the free vibration problem, the coupled eigenproblems derived from the continuum equations and boundary constraints can be solved numerically. This approach can be applied for any given rotational speed. To avoid having to solve the equations repeatedly, an alternative model is formulated based on the zero-speed mode-shapes which has a simple parametric dependency on rotational speed. The method is applied to the dynamic modelling of an experimental system comprising a 0.8 m long steel rotor with outer diameter of 0.166 m and wall-thickness of 3.1 mm supported by two radial active magnetic bearings. The dynamic behaviour of the system is identified by frequency response testing at different rotational speeds, where excitation forces are applied through the bearings. The results confirm the accuracy and applicability of the developed shell theory model for practical use in rotordynamic prediction and analysis.

Keywords: thin-walled structure, shell theory, rotation effects, forced response, rotordynamics

1. Introduction

Rotating cylindrical shell structures are essential components in various mechanical systems and processes. Gear and shaft transmissions, wheel, roller and tire assemblies, thin-walled tubes under machining, and turbo-machine rotors, are common examples. Vibration characteristics of rotating cylindrical shells differ from those of stationary shells due to the effects of centrifugal and Coriolis forces as well as initial hoop tension. The presence of Coriolis forces leads to traveling-wave phenomenon for free vibration, as first reported in 1890 by Bryan [1]. Distinct natural wave speeds arise for forward and backward-traveling waves, and these can vary significantly with rotational speed [2, 3]. Various thin-shell theories (characterized by differing sets of strain-displacement relations) may be used to derive the equations of motion [4, 5, 6, 7]. In terms of simplicity and accuracy, the theory of Love is often considered appropriate [8, 9], although a drawback of the theory is that certain rigid-body motions will not be correctly described [10].

For free vibration of cylindrical shells, analytical solutions for the displacement field can be expressed as two multiplicative components: the angular mode-shape function that describes the circumferential traveling waves and the axial mode-shape function that describes longitudinal deformation and which depends on the

*Corresponding author
Email addresses: wichaphon.fa@up.ac.th (Wichaphon Fakkaew), motcole@dome.eng.cmu.ac.th (Matthew O. T. Cole), chakkapong.ch@up.ac.th (Chakkapong Chamroon)

boundary conditions. For simply supported boundary conditions, the axial functions will involve known sine and cosine functions [6, 11, 12, 13]. To deal with other types of boundary conditions, some authors have used characteristic mode shapes for beam bending as approximate axial modal functions [9, 14, 15]. Unfortunately, the frequency characteristics obtained in this way are of limited accuracy as the governing equations cannot be exactly satisfied. More accurate results can be obtained with series functions such as differential quadrature functions [16], Fourier series [17] or orthogonal polynomials [18]. However, such solutions can require many terms to obtain accurate results for general sets of boundary conditions.

Exact axial mode shapes for arbitrary homogeneous boundary conditions can be expressed as a finite sum of weighted exponential functions [19]. As the exact solutions satisfy both the equations of motion and boundary conditions, they involve orthogonal functions. This property is important for decoupling the modal response equations in the case of forced vibration. Alujevic et al. [7] employed this approach to find exact solutions for free vibration of a free-free rotating cylinder. As the method is semi-analytical, care must be taken to formulate the solution in a way that avoids numerical conditioning problems. Natural frequency values were compared with published experimental data [20, 21] and good agreement was shown, but only for non-rotating cases. Also, non-zero natural frequencies were obtained for rigid-body tilting modes, even without rotation, due to the aforementioned limitation of Love's theory.

Experimental studies on the vibration of short rotating cylindrical shells have been undertaken previously, and the applicability of simplified 2D shell/ring models shown [22, 23]. The case of rotating cylindrical shells of short axial length subject to harmonic excitation has also been investigated in the context of rolling tire vibration and noise [6, 24, 25]. To the authors' knowledge, comparisons of theoretical and experimental results for rotating cylindrical shells of large axial length have not previously been reported.

For the present work, a key motivation is the potential application of thin-walled rotors in rotating machines, where benefits from low weight and high natural frequencies for beam bending modes are anticipated. Importantly, critical speeds for bending vibration may be shifted outside the operating speed range so that excitation by imbalance is negligible. However, flexural vibration of the rotor wall, e.g. due to excitation from noncircularity effects, must then be considered [23]. The ability to predict this behaviour using analytical models is therefore important. This paper describes the solution of this problem for a uniform cylindrical rotor based on Love's shell theory and with exact deformation solutions obtained as a sum of exponential functions. To accurately capture the speed-dependent dynamics, including rigid-body modes, a parametric model is introduced based on the orthogonality properties of the axial mode-shape functions. For an exemplary case involving a novel experimental system with active magnetic bearings, comparisons of experimental and model-based results are also provided. These yield important information on the validity of the modeling approach, and on the incorporation of rotation effects within shell theory models.

2. Rotating cylindrical shell model

2.1. Governing equations

A uniform cylindrical shell, rotating at constant angular speed Ω about its axis, may be considered as shown in Fig. 1a. The radius, axial length and thickness are denoted by R, L and h, respectively. Let $x_0y_0z_0$ and xyz be local Cartesian coordinate systems fixed at the undeformed and deformed middle surface within the cylinder wall. The components of displacement along the undeformed axes are denoted by $u_r(\phi,\, z,\, t)$, $v_r(\phi,\, z,\, t)$ and $w_r(\phi,\, z,\, t)$. The cylinder is homogeneous, isotropic and linearly elastic with Young's modulus E, Poisson ratio ν and density ρ. It is assumed that the axis of rotation aligns with z_0. Figure 1b shows the internal forces and couples acting on a shell element, which are aligned with deformed coordinate axes. Here, $Q_0 = \rho h R^2 \Omega^2$ is the mean circumferential stress due to centrifugal loading. The components of the external force per unit area are denoted by f_x, f_y, and f_z. The equations of motion with respect to the undeformed rotating coordinate system may be derived as

$$\frac{1}{R}\frac{\partial Q_{yx}}{\partial \phi} + \frac{\partial Q_{zx}}{\partial z} + \frac{Q_{yy}}{R} + \frac{Q_0}{R}\left(1 + \frac{\partial \beta_z}{\partial \phi}\right) + f_x = \rho h\left(\ddot{u}_r + 2\Omega\dot{v}_r + \Omega^2(R - u_r)\right) \tag{1}$$

$$\frac{1}{R}\frac{\partial Q_{yy}}{\partial \phi} + \frac{\partial Q_{zy}}{\partial z} - \frac{Q_{yx}}{R} + \frac{Q_0}{R}\left(\frac{\partial \epsilon_z}{\partial \phi} - \beta_z\right) + f_y = \rho h\left(\ddot{v}_r - 2\Omega\dot{u}_r - \Omega^2 v_r\right) \tag{2}$$

$$\frac{1}{R}\frac{\partial Q_{yz}}{\partial \phi} + \frac{\partial Q_{zz}}{\partial z} - \frac{Q_0}{R}\frac{\partial \beta_x}{\partial \phi} + f_z = \rho h \ddot{w}_r \tag{3}$$

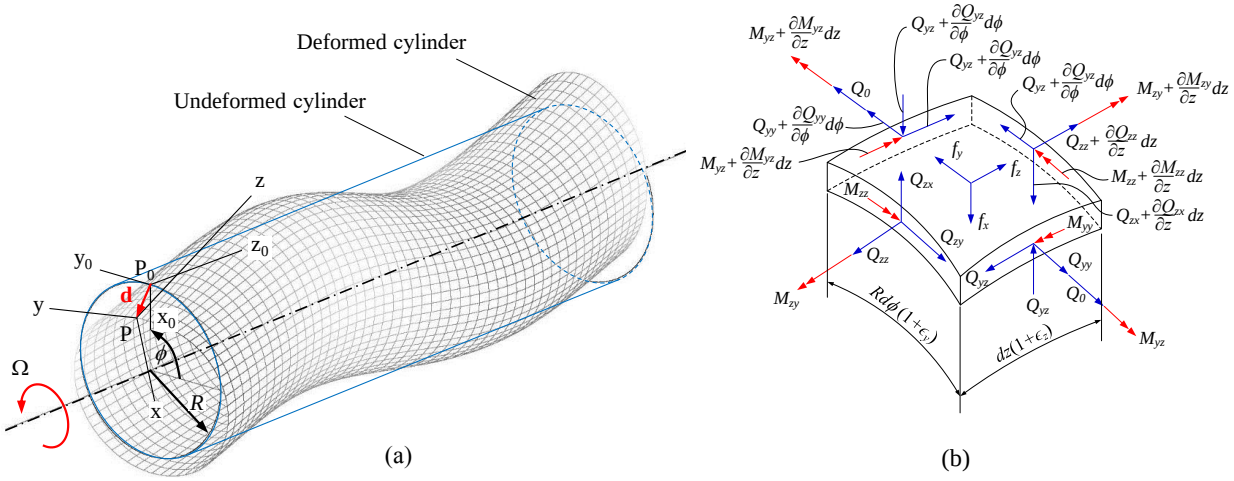

Figure 1: Thin-walled cylindrical rotor model: (a) coordinate systems (b) internal forces/moments acting on shell element

$$Q_{yx} = \frac{1}{R}\frac{\partial M_{yy}}{\partial \phi} + \frac{\partial M_{zy}}{\partial z}, \quad Q_{zx} = -\frac{1}{R}\frac{\partial M_{yz}}{\partial z} - \frac{\partial M_{zz}}{\partial z} \tag{4}$$

Also, $Q_{yz} = Q_{zy}$ and $M_{yz} = -M_{zy}$.

The derivation of these equations can be found in other sources, although some differences are seen for the terms in Ω^2 and Q_0, depending on whether the equations of motion are formulated and linearized using the deformed or undeformed coordinate system [9]. In our derivation, the acceleration and force components were related by applying Newton-Euler's equations in the undeformed axis system, with the assumption that rotation occurs about the undisplaced cylinder axis (aligned with the z_0 axis).

The internal forces/moments are described by the constitutive equations from Kirchhoff-Love theory [26]:

$$[Q_{yy},\, Q_{zz},\, Q_{zy}] = C\left[\epsilon_y + \nu\epsilon_z,\ \epsilon_z + \nu\epsilon_y,\ \tfrac{1-\nu}{2}\gamma_{yz}\right] \tag{5}$$

$$[M_{yy},\, M_{zz},\, M_{yz}] = D\left[-\frac{1}{R}\frac{\partial \beta_z}{\partial \phi} - \nu\frac{\partial \beta_y}{\partial z},\ \frac{\partial \beta_y}{\partial z} + \frac{\nu}{R}\frac{\partial \beta_z}{\partial \phi},\ \frac{1-\nu}{2R}\left(\frac{\partial \beta_y}{\partial \phi} + \frac{\partial \beta_z}{\partial z}\right)\right] \tag{6}$$

with $C = \frac{Eh}{1-\nu^2}$ and $D = \frac{Eh^3}{12(1-\nu^2)}$ and

$$\epsilon_y = \frac{1}{R}\frac{\partial v_r}{\partial \phi} - \frac{u_r}{R}, \quad \epsilon_z = \frac{\partial w_r}{\partial z}, \quad \gamma_{yz} = \frac{\partial v_r}{\partial z} + \frac{1}{R}\frac{\partial w_r}{\partial \phi}, \tag{7}$$

$$\beta_x = -\frac{1}{R}\frac{\partial w_r}{\partial \phi}, \quad \beta_y = \frac{\partial u_r}{\partial z}, \quad \beta_z = \frac{1}{R}\frac{\partial u_r}{\partial \phi} + \frac{v_r}{R}. \tag{8}$$

To describe the interaction with space-fixed elements (which for a rotor system may include bearing supports and other stator-mounted parts), a transformation to stationary-frame coordinates is required. Stationary-frame displacements are defined by $u(\theta,\, z,\, t) = u_r(\phi,\, z,\, t)$, $v(\theta,\, z,\, t) = v_r(\phi,\, z,\, t)$ and $w(\theta,\, z,\, t) = w_r(\phi,\, z,\, t)$, where $\theta = \phi + \Omega t$. The following relations hold for each pair of variables:

$$\frac{\partial u_r}{\partial \phi} = \frac{\partial u}{\partial \theta}, \quad \dot{u}_r = \dot{u} + \Omega\frac{\partial u}{\partial \theta}, \quad \ddot{u}_r = \ddot{u} + 2\Omega\frac{\partial \dot{u}}{\partial \theta} + \Omega^2\frac{\partial^2 u}{\partial \theta^2} \tag{9}$$

Using Eqs (4)-(6) in Eqs (1)-(3) and applying Eq. (9) gives

$$\begin{aligned} L_x(u,\, v,\, w) + f_x &= \rho h\left[\ddot{u} + 2\Omega\left(\frac{\partial \dot{u}}{\partial \theta} + \dot{v}\right) + \Omega^2\left(\frac{\partial v}{\partial \theta} - u\right)\right] \\ L_y(u,\, v,\, w) + f_y &= \rho h\left[\ddot{v} + 2\Omega\left(\frac{\partial \dot{v}}{\partial \theta} - \dot{u}\right) + \Omega^2\frac{\partial}{\partial \theta}\left(\frac{\partial v}{\partial \theta} - u - R\frac{\partial w}{\partial z}\right)\right] \\ L_z(u,\, v,\, w) + f_z &= \rho h\left[\ddot{w} + 2\Omega\frac{\partial \dot{w}}{\partial \theta}\right] \end{aligned} \tag{10}$$

where

$$
\begin{aligned}
L_x(u,\,v,\,w) &= C\left[\tfrac{1}{R^2}\left(\tfrac{\partial v}{\partial\theta}-u\right)+\tfrac{\nu}{R}\tfrac{\partial w}{\partial z}\right]-D\left[\tfrac{\partial^4 u}{\partial z^4}+\tfrac{1}{R^2}\tfrac{\partial^3 v}{\partial\theta\partial z^2}+\tfrac{2}{R^2}\tfrac{\partial^4 u}{\partial\theta^2\partial z^2}+\tfrac{1}{R^4}\tfrac{\partial^4 u}{\partial\theta^4}+\tfrac{1}{R^4}\tfrac{\partial^3 v}{\partial\theta^3}\right]\\
L_y(u,\,v,\,w) &= C\left[\tfrac{1-\nu}{2}\tfrac{\partial^2 v}{\partial z^2}+\tfrac{1+\nu}{2R}\tfrac{\partial^2 w}{\partial\theta\partial z}+\tfrac{1}{R^2}\left(\tfrac{\partial^2 v}{\partial\theta^2}-\tfrac{\partial u}{\partial\theta}\right)\right]+D\left[\tfrac{1-\nu}{2R^2}\tfrac{\partial^2 v}{\partial z^2}+\tfrac{1}{R^4}\tfrac{\partial^2 v}{\partial\theta^2}+\tfrac{1}{R^4}\tfrac{\partial^3 u}{\partial\theta^3}+\tfrac{1}{R^2}\tfrac{\partial^3 u}{\partial\theta\partial z^2}\right]\\
L_z(u,\,v,\,w) &= C\left[\tfrac{\partial^2 w}{\partial z^2}+\tfrac{1+\nu}{2R}\tfrac{\partial^2 v}{\partial\theta\partial z}-\tfrac{\nu}{R}\tfrac{\partial u}{\partial z}+\tfrac{1-\nu}{2R^2}\tfrac{\partial^2 w}{\partial\theta^2}\right]
\end{aligned}
$$

For rotordynamic analysis, it is appropriate to consider free boundaries at both ends of the cylinder. According to Fig. 1b, there are five resultant forces at the end surfaces. As the order of the equations of motion is four, only four boundary constraints are needed. Kirchhoff effective shear stress resultants [9, 11] are used to combine shear force and moment values as $V_{zx}=Q_{zx}+\frac{1}{R}\frac{\partial M_{zy}}{\partial\phi}$ and $V_{zy}=Q_{zy}-\frac{1}{R}M_{zy}$. Setting $Q_{zz}=M_{zz}=V_{zx}=V_{zy}=0$ at the boundaries then yields

$$
\begin{aligned}
\left[\tfrac{\partial w}{\partial z}+\tfrac{\nu}{R}\left(\tfrac{\partial v}{\partial\theta}-u\right)\right]_{z=\pm L/2}&=0\\
\left[\tfrac{\partial^2 u}{\partial z^2}+\tfrac{\nu}{R^2}\left(\tfrac{\partial^2 u}{\partial\theta^2}+\tfrac{\partial v}{\partial\theta}\right)\right]_{z=\pm L/2}&=0\\
\left[\tfrac{1}{R^2}\tfrac{\partial^2 v}{\partial\theta\partial z}+\tfrac{2-\nu}{R^2}\tfrac{\partial^3 u}{\partial\theta^2\partial z}+\tfrac{\partial^3 u}{\partial z^3}\right]_{z=\pm L/2}&=0\\
\left[\tfrac{\partial v}{\partial z}+\tfrac{1}{R}\tfrac{\partial w}{\partial\theta}+\tfrac{h^2}{12R^2}\left(\tfrac{\partial v}{\partial z}+2\tfrac{\partial^2 u}{\partial\theta\partial z}\right)\right]_{z=\pm L/2}&=0
\end{aligned}
\tag{11}
$$

2.2. Analytical solutions for free vibration

To obtain solutions for free vibration, the external forces are set to zero and the following forms assumed:

$$
u=\alpha e^{\lambda z}\cos(m\theta\pm\omega_m t),\quad v=-\beta e^{\lambda z}\sin(m\theta\pm\omega_m t),\quad w=\gamma e^{\lambda z}\cos(m\theta\pm\omega_m t) \tag{12}
$$

where m is the integer-valued circumferential wavenumber, ω_m is the natural frequency and λ, α, β and γ are arbitrary constants. Note that the '+' and '−' correspond to the backward and forward traveling wave solutions, respectively. Substituting Eq. (12) into Eq. (10), yields

$$
\begin{bmatrix}
a_4\lambda^4+a_2\lambda^2+a_0+a_\omega, & d_2\lambda^2+d_0+d_\omega, & e_1\lambda\\
d_2\lambda^2+d_0+d_\omega, & b_2\lambda^2+b_0+b_\omega, & (f_1+f_2)\lambda\\
-e_1\lambda, & -f_1\lambda, & c_2\lambda^2+c_0+c_\omega
\end{bmatrix}
\begin{bmatrix}\alpha\\ \beta\\ \gamma\end{bmatrix}=0 \tag{13}
$$

where, with $\delta=h^2/12R^2$, the coefficients are given by

$$
\begin{aligned}
&a_4=-\delta R^4,\quad a_2=2\delta m^2R^2,\quad a_0=-\delta m^4-1,\quad a_\omega=\tfrac{\rho hR^2}{C}(\omega_m^2+\Omega^2\pm2\Omega\omega_m m),\\
&b_2=\tfrac{1-\nu}{2}(1+\delta)R^2,\quad b_0=-(1+\delta)m^2,\quad b_\omega=\tfrac{\rho hR^2}{C}(\omega_m^2+\Omega^2m^2\pm2\Omega\omega_m m),\\
&c_2=R^2,\quad c_0=-\tfrac{1-\nu}{2}m^2,\quad c_\omega=\tfrac{\rho hR^2}{C}(\omega_m^2\pm2\Omega\omega_m m)\\
&d_2=\delta mR^2\quad d_0=-\delta m^3-m,\quad d_\omega=\tfrac{\rho hR^2}{C}(\Omega^2m\pm2\Omega\omega_m),\\
&e_1=\nu R,\quad f_1=\tfrac{1+\nu}{2}mR,\quad f_2=\tfrac{\rho hR^3}{C}\Omega^2m
\end{aligned}
$$

The equations of motion can be satisfied only if the determinant of the matrix in Eq. (13) is zero. This yields a biquartic polynomial in λ:

$$
A_8\lambda^8+A_6\lambda^6+A_4\lambda^4+A_2\lambda^2+A_0=0 \tag{14}
$$

where the coefficients are defined in appendix A. The displacements can therefore be expressed

$$
u=U(z)\cos(m\theta\pm\omega_m t),\quad v=-V(z)\sin(m\theta\pm\omega_m t),\quad w=W(z)\cos(m\theta\pm\omega_m t) \tag{15}
$$

where the z-dependent factors are a linear combination of the eight eigensolutions:

$$U(z) = \sum_{k=1}^{8} C_k \alpha_k \exp(\lambda_k z),\ V(z) = \sum_{k=1}^{8} C_k \beta_k \exp(\lambda_k z),\ W(z) = \sum_{k=1}^{8} C_k \gamma_k \exp(\lambda_k z). \tag{16}$$

Here, C_k are complex constants, to be determined. At this stage, the roots λ_k must be calculated by assuming a value for the frequency ω_m and then solving Eq. (14). The corresponding eigenvectors $\Psi_k = [\alpha_k,\, \beta_k,\, \gamma_k]^T$ can then be constructed from the null space of the matrix in Eq. (13). The axial mode shape function $G(z) = [U(z),\, V(z),\, W(z)]^T$ can be changed from complex to real-valued representation according to

$$G(z) = \sum_{k=1}^{8} C_k \Psi_k \exp(\lambda_k z) = \sum_{k=1}^{8} \kappa_k \Gamma_k(z) \tag{17}$$

where $\Gamma_k(z) : \mathbb{R} \rightarrow \mathbb{R}^3$ are given in appendix B for each possible type of root for Eq. (14). The real coefficients κ_k must be determined such that $G(z)$ satisfies the boundary conditions. This will only be possible if a correct natural frequency value has been assumed for ω_m. Although the transformation to real functions and coefficients in Eq. (17) complicates the formulation, it simplifies the solution procedure and helps in avoiding numerical conditioning problems. Equation (17) may be expressed in the matrix form:

$$G(z) = \mathbf{\Gamma}(z) K \tag{18}$$

where $K = \left[\ \kappa_1 \quad \kappa_2 \quad ... \quad \kappa_8\ \right]^T$ and $\mathbf{\Gamma}(z) = \left[\ \Gamma_1(z) \quad \Gamma_2(z) \quad ... \quad \Gamma_8(z)\ \right]$ is a $3{\times}8$ matrix. By substituting Eq. (15) into Eq. (11), the boundary constraints may be expressed

$$\mathbf{B} K = 0, \tag{19}$$

where

$$\mathbf{B} = \begin{bmatrix} \left[\mathbf{B}_0 \mathbf{\Gamma}(z) + \mathbf{B}_1 \mathbf{\Gamma}'(z) + \mathbf{B}_2 \mathbf{\Gamma}''(z) + \mathbf{B}_3 \mathbf{\Gamma}'''(z)\right]_{z=-L/2} \\ \left[\mathbf{B}_0 \mathbf{\Gamma}(z) + \mathbf{B}_1 \mathbf{\Gamma}'(z) + \mathbf{B}_2 \mathbf{\Gamma}''(z) + \mathbf{B}_3 \mathbf{\Gamma}'''(z)\right]_{z=L/2} \end{bmatrix}$$

with

$$\mathbf{B}_0 = \begin{bmatrix} -\nu & -\nu m & 0 \\ -\nu m^2 & -\nu m & 0 \\ 0 & 0 & m/R \\ 0 & 0 & 0 \end{bmatrix}, \quad \mathbf{B}_1 = \begin{bmatrix} 0 & 0 & R \\ 0 & 0 & 0 \\ 2\delta m & 1+\delta & 0 \\ -(2-\nu)m^2 & -m & 0 \end{bmatrix},$$

$$\mathbf{B}_2 = \begin{bmatrix} 0 & 0 & 0 \\ R^2 & 0 & 0 \\ 0 & 0 & 0 \\ 0 & 0 & 0 \end{bmatrix}, \quad \mathbf{B}_3 = \begin{bmatrix} 0 & 0 & 0 \\ 0 & 0 & 0 \\ 0 & 0 & 0 \\ R^2 & 0 & 0 \end{bmatrix}.$$

The determinant of $\mathbf{B}$ must be zero in order to obtain a non-trivial solution for K.

To determine the natural frequencies, the frequency range of interest is first discretized. Each frequency value is then substituted into Eq. (14), with m set to a fixed integer, in order to solve for λ_k and corresponding Ψ_k. It is then possible to construct $\mathbf{B}$ and calculate its determinant. Existence of a solution is indicated by a change in the sign of the determinant for two adjacent frequencies. A secant method can then be used to refine the solution to the required accuracy. The coefficient vector K can then be calculated by construction from the null space of $\mathbf{B}$ e.g. using a singular value decomposition algorithm. If $G(z)$ is represented using complex coefficients and functions, then the determinant of $\mathbf{B}$ can take complex values. In this case, the zero-crossing method cannot be used and finding the natural frequencies becomes more difficult.

Equation (16) is valid only if the roots λ_k are non-zero. For $m = 1$ and $\omega_m = 0$, the coefficient A_0 vanishes and so there are two zero-valued roots. In addition, for $m = 0$ and $\omega_m = 0$, both A_0 and A_2 vanish and this give four zero-valued roots. These solutions, which correspond to the rigid-body modes, are not correctly represented by Eq. (16). However, a simpler form for $G(z)$ may be assumed and substituted into Eq. (10) to obtain the corresponding natural frequencies. This approach is described in detail in section 2.3.

Table 1: Physical properties of cylinder for case study

Parameter	Symbol	Value	Units
Length	L	0.8	m
Radius	R	0.0815	m
Wall thickness	h	0.00306	m
Young's modulus	E	2.08×10^{11}	$\mathrm{N/m^2}$
Density	ρ	7850	$\mathrm{kg/m^3}$
Poisson's ratio	ν	0.3	

2.3. Numerical evaluation and preliminary analysis

Numerical results were obtained using physical properties listed in Table 1. These match the experimental system described later in section 4. For the experimental system, the recorded data relates to bending mode vibration within a frequency range of 0-2000 Hz. For construction of a theoretical model, a broader range of natural frequencies and mode types was first considered. Figure 2 shows the natural frequencies for the non-rotating cylinder, obtained by the solution method in section 2.2 (with $\Omega = 0$). Selected mode shapes are shown in Figs 3 and 4. The mode shapes may be classified as out-of-surface bending or in-surface shear and extensional, depending on the dominant displacement directions. For the z-dependent mode shape function, the notation $G_{mn}(z)$ is adopted where the index m is the circumferential wavenumber, as previously defined. For the bending modes, the index n is equal to the number of nodes (zero-crossings) of $U(z)$.

Natural frequencies for bending modes are shown in Fig. 2a. The modes with $m = 1$ include the rigid-body translation and tilting modes (with $n = 0, 1$, respectively), as well as the beam bending modes ($n > 1$), as shown in Fig. 3. Note that, for a given value of n, the trend of changing natural frequency with increasing circumferential wavenumber m depends on the length-to-radius ratio of the cylinder.

Modes with $m = 0$ include those for which either axial extension or bending are dominant, as shown in Fig. 4. For modes where the axial extension is dominant, then n^* denotes the number of nodes of $W(z)$. The natural frequencies shown in Fig. 2b also include torsional shear modes, as indicated by $\square$ symbols. Modes with $n^* = 0$ are axial shear modes, while other modes for which $m \neq 0$ and $n^* \neq 0$ involve more complex in-surface shear and extension, some examples of which are also shown in Fig. 4. For the experimental tests, the excitation of these modes is negligible.

To obain the physically correct results for the rigid-body modes, solutions were constructed using the assumed modes method. For cases with $m = 0$, setting $G(z) = [\alpha,\, \beta,\, \gamma]^T$ in Eq. (15) and substituting into Eq. (10) yields $\omega_{0,0} = \omega_{0,0^*} = 0$, and $G_{0,0}(z) = [0,\, 0,\, 1]^T$, $G_{0,0^*}(z) = [0,\, 1,\, 0]^T$, which correspond to translation along the z-axis and rotation about the z-axis, respectively. For $m = 1$, setting $G(z) = [\alpha,\, \beta,\, \gamma]^T$ and $G(z) = [\alpha z,\, \beta z,\, R]^T$, yields $\omega_{1,0} = \omega_{1,1} = 0$ and $G_{1,0}(z) = [1,\, -1,\, 0]^T$, $G_{1,1}(z) = [z,\, -z,\, R]^T$, which describe lateral translation and tilting motions. For the flexible modes, the exact solution method was used to find the natural frequencies and mode shapes in all cases.

To obtain exact solutions for the rotating cylinder, the same solution method may be applied but with Ω set to non-zero value in Eq. (13).

3. Speed-dependent rotordynamic model

3.1. Mode-shape invariance and modal decoupling

To construct a speed-dependent parametric model, the issues of orthogonality and invariance of the mode shape functions is first considered. Substituting the zero-speed eigensolutions in Eq. (10) yields

$$\mathcal{K}_{mn} = -\omega_{mn}^2 G_{mn}, \quad \Omega = 0 \tag{20}$$

where

$$\mathcal{K}_{mn} = \frac{C}{\rho h R^2} \begin{bmatrix} a_4 U''''_{mn} + a_2 U''_{mn} + a_0 U_{mn} + d_2 V''_{mn} + d_0 V_{mn} + e_1 W'_{mn} \\ d_2 U''_{mn} + d_0 U_{mn} + b_2 V''_{mn} + b_0 V_{mn} + f_1 W'_{mn} \\ -e_1 U'_{mn} - f_1 V'_{mn} + c_2 W''_{mn} + c_0 W_{mn} \end{bmatrix} \tag{21}$$

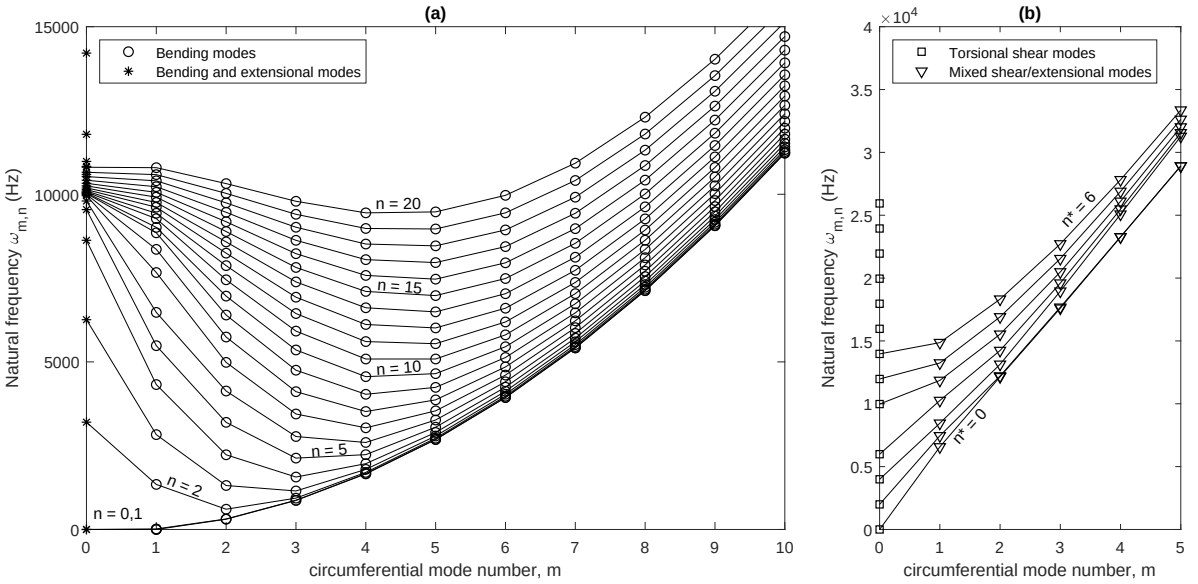

Figure 2: The natural frequencies of a non-rotating cylindrical shell with properties in Table 1: a) bending and extensional modes, b) torsional and mixed shear/extensional modes

For the case with rotation,

$$\left.\begin{aligned}\mathcal{K}_{mn} &= -(\omega^b_{mn})^2 G_{mn} - 2\Omega\omega^b_{mn}\mathbf{\Lambda}_m G_{mn} - \Omega^2\mathbf{\Pi}_m G_{mn}\\ \mathcal{K}_{mn} &= -(\omega^f_{mn})^2 G_{mn} + 2\Omega\omega^f_{mn}\mathbf{\Lambda}_m G_{mn} - \Omega^2\mathbf{\Pi}_m G_{mn}\end{aligned}\right\} \quad \Omega \neq 0 \tag{22}$$

where the backward and forward mode frequencies are denoted ω^b_{mn} and ω^f_{mn}, respectively. If the centrifugal stress term in Eq. (2) associated with the axial strain gradient $\left(\frac{Q_0}{R}\frac{\partial \epsilon_z}{\partial \phi}\right)$ is neglected (so that $f_2 = 0$ in Eq. (13)) then both $\mathbf{\Lambda}_m$ and $\mathbf{\Pi}_m$ have symmetric forms:

$$\mathbf{\Lambda}_m = \begin{bmatrix} m & 1 & 0 \\ 1 & m & 0 \\ 0 & 0 & m \end{bmatrix}, \quad \mathbf{\Pi}_m = \begin{bmatrix} 1 & m & 0 \\ m & m^2 & 0 \\ 0 & 0 & 0 \end{bmatrix} \tag{23}$$

The boundary constraints from Eq. (11), are

$$\begin{aligned}\left[W'_{mn} - \tfrac{\nu}{R}\left(U_{mn} + mV_{mn}\right)\right]_{z=\pm L/2} &= 0\\ \left[U''_{mn} - \tfrac{\nu}{R^2}\left(m^2 U_{mn} + mV_{mn}\right)\right]_{z=\pm L/2} &= 0\\ \left[U'''_{mn} - (2-\nu)\tfrac{m^2}{R^2}U'_{mn} - \tfrac{m}{R^2}V'_{mn}\right]_{z=\pm L/2} &= 0\\ \left[2\delta m U'_{mn} + (1+\delta)\,V'_{mn} + \tfrac{m}{R}W_{mn}\right]_{z=\pm L/2} &= 0\end{aligned} \tag{24}$$

By applying Eq. (24), it can be shown that

$$\int_{-L/2}^{L/2} G^T_{mq}\mathcal{K}_{mn} - G^T_{mn}\mathcal{K}_{mq}dz = 0. \tag{25}$$

Therefore, from Eq. (20), $(\omega^2_{mn} - \omega^2_{mq})\int_{-L/2}^{L/2} G^T_{mq}G_{mn}dz = 0$. Since $\omega_{mn} \neq \omega_{mq}$, it can be concluded that

$$\int_{-L/2}^{L/2} G^T_{mq}G_{mn}dz = \begin{cases} a_{mn}, & q = n \\ 0, & q \neq n \end{cases} \tag{26}$$

Table 2: Numerical results for bending mode dynamics of free cylinder. Natural frequency values are shown from exact solution and from using parametric formula Eq. (29)

	$\Omega/2\pi = 0$ Hz			$\Omega/2\pi = 30$ Hz				$\Omega/2\pi = 300$ Hz			
mode shape indices		coefficients		formula		exact		formula		exact	
	ω_{mn} (Hz)	$\frac{b_{mn}}{a_{mn}}$	$\frac{c_{mn}}{a_{mn}}$	ω^f_{mn} (Hz)	ω^b_{mn}	ω^f_{mn} (Hz)	ω^b_{mn}	ω^f_{mn} (Hz)	ω^b_{mn}	ω^f_{mn} (Hz)	ω^b_{mn}
$m=2,\ n=0$	305.99	-0.80022	7.5358e-7	344.09	272.10	344.09	272.10	832.35	112.49	832.16	112.51
$m=2,\ n=1$	313.40	-0.79535	1.4149e-6	351.61	279.33	351.61	279.33	839.75	116.96	839.49	116.95
$m=2,\ n=2$	603.90	-0.78598	1.8652e-4	641.41	568.57	641.40	568.55	1069.4	341.00	1067.7	339.47
$m=3,\ n=0$	865.19	-0.60054	5.3070e-6	940.16	796.19	940.16	796.19	1845.3	405.65	1845.3	405.70
$m=3,\ n=1$	872.60	-0.59996	9.7775e-6	947.57	803.56	947.56	803.56	1851.3	411.29	1850.9	411.28
$m=3,\ n=2$	934.81	-0.59975	6.8217e-5	1009.6	865.57	1009.6	865.56	1900.1	459.91	1899.2	459.35
$m=3,\ n=3$	1149.1	-0.59998	2.8198e-4	1223.4	1079.4	1223.4	1079.4	2076.1	636.05	2074.3	634.59
$m=2,\ n=3$	1311.9	-0.77816	6.4058e-4	1349.1	1275.7	1349.0	1275.7	1728.7	995.57	1726.0	993.10
$m=1,\ n=2$	1344.1	-0.86113	1.0239e-3	1348.3	1339.9	1348.3	1339.9	1386.4	1303.1	1384.2	1300.9
$m=4,\ n=2$	1703.6	-0.4725	5.9478e-5	1812.7	1601.0	1812.7	1601.0	3063.8	947.26	3063.1	947.00

where $a_{mn} = \int_{-L/2}^{L/2} G_{mn}^T G_{mn} dz$. This implies orthogonality of the stationary mode shapes.

Using Eq. (20) to substitute for $\mathcal{K}_{mn}$ in Eq. (22) and applying Eq. (26), it may be shown that, if $\mathbf{\Lambda}_m = \mathbf{\Lambda}_m^T$ and $\mathbf{\Pi}_m = \mathbf{\Pi}_m^T$, then $(\omega^b_{mn} - \omega^b_{mq}) \int_{-L/2}^{L/2} G_{mq}^T \mathbf{\Lambda}_m G_{mn} dz = 0$. Since $\omega^b_{mn} \neq \omega^b_{mq}$, it can be concluded

$$\int_{-L/2}^{L/2} G_{mq}^T \mathbf{\Lambda}_m G_{mn} dz = \begin{cases} m a_{mn} + b_{mn}, & q = n \\ 0, & q \neq n \end{cases} \tag{27}$$

where $b_{mn} = 2\int_{-L/2}^{L/2} U_{mn} V_{mn} dz$. It then also follows from Eq. (22), that

$$\int_{-L/2}^{L/2} G_{mq}^T \mathbf{\Pi}_m G_{mn} dz = \begin{cases} c_{mn}, & q = n \\ 0, & q \neq n \end{cases} \tag{28}$$

where $c_{mn} = \int_{-L/2}^{L/2} (U_{mn} + m V_{mn})^2 dz$. Note that the coefficient c_{mn} is a measure of the circumferential extension. With no extension, $u = \partial v / \partial \theta$ and so $U_{mn} + m V_{mn} = 0$.

The implication of equations (27) and (28) is that, with symmetric matrices $\mathbf{\Lambda}_m$ and $\mathbf{\Pi}_m$ (as in Eq. (23)), the zero-speed mode shapes G_{mn} are also eigensolutions of Eq. (22), i.e. the mode shapes are unaffected by rotation. Now, substituting Eq. (20) into Eq. (22), then premultiplying by G_{mn}^T and integrating over $z \in [-L/2, L/2]$ yields a set of quadratic equations for the natural frequencies, the solutions for which are

$$\omega^{b,f}_{mn} = \sqrt{\omega^2_{mn} + \Omega^2 \left[\left(m + \tfrac{b_{mn}}{a_{mn}} \right)^2 - \tfrac{c_{mn}}{a_{mn}} \right]} \mp \Omega \left(m + \tfrac{b_{mn}}{a_{mn}} \right) \tag{29}$$

Here, the lower value corresponds to the backwards wave solution. Table 2 shows natural frequency values for the cylindrical rotor (Table 1) for two cases: 1) based on exact solution with inclusion of the $\partial \epsilon_z / \partial \phi$ term in Eq. (2); and 2) using the formula from Eq. (29), which neglects the $\partial \epsilon_z / \partial \phi$ term. For the first ten bending modes, there is agreement within four significant figures when $\Omega/2\pi$=30 Hz. For higher rotational speeds, the difference becomes more apparent for higher order modes, although agreement within three significant figures is still obtained for the cases shown with $\Omega/2\pi$=300 Hz. The formula Eq. (29) can be used directly to construct a Campbell diagram for the free rotating cylinder, as shown in Fig. 5. The decoupling equations (27) and (28) also facilitate the construction of a parametric speed-dependent model for forced vibration, as described in section 3.2.

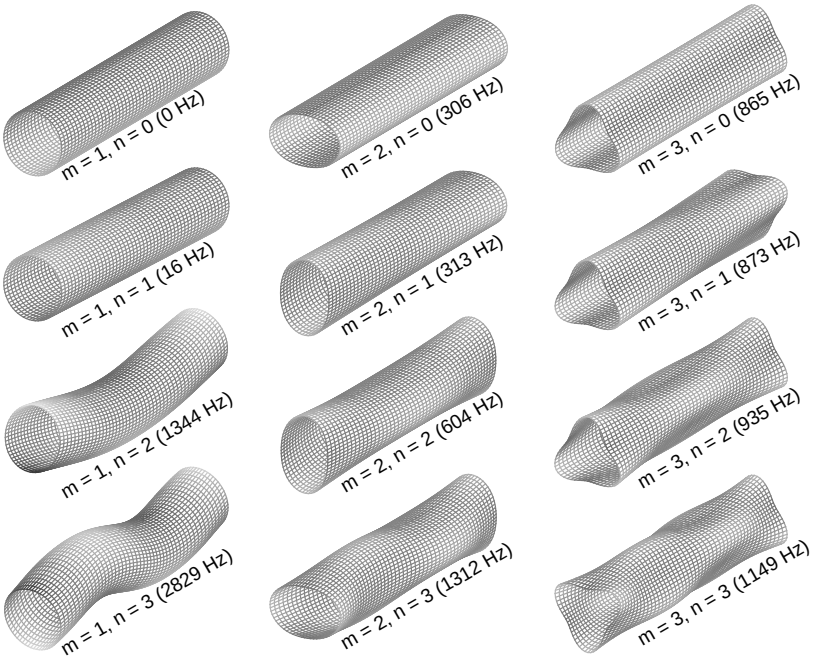

Figure 3: Example mode shapes for free vibration of cylindrical shell in low natural frequency range

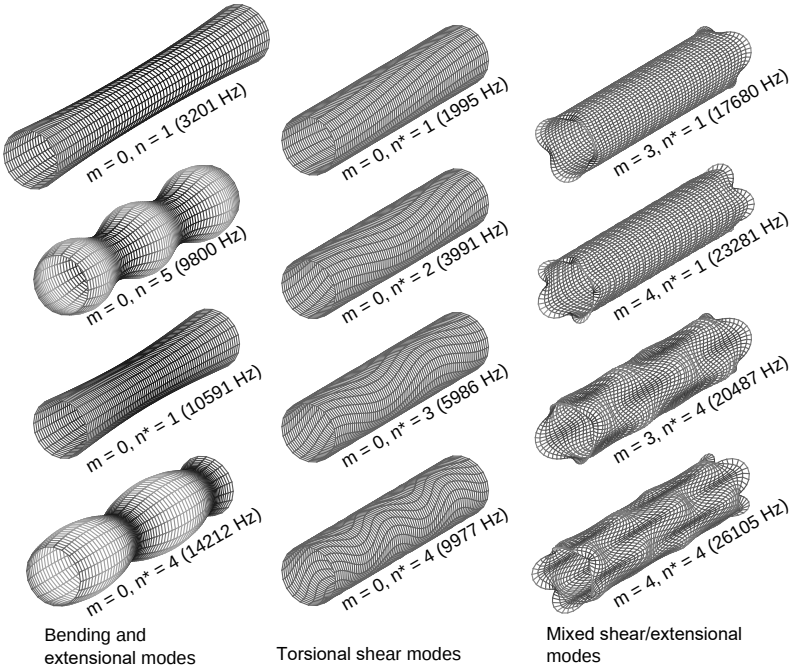

Figure 4: Example mode shapes for free vibration of cylindrical shell in high natural frequency range

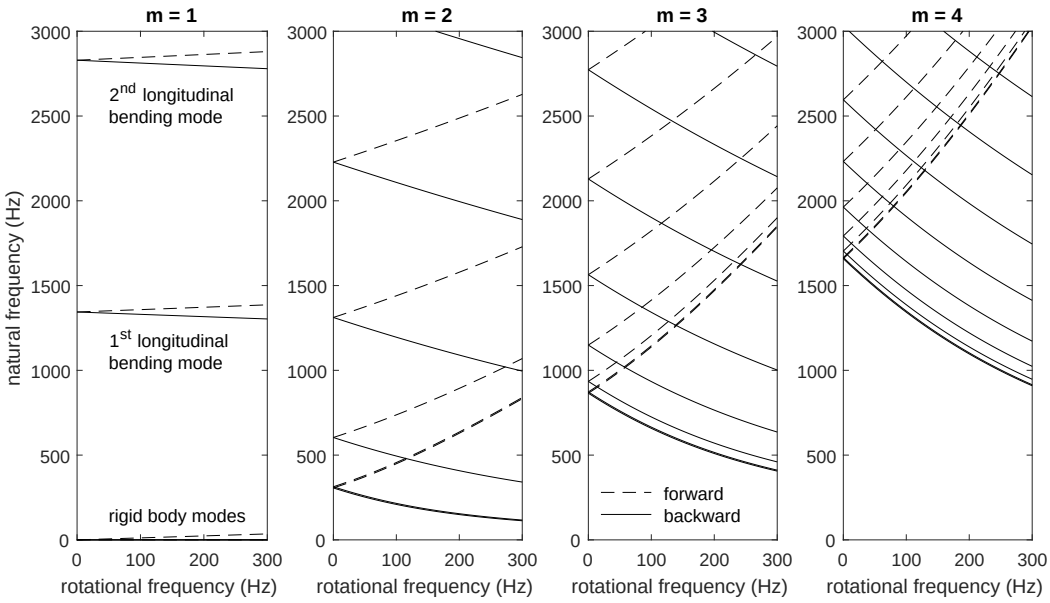

Figure 5: Campbell diagram for free rotating cylinder with properties in Table 1.

3.2. Parametric model for forced vibration

For the prediction of forced vibration involving rigid-body and bending mode excitation ($m \geq 1$), a truncated modal expansion is adopted where $p_{mn}(t)$ and $q_{mn}(t)$ are modal response variables:

$$\begin{aligned} u(\theta,z,t) &= \sum_{m=1}^{M}\sum_{n=0}^{N} U_{mn}(z)\left[p_{mn}(t)\sin m\theta + q_{mn}(t)\cos m\theta\right] \\ v(\theta,z,t) &= \sum_{m=1}^{M}\sum_{n=0}^{N} V_{mn}(z)\left[p_{mn}(t)\cos m\theta - q_{mn}(t)\sin m\theta\right] \\ w(\theta,z,t) &= \sum_{m=1}^{M}\sum_{n=0}^{N} W_{mn}(z)\left[p_{mn}(t)\sin m\theta + q_{mn}(t)\cos m\theta\right] \end{aligned} \tag{30}$$

Suppose an external point load $P(t) = [P_x(t),\, P_y(t),\, P_z(t)]^T$ is applied at $(\theta, z) = (\theta_P, z_P)$, then

$$[f_x,\, f_y,\, f_z]^T = \tfrac{1}{R}P(t)\delta(\theta-\theta_P)\delta(z-z_P) \tag{31}$$

Substituting Eqs (30) and (31) into Eq. (10) and exploiting the orthogonality properties of $\sin m\theta$ and $\cos m\theta$ yields a set of $2M$ equations:

$$\begin{aligned} \sum_{n=0}^{\infty}\mathcal{K}_{mn}p_{mn} + \mathcal{F}_m^p &= \sum_{n=0}^{\infty}\left[G_{mn}\ddot{p}_{mn} - 2\Omega\mathbf{\Lambda}_m G_{mn}\dot{q}_{mn} - \Omega^2\mathbf{\Pi}_m G_{mn}p_{mn}\right] \\ \sum_{n=0}^{\infty}\mathcal{K}_{mn}q_{mn} + \mathcal{F}_m^q &= \sum_{n=0}^{\infty}\left[G_{mn}\ddot{q}_{mn} + 2\Omega\mathbf{\Lambda}_m G_{mn}\dot{p}_{mn} - \Omega^2\mathbf{\Pi}_m G_{mn}q_{mn}\right] \end{aligned} \tag{32}$$

where $\mathcal{F}_m^{p,q} = (\rho\pi Rh)^{-1}\mathbf{H}_m^{p,q}(\theta_P)P(t)\delta(z-z_P)$ with $\mathbf{H}_m^p(\theta) = \mathrm{diag}\,([\sin m\theta,\, \cos m\theta,\, \sin m\theta])$ and $\mathbf{H}_m^q(\theta) = \mathrm{diag}\,([\cos m\theta,\, -\sin m\theta,\, \cos m\theta])$. Substituting $\mathcal{K}_{mn} = -\omega_{mn}^2 G_{mn}$, and premultiplying by G_{mq}^T, then inte-

grating over $z \in [-L/2, L/2]$ and applying orthogonality properties from Eqs. (26)-(28), yields

$$\begin{aligned}
\ddot{p}_{mn} - 2\Omega\left(m + \tfrac{b_{mn}}{a_{mn}}\right)\dot{q}_{mn} + \left(\omega_{mn}^2 - \Omega^2\tfrac{c_{mn}}{a_{mn}}\right)p_{mn} &= \tfrac{1}{\mu_{mn}}G_{mn}^T(z_P)\mathbf{H}_m^p(\theta_P)P(t) \\
\ddot{q}_{mn} + 2\Omega\left(m + \tfrac{b_{mn}}{a_{mn}}\right)\dot{p}_{mn} + \left(\omega_{mn}^2 - \Omega^2\tfrac{c_{mn}}{a_{mn}}\right)q_{mn} &= \tfrac{1}{\mu_{mn}}G_{mn}^T(z_P)\mathbf{H}_m^q(\theta_P)P(t)
\end{aligned} \tag{33}$$

where $\mu_{mn} = \rho\pi R h a_{mn}$.

It can be easily verified that the rigid-body dynamics are correctly represented by Eq. (33) when the assumed mode shapes given in section 2.3 are adopted. Of special importance for rotordynamic analysis are the tilting modes with $G_{1,1}(z) = [z,\, -z,\, R]^T$, as these are subject to gyroscopic effects when the cylinder is rotating. For this case, $a_{11} = \frac{1}{6}L^3 + R^2L$, $b_{11} = -\frac{1}{6}L^3$, $c_{11} = 0$ and so Eq. (33) becomes

$$\begin{aligned}
(\tfrac{1}{12}m_0L^2 + \tfrac{1}{2}m_0R^2)\ddot{p}_{11} - \Omega m_0R^2\dot{q}_{11} &= z_P\sin(\theta_P)P_x(t) - z_P\cos(\theta_P)P_y(t) + R\sin(\theta_P)P_z(t) \\
(\tfrac{1}{12}m_0L^2 + \tfrac{1}{2}m_0R^2)\ddot{q}_{11} + \Omega m_0R^2\dot{p}_{11} &= z_P\cos(\theta_P)P_x(t) + z_P\sin(\theta_P)P_y(t) + R\cos(\theta_P)P_z(t)
\end{aligned} \tag{34}$$

where $m_0 = 2\rho\pi RhL$ is the total mass of the cylinder. Here, the gyroscopic cross-coupling terms, which involve the axial moment of inertia $I_{zz} = m_0R^2$, result in non-zero natural frequencies for conical precession.

Equation (33) can be written in matrix form for multiple point loads P_j, and with the inclusion of damping, as

$$\mathbf{M}_{mn}\ddot{\xi}_{mn} + (\mathbf{C}_{mn} + 2\Omega\mathbf{J}_{mn})\,\dot{\xi}_{mn} + \left(\mathbf{K}_{mn} - \Omega^2\mathbf{K}_{mn}^{\Omega}\right)\xi_{mn} = \sum_j \mathbf{E}_{mn}(\theta_j, z_j)P_j(t) \tag{35}$$

where $\xi_{mn}^T = [p_{mn},\, q_{mn}]$ and

$$\mathbf{M}_{mn} = \mu_{mn}\begin{bmatrix} 1 & 0 \\ 0 & 1 \end{bmatrix},\ \mathbf{J}_{mn} = \mu_{mn}\left(m + \frac{b_{mn}}{a_{mn}}\right)\begin{bmatrix} 0 & -1 \\ 1 & 0 \end{bmatrix},$$

$$\mathbf{E}_{mn}(\theta, z) = \begin{bmatrix} U_{mn}(z)\sin m\theta & V_{mn}(z)\cos m\theta & W_{mn}(z)\sin m\theta \\ U_{mn}(z)\cos m\theta & V_{mn}(z)\sin m\theta & W_{mn}(z)\cos m\theta \end{bmatrix},$$

$$\mathbf{K}_{mn} = \omega_{mn}^2\mathbf{M}_{mn},\ \mathbf{K}_{mn}^{\Omega} = \frac{c_{mn}}{a_{mn}}\mathbf{M}_{mn},\ \mathbf{C}_{mn} = 2\zeta_{mn}\mathbf{K}_{mn}.$$

Combining the uncoupled equations (35) for all $2M(N+1)$ modes gives

$$\mathbf{M}\ddot{\boldsymbol{\xi}} + (\mathbf{C} + 2\Omega\mathbf{J})\,\dot{\boldsymbol{\xi}} + \left(\mathbf{K} - \Omega^2\mathbf{K}_{\boldsymbol{\Omega}}\right)\boldsymbol{\xi} = \sum_j \mathbf{E}(\theta_j, z_j)P_j(t) \tag{36}$$

where $\boldsymbol{\xi}^T = (\xi_1^T,\, \xi_2^T,\, ...,\, \xi_M^T) \in \mathbb{R}^{2M(N+1)}$, with $\xi_m^T = \left[\xi_{m0}^T,\, \xi_{m1}^T,\, ...,\, \xi_{mN}^T\right]$. Consequently, $\mathbf{M}$, $\mathbf{C}$, $\mathbf{J}$, $\mathbf{K}$, $\mathbf{K}_{\boldsymbol{\Omega}} \in \mathbb{R}^{2M(N+1)\times 2M(N+1)}$ are block diagonal matrices in correspondence with Eq. (35). Also, $\mathbf{E} \in \mathbb{R}^{2M(N+1)\times 3}$ and the displacements at an arbitrary space-fixed location can be expressed

$$[u(\theta, z, t), v(\theta, z, t), w(\theta, z, t)]^T = \mathbf{E}^T(\theta, z)\boldsymbol{\xi}(t) \tag{37}$$

4. Experiments

4.1. Experimental system

The experimental system is comprised of a horizontal cylindrical rotor of length 0.8 m with two radial magnetic bearings, as shown in Fig. 6. The rotor is a uniform steel tube with properties given in Table 1. The rotor has very high natural frequencies for beam bending modes (>1300 Hz) due to its thin-walled structure. The bearings are of a specialized design for thin-walled rotors and are based on a distributed actuation magnetic bearing (DAMB) topology [27]. Each bearing comprises a circular array of 24 small U-shape

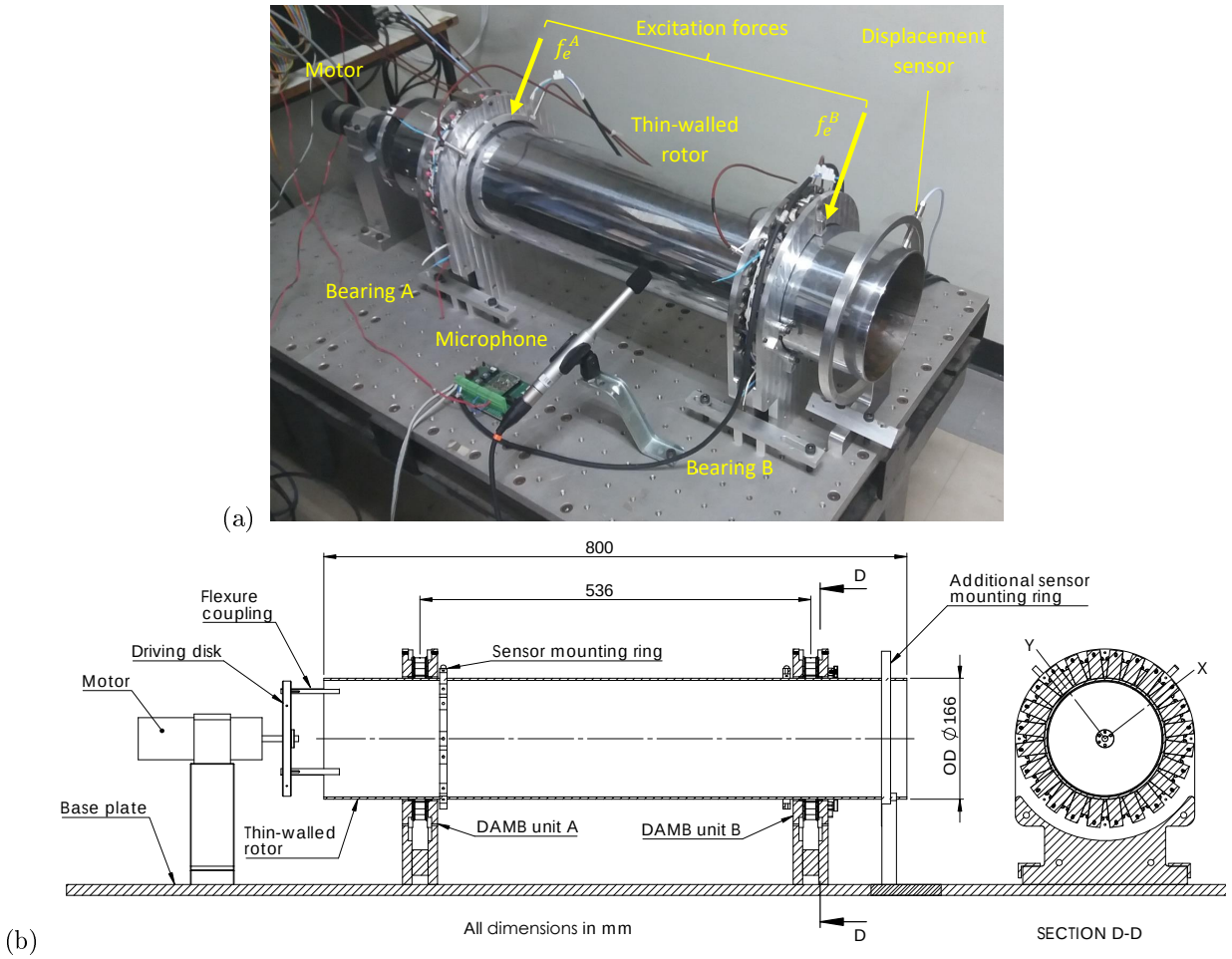

Figure 6: Experimental thin-walled cylindrical rotor supported by distributed actuation magnetic bearings (a) photograph (b) cross-section drawings

Table 3: Properties of magnetic bearing actuators

Parameter	Symbol	Value	Units
Pole face area	A	72	mm^2
Permeability of free space	μ_0	$4\pi \times 10^{-7}$	H/m^{-1}
Effective flux path length	l	1.2	mm
Maximum number of coil-turns	N_0	100	
Bias current	i_0	2.2	A

electromagnetic actuators that apply attractive forces around the periphery of the rotor. Using multiple compact actuators helps to avoid magnetic flux saturation within the rotor wall and thereby achieve high load capacity. The coil winding pattern and driving scheme are devised such that the orthogonal components of the net bearing force (X-Y axes) depend principally on two (X-Y) control current components within the two coils on each actuator. Hence, the bearing forces can be controlled using strategies similar to those applied with conventional AMBs. In open-loop configuration, the bearings are unstable due to the negative stiffness effects from coil bias currents. Stable support of the rotor can be achieved using feedback control of the coil currents based on the measured rotor position. Further details on the operation and modelling of the bearing are given in section 4.2.

The rotor is driven by a brushless d.c. motor connected via a flexible coupling. This coupling comprises a disk mounted on the motor shaft with four foam rubber flexures (length 40 mm) that connect between the disk periphery and the end of the rotor. This coupling supports the transmission of a driving torque to the rotor but has negligible effect on the flexible mode dynamics of the rotor.

The system has two pairs of rotor position sensors located in two transverse planes adjacent to each bearing (see Fig. 6). These sensors are standard eddy current proximity probes and are used for feedback control of the bearings. In addition, a single high-sensitivity proximity probe is mounted on a movable ring that can be positioned to measure the radial vibration at any point on the rotor surface.

Each bearing has one actuator that is wound with an extra coil. The extra coils are used to apply localized excitation forces to the rotor wall that are aligned with the $+X$ axis direction, as shown in Fig. 6. The excitation forces couple strongly with the flexural dynamics of the rotor wall and so can be used for vibration response testing and modal identification of the overall structure during operation.

4.2. Active magnetic bearing model

For the DAMBs, the attractive force applied to the rotor wall by the j^{th} actuator at location (θ_j, z_j) may be described by a standard reluctance force model [28]:

$$P_{x,j}(t) = f_j(x_j, I_1, I_2, i_e) = -\mu_0 A \frac{(N_1 I_1 + N_2 I_2 + N_e i_e)^2}{(l + 2x_j)^2} \tag{38}$$

Here, A is the pole face area, l is the effective flux path length for the equilibrium position (accounting for the total reluctance including air gap) and $x_j = u(\theta_j, z_j, t)$ is the radial displacement of the rotor wall. Frictional forces may be neglected, and so $P_{y,j}(t) = P_{z,j}(t) = 0$. Physical values for the experimental system are given in Table 3. Two of the coils, having number of turns $N_1(\theta_j)$ and $N_2(\theta_j)$, are used for levitation control and are supplied currents I_1 and I_2 according to a differential driving mode with constant bias component i_0 and control currents i_1 and i_2 [28]. The excitation coil, having N_e turns, is supplied current i_e. This is used for excitation only and is powered separately to provide a localized forcing that can be utilized in dynamic response testing. For the levitation coils, the coil winding and driving scheme is defined by

$$N_1(\theta) = N_0 \frac{|\cos\theta|}{\sqrt{|\sin\theta| + |\cos\theta|}},\ N_2(\theta) = N_0 \frac{|\sin\theta|}{\sqrt{|\sin\theta| + |\cos\theta|}}$$

$$I_1(\theta, t) = i_0 + \text{sgn}(\cos\theta) i_1(t),\ I_2(\theta_j, t) = i_0 + \text{sgn}(\sin\theta) i_2(t)$$

where N_0 is the maximum number of coil turns. This scheme helps to decouple the levitation forces from the flexible mode dynamics and can be realized with just four current-controlled drives powering four sets of coils connected in series [27]. Linearizing Eq. (38) about the operating point E with $x_j = i_1 = i_2 = i_e = 0$ gives an equation in the form

$$f_j(t) = f_0 + k_a x_j + \sum_{k=1}^{2} \sigma_k i_k + \sigma_e i_e \tag{39}$$

where $f_0 = \mu_0 A l^{-2} i_0^2 (N_1 + N_2)^2$ and

$$k_a(\theta_j) = \left.\frac{df_j}{dx_j}\right|_E = 4\mu_0 A l^{-3} i_0^2 (N_1 + N_2)^2 \tag{40}$$

$$\sigma_k(\theta_j) = \left.\frac{df_j}{di_k}\right|_E = \mathrm{sgn}(g_k(\theta_j)) 2\mu_0 A N_k l^{-2} i_0 (N_1 + N_2) \tag{41}$$

$$\sigma_e(\theta_j) = \left.\frac{df_j}{di_e}\right|_E = \mathrm{sgn}(g_k(\theta_j)) 2\mu_0 A N_e l^{-2} i_0 (N_1 + N_2) \tag{42}$$

For the experimental system, the two identical radial bearings, A and B, have axial locations $z = -268$ mm and $z = 268$ mm respectively. Combining Eq. (39) for all 24 actuators, the bearing forces are expressed

$$F^{A,B} = F_0 + \mathbf{D} x^{A,B} + \mathbf{\Sigma} i^{A,B} + \mathbf{\Sigma}_e i_e^{A,B} \tag{43}$$

where $\mathbf{\Sigma}$ is a 24×2 matrix with coefficients $\Sigma_{jk} = \sigma_k(\theta_j)$, $i = 1, 2, ..., 24$, $k = 1, 2$, $\mathbf{\Sigma}_e$ is a 24×1 matrix with coefficients $\Sigma_{e,j} = \sigma_e(\theta_j)$, $j = 1, 2, ..., 24$ and $\mathbf{D}$ is a 24×24 diagonal matrix containing the negative stiffness coefficients $D_{j,j} = k_a(\theta_j)$.

To stabilize the bearings and give suitable stiffness and damping properties, feedback of the radial displacement of the rotor $y_s(t)$ measured at four locations is required. The combination of two bearings with an arbitrary linear feedback controller may be represented in state-space form as

$$\begin{aligned} \dot{x}_c &= \mathbf{A}_c x_c + \mathbf{B}_c y_s \\ i^{A,B} &= \mathbf{C}_c^{A,B} x_c \end{aligned} \tag{44}$$

where the matrices capture the dynamics of the feedback controller and drives. Combining Eqs (43) and (44) gives the complete linearized DAMB model as

$$\begin{aligned} \dot{x}_c &= \mathbf{A}_c x_c + \mathbf{B}_c y_s \\ F^{A,B} &= F_0 + \mathbf{D} x^{A,B} + \mathbf{\Sigma} \mathbf{C}_c^{A,B} x_c + \mathbf{\Sigma}_e i_e^{A,B} \end{aligned} \tag{45}$$

Combining the state variables for rotor vibration in Eq. (36) with the dynamic states in Eq. (45) and using $y_s(t) = \mathbf{E}_s^T \boldsymbol{\xi}(t)$ gives the complete system model in the form

$$\begin{aligned} \frac{d}{dt}\begin{bmatrix} \boldsymbol{\xi} \\ \dot{\boldsymbol{\xi}} \\ x_c \end{bmatrix} &= \begin{bmatrix} \mathbf{0} & \mathbf{I} & \mathbf{0} \\ -\mathbf{M}^{-1}\left(\mathbf{K}_{cl} - \Omega^2 \mathbf{K}_{\mathbf{\Omega}}\right) & -\mathbf{M}^{-1}\left(\mathbf{C} + 2\Omega \mathbf{J}\right) & \mathbf{M}^{-1}\left(\mathbf{E}_A \mathbf{\Sigma}^A \mathbf{C}_c^A + \mathbf{E}_{A,B} \mathbf{\Sigma}^B \mathbf{C}_c^B\right) \\ \mathbf{B}_c \mathbf{E}_s^T & \mathbf{0} & \mathbf{A}_c \end{bmatrix} \begin{bmatrix} \boldsymbol{\xi} \\ \dot{\boldsymbol{\xi}} \\ x_c \end{bmatrix} \\ &\quad + \begin{bmatrix} \mathbf{0} & \mathbf{0} \\ \mathbf{M}^{-1} \mathbf{E}_A \mathbf{\Sigma}_e^A & \mathbf{M}^{-1} \mathbf{E}_B \mathbf{\Sigma}_e^B \\ \mathbf{0} & \mathbf{0} \end{bmatrix} \begin{bmatrix} f_e^A \\ f_e^B \end{bmatrix} \end{aligned} \tag{46}$$

where $\mathbf{K}_{cl} = \mathbf{K} - \mathbf{E}_A \mathbf{D}^A \mathbf{E}_A^T - \mathbf{E}_B \mathbf{D}^B \mathbf{E}_B^T$ and the excitation forces are $f_e^A = \mathbf{\Sigma}_e^A i_e$, $f_e^B = \mathbf{\Sigma}_e^B i_e$.

4.3. Results

Frequency response testing was undertaken for a range of forcing conditions and rotational speeds. Radial excitation forces were applied to the wall of the levitated rotor using the two excitation coils located at bearings A and B, as shown in Fig. 6a. Two different forcing patterns were adopted involving symmetric ($f_e^A = f_e^B$) and anti-symmetric ($f_e^A = -f_e^B$) excitation. The first case predominantly excites modes with even values of n, while the second case excites modes with odd values of n. During testing, the DAMBs were operated with low gain PID feedback using a standard centralized control strategy to achieve decoupled control of parallel and conical rigid-body modes (see [28], Chapter 8). The resulting bearing forces produce very soft support charateristics and yield natural frequencies for rigid-body modes close to 30 Hz.

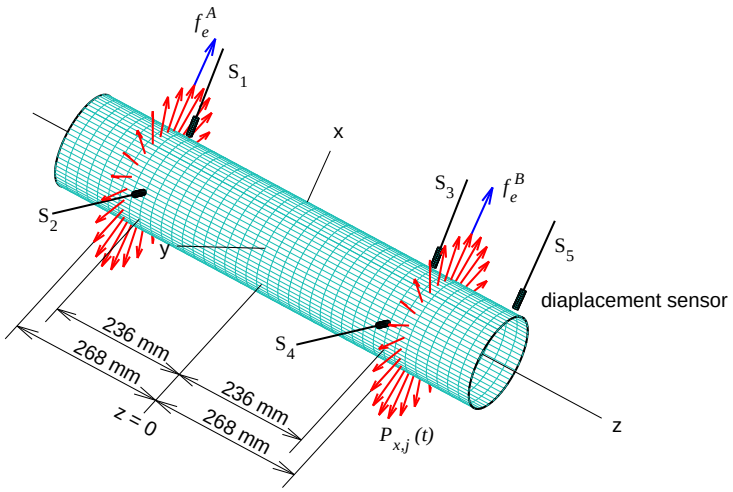

Figure 7: Schematic diagram of rotating cylinder model for the experimental system showing location of DAMB forces and displacement sensors

Tests were first performed without rotation and without attachment of the rotor coupling. Results are shown in Fig. 8. The data shown is for displacement measured by the sensor at the free end of the rotor. The model-based predictions show an agreement within 0.5 % for all natural frequencies within the testing range, with the maximum difference in natural frequency being 3.5 Hz for the $m = 3, n = 1$ mode (875 Hz). Non-uniformity of the cylindrical rotor due to machining error is a possible source of error, in addition to uncertainty in the DAMB properties. Note that the force gains for the two excitation coils are slightly different which leads to mixed excitation of symmetric and anti-symmetric modes for the two cases. Some extra resonances occur in the low frequency range (50 - 200 Hz) due to flexibility of the foundation structure on which the bearings are mounted.

For tests with rotation, imbalance excitation arose due to non-uniformity of the cylinder rotor. Disturbances from sensor run-out error and the flexible coupling were also present. These were suppressed by using a harmonic vibration control algorithm to generate disturbance-canceling forces, applied through the bearings [29]. This had negligible effect on the dynamic response characteristics of the system. Frequency response data for a rotational speed of 11.1 Hz ($\Omega = 70$ rad/s) are shown in Fig. 9. The numerical results are based on the parametric model for the speed-dependent dynamics, as described in section 3. The splitting of natural frequencies for forward and backward modes due to rotation effects is clearly evident for all flexible modes. A high level of agreement between the theoretical model and experimental data is seen. The small amplitude behaviour, which might reveal frequencies for anti-resonance, cannot be easily verified from the experimental data due to measurement errors from noise and electrical interference. This introduces a 'noise floor' for the sensitivity measurements which tends to increase with rotational speed, making accurate response testing more challenging for higher speeds.

The complete set of experimental data is superimposed on the model-based Campbell diagram in Fig. 11. The experimental values for the natural frequencies show a high level of consistency with the model-based results. Even though, for certain modes, there is a visible offset error in the frequencies, the trend for changing rotational speed matches closely. To perform tests at higher rotational speeds (>12 Hz), the rotor imbalance was reduced by the addition of small correction masses on the inner surface of the rotor. A partial balancing solution with masses of 45 g $\angle 10°$ at the driven end and 90 g $\angle 170°$ at the non-driven end was used. This resulted in a slight splitting of the degenerate mode natural frequencies, even at zero rotational speed, due to the asymmetry introduced by the added masses. For certain modes, the change (lowering) of natural frequency is quite evident, but the overall trend for higher speeds is consistent with the model-based results.

By using acoustic signal measurements, the natural frequencies could be identified over a wider range

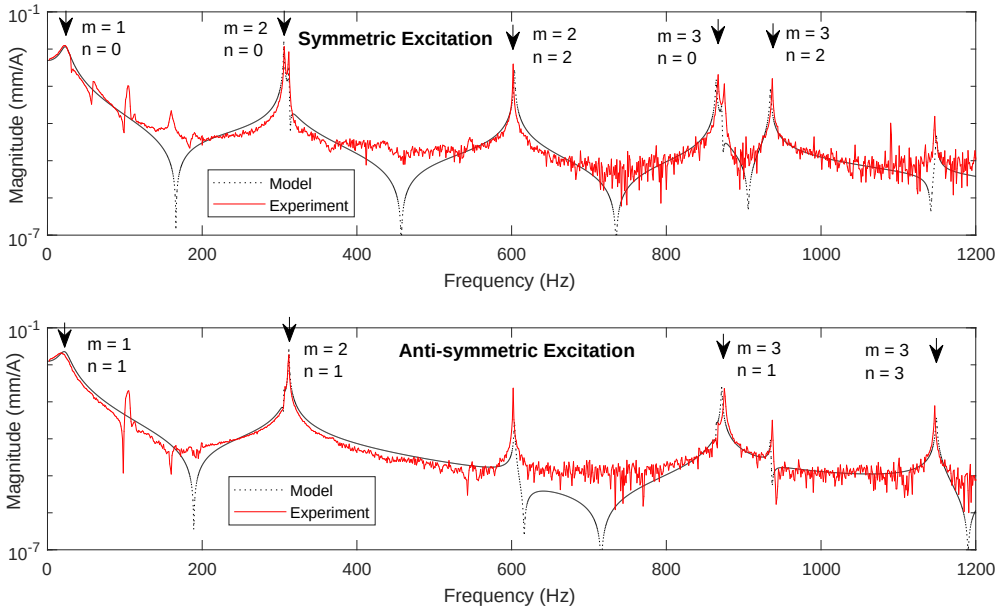

Figure 8: Frequency response data from experiment and theoretical modeling for no rotation

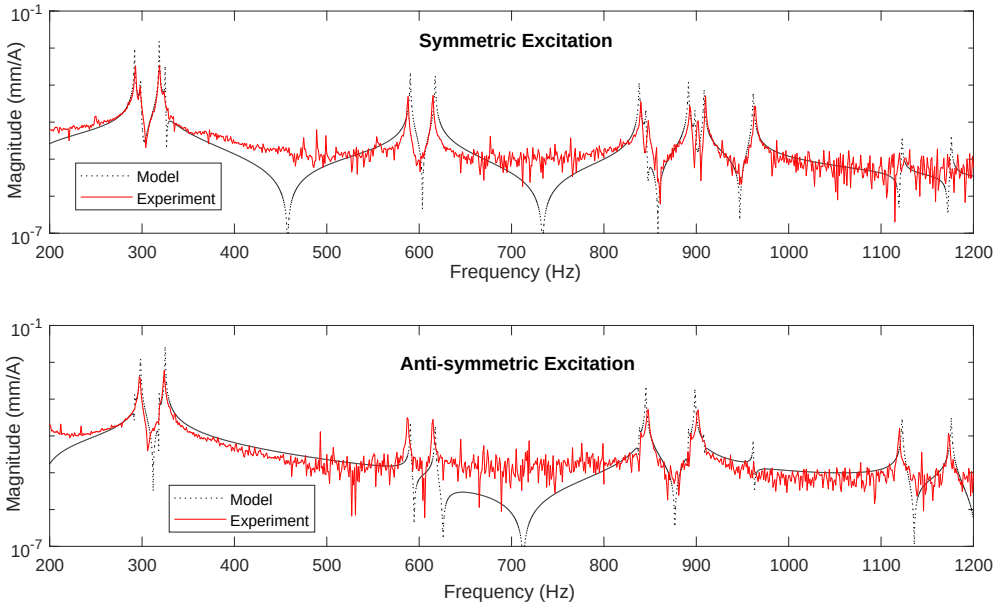

Figure 9: Frequency response data from experiment and theoretical modeling for rotation with $\Omega/2\pi = 11.1$ Hz

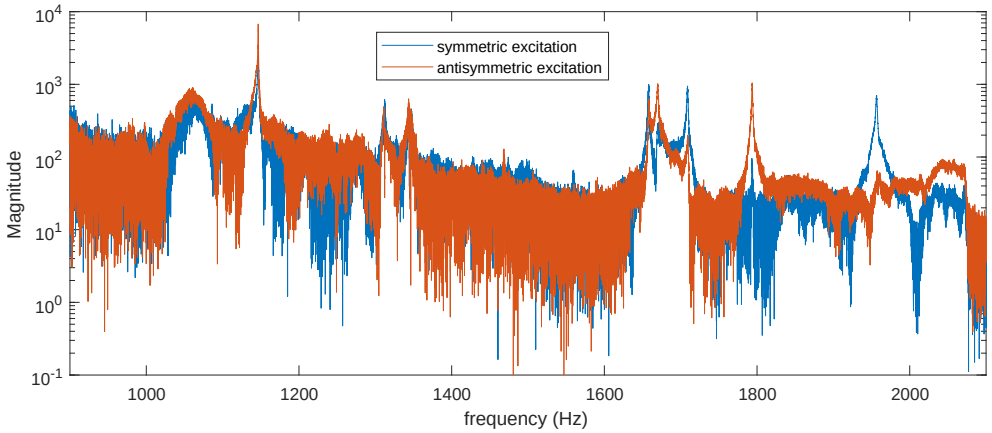

Figure 10: Example data for natural frequency identification over range 1100-2000 Hz: FFT of acoustic signal measurements

than was possible with displacement signals alone. Tests were performed with short duration harmonic 'chirp' signals for excitation, with frequency sweep covering the range of interest. Example data is shown in Fig. 10. The FFT of the acoustic signal gives a clear indication of the natural frequencies within the target interval of 1100 to 2000 Hz. Identified natural frequencies for the rotor without balance masses within this range are shown, together with model-based predictions, in Fig. 12. The overall consistency between the experimental and theoretical results provides important validation for the described shell theory and for the use of the parametric forced-response model (Eq. (36)) in rotordynamic prediction.

5. Conclusions

This paper has defined and experimentally verified a 3-dimensional multi-mode model for the vibration behaviour of a thin-walled cylindrical rotor based on shell theory. Salient points from the study are that

1. The described model can provide a complete and accurate description of the vibrational dynamics of a thin-walled cylindrical rotor for a practical range of excitation types and rotational speeds.
2. The shown invariance properties of the mode-shapes allows the construction of a discrete model having a simple parametric dependency on rotational speed, with negligible impact on accuracy.
3. The parametric model for speed-dependent natural frequencies (Eq. (29)) indicates that, for the low order bending modes, the effect from circumferential extension is very small.

An implication of point 3 is that, even for experiments with higher rotational speeds, the correctness of the centripetal (Ω^2) terms in the equations of motion may not be exposed unless modes with significant in-surface extension are excited and identified.

The described theoretical model may be used to construct benchmark cases for validation of finite element codes for rotating shell structures. It also has good suitability for use in the design of active vibration control strategies. This will be considered in future work.

Acknowledgement

This work was support by the Thailand Research Fund and Chiang Mai University [grant number BRG5980013].

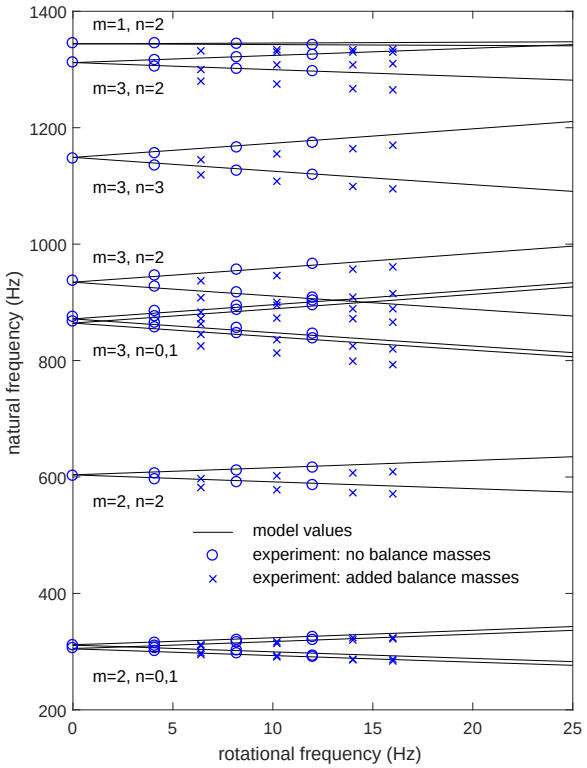

Figure 11: Campbell diagram for experimental system: theoretical model and experimental data is shown for low frequency modes

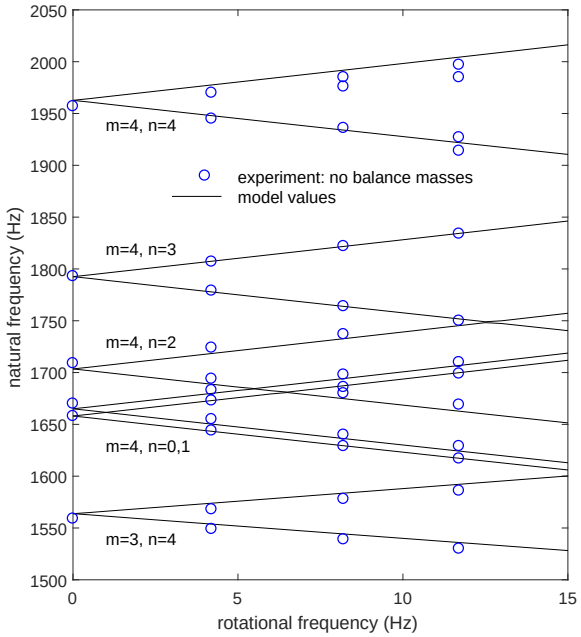

Figure 12: Campbell diagram for experimental system: theoretical model and experimental data is shown for high frequency modes

References

[1] G. H. Bryan. On the beats in the vibrations of a revolving cylinder or bell. *Proceedings of the Cambridge Philosophical Society*, pages 101 – 111, 1890.

[2] R.A. DiTaranto and M. Lessen. Coriolis acceleration effect on the vibration of a rotating thin-walled circular cylinder. *ASME Journal of Applied Mechanics*, 31(4):700–701, 1964. doi: 10.1115/1.3629733.

[3] A. V. Srinivasan and G. F. Lauterbach. Traveling waves in rotating cylindrical shells. *ASME Journal of Engineering for Industry*, 93(4):1229–1232, 1971. doi: 10.1115/1.3428067.

[4] J. Padovan. Natural frequencies of rotating prestressed cylinders. *Journal of Sound and Vibration*, 31(4):469 – 482, 1973. ISSN 0022-460X. doi: 10.1016/S0022-460X(73)80261-5.

[5] C.T. Loy and K.Y. Lam. Vibrations of rotating thin cylindrical panels. *Applied Acoustics*, 46(4):327 – 343, 1995. ISSN 0003-682X. doi: 10.1016/0003-682X(96)81499-X.

[6] Y.-J. Kim and J.S. Bolton. Effects of rotation on the dynamics of a circular cylindrical shell with application to tire vibration. *Journal of Sound and Vibration*, 275(3):605 – 621, 2004. doi: 10.1016/j.jsv.2003.06.003.

[7] N. Alujevic, N. Campillo-Davo, P. Kindt, W. Desmet, B. Pluymers, and S. Vercammen. Analytical solution for free vibrations of rotating cylindrical shells having free boundary conditions. *Engineering Structures*, 132:152–171, 2017. doi: 10.1016/j.engstruct.2016.11.008.

[8] K.Y. Lam and C.T. Loy. Analysis of rotating laminated cylindrical shells by different thin shell theories. *Journal of Sound and Vibration*, 186(1):23 – 35, 1995. ISSN 0022-460X. doi: 10.1006/jsvi.1995.0431.

[9] L. Hua, K.Y. Lam, and T.Y. Ng. *Rotating Shell Dynamics*. Elsevier, 2005.

[10] J. L. Sanders. An improved first-approximation theory for thin shells. *Langley Research Center, NASA Technical Report, NASA TR R-24*, 1959.

[11] W. Soedel. *Vibrations of Shells and Plates*. Marcel Dekker Inc., 1981.

[12] T. Saito and M. Endo. Vibration of finite length, rotating cylindrical shells. *Journal of Sound and Vibration*, 107(1):17 – 28, 1986. ISSN 0022-460X. doi: 10.1016/0022-460X(86)90279-8.

[13] S. Sun, D. Cao, and S. Chu. Free vibration analysis of thin rotating cylindrical shells using wave propagation approach. *Archive of Applied Mechanics*, 83(4):521 – 531, 2013. ISSN 1432-0681. doi: 10.1007/s00419-012-0701-x.

[14] Z. Luo, Y. Zhu, N. Sun, Q. Han, and B. Wen. Approximate method in analyzing forced vibration response of rotating short thin-wall cylindrical shells in different boundary conditions. *Journal of Vibrational Engineering and Technologies*, 2:567–579, 12 2014.

[15] K.Y. Lam and C.T. Loy. Influence of boundary conditions for a thin laminated rotating cylindrical shell. *Composite Structures*, 41(3):215 – 228, 1998. ISSN 0263-8223. doi: 10.1016/S0263-8223(98)00012-9.

[16] L. Hua and K.Y. Lam. Frequency characteristics of a thin rotating cylindrical shell using the generalized differential quadrature method. *International Journal of Mechanical Sciences*, 40(5):443 – 459, 1998. ISSN 0020-7403. doi: 10.1016/S0020-7403(97)00057-X.

[17] S. Sun, S. Chu, and D. Cao. Vibration characteristics of thin rotating cylindrical shells with various boundary conditions. *Journal of Sound and Vibration*, 331:4170–4186, 2012. doi: 10.1016/j.jsv.2012.04.018.

[18] S. Sun, D. Cao, and Q. Han. Vibration studies of rotating cylindrical shells with arbitrary edges using characteristic orthogonal polynomials in the rayleigh–ritz method. *International Journal of Mechanical Sciences*, 68:180 – 189, 2013. ISSN 0020-7403. doi: 10.1016/j.ijmecsci.2013.01.013.

[19] K. Forsberg. Influence of boundary conditions on the modal characteristics of thin cylindrical shells. *American Institute of Aeronautics and Astronautics*, 2(12):2150 – 2157, 1964. ISSN 0001-1452. doi: 10.2514/3.55115.

[20] J.D. Watkins and R.C. Clary. Vibrational characteristics of some thin-walled cylindrical and conical frustum shells. *Langley Research Center, NASA Technical Note, NASA TN D-2729*, 1965.

[21] J. L. Sewall and E.C. Naumann. An experimental and analytical vibration study of thin cylindrical shells with and without longitudinal stiffeners. *Langley Research Center, NASA Technical Note, NASA TN D-4705*, 1968. doi: 10.1121/1.405248.

[22] M. Endo, K. Hatamura, M. Sakata, and O. Taniguchi. Flexural vibration of a thin rotating ring. *Journal of Sound and Vibration*, 92(2):261 – 272, 1984. doi: 10.1016/0022-460X(84)90560-1.

[23] W. Fakkaew and M.O.T. Cole. Vibration due to non-circularity of a rotating ring having discrete radial supports - with application to thin-walled rotor/magnetic bearing systems. *Journal of Sound and Vibration*, 423:355 – 372, 2018. ISSN 0022-460X. doi: 10.1016/j.jsv.2018.02.055.

[24] Z. Luo, Y. Zhu, N. Sun, Q. Han, and B. Wen. Approximate method in analyzing forced vibration response of rotating short thin-wall cylindrical shells in different boundary conditions. *Journal of Vibrational Engineering and Technologies*, 2:567–579, 2014.

[25] S.C. Huang and W. Soedel. Response of rotating rings to harmonic and periodic loading and comparison with the inverted problem. *Journal of Sound and Vibration*, 118(2):253 – 270, 1987. doi: 10.1016/0022-460X(87)90524-4.

[26] A. E. H. Love. On the small free vibrations and deformations of elastic shells,. *Philosophical Trans. of the Royal Society (London), Series A*, 17:491–549, 1888.

[27] M.O.T. Cole and W. Fakkaew. An active magnetic bearing for thin-walled rotors: vibrational dynamics and stabilizing control. *IEEE/ASME Transactions on Mechatronics*, 23(6):2859–2869, 2018. doi: 10.1109/TMECH.2018.2877777.

[28] G. Schweitzer and E. H. Maslen. *Magnetic Bearings: Theory, Design, and Application to Rotating Machinery*. Springer-Verlag, Berlin, 2009.

[29] C. Chamroon, M.O T. Cole, and W. Fakkaew. Model and control system development for a distributed actuation magnetic bearing and thin-walled rotor subject to noncircularity. *ASME Journal of Vibration and Acoustics*, 141(5):Art. No. 051006, 2019.

Appendix A: Characteristic equation coefficients

Coefficients for the biquartic polynomial in Eq. (14) are

$$\begin{aligned}
A_8 &= a_4 b_2 c_2 \\
A_6 &= a_4 g_1 + c_2\left(a_2 b_2 - d_2^2\right) \\
A_4 &= a_4(b_0+b_\omega)(c_0+c_\omega) + a_2 g_1 + b_2\left(e_1^2 + a_0 c_2 + a_\omega c_2\right) - d_2\left(c_2 d_0 + c_2 d_\omega + g_2\right) \\
A_2 &= (a_0+a_\omega) g_1 + (b_0+b_\omega)\left(e_1^2 + a_2 c_0 + a_2 c_\omega\right) - (d_0+d_\omega)\left(c_0 d_2 + c_\omega d_2 + g_2\right) \\
A_0 &= (a_0+a_\omega)(b_0+b_\omega)(c_0+c_\omega) - (c_0+c_\omega)(d_0+d_\omega)^2 \\
g_1 &= (b_0+b_\omega)c_2 + b_2(c_0+c_\omega) + f_1^2 + f_1 f_2 \\
g_2 &= c_2(d_0+d_\omega) + (c_0+c_\omega)d_2 + 2e_1 f_1 + e_1 f_2
\end{aligned}$$

Appendix B: Real eigenfunctions

For a given root $\lambda = \alpha + j\beta$ of Eq. (14) and corresponding eigenvector $\Psi^T = [a+jb,\, c+jd,\, e+jf]$ (with $j = \sqrt{-1}$), a set of real-valued function vectors may be defined as

$$\begin{aligned}
\mathcal{R}_1(\lambda,\Psi,z) &= \cosh\alpha z \begin{bmatrix} a\cos\beta z - b\tanh\alpha z\sin\beta z \\ c\cos\beta z - d\tanh\alpha z\sin\beta z \\ e\tanh\alpha z\cos\beta z - f\sin\beta z \end{bmatrix} \\
\mathcal{R}_2(\lambda,\Psi,z) &= \cosh\alpha z \begin{bmatrix} a\sin\beta z + b\tanh\alpha z\cos\beta z \\ c\sin\beta z + d\tanh\alpha z\cos\beta z \\ e\tanh\alpha z\sin\beta z + f\cos\beta z \end{bmatrix} \\
\mathcal{R}_3(\lambda,\Psi,z) &= \cosh\alpha z \begin{bmatrix} a\tanh\alpha z\sin\beta z + b\cos\beta z \\ c\tanh\alpha z\sin\beta z + d\cos\beta z \\ e\sin\beta z + f\tanh\alpha z\cos\beta z \end{bmatrix} \\
\mathcal{R}_4(\lambda,\Psi,z) &= \cosh\alpha z \begin{bmatrix} a\tanh\alpha z\cos\beta z - b\sin\beta z \\ c\tanh\alpha z\cos\beta z - d\sin\beta z \\ e\cos\beta z - f\tanh\alpha z\sin\beta z \end{bmatrix}
\end{aligned}$$

It can be shown that the derivatives are given by $\mathcal{R}_1' = \alpha\mathcal{R}_4 - \beta\mathcal{R}_2$, $\mathcal{R}_2' = \alpha\mathcal{R}_3 + \beta\mathcal{R}_1$, $\mathcal{R}_3' = \alpha\mathcal{R}_2 + \beta\mathcal{R}_4$ and $\mathcal{R}_4' = \alpha\mathcal{R}_1 - \beta\mathcal{R}_3$.

For four complex roots, $\lambda_1 = \alpha + j\beta$, $\lambda_2 = \alpha - j\beta$, $\lambda_3 = -\alpha - j\beta$, $\lambda_4 = -\alpha + j\beta$, and $\Psi_1^T = [a+jb,\, c+jd,\, e+jf]$, $\Psi_2^T = [a-jb,\, c-jd,\, e-jf]$, $\Psi_3^T = [a+jb,\, c+jd,\, -e-jf]$, $\Psi_4^T = [a-jb,\, c-jd,\, -e+jf]$ then

$$\sum_{k=1}^{4} C_k \Psi_k \exp(\lambda_k z) = \sum_{k=1}^{4} \kappa_k \mathcal{R}_k(\lambda_k, \Psi_k, z) \tag{47}$$

where $\kappa_1 = C_1 + C_2 + C_3 + C_4$, $\kappa_2 = j\,(C_1 - C_2 - C_3 + C_4)$, $\kappa_3 = j\,(C_1 - C_2 + C_3 - C_4)$ and $\kappa_4 = C_1 + C_2 - C_3 - C_4$.

For a pair of imaginary roots $\lambda_1 = j\beta$, $\lambda_2 = -j\beta$ and $\Psi_1^T = [a,\, c,\, jf]$, $\Psi_2^T = [a,\, c,\, -jf]$ then

$$\sum_{k=1}^{2} C_k \Psi_k \exp(\lambda_k z) = \kappa_1 \mathcal{R}_1(\lambda_1,\Psi_1,z) + \kappa_2 \mathcal{R}_1(\lambda_1,\Psi_1,z) = \kappa_1 \begin{bmatrix} a\cos\beta z \\ c\cos\beta z \\ -f\sin\beta z \end{bmatrix} + \kappa_2 \begin{bmatrix} a\sin\beta z \\ c\sin\beta z \\ f\cos\beta z \end{bmatrix} \tag{48}$$

where $\kappa_1 = C_1 + C_2$ and $\kappa_2 = j\,(C_1 - C_2)$.

For a pair of real roots, $\lambda_1 = \alpha$, , $\lambda_2 = -\alpha$ and $\Psi_1^T = [a,\, c,\, e]$, $\Psi_2^T = [a,\, c,\, -e]$ then

$$\sum_{k=1}^{2} C_k \Psi_k \exp(\lambda_k z) = \kappa_1 \mathcal{R}_1(\lambda_1,\Psi_1,z) + \kappa_2 \mathcal{R}_4(\lambda_1,\Psi_1,z) = \kappa_1 \begin{bmatrix} a\cosh\alpha z \\ c\cosh\alpha z \\ e\sinh\alpha z \end{bmatrix} + \kappa_2 \begin{bmatrix} a\sinh\alpha z \\ c\sinh\alpha z \\ e\cosh\alpha z \end{bmatrix} \tag{49}$$

where $\kappa_1 = C_1 + C_2$ and $\kappa_2 = C_1 - C_2$.

Although there are eight possible type combinations for the roots of Eq. (14), the axial mode shape function can always be constructed as in Eq. (17) with $\Gamma_k(z) = \mathcal{R}_{1,2,3,4}$ and κ_k selected from Eq. (47)-(49) according to each root type. For improved numerical behaviour, a normalized version may also be used:

$$G(z) = \sum_{k=1}^{8} \kappa_k^* \Gamma_k^*(z) \tag{50}$$

where $\kappa_k^* = a\kappa_k$, $\Gamma_k^*(z) = a^{-1}\Gamma_k(z)$ with $a = \cosh\left(\frac{\mathrm{Re}(\lambda_k)L}{2}\right)$.

Controllability and actuator placement optimization for active damping of a thin rotating ring with piezo-patch transducers

Ziv Brand, Matthew O. T. Cole*

Department of Mechanical Engineering, Chiang Mai University, Chiang Mai 50200, Thailand

Abstract

A study on optimal actuator placement for controlling flexural vibration of a thin ring under rotation is reported. Piezoelectric patch actuators and sensors may be applied with a feedback control system to provide active damping of structural vibration involving circumferential traveling waves. To assess the interaction of vibration with actuator and sensor operation, a theoretical model of a rotating annulus is first considered. This model shows that, for the non-rotating case, a minimum of two actuators is required to achieve controllability of any given set of natural vibration modes. To determine the optimum positioning, a controllability metric is further defined that accounts for rotational-speed-dependent dynamics and initial passive damping of targeted modes. This metric involves a time-weighted controllability Gramian matrix derived from a balanced model realization for combined treatment of sensors and actuators in collocated pairs. The results show that the optimal angular separation of two actuator/sensor pairs varies with rotational speed due to the combined influence of initial damping and Coriolis forces. To provide a practical solution, a finite range of speeds is considered within a mini-max optimization criterion. Experiments have been conducted on a thin steel ring with collocated piezo-patch sensor/actuator pairs. A decentralized active damping control scheme based on a synthetic proof-mass-damper control law was used to suppress vibration involving the six lowest frequency vibration modes (with natural frequencies of 161, 442 and 846 Hz without rotation). The experiments confirm the theoretical results and show that, although a single actuator-sensor pair can achieve improved damping at high rotational speeds, the optimized configuration of two pairs provides effective damping over the full range of operating speeds.

Keywords: Vibration control, Travelling wave, Controllability Gramian, Active mass damper, Piezoelectric patch

1. Introduction

The vibration characteristics of rotating cylindrical shells differ from those of stationary shells due to the influence of centrifugal and Coriolis forces, as well as initial hoop tension. The effect of rotation may be observed as a beating vibration caused by the differing wave speeds for forward and backward travelling waves [1]. To apply active vibration control methods to rotating cylindrical shells, it is important to understand how the effects from rotation will impact on the effectiveness of any proposed control implementation. Important aspects include the number and positioning of actuators and sensors on the structure, the size and shape of actuators and sensors, the type of control algorithm, and the methodology for controller design. This paper focuses on the first of these issues and reports both theoretical and experimental results for piezo-based active damping control of a short rotating cylindrical shell.

Piezoelectric patch actuators and sensors are important components for vibration control of shell structures as they are lightweight and flexible, have high frequency response and can be easily bonded to a

*Corresponding author

Email addresses: brand_ziv@cmu.ac.th (Ziv Brand), motcole@dome.eng.cmu.ac.th (Matthew O. T. Cole)

structure. Their low mass and flexibility means they can be applied with very little impact on the structural dynamics [2]. Application to thin-walled rotor systems is also possible, where dynamic instability, high-cycle fatigue and stress-related damage to bearings may be alleviated through active vibration control [3].

Many research studies and applications have considered piezoelectric actuators for vibration damping of stationary structures. The benchmark case of a cantilever beam has been investigated extensively since it offers the possibility to validate and compare different approaches [4, 5, 6]. Nestorović et al. [4] performed experiments on a cantilever beam with four ceramic piezoelectric patches and with control laws based on optimal linear quadratic regulation (LQR) and Kalman filtering. Junqiang et al. [6] presented the experimental identification and multi-mode vibration suppression of a flexible manipulator with piezoelectric actuators and strain sensors using optimal multi-pole-placement control. Xiang et al. [2], studied the optimal location of piezoelectric actuators for active vibration control of a membrane structure with optimization criterion based on the controllability Gramian. The optimization problem was solved using a genetic algorithm (GA) and particle swarm optimizer (PSO) algorithm. The classical LQR performance index was also considered as an objective function for the optimization process.

Active damping of vibration in cylindrical structures has been considered for applications such as cabins of aircrafts, hulls of submarines and bodies of rockets and missiles. In previous studies, however, only the non-rotating case has been studied [7, 8, 9, 10]. Ray and Baz [8] and Ray and Reddy [9] investigated active constrained layer damping (ACLD) of thin cylindrical composite shells using piezoelectrics. Caner [10], in addition to designing the control law for vibration suppression, investigated the optimal placement of piezoelectric patch actuators for a cylinderical tube with free ends. The optimization criterion involved the eigenvalues of the controllability Gramian matrix and took into account three measures: 1) standard deviation in order to achieve similar controllability degree for each mode, 2) summation of the eigenvalues to achieve small mean value and 3) a multiplication term involving all the eigenvalues to prevent any modes having very low controllability.

For vibration suppression in rotating shell structures, piezoelectric actuation and sensing has been proposed for decreasing fan blade vibration to achieve lighter, quieter, and more efficient turbomachinery. Duffy et al. [11] examined the viability of using piezoelectric sensors and actuators as part of an active control system to reduce resonance vibrations in composite fan blades under centrifugal load. The locations of the piezoelectric patches were chosen to coincide with the highest strain for the first bending mode of the blade at 0 rpm. Test results showed increased damping and reduced vibration over a range of rotational speeds.

Kumar and Ray [12] studied the performance of piezoelectric patches within an ACLD treatment of rotating conical shells. In their work, the effect of ACLD structure (fibre type and orientation) was investigated using a three-dimensional finite element model. A simple velocity feedback control law was adopted for simulation and assessment of various cases. Examination of the optimal location and/or number of piezoelectric actuators was not undertaken.

To describe the vibrational dynamics of cylindrical and conical elements, shell theories may be usefully applied [13, 14]. With the inclusion of rotation effects, free vibration behavior is seen to involve travelling waves that propagate around the circumference of the structure [15, 16]. Although the wavelength of circumferential waves is fixed by symmetry, the natural frequencies (and wave speed) vary significantly with rotational speed due to Coriolis forces and the hoop stress induced by centripetal acceleration. A number of studies have experimentally validated theoretical models of this behaviour [17, 18], including for the case of piezo-electric patch actuation and sensing [19]. However, to the authors' knowledge, the impact of the travelling wave dynamics on controllability, and the solution of the actuator/sensor placement problem for the case of a rotating cylindrical shell structure, has not been previously reported.

2. Theoretical model of a thin rotating ring with piezo patch elements

To derive a theoretical model for elastic vibration of a thin rotating cylinder/ring with piezoelectric patches, the geometry shown in Fig. 1 is first considered. To develop the equations of motion in the rotating frame, the angular position coordinate θ is defined relative to a fixed datum on the ring aligned with the X axis. Considering bending and extension in the plane of rotation only, the displacement of the neutral

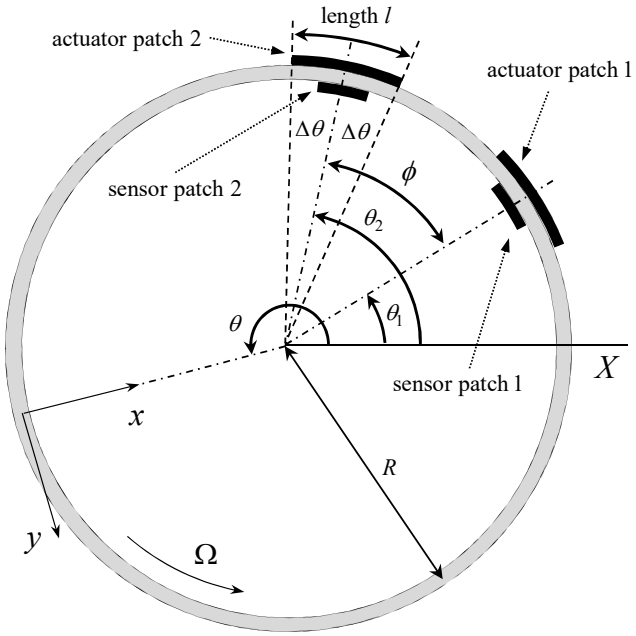

Figure 1: System schematic for model development showing geometry of two collocated actuator/sensor pairs

plane in the local (x, y) axes directions is defined by functions $u(t, \theta)$ and $v(t, \theta)$. These correspond to deflection in the radial and tangential directions respectively. First order approximation theory [20] gives the circumferential strain as

$$\varepsilon_\theta = \frac{1}{R}\left(\frac{\partial v}{\partial \theta} - u\right) - \frac{x}{R^2}\left(\frac{\partial v}{\partial \theta} + \frac{\partial^2 u}{\partial \theta^2}\right) \tag{1}$$

The stress-strain relation can be expressed

$$\sigma_\theta = \sigma_0 + E\varepsilon_\theta + C\dot{\varepsilon}_\theta \tag{2}$$

where E is Young's modulus and C is the material damping coefficient. For constant rotational speed, the mean component of the hoop stress due to rotation is $\sigma_0 = \rho R^2\Omega^2$ and the equations of motion for a differential element (neglecting rotational inertia) are [15, 16]:

$$\frac{\partial F_x}{\partial \theta} + RF_y\kappa_z = \rho AR\left[\ddot{u} + 2\Omega\dot{v} + \Omega^2\left(R - u\right)\right] \tag{3}$$

$$\frac{\partial F_y}{\partial \theta} - RF_x\kappa_z = \rho AR\left[\ddot{v} - 2\Omega\dot{u} + \Omega^2\frac{\partial u}{\partial \theta}\right] \tag{4}$$

$$\frac{\partial M_z}{\partial \theta} - RF_x + R\frac{\partial M_e}{\partial \theta} = 0 \tag{5}$$

where A is the cross-sectional area, κ_z is the curvature of the neutral plane about the axis of rotation, M_z is the internal bending moment and M_e is a moment distribution (per unit length) due to external forcing/actuation. Applying the first order approximation $RF_x\kappa_z \approx F_x$ and using the third equation to eliminate F_x from the first two gives

$$\frac{1}{R}\frac{\partial^2 M_z}{\partial \theta^2} + \rho AR\Omega^2\left(\frac{\partial^2 u}{\partial \theta^2} + \frac{\partial v}{\partial \theta}\right) + f_y + \frac{\partial^2 M_e}{\partial \theta^2} = \rho AR\left[\ddot{u} + 2\Omega\dot{v} - \Omega^2 u\right] \tag{6}$$

$$\frac{\partial f_y}{\partial \theta} - \frac{1}{R}\frac{\partial M_z}{\partial \theta} - \frac{\partial M_e}{\partial \theta} = \rho AR\left[\ddot{v} - 2\Omega\dot{u} + \Omega^2\frac{\partial u}{\partial \theta}\right] \tag{7}$$

where $f_y = F_y - \rho R^2\Omega^2$. Applying the standard inextensibility relation $u = \frac{\partial v}{\partial \theta}$, eliminating f_y and substituting for M_z based on Eqs (1) and (2) gives the governing equation as

$$\frac{d^2}{dt^2}\left(\frac{\partial^2 v}{\partial\theta^2} - v\right) + 4\Omega\frac{d}{dt}\frac{\partial v}{\partial\theta} - \Omega^2\left(\frac{\partial v^4}{\partial\theta^4} + 3\frac{\partial^2 v}{\partial\theta^2}\right) + \frac{EI_z}{\rho AR^4}\left(\frac{\partial v^2}{\partial\theta^2} + 2\frac{\partial v^4}{\partial\theta^4} + \frac{\partial v^6}{\partial\theta^6}\right) + \frac{CI_z}{\rho AR^4}\frac{d}{dt}\left(\frac{\partial v^2}{\partial\theta^2} + 2\frac{\partial v^4}{\partial\theta^4} + \frac{\partial v^6}{\partial\theta^6}\right) = \frac{1}{\rho AR}\left(\frac{\partial^3 M_e}{\partial\theta^3} + \frac{\partial M_e}{\partial\theta}\right) \quad (8)$$

where I_z is the second moment of area for the ring cross section.

To obtain a discrete model incorporating a finite number of modes, the displacements may be expressed:

$$u(t,\theta) = \sum_{m=1}^{M} p_m(t)\sin m\theta + q_m(t)\cos m\theta \quad (9)$$

$$v(t,\theta) = \frac{1}{m}\sum_{m=1}^{M} q_m(t)\sin m\theta - p_m(t)\cos m\theta \quad (10)$$

where $p_m(t)$ and $q_m(t)$ are modal displacement variables and $\sin m\theta$ and $\cos m\theta$ are the mode shapes for free vibration, having integer wavenumber m. Substituting for $v(t,\theta)$ then multiplying by $\sin m\theta$ and integrating over $\theta \in (0, 2\pi)$ gives

$$\left(m^2+1\right)\ddot{q}_m - 4m\Omega\dot{p}_m + \Omega^2\left(m^4 - 3m^2\right)q_m + \frac{EI_z}{\rho AR^4}\left(m^3-m\right)^2 q_m + \frac{CI_z}{\rho AR^4}\left(m^3-m\right)^2\dot{q}_m = -\frac{m}{2\pi\rho AR}\int_0^{2\pi}\left(\frac{\partial^3 M_e}{\partial\theta^3} + \frac{\partial M_e}{\partial\theta}\right)\sin m\theta d\theta \quad (11)$$

Similarly, multiplying by $\cos m\theta$ and integrating gives

$$\left(m^2+1\right)\ddot{p}_m + 4m\Omega\dot{q}_m + \Omega^2\left(m^4 - 3m^2\right)p_m - \frac{EI_z}{\rho AR^4}\left(m^3-m\right)^2 p_m + \frac{CI_z}{\rho AR^4}\left(m^3-m\right)^2\dot{p}_m = \frac{m}{2\pi\rho AR}\int_0^{2\pi}\left(\frac{\partial^3 M_e}{\partial\theta^3} + \frac{\partial M_e}{\partial\theta}\right)\cos m\theta d\theta \quad (12)$$

Suppose identical piezoelectric patch actuators having length $l = 2R\Delta\theta$ are positioned at angular locations $\theta_1^A, \theta_2^A, \ldots, \theta_N^A$. The case of two actuator/sensor pairs is shown in Fig. 1. The effect of the patch with excitation voltage $u_n(t)$ can be modelled by a uniform moment distribution over the length of the patch:

$$M_e(\theta,t) = \begin{cases} \sum_n K_A u_n(t), & \theta_n^A - \Delta\theta \le \theta \le \theta_n^A + \Delta\theta \\ 0, & \text{otherwise} \end{cases} \quad (13)$$

where K_A is an electro-mechanical coupling coefficient that takes account of the finite width of the patch. Substituting Eq. (13) in Eq. (11) and (12) gives

$$\left(m^2+1\right)\ddot{q}_m - 4m\Omega\dot{p}_m + \Omega^2 m^2\left(m^2-3\right)q_m + \frac{EI_z}{\rho AR^4}\left(m^3-m\right)^2 q_m + \frac{CI_z}{\rho AR^4}\left(m^3-m\right)^2\dot{q}_m = \left(m^2+1\right)b_m\sum_n \cos m\theta_n^A . u_n \quad (14)$$

$$\left(m^2+1\right)\ddot{p}_m + 4m\Omega\dot{q}_m + \Omega^2 m^2\left(m^2-3\right)p_m + \frac{EI_z}{\rho AR^4}\left(m^3-m\right)^2 p_m + \frac{CI_z}{\rho AR^4}\left(m^3-m\right)^2\dot{p}_m = \left(m^2+1\right)b_m\sum_n \sin m\theta_n^A . u_n \quad (15)$$

where

$$b_m = \frac{K_A \sin m\Delta\theta}{\pi\rho A} \cdot \frac{m\left(1-m^2\right)}{\left(m^2+1\right)}$$

The inclusion of piezo patch elements for strain sensing is also considered for feedback control purposes. For a small patch attached to the surface of the cylinder, measurements of localized bending strain will be obtained, as given by

$$\varepsilon_S(\theta) = \frac{d}{2R^2}\left(\frac{\partial v}{\partial\theta} + \frac{\partial^2 u}{\partial\theta^2}\right) \tag{16}$$

where d is wall thickness. Therefore, the output voltage for sensor p located at $\theta = \theta_p^S$ may be expressed

$$y_p = K_S\varepsilon_S\left(\theta_p^S\right) = \frac{K_S d}{2R^2}\sum_{m=1}^{M}\left(1-m^2\right)\left(p_m \sin m\theta_p^S + q_m \cos m\theta_p^S\right) \tag{17}$$

where K_S is an electro-mechanical coupling coefficient. Note that the mass and stiffness contribution from the patches is considered negligible in this model.

Defining the vector of state variables as $x_m(t) = \left[\begin{array}{cccc} p_m & q_m & \dot{p}_m & \dot{q}_m \end{array}\right]^T$, the state evolution equations for each mode-pair (value of m) have the form

$$\dot{x}_m = A_m(\Omega)x_m + B_m u_n \tag{18}$$

where

$$A_m(\Omega) = \left[\begin{array}{cccc} 0 & 0 & 1 & 0 \\ 0 & 0 & 0 & 1 \\ -\omega_m^2 - \Omega^2 d_m & 0 & -2\zeta_m\omega_m & -\Omega g_m \\ 0 & -\omega_m^2 - \Omega^2 d_m & \Omega g_m & -2\zeta_m\omega_m \end{array}\right] \tag{19}$$

with constant coefficients

$$\omega_m = \frac{m\left(m^2-1\right)}{\sqrt{m^2+1}} \cdot \sqrt{\frac{EI_z}{\rho A R^4}},\ d_m = \frac{m^2\left(m^2-3\right)}{m^2+1},\ g_m = \frac{4m}{m^2+1},\ \zeta_m = \frac{C}{2E}\omega_m$$

For the case of a single actuator located at $\theta = \theta_1^A = 0$,

$$B_m = b_m \left[\begin{array}{c} 0 \\ 0 \\ \sin m\theta_1^A \\ \cos m\theta_1^A \end{array}\right] = b_m \left[\begin{array}{c} 0 \\ 0 \\ 0 \\ 1 \end{array}\right] \tag{20}$$

The model Eq. (18) predicts the splitting of natural frequencies for forward and backward wave solutions that occurs for non-zero rotational speed. The two natural frequencies can be found from the eigenvalues of A_m and, for $\zeta_m = 0$, are given by

$$\omega_m^{b,f} = \pm\frac{g_m\Omega}{2} + \sqrt{\omega_m^2 + d_m\Omega^2 + \left(\frac{g_m\Omega}{2}\right)^2} \tag{21}$$

Note that, for rotating frame observations, it is the lower frequency that corresponds to the forward travelling wave [17].

A complete multi-input-multi-output system model, retaining a finite number of modes, can be constructed in the form

$$\begin{aligned} \dot{x} &= \left[\begin{array}{cccc} A_1 & 0 & \cdots & 0 \\ 0 & A_2 & & 0 \\ \vdots & & \ddots & \\ 0 & 0 & & A_M \end{array}\right] x + \left[\begin{array}{c} B_1 \\ B_2 \\ \vdots \\ B_M \end{array}\right] u \\ y &= \left[\begin{array}{cccc} C_1 & C_2 & \cdots & C_M \end{array}\right] x \end{aligned} \tag{22}$$

where A_m,B_m,C_m are defined according to the preceding equations.

It can be seen that, for the case of a single actuator (Eq. (20)), the control input does not couple with p_m when $\Omega = 0$ and so this state is uncontrollable. For effective control to be achieved over a range of rotational speeds, at least two actuators and sensors are required. The use of collocated actuator/sensor pairs allows model-free passivity-based control schemes to be employed. Therefore, the results in this paper focus on the key case of two collocated transducer pairs having arbitrary angular separation ϕ, for which

$$B_m = b_m \begin{bmatrix} 0 & 0 \\ 0 & 0 \\ 0 & \sin m\phi \\ 1 & \cos m\phi \end{bmatrix}, \; C_m = \frac{K_S d}{2R^2}\left(1-m^2\right) \begin{bmatrix} 1 & 0 & 0 & 0 \\ \sin m\phi & \cos m\phi & 0 & 0 \end{bmatrix}. \tag{23}$$

The transfer function for a collocated actuator/sensor pair, as calculated from this model, is shown in Fig. 2. The model parameters where chosen to match the experimental system having the properties given in Table 1. The splitting of natural frequencies due to rotation effects is clearly evident for a rotational frequency of 13 Hz (81.7 rad/s). This splitting of natural frequencies leads to observations of amplitude beating in the free response [1].

Table 1: Properties of experimental system: rotating steel cylinder

parameter	symbol	value	units
cylinder radius	r	111	mm
wall thickness	d	3.1	mm
material density	ρ	7740	kg/m^3
Young's modulus	E	2.07×10^{11}	N/m^2
actuator patch length	l	50	mm
actuator patch width	w	30	mm
cylinder axial length		51	mm

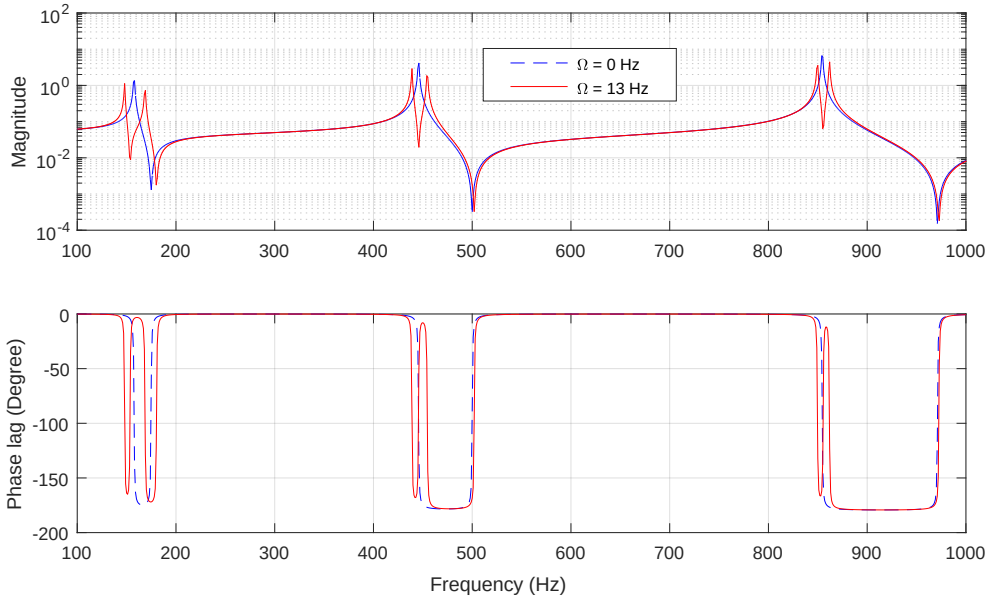

Figure 2: Frequency reponse function for theoretical model with properties given in Table 1 for rotational frequencies of 0 and 13 Hz.

3. Actuator/sensor placement optimization subject to rotation effects

3.1. Rotational-speed-dependent controllability

To assess the effectiveness of actuator deployment, many previous studies have considered evaluations of the controllability Gramian that arises in the state-transition problem for a linear system [5, 21, 22]. For a dynamic system defined by $\dot{x} = Ax + Bu$, the state trajectory is given by

$$x(t) = e^{At}x_0 + e^{At}\int_0^t e^{-A\tau}Bu(\tau)\,d\tau \tag{24}$$

where initial state values are $x(0) = x_0$. For given final state values $x(t_f) = x_f$, the minimum-energy control action that achieves state transfer is $u^*(t) = -B^T e^{A^T(t_f-t)}W(t_f)^{-1}\left(e^{At_f}x_0 - x_f\right)$ where $W(t) = \int_0^t e^{A\tau}BB^T e^{A^T\tau}d\tau$ is the controllability Gramian [23]. The minimized cost (control input energy) is

$$J^*(t_f) = \int_0^{t_f} u^{*^T}(\tau)\,u^*(\tau)\,d\tau = \left(e^{At_f}x_0 - x_f\right)^T W(t_f)^{-1}\left(e^{At_f}x_0 - x_f\right) \tag{25}$$

For the limiting case of infinite time, $W_c = \lim_{t_f\to\infty} W(t_f)$ satisfies the Lyapunov equation

$$AW_c + W_cA^T + BB^T = 0 \tag{26}$$

and the minimized cost is $J_c = x_f^T W_c^{-1} x_f$.

This approach may be applied to Eq. (18). With a scaling of state variables according to $\tilde{x}_m = [\tilde{\omega}_m p_m, \tilde{\omega}_m q_m, \dot{p}_m, \dot{q}_m]$, where $\tilde{\omega}_m = \sqrt{\omega_m^2 + \Omega^2 d_m}$, the solution of Eq. (26) can be obtained algebraically as

$$W_c = \begin{bmatrix} W_m & 0 \\ 0 & W_m \end{bmatrix} \tag{27}$$

where

$$W_m = \frac{b_m^2}{4\zeta_m\omega_m\left(\left(\frac{g_m\Omega}{2\zeta_m\omega_m}\right)^2 + 1\right)}\begin{bmatrix} \frac{1}{8}\left(\frac{g_m\Omega}{\zeta_m\omega_m}\right)^2 & -\frac{g_m\Omega}{4\zeta_m\omega_m} \\ -\frac{g_m\Omega}{4\zeta_m\omega_m} & \frac{1}{8}\left(\frac{g_m\Omega}{\zeta_m\omega_m}\right)^2 + 1 \end{bmatrix} \tag{28}$$

Figure 3 shows a plot of the singular values (SVs) of W_m for the pair of modes with $m = 2$, for various values of ζ_m. It can be easily verified from Eq. (28) that, for no rotation ($\Omega = 0$), one singular value is zero (i.e. one mode is uncontrollable), while the other matches the previously published result for a single mode system $\sigma_2 = \frac{b_m^2}{4\zeta_m\omega_m}$ [21]. However, as the speed of rotation increases, the two singular values converge and, in the limit $\Omega \to \infty$, the two modes have equal controllability ($\sigma_{1,2}(W_m) \to \frac{b_m^2}{8\zeta_m\omega_m}$). The practical implication is that, without rotation, more than one actuator is required to achieve full controllability. However, one actuator may suffice for high-speed rotation. This somewhat surprising property is due to the changing character of vibration, from standing waves when stationary to travelling-waves when rotating.

It is clear from Eq. (28) that the Coriolis term $g_m\Omega$ and initial damping level ζ_m play an important combined role in the rotational-speed-dependent controllability. However, there are two potential flaws with employing a controllability metric based on some measure/norm of W_m in the actuator placement optimization problem. Firstly, the controllability measure is higher when ζ_m is smaller. This implies that modes with lower damping would be considered 'more controllable' and, hence, would have a lower weighting in the multi-mode optimization problem. In practice, modes with lower damping should be given more weighting than those which are already well damped. A further issue is that the change in controllability with rotational speed is dependent on ζ_m. It can be seen from Eq. (28) that the transition from uncontrollable to uniform controllability with increasing speed occurs more quickly for lower damping than for higher damping (and, for zero damping, would be instantaneous). These somewhat unsatisfactory results relate largely to the conventional definition of controllability.

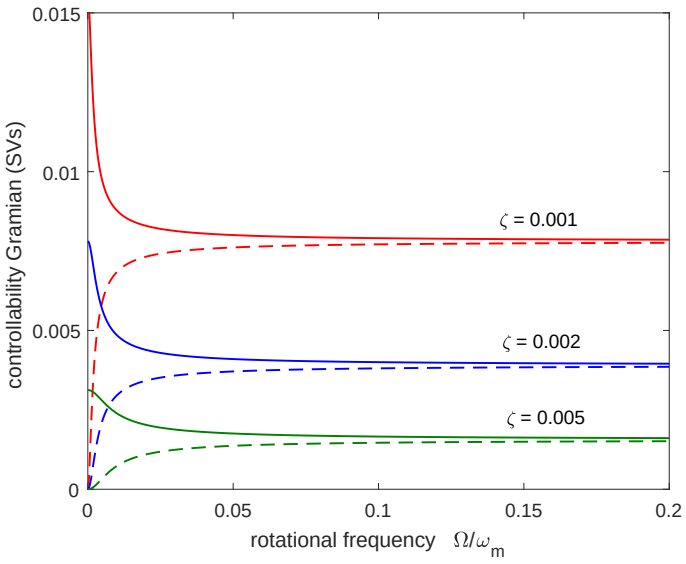

Figure 3: Singular values of controllability Gramian W_m from Eq. (28) for $m = 2$ mode with various damping levels:

3.2. Time-weighted controllability metric for active damping problem

For active vibration control, the broad aim is to maximize damping (energy dissipation) for the vibratory modes of a structure subject to the available actuation capacity/energy. As an optimization problem, it is appropriate to consider the control effort required to achieve convergence of the state variables to zero for a given set of initial conditions. However, for the standard controllability problem with solution given by Eq. (25), if x_f is zero then the optimized cost $J^*(t_f) = x_0^T e^{A^T t_f} W(t_f)^{-1} e^{A t_f} x_0$ tends to zero as $t_f \to \infty$. Moreover, the solution for $u^*(t)$ is zero for the infinite-time case. To overcome this issue, a modified cost with a time-dependent exponential weighting may be considered:

$$\tilde{J}(t) = \int_0^t e^{2\gamma\tau} u^T(\tau)\, u(\tau)\, d\tau \tag{29}$$

where γ is a positive scalar that is selected to match the target convergence rate for actively damped free vibration. Defining the time-weighted control input $\tilde{u}(t) = e^{\gamma t} u(t)$, the state evolution Eq. (24) may be expressed

$$x(t) = e^{At} x_0 + e^{At} \int_0^t e^{(-A-\gamma I)\tau} B \tilde{u}(\tau)\, d\tau, \tag{30}$$

The minimized cost is

$$\tilde{J}^*(t_f) = \int_0^{t_f} \tilde{u}^{*^T}(\tau)\, \tilde{u}^*(\tau)\, d\tau = x_0^T \tilde{W}(t_f)^{-1} x_0, \tag{31}$$

where $\tilde{W}(t_f) = \int_0^{t_f} e^{(-\gamma I - A)\tau} B B^T e^{\left(-\gamma I - A^T\right)\tau} d\tau$ is the time-weighted controllability Gramian. In the limit $t_f \to \infty$, the solution may be obtained as a real positive definite solution to

$$(-\gamma I - A)\tilde{W}_c + \tilde{W}_c\left(-\gamma I - A^T\right) + B B^T = 0, \tag{32}$$

Existence of the solution requires that all modes are controllable and that the eigenvalues $\lambda_i = \mathrm{eig}(A)$ satisfy $\mathrm{Re}(\lambda_i) > -\gamma\ \forall i$.

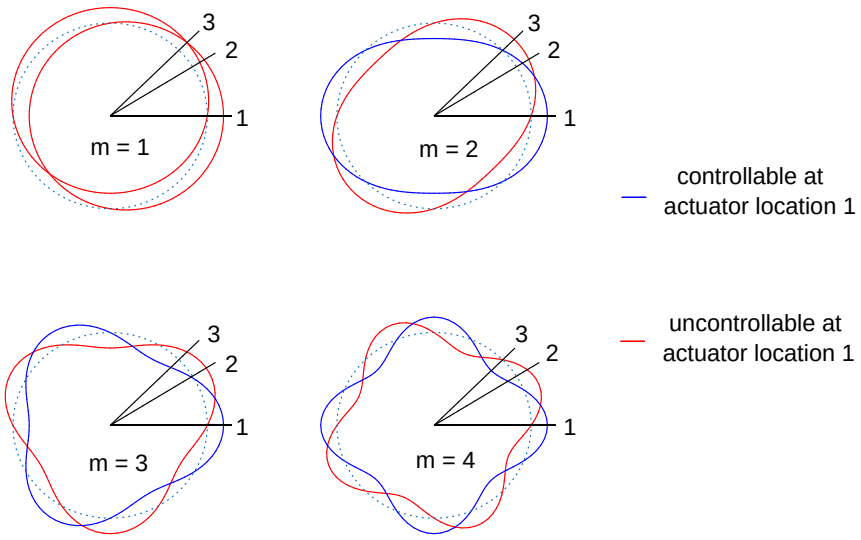

Figure 4: Mode shapes for pairs of degenerate modes with wave numbers $m = 1, 2, 3, 4$. Line colour indicates controllability for actuator location 1 based on standing mode assumptions, as appropriate for zero rotational speed.

3.3. Actuator/sensor placement optimization

Inclusion of the exponential weighting in Eq. (25) ensures that the optimal solution $\tilde{u}^*(t)$ converges to zero as t tend to infinity and therefore $u^*(t) = -B^T e^{(-2\gamma I - A)t} \tilde{W}(t_f)^{-1} x_0$ is well-defined and non-zero even when $t_f \to \infty$. For a solution to exist, the target convergence rate γ must be selected higher than the convergence rate of the uncontrolled modes: $\gamma > \zeta_m \omega_m$. Modes for which the damping level is much lower than the target value will lead to small singular values of $\tilde{W}_c$, while modes that already have damping levels close to the target value will give large singular values.

For multi-mode cases, the following controllablity metric may be adopted as a cost function for the placement optimization:

$$P_c = \sqrt{\text{trace}\left(\Delta \tilde{W}_c^{-1} \Delta\right)} \tag{33}$$

Here, $\tilde{W}_c$ is the time-weighted controllability Gramian and Δ is a diagonal weighting matrix having the form

$$\Delta = \begin{bmatrix} \delta_1 I_{4\times4} & 0 & \cdots & 0 \\ 0 & \delta_2 I_{4\times4} & & 0 \\ \vdots & & \ddots & \\ 0 & 0 & & \delta_M I_{4\times4} \end{bmatrix} \tag{34}$$

where the scalar weights δ_m may be set to zero for neglected modes and unity for targeted modes. The controllability metric P_c is an indicator of the minimum input signal energy that is required to drive the system to rest, averaged over all possible initial excitations of the targeted modes (i.e. over all initial state values for which $\|x_0\|_2 = 1$). For a system with two actuator pairs, the metric P_c may be treated as a function of the separation angle ϕ and the rotational speed Ω:

$$P_c = g(\phi, \Omega) \tag{35}$$

For a given fixed rotational speed Ω_o, the optimization problem may be defined as

$$\text{Minimize } g(\phi, \Omega_o) \text{ over } \phi \in (0, \pi). \tag{36}$$

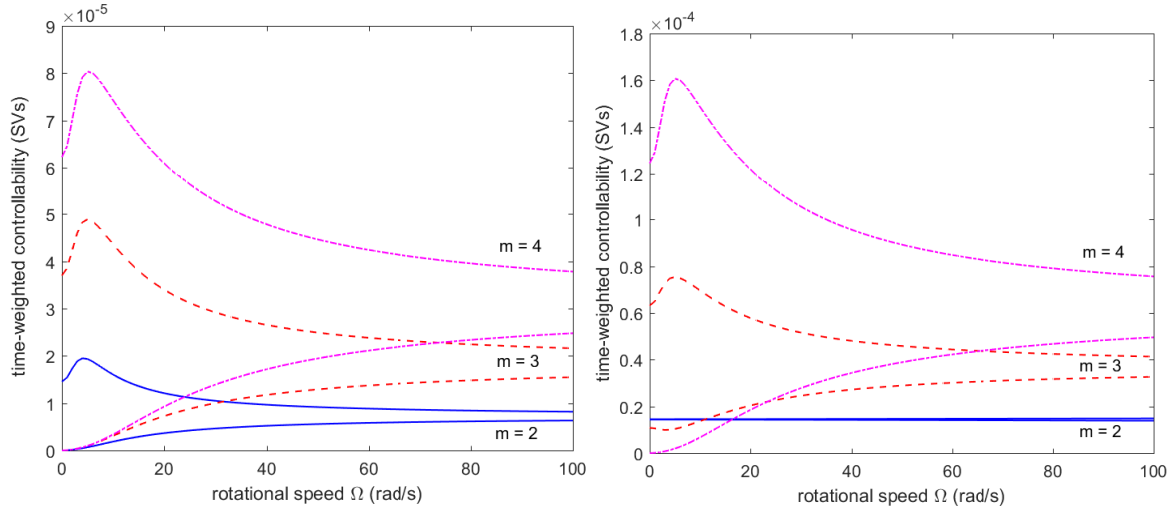

(a) one actuator

(b) two actuators with separation $\phi = 45°$

Figure 5: Singular values of time-weighted controllability Gramian for cases with (a) one actuator and (b) two actuators with separation $\phi = 45°$.

In practice, the rotational speed is likely to vary according to the system operation. Considering a finite range of rotational frequencies within the interval (a, b), the problem of maximizing the controllability for the worst-case operating speed may be defined by the following mini-max optimization problem:

$$\text{Minimize} \max_{\Omega \in (a,b)} g\left(\phi, \Omega\right) \text{ over } \phi \in (0, \pi) \tag{37}$$

So far, the issue of sensor placement has not been addressed. In general, the problem of sensor placement optimization based on observability analysis is separable from that of actuator placement [22]. However, under the restriction of actuator-sensor collocation, which is advantageous in admitting simple passivity-based control laws to be used, the problem must be dealt with in an integrated manner. By transforming the model in Eq. (22) to a balanced realization using the standard state transformations [23], the controllability and observability Gramians can be made equal. In this way, the actuator and sensor placement problems become equivalent and a minimization of the cost function in Eq. (33) provides an optimal solution for the case of collocated actuator-sensor pairs.

3.4. Numerical results

Without rotation, the cross-coupling terms in A_m due to Coriolis effects ($\pm\Omega g_m$) become zero and so the modal state variables $p_m(t)$ and $q_m(t)$ are dynamically uncoupled. In this case, for each circumferential wavenumber m, there are a pair of degenerate modes having equal natural frequency ω_m. These modes involve standing waves with mode shapes differing by a rotation of one quarter of a wavelength, as shown in Fig. 4 for $m = 1, \ldots, 4$. The modes with $m = 1$ correspond to rigid body translation. These do not couple with the piezo patch actuation or sensing. For the flexural modes ($m > 1$), only one of each pair of degenerate modes will couple with a single actuator. The line colors in Fig. 4 indicate which of the modes can be excited/controlled by an actuator at location 1.

If both degenerate modes are to be controlled at low or zero rotational speeds then, clearly, at least two actuators are required. For a pair of actuators with separation of $\phi = 45°$ (as shown by locations 1 and 3 in Fig. 4) an optimal coupling with the $m = 2$ mode-pair is achieved because the bending for each mode shape is maximum at locations 1 and 3. Coupling is also achieved for both modes with $m = 3$. However, for the mode-pair with $m = 4$, the location of actuator 3 is effectively equivalent to that of actuator 1 and so controllability of both degenerate modes cannot be attained in the non-rotating case. These observations are supported by the analysis of the time-weighted controllability Gramian $\tilde{W}_c$, as defined by Eq. (32). The

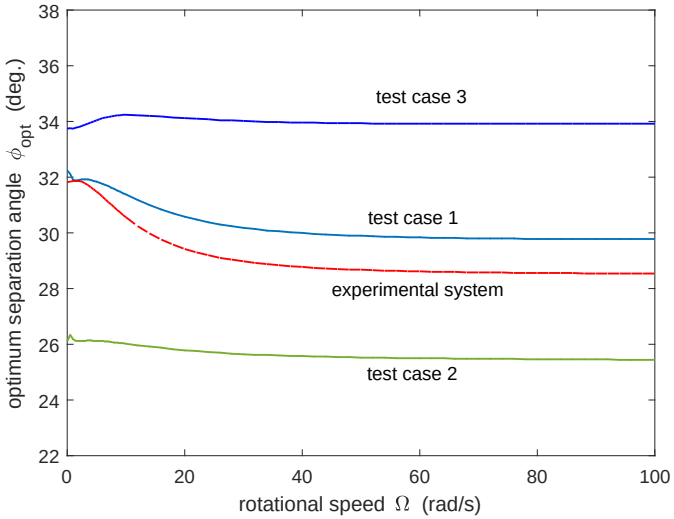

Figure 6: Variation in optimal separation of two actuator/sensor pairs with rotational speed. All cases are for targeted modes $m = 2, 3, 4$ with different initial modal damping levels (see table 2)

singular values of $\tilde{W}_c$ with $\gamma = 10\, s^{-1}$ are shown in Fig. 5 for the six modes with $m = 2, 3, 4$. These results were obtained using parameter values based on the experimental system (Table 1). For the case of a single actuator, it can be seen that three of the six singular values are zero when $\Omega = 0$ (Fig. 5a). For the case of two actuators with $\phi = 45°$, only one singular value (corresponding to $m = 4$) is zero when $\Omega = 0$ (Fig. 5b).

For a single mode-pair, the optimal separation of two actuators is given by ϕ satisfying $\sin m\phi = \pm 1$ (see Eq. (23)). Conversely, a mode-pair is uncontrollable (without rotation) if $\sin m\phi = 0$. Accordingly, the best and worst separation angles for the single-mode actuation problem are

$$\phi_{best} = \frac{1+2n}{m} \times 90°,\ \phi_{worst} = \frac{n}{m} \times 180°,\ n = 0, 1, m.$$

So it can be seen that, the best actuator separations for controlling each mode pair $m = 2, 3, 4$, are $\phi = 45°, 30°, 22.5°$, respectively.

Based on Fig. 4, it may be expected that positioning a second actuator at location 2 instead of location 3 would provide coupling with the full set of modes with $m = 2, 3, 4$. However, to find an optimum solution that accounts for both rotation effects and the initial damping levels of the modes, a numerical optimization based on Eq. (36) must be undertaken. Four test cases were considered involving the same target modes, but with different initial levels of damping, as shown in Table 2. For case 1, with equal damping ratios $\zeta_{1,2,3} = 0.0001$, the optimal solution for the separation of two actuators with no rotation is $\phi_{opt}^{\Omega=0} = 31.8°$. For case 2, which involves increased damping for $m = 2$ modes, the optimal solution is weighted towards the other two mode-pairs and decreases to $\phi_{opt}^{\Omega=0} = 26.1°$. For case 3, the damping values result in reduced weighting of the $m = 4$ mode and so the optimal separation increases to $\phi_{opt}^{\Omega=0} = 33.7°$. The variation in the optimal solution ϕ_{opt} with rotational speed is shown in Fig. 6. These results confirm that the controllability metric defined in Eq. (33) has suitable properties for capturing the influence of rotational speed and initial damping for multi-mode optimization problems.

As the optimal separation ϕ_{opt} changes significantly with rotational speed, to obtain a unique (and therefore practical) solution for the actuator placement problem, a finite range of rotational speeds $\Omega \in (0, 100)$ rad/s was considered within the mini-max optimization problem defined by Eq. (37). The objective function involves a two-dimensional surface $g(\phi, \Omega)$ which was evaluated at discrete points within $\phi, \Omega \in (0, \pi) \times (0, 100)$ in order to solve by a direct search method. The optimization results for the test cases are shown in the bottom row of Table 2. Curves for the controllablilty metric for the experimental system with $\Omega \in (0, 100)$ are shown in Fig. 7. It can be seen that the optimal values for ϕ (indicated by the vertical

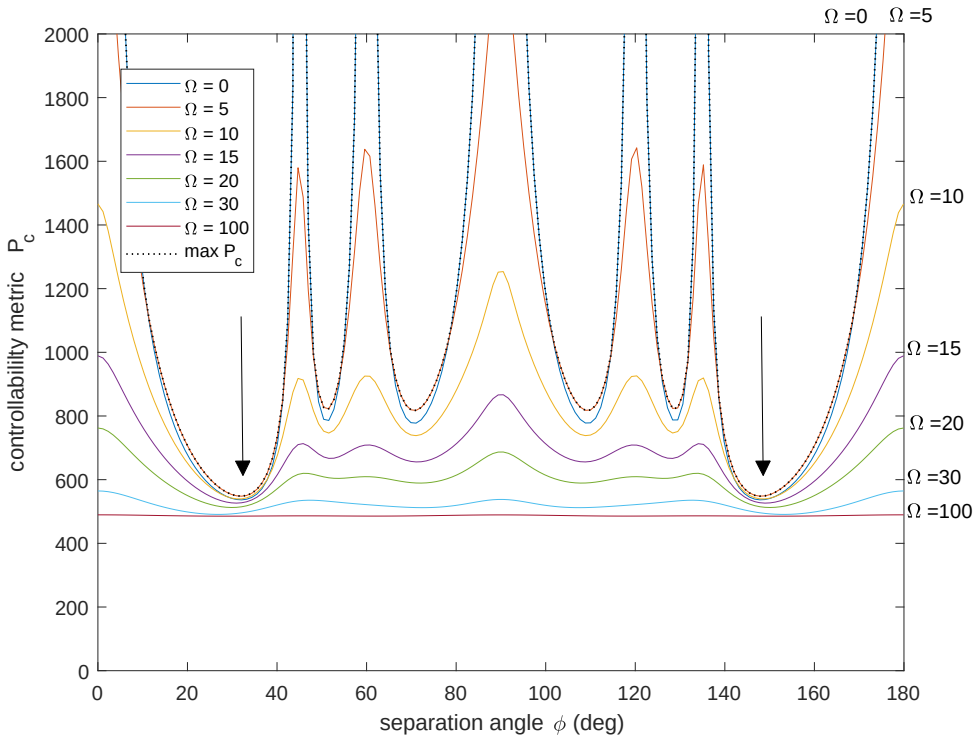

Figure 7: Optimization curves for actuator placement problem with targeted modes m=2,3,4. Curves are shown for selected rotational speeds. The lowest upper bound provides the optimal solution of the mini-max problem for a speed range $\Omega \in (0, 100)$ rad/s, as indicated by arrows.

arrows) are very close to the optimal values for zero-speed. This is because the worst-case controllability is found to arise when the rotational frequency is close to zero, irrespective of the actuator locations. This behaviour is seen for all the test cases in Table 2 and implies that optimizing the actuator placement for the zero-speed case can give a near-optimal solution for any finite range of speeds that includes zero.

Table 2: Test cases for placement optimization of two actuator/sensor pairs for target modes $m = 2, 3, 4$. The four cases involve differing levels of initial modal damping.

		Experimental system	Test case 1	Test case 2	Test case 3
	Index	ζ_m	ζ_m	ζ_m	ζ_m
Modal damping	$m = 2$	0.003	0.0001	0.01	0.0001
	$m = 3$	0.0009	0.0001	0.0001	0.0001
	$m = 4$	0.0004	0.0001	0.0001	0.001
Optimization for $\Omega = 0$ rad/s	$\phi_{opt}^{\Omega=0}$	$31.8°, 148.2°$	$32.2°, 147.8$	$26.1°, 153.9°$	$33.7°, 146.3°$
Optimization for $\Omega \in (0, 100)$ rad/s	$\phi_{opt}^{\Omega\in(0,100)}$	$31.9°, 148.1°$	$32.0°, 148.0°$	$26.2°, 153.8°$	$33.8°, 146.2°$

4. Experiments

4.1. System description

The main components of the experimental system are shown in Fig. 8. The system comprises a thin-walled cylinder with radius $r = 222$ mm, wall thickness $d = 3.1$ mm and axial length of 51 mm. The cylinder was machined from stainless steel (grade 420J2) and has the mechanical properties listed in Table

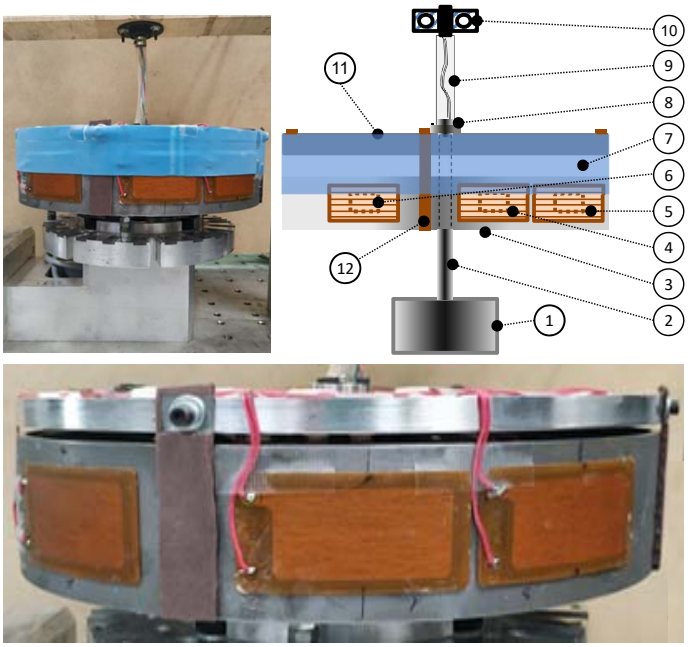

Figure 8: Test system: Schematic (Right); Photograph (Left); Photograph without silicone rubber tube (Bottom). Main components are 1, motor; 2, rigid shaft; 3, steel cylinder; 4-6, piezo patch actuator/sensor pairs; 7, soft silicone rubber connecting tube; 8, mechanical hub; 9, electric wires; 10, slip ring; 11, circular disk; 12, foam rubber strip.

1. The cylinder was coupled to a circular disk with rigid shaft driven by a brushless d.c. motor. The method of supporting the cylinder includes a soft silicone rubber tube and four foam rubber straps (90° separation). These were attached to the outside of the cylinder and circular disk with adhesive. The space between the cylinder and the circular disc was 4 mm. This architecture was designed to minimize the external constraints on the radial dynamics of the cylinder. Three piezoelectric patch actuators of the type P-876A15 from Physik Instrumente were bonded to the outside surface of the cylinder at angular positions $\theta = 0°$, 31.8° and 45° . Three piezoelectric sensors (PI P-876SP1) were attached to the inside surface of the cylinder, concentric with the actuators. The electric wires for the actuators and sensors were connected to the rotating system through slip-rings. The data acquisition, analysis and feedback control algorithms were implemented digitally with PC-based hardware. The sampling frequency was set to 8000 Hz for all tests. A schematic of the control system structure is shown in Fig. 9.

4.2. Control implementation

The decentralized controller implementation involved up to three separate control loops for each collocated actuator/sensor pair. Active damping control was implemented in the form of a synthetic proof-mass-damper (PMD) control law with parameters tuned to provide effective damping for each resonance seen in the system FRF. Hence, each collocated actuator/sensor pair was controlled with feedback based on the following continuous-time transfer function:

$$F_m(s) = \frac{K_m s}{s^2 + 2\tilde{\zeta}_m \tilde{\omega}_m s + \tilde{\omega}_m^2} \tag{38}$$

The natural frequency $\tilde{\omega}_m$ and damping ratio $\tilde{\zeta}_m$ of each PMD was tuned to match the anti-resonance seen in the system FRF (which occurs above each resonance frequency of the cylinder). In this way, the control loop provides increased phase advance and gain close to the resonance frequency. The fast gain roll-off above $\tilde{\omega}_m$ helps to avoid destabilization of higher frequency modes that are not targeted in the design. As the

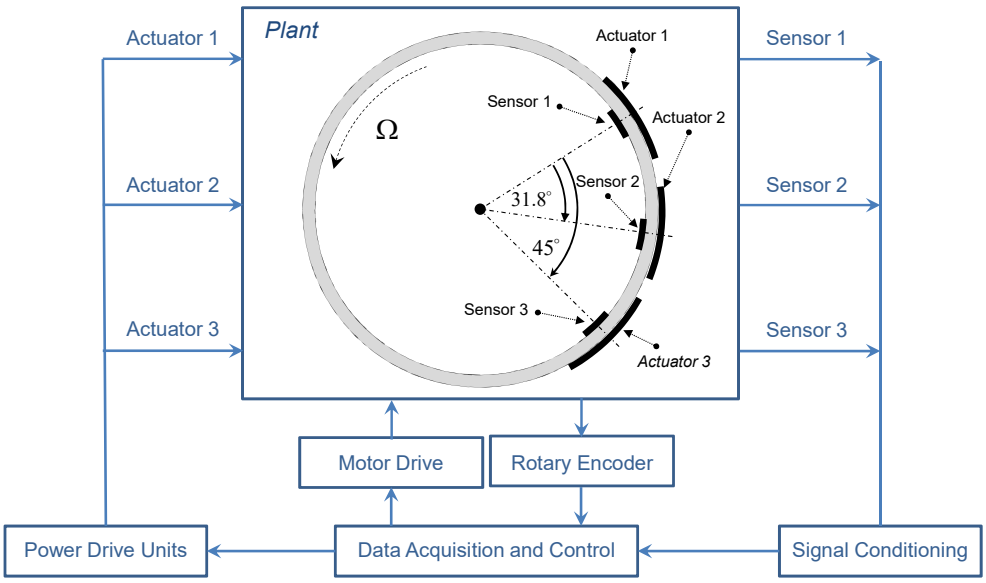

Figure 9: Schematic showing patch locations and control system structure for experimental system.

frequencies for resonance and anti-resonance vary with rotational speed of the cylinder, the transfer function parameters were tuned to match specific values of Ω. Controller tunings are summarized in Table 3 for rotational frequencies of 0, 3 and 13 Hz (or 0, 18.8, 81.7 rad/s). The PMD parameters were determined using the open-loop frequency response measurements, as shown in Fig. 10, while the gain values K_m were tuned empirically.

For implementation, a discrete-time equivalent was calculated based on a direct pole-zero mapping:

$$C_m(z) = K_m \frac{z-1}{T_s} \cdot \frac{z+1}{z^2 - 2\mathrm{Re}(\alpha_m)\, z + |\alpha_m|^2} \tag{39}$$

where α_m is the complex-valued z-plane pole given by $\alpha_m = e^{\tilde{q}_m T_s}$, with $\tilde{q}_m = -\tilde{\zeta}_m \tilde{\omega}_m + \mathrm{j}\tilde{\omega}_m \sqrt{1-\tilde{\zeta}_m^2}$, and T_s is the sampling period. The overall control law for each control loop is then obtained as a summation of $C_m(z)$ for all targeted modes. Thus, each control loop is defined in the z-domain by $U_n(z) = G_d(z) Y_n(z)$ where

$$G_d(z) = \frac{z-1}{T_s} \sum_m K_m \cdot \frac{z+1}{z^2 - 2\mathrm{Re}(\alpha_m)\, z + |\alpha_m|^2} \tag{40}$$

4.3. Experimental results

Figure 10 shows the measured frequency response using actuator/sensor pair 1 for cases without control and with control via a single PMD control loop. The subplots show cases without rotation and with rotation

Table 3: System dynamic properties and coefficients of control law.

	System modes $\Omega = 0$		PMD tuning $\Omega = 0$		PMD transfer function gains K_m		
Modes	ω_m (Hz)	ζ_m	$\tilde{\omega}_m$ (Hz)	$\tilde{\zeta}_m$	$\Omega = 0$ Hz	$\Omega = 3$ Hz	$\Omega = 13$ Hz
$m = 2$	161	0.003	171	0.01	0.0176	0.0178	0.0193
$m = 3$	442	0.009	470	0.01	0.0263	0.0263	0.0265
$m = 4$	846	0.0004	899	0.01	0.0932	0.0930	0.0937
$m = 5$	1376	0.0002	-	-	-	-	-

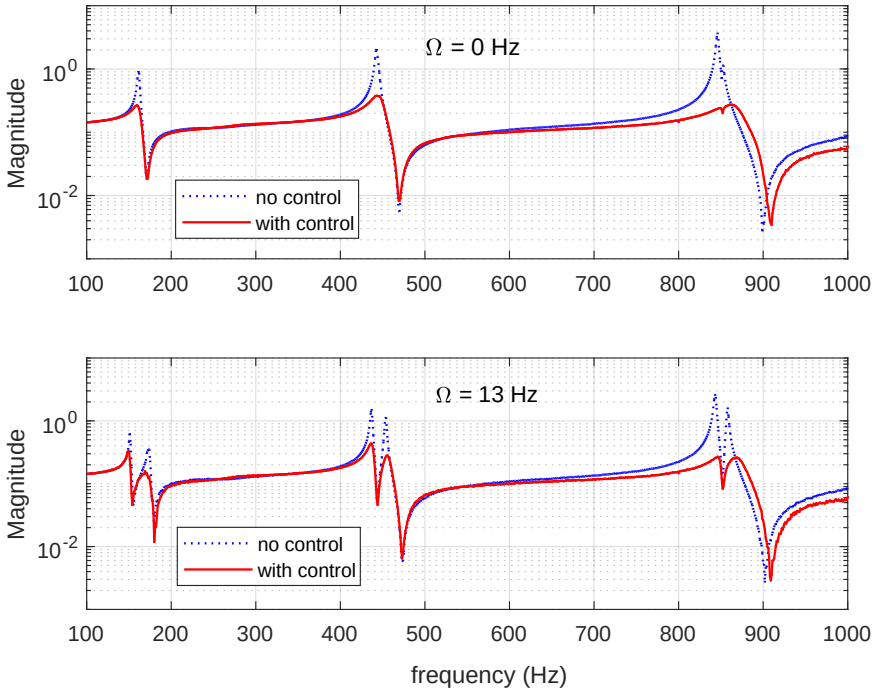

Figure 10: Frequency response measurements with single PMD feedback control loop: Control and excitation applied through transducer pair 1.

at a frequency of 13 Hz. With closed loop control, increased damping is evident for all the modes excited through actuator 1, both with and without rotation. It should be recognised, however, that the complete situation with regard to modal damping levels is not revealed by these single-input single-output test results.

Figure 11 shows the frequency response data for the same case, where control is applied using actuator/sensor pair 1, but with excitation and measurement using pair 3. In the non-rotating case, large resonances are seen, caused by the modes that are not controlled effectively by actuator 1 (i.e. for the $m = 2$ and $m = 3$ modes). However, with rotation, effective damping of each mode-pair is achieved and the resonances are significantly reduced. For the $m = 4$ modes, no resonance is seen, either with or without rotation. This result is consistent with the theoretical prediction that, in the non-rotating case, there is one $m = 4$ mode that is uncontrollable by actuator 1. However, this mode is also unexcitable by actuator 3 because the separation of the two actuators is $\phi = 45°$. Consequently, low damping of the uncontrolled mode is not exposed by the test data.

Figure 12 shows transient response measurements for excitation with a half sine impulse of 5 ms duration. The PMD control loops were applied for three different cases:

1. Without control.
2. With one PMD control loop via actuator/sensor pair 1.
3. With two PMD control loops via actuator/sensor pairs 1 and 3 (having 45° separation).

All cases were examined for three rotation speeds of 0, 3 and 13 Hz (0, 18.8, 81.7 rad/s). Note that, for the results in Fig. 12, the $m = 2$ modes dominate the vibration response. The beating vibration due to the differing natural frequencies of the mode-pair can be clearly observed for high speed rotation. Qualitatively, these results can be directly related to the theoretical evaluations. The use of one actuator is sufficient to dampen the vibration at a high rotation speed (13 Hz). However, at a low rotational speed (3 Hz) or without rotation (0 Hz), the results with only one actuator are similar to the cases without control as the damping of the weakly controllable modes is unchanged.

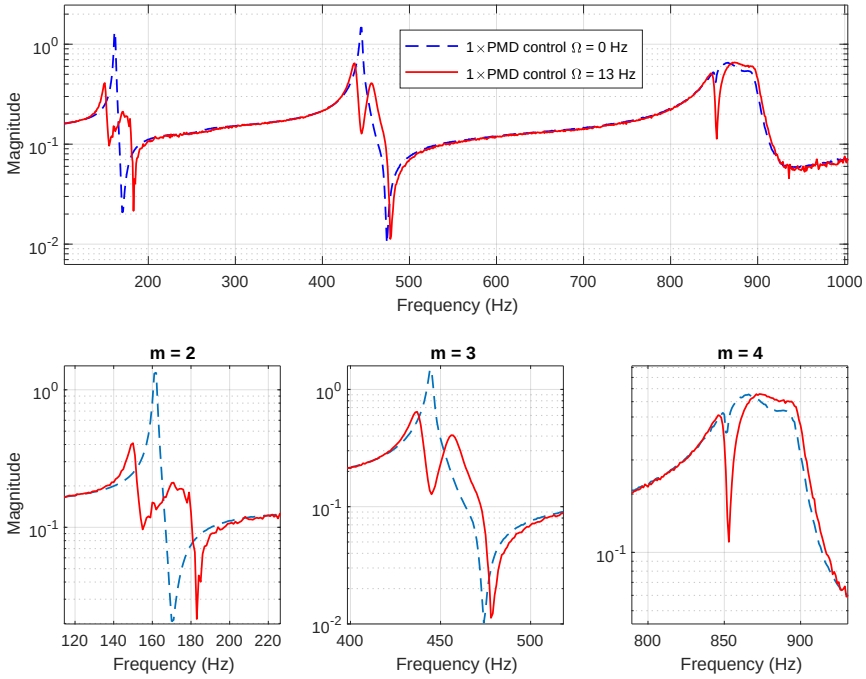

Figure 11: Frequency response with single PMD control loop applied using transducer pair 1 and with excitation/measurement through pair 3.

Frequency response measurements for the case of two PMD control loops with patch angular separation of $\phi = 45°$ (pairs 1 and 3) are shown in Fig. 13. Without rotation, the controller achieves effective damping of the $m = 2$ modes only. However, with rotation, improved damping of all three mode pairs is achieved. These results are consistent with the theoretical analyses of speed-dependent controllability, and with the transient response measurements in Fig. 12.

To achieve effective damping of all three mode pairs ($m = 2, 3, 4$), the PMD control loops were implemented via the actuator/sensor pairs 1 and 2 having angular separation of $\phi = 31.8°$. According to the controllability optimization results, this should provide effective coupling with the complete set of modes $m = 2, 3, 4$. Figure 14 shows the frequency response measurements where excitation is through pair 3. Significantly higher damping ratios are achieved for the $m = 3$ and $m = 4$ mode-pairs compared with the case $\phi = 45°$, and the reduction of the resonance peaks is similar for all three mode-pairs. Also, effective damping control is achieved over the full range of rotational speeds. These results confirm the suitability of the time-weighted controllability metric as an objective function within the actuator placement optimization problem.

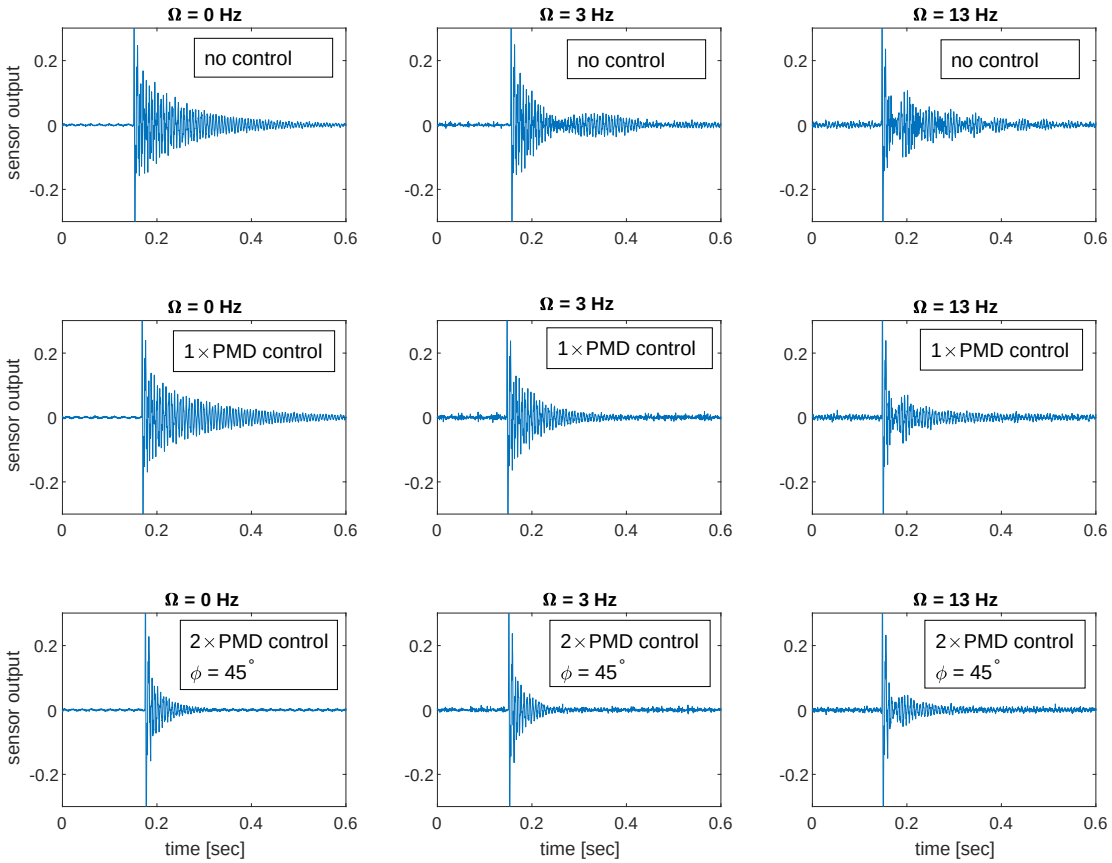

Figure 12: Time response plots for half-sine impulse excitation: PMD control loops applied using transducer pair 1 and pair 3 (45° separation) with excitation through pair 2.

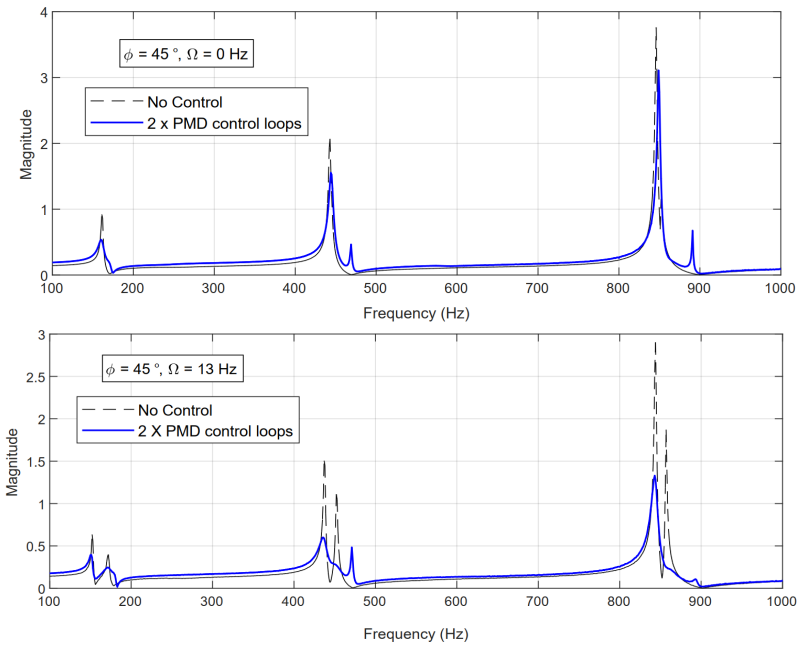

Figure 13: Results of applying two PMD control loops with separation of 45° (pairs 1 and 3) with excitation through transducer pair 2.

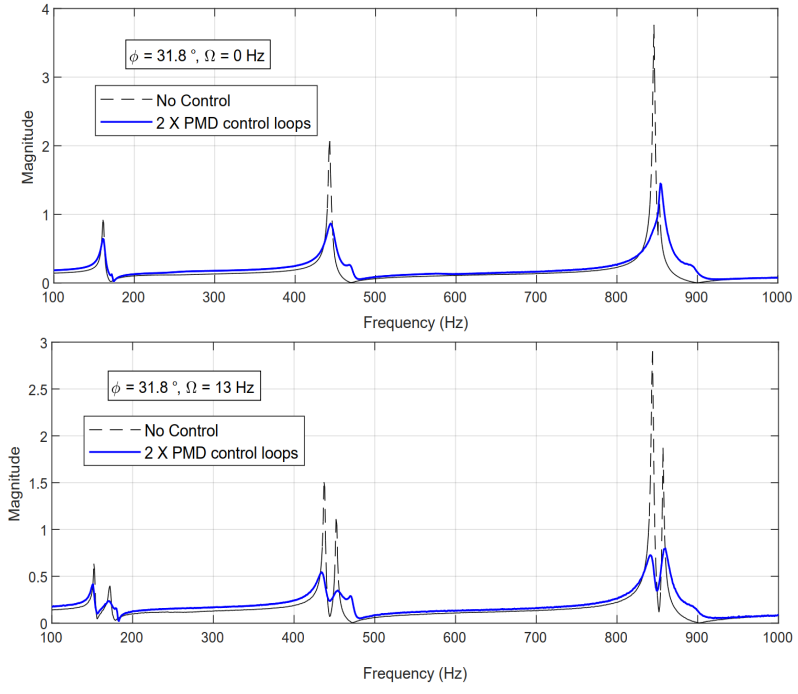

Figure 14: Results of applying two PMD control loops with optimal separation of 31.8° (pairs 1 and 2) with excitation through transducer pair 3.

5. Conclusions

In this paper, the optimal placement of piezoelectric actuators for suppressing elastic vibration of a thin rotating ring has been investigated. A theoretical model for flexural dynamics involving bending and extension in the plane of a rotation was adopted and a time-weighted controllability metric used to calculate the optimal locations of actuators for a given set of targeted modes and range of rotational speeds. The proposed metric takes account of speed-dependent Coriolis effects and also the initial damping level of targeted modes. In addition to the mode shapes, these are found to be key factors in determining the optimal location for actuator placement. For the case of a rotating cylinder, only one actuator is required to achieve active damping of vibration modes involving circumferential traveling waves. However, for systems that operate over a range of rotational speeds, at least two actuators are required to achieve effective control of any given set of vibration modes at low or zero rotational speed.

An experimental validation was undertaken involving a thin steel cylinder, where decentralized feedback controllers were implemented using a synthetic proof-mass-damper control law. The results demonstrated that the use of two actuator/sensor pairs was sufficient to achieve significant increases in damping for the six lowest frequency vibration modes over the designated range of operating speeds, but only if the actuator placement was consistent with the described optimization criteria. The results also confirm the suitability of the theoretical models and quantitative analysis of speed-dependent control influence for the actuator/sensor placement problem. The results have important implications and may be extended for cases with more complex thin-walled rotating structures, where the impact of rotation effects on controllability should be accounted for in the design of active vibration control strategies.

Acknowledgments

This work was supported by the Thailand Research Fund and Chiang Mai University under grant [BRG5980013].

References

[1] G. H. Bryan. On the beats in the vibrations of a revolving cylinder or bell. *Proceedings of the Cambridge Philosophical Society*, pages 101 – 111, 1890.

[2] X. Liu, G. Cai, F. Peng, and H. Zhang. Piezoelectric actuator placement optimization and active vibration control of a membrane structure. *Acta Mechanica Solida Sinica*, 31(8):66–79, Aug 2018.

[3] C. Chamroon, M.O.T. Cole, and W. Fakkaew. Model and control system development for a distributed actuation magnetic bearing with thin-walled rotor subject to non-circularity. *ASME Journal of Vibration and Acoustics*, 141:051006–1–11, 2019.

[4] T. Nestorovic, N. Durrani, and M. Trajkov. Experimental model identification and vibration control of a smart cantilever beam using piezoelectric actuators and sensors. *Journal of Electroceramics*, 29(1):42–55, 2012.

[5] V. Guota, M. Sharma, and N. Thakur. Optimization criteria for optimal placement of piezoelectric sensors and actuators on a smart structure: A technical review. *Journal of Intelligent Material Systems and Structures*, 21:1227–1243, 2010.

[6] J. Lou, J. Liao, Y. Wei, Y. Yang, and G. Li. Experimental identification and vibration control of a piezoelectric flexible manipulator using optimal multi-poles placement control. *Journal of Applied Sciences*, 7(6):309, Jun 2017.

[7] M.Jeong M.K. Kwak, S.Heo. Dynamic modelling and active vibration controller design for a cylindrical shell equipped with piezoelectric sensors and actuators. *Journal of Sound and Vibration*, 321:510–524, 2009.

[8] J. Oh M.C. Ray and A. Baz. Active constrained layer damping of thin cylindrical shells. *Journal of Sound and Vibration*, 240(5)(1):921–935, 2001.

[9] M.C. Ray and J.N. Reddy. Active control of laminated cylindrical shells using piezoelectric fiber reinforced composites. *Composites Science and Technology*, 65(5):1226–1236, 2005.

[10] G. Caner. *Active Vibration Control of Beams and Cylindrical Structures using Piezoelectric Patches*. PhD thesis, Middle East Technical University, 2014.

[11] K. P. Duffy, B. B. Choi, A. J. Provenza, J. B. Min, and N. Kray. Active piezoelectric vibration control of subscale composite fan blades. *Journal of Engineering for Gas Turbines and Power*, 135(7):011601, 2013.

[12] Ashish Kumar and M.C. Ray. Control of smart rotating laminated composite truncated conical shell using acld treatment. *International Journal of Mechanical Sciences*, 89(1):123–141, 2014.

[13] Y. Xing, B. Liu, and T. Xu. Exact solutions for free vibration of circular cylindrical shells with classical boundary conditions. *International Journal of Mechanical Sciences*, 75(4):178–188, 2013.

[14] N. Alujevic, N. Campillo-Davo, P. Kindt, W. Desmet, B. Pluymers, and S. Vercammen. Analytical solution for free vibrations of rotating cylindrical shells having free boundary conditions, engineering structures. *Engineering Structures*, 132:152–171, 2017.
[15] W. Soedel. *Vibration of Shells and Plates*. CRC Press, 2004.
[16] G. Genta. *Dynamics of rotating systems*. Springer Science & Business Media, 2009.
[17] M. Endo, K. Hatamura, M. Sakata, and O. Taniguchi. Flexural vibration of a thin rotating ring. *Journal of Sound and Vibration*, 92(2):261 – 272, 1984.
[18] M.O.T. Cole and W. Fakkaew. An active magnetic bearing for thin-walled rotors: vibrational dynamics and stabilizing control. *IEEE/ASME Transactions on Mechatronics*, 23:2859–2869, 2018.
[19] Z. Brand and M.O.T. Cole. Results on active damping control of a thin-walled rotating cylinder with piezoelectric patch actuation and sensing. *The Third IEEE Conference on Control Technology and Applications, Hong Kong, August,*, 2019.
[20] A. E. H. Love. *A treatise on the mathematical theory of elasticity, 4th Edition*. Dover Publication, 1944.
[21] A. Hac and L. Liu. Sensor and actuator location in motion control of flexible structures. *Journal of Sound and Vibration*, 167:239–261, 1993.
[22] I. Bruant, L. Gallimard, and S. Nikoukar. Optimal piezoelectric actuator and sensor location for active vibration control, using genetic algorithm. *Journal of Sound and Vibration*, 329:1616–1635, 2010.
[23] K. Zhou, J.C. Doyle, and K. Glover. *Robust and Optimal Control*. Pearson, 1995.